JSCSEN 91(3)213-330(2026)

ISSN 1820-7421(Online)

Journal of the Serbian Chemical Society

Electronic version

VOLUME 91

No 3

BELGRADE 2026

Available on line at

www.shd.org.rs/JSCS/

The full search of JSCS is available through

DOAJ DIRECTORY OF OPEN ACCESS JOURNALS

www.doaj.org

The **Journal of the Serbian Chemical Society** (formerly Glasnik Hemijskog društva Beograd), one volume (12 issues) per year, publishes articles from the fields of chemistry. The **Journal** is financially supported by the **Ministry of Science, Technological Development and Innovation of the Republic of Serbia.**
Articles published in the **Journal** are indexed in **Clarivate Analytics products: Science Citation Index-Expanded™** – accessed *via* **Web of Science®** and **Journal Citation Reports®**.
Impact Factor announced for the year 2024: **0.700; 5-year Impact Factor**: **0.900**.
Articles appearing in the **Journal** are also abstracted by: **Scopus, Chemical Abstracts Plus (CAplus℠), Directory of Open Access Journals, Referativnii Zhurnal (VINITI), RSC Analytical Abstracts, EuroPub, Pro Quest** and **Asian Digital Library.**

Publisher:	**Serbian Chemical Society**, Karnegijeva 4/III, P. O. Box 36, 1120 Belgrade 35, Serbia tel./fax: +381–11–3370–467, E-mails: **Society** – shd@shd.org.rs; **Journal** – jscs@shd.org.rs Home Pages: **Society** – http://www.shd.org.rs/, **Journal** – http://www.shd.org.rs/JSCS/
Internet Service:	Contents, Abstracts and full papers (from Vol. 64, No. 1, 1999) are available in the electronic form at the Web Site of the **Journal** (http://www.shd.org.rs/JSCS/).
Former Editors:	**Nikola A. Pušin** (1930–1947), **Aleksandar M. Leko** (1948–1954), **Panta S. Tutundžić** (1955**–**1961), **Miloš K. Mladenović** (1962–1964), **Đorđe M. Dimitrijević** (1965–1969), **Aleksandar R. Despić** (1969–1975), **Slobodan V. Ribnikar** (1975–1985), **Dragutin M. Dražić** (1986–2006), **Branislav Ž. Nikolić** (2006-2026).
Editor-in-Chief:	DUŠAN **SLADIĆ**, Faculty of Chemistry, University of Belgrade
Deputy Editors:	MARIO **ZLATOVIĆ**, Faculty of Chemistry, University of Belgrade, VLADIMIR **PANIĆ**, Institute of Chemistry, Technology and Metallurgy, University of Belgrade
Sub editors:	
,	
Organic Chemistry	DEJAN **OPSENICA**, Institute of Chemistry, Technology and Metallurgy, University of Belgrade
	JÁNOS **CSANÁDI**, Faculty of Science, University of Novi Sad
Biochemistry and Biotechnology	OLGICA **NEDIĆ**, INEP – Institute for the Application of Nuclear Energy, University of Belgrade
Inorganic Chemistry	BILJANA **GLIŠIĆ**, Faculty of Science, University of Kragujevac
Theoretical Chemistry	MATIJA **ZLATAR**, Institute of Chemistry, Technology and Metallurgy, University of Belgrade
	MILOŠ **MILIČIĆ**, Faculty of Chemistry, University of Belgrade
Physical Chemistry	LJILJANA **DAMJANOVIĆ-VASILIĆ**, Faculty of Physical Chemistry, University of Belgrade
Electrochemistry	SNEŽANA **GOJKOVIĆ**, Faculty of Technology and Metallurgy, University of Belgrade
Analytical Chemistry	RADA **BAOŠIĆ**, Faculty of Chemistry, University of Belgrade
Polymers	BRANKO **DUNJIĆ**, Faculty of Technology and Metallurgy, University of Belgrade
Thermodynamics	MIRJANA **KIJEVČANIN**, Faculty of Technology and Metallurgy, University of Belgrade
Chemical Engineering	TATJANA **KALUĐEROVIĆ RADOIČIĆ**, Faculty of Technology and Metallurgy, University of Belgrade
Materials	RADA **PETROVIĆ**, Faculty of Technology and Metallurgy, University of Belgrade
Metallic Materials and Metallurgy	ANA **KOSTOV**, Mining and Metallurgy Institute Bor, University of Belgrade
Environmental and Geochemistry	VESNA **ANTIĆ**, Faculty of Agriculture, University of Belgrade
History of and Education in Chemistry	DRAGICA **TRIVIĆ**, Faculty of Chemistry, University of Belgrade
English Language Editors:	VLATKA **VAJS**, Serbian Chemical Society
	MIROSLAV **PAVLOVIĆ**, Institute of Chemistry, Technology and Metallurgy, University of Belgrade
Journal Manager & Web Master:	MARIO **ZLATOVIĆ**, Faculty of Chemistry, University of Belgrade
Office:	VERA **ĆUŠIĆ**, Serbian Chemical Society

Editorial Board

From abroad: **R. Adžić**, Brookhaven National Laboratory (USA); **A. Casini**, University of Groningen (The Netherlands); **G. Cobb**, Baylor University (USA); **D. Douglas**, University of British Columbia (Canada); **G. Inzelt**, Etvos Lorand University (Hungary); **J. Kenny**, University of Perugia (Italy); **Ya. I. Korenman**, Voronezh Academy of Technology (Russian Federation); **M. D. Lechner**, University of Osnabrueck (Germany); **S. Macura**, Mayo Clinic (USA); **M. Spiteller**, INFU, Technical University Dortmund (Germany); **M. Stratakis**, University of Crete (Grecce); **M. Swart**, University de Girona (Cataluna, Spain); **G. Vunjak-Novaković**, Columbia University (USA); **P. Worsfold**, University of Plymouth (UK); **J. Zagal**, Universidad de Santiago de Chile (Chile).

From Serbia: **B. Abramović**, **V. Antić**, **R. Baošić**, **V. Beškoski**, **J. Csanadi**, **Lj. Damjanović-Vasilić**, **A. Dekanski**, **V. Dondur**, **B. Dunjić**, **M. Đuran, B. Glišić, S. Gojković**, **I. Gutman**, **B. Jovančićević**, **I. Juranić**, **T. Kaluđerović Radoičić**, **L. Katsikas**, **M. Kijevčanin**, **A. Kostov**, **V. Leovac**, **S. Milonjić**, **V.B. Mišković-Stanković**, **O. Nedić**, **D. Opsenica**, **V. Panić**, **M. Pavlović**, **M. Petkovska**, **R. Petrović**, **I. Popović**, **B. Radak**, **S. Ražić**, **D. Sladić**, **S. Sovilj**, **S. Šerbanović**, **B. Šolaja**, **Ž. Tešić**, **D. Trivić**, **V. Vajs, M. Zlatović**.

Subscription: The annual subscription rate is **150.00 €** including postage (surface mail) and handling. For Society members from abroad rate is **50.00 €**. For the proforma invoice with the instruction for bank payment contact the Society Office (E-mail: shd@shd.org.rs) or see JSCS Web Site: http://www.shd.org.rs/JSCS/, option Subscription.
Godišnja pretplata: Za članove SHD: **2.500,00 RSD**, za penzionere i studente: **1000,00 RSD**, a za ostale: **3.500,00 RSD**:za organizacije i ustanove: **16.000,00 RSD**. Uplate se vrše na tekući račun Društva: **205-13815-62**, poziv na broj **320**, sa naznakom "pretplata za JSCS".

Nota: Radovi čiji su svi autori članovi SHD prioritetno se publikuju.
Odlukom Odbora za hemiju Republičkog fonda za nauku Srbije, br. 66788/1 od 22.11.1990. godine, koja je kasnije potvrđena odlukom Saveta Fonda, časopis je uvršten u kategoriju međunarodnih časopisa (**M-23**). Takođe, aktom Ministarstva za nauku i tehnologiju Republike Srbije, 413-00-247/2000-01 od 15.06.2000. godine, ovaj časopis je proglašen za publikaciju od posebnog interesa za nauku. **Impact Factor** časopisa objavljen za 2024. godinu je **0,700**, a petogodišnji **Impact Factor 0,900**.

Journal of the Serbian Chemical Society
JSCS-info@shd.org.rs • www.shd.org.rs/JSCS

J. Serb. Chem. Soc. Vol. 91, No. 3 (2026)

CONTENTS*

Published by the Serbian Chemical Society
Karnegijeva 4/III, P.O. Box 36, 11120 Belgrade, Serbia
Printed by the Faculty of Technology and Metallurgy
Karnegijeva 4, P.O. Box 35-03, 11120 Belgrade, Serbia

* For colored figures in this issue please see electronic version at the Journal Home Page: http://www.shd.org.rs/JSCS/

Journal of the Serbian Chemical Society
JSCS@tmf.bg.ac.rs • www.shd.org.rs/JSCS
J. Serb. Chem. Soc. *91* (3) 213–225 (2026)
JSCS–5487
Original scientific paper
Published 23 February, 2026

Synthesis and biological evaluation of some drug-like scaffolds of benzo- and pyrido-fused medium-sized *N*-heterocycles obtained *via* intramolecular Friedel–Crafts acylation reactions

HASSAN ABDOU KOTB ABD EL-AAL*

Chemistry Department, Faculty of Science, Assiut University, Assiut, 71516, Egypt

(Received 19 July, revised 17 November 2025, accepted 9 January 2026)

Abstract: An unprecedented, concise and environmentally-friendly protocol for the synthesis of benzo-and pyrido-annulated azocinones, azoninones and azecinones **8a**–**h** *via* Friedel–Crafts reactions is described. These simple and efficient procedures involve cycliacylations of heterocyclic esters **7a**–**h** in the presence of catalytic amount of $AlCl_3/CH_3NO_2$ or TfOH or PPA catalysts as the key step. Starting amides **3a**–**d** were readily obtained by coupling reactions of acryloyl chlorides **2a** and **b** with pyridin-2-amines **1a** and **b**. Developed strategy offers some high selectivity reactions, mild reaction conditions and easy access to complex medium-sized *N*-heterocycles in moderate to good yields. All tetracyclic fused compounds have been screened for antimicrobial activity.

Keywords: Friedel–Crafts cycliacylations; Brønsted acid; azocines; azoninones; azecinones.

INTRODUCTION

Condensed medium-sized *N*-heterocycles containing azepines, azocines and azonines are widely found in pharmacologically active natural products[1] and often incorporated into drugs.[2] A few examples are given in Fig. 1. Interestingly, their aryl- and heteroaryl derivatives are particularly noted for their diverse biological activities[3] and in many industrial applications such as polymeric[4] organic semiconductors and luminescent materials.[5]

Despite the high transannular strain,[6] enthalpic and entropic barriers[7] encountered in the synthesis of nitrogen containing ring systems, the last few decades have witnessed a much efforts dedicated to developing methods for the construction of such ring systems.

In the literature, a variety of well-established methods are used for the synthesis of medium-sized *N*-heterocycles of various ring sizes and include well

* Correspondnce E-mail: hassankotb33@yahoo.com; hassankotb@aun.edu.eg
https://doi.org/10.2298/JSC250719002A

known: transition-metal mediated cyclizations and annulations,[8] ring-closing metathesis (RCM),[9] tandem cleavage-cyclizations,[10] sigmatropic cyclizations,[11] radical-mediated ring expansions and fragmentations,[12] Fischer carbene complexes (FCCs),[13] Diels–Alder reactions,[14] domino cycloadditions[15] and Cope rearrangements.[16]

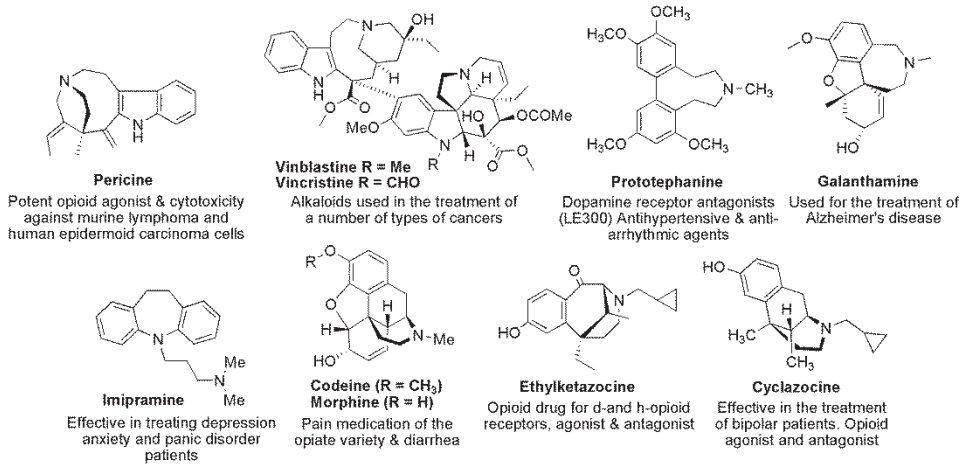

Fig. 1. Some of biologically active alkaloids containing medium-sized *N*-heterocycles.

On the other hand, a significant number of cases are described in the literature related to construction and isolation of benzo-annulated azonines and higher ring systems as in the total synthesis of dopamine antagonists, erythrina and vincristine alkaloids.[17]

A number of the most commonly used methods for the construction of polycyclic azonines include, the Beckmann ring expansion of unsymmetrical oximes,[18] biosynthesis of (*s*)-*N*-benzylisoquinolines and their dienone derivatives,[19] Schmidt rearrangement of alicyclic ketones,[20] ring-closing metathesis (RCM) of 2-pentenylphenyl-*N*-benzamides,[21] Fischer indolization of 1,2,3,4-tetrahydrocarbazole phenylhydrazones,[22] acyloin condensation of diesters,[23] asymmetric induction by the addition of Grignard reagents to phenylglyoxylate derivatives of the phenyldihydrothebaine alkaloids[24] aza-Claisen rearrangement of α-silyloxyamides mediated by lithium hexamethyldisilazide (LHMDS) in toluene,[25] fragmentation/ /acylation reactions of enol-ether of dihydropyridone[26] and coupling of palladated 3-phenylpropanamides with alkynes followed by CO-insertions.[27]

Given the wide array of biologically and industrial applications of *N*-heterocycles, a flexible route to access these types of structures from readily available acyclic precursors would be interesting. Recently we have studied the formation of a diverse drug like carb- and heterocycles[28–30] *via* intramolecular Friedel–Crafts[31] methodology with broad functional group compatibility. In continuation

of research activity on polyfunctionalized heterocyclic systems, herein, we wish to report the synthesis of newly fused and bridged nitrogen containing [6,(6/7),(8/9/10),6]-ring systems namely; benzo- and pyrido-annulated azocinones, azoninones and azecinones *via* Friedel–Crafts cycliacylation reactions of nitrogen containing ester precursors. Furthermore, these polycyclic substrates were tested against bacteria and fungi.

EXPERIMENTAL

Commercially available reagents were used without further purification unless otherwise stated; solvents were dried by standard procedures. Melting points were taken on a digital Gallenkamp capillary melting point apparatus and are uncorrected. Infrared (IR) spectra were obtained on a Perkin–Elmer 1600 FT-IR spectrophotometer using KBr wafer and thin film techniques (ν / cm^{-1}). The ^{1}H- and ^{13}C-NMR spectra were recorded on Jeol LA 400 MHz FT-NMR (400 MHz for ^{1}H-NMR, 100 MHz for ^{13}C-NMR) using $CDCl_3$ solvent with tetramethylsilane (Me_4Si, TMS) as internal standard. Chemical shifts (δ) are given in ppm, and the coupling constants (J) are given in Hz, respectively. Mass spectra were measured on a Perkin––Elmer PE SCIEX-API 2000 mass spectrometer at an ionizing potential of 70 eV using the direct inlet system. Elemental analyses were carried out by a GmbH Vario EL III, 2400, CHNOS-elemental analyzer. Antimicrobial screenings were performed at Assiut University Mycological Center (AUMC) in DMF by disc diffusion. The progress of reactions was accomplished by thin-layer chromatography (TLC) analysis on coated silica plates (Silufol, UV-254 TLC, aluminum sheets) and plates were visualized with UV light (at 254 and/or 360 nm). Flash column chromatography was performed on silica gel (230–400 mesh) or basic alumina using AcOEt and hexane as eluents. The 3-(pyridine-2-yl)acryloyl chloride **2b** was obtained by refluxing a mixture of 3-(pyridin-2-yl)acrylic acid (Lit.[33] m.p. 233–236 °C) with excess PCl_5 in benzene for 5 h on a water bath.

Analytical and spectral data are given in the Supplementary material to this paper.

Chemistry

*General procedure for synthesis of arylamides (**3a**–**d**).* A solution of acid chloride (cinnamoyl chloride **2a** or 3-(pyridine-2-yl)acryloyl chloride **2b** (32 mmol) in benzene (20 mL) was added dropwise with stirring over a period of 30 min to a solution of amines **1a** or **b** (30 mmol) in dry benzene (30 mL) containing a catalytic amount of pyridine (0.5 mL). The resulting mixture was stirred at room temperature for 4 h, and then refluxed on a steam bath for 3 h. The mixture was cooled and the solvent was then concentrated *in vacuo*. After standing, the resulting solid was filtered to give the crude amides. The residue was purified by flash chromatography (basic alumina, AcOEt/hexane, 1:1) to afford pure amides **3a**–**d**.

*General procedure for synthesis of lactams (**4a**–**d**).* A mixture of amide **3a**–**h** (20 mmol) with anhydrous $AlCl_3$ (50 mmol) and NaCl (5 g) was warmed with stirring at 80–90 °C for 1 h. After which TLC analysis (EtOAc/*n*-hexane, 1/3) indicated that the reaction was complete, the resulting hot mixture was poured into an excess of well-stirred ice water (150 mL) and then basified with NaOH solution (40 mL, 20 %). The mother liquor was diluted with water (100 mL) and extracted with EtOAc (3×30 mL). The combined extracts were washed with water, dried over $MgSO_4$ and filtered. The solvent was removed *in vacuo* to give a crude product. Purification by flash column chromatography (basic alumina, EtOAc/*n*-hexane, 1/1) gave pure products **4a**–**d**.

*General procedure for synthesis of bicyclic amines (**5a**–**d**).* To an ice-cold stirred suspension of $LiAlH_4$ (30 mmol) in ether (40 mL), was added a solution of lactam **4a**–**d** (10 mmol) in THF (30 mL) dropwise with efficient stirring over a period of 30 min. The mixture was stirred at room temperature for 2 h and then refluxed for 4 h on water bath. After cooling in ice-bath, excess hydride was carefully destroyed by sequential addition of cold water (5 mL) and aqueous NaOH solution (20 mL, 10 %) with efficient stirring. The resulting suspension was stirred for 30 min. After filtration and washing the precipitate with AcOEt, the precipitate was discarded and the filtrate was extracted with AcOEt (3×30 mL). The combined organic phase was washed with water, $NaHCO_3$ (30 mL, 5 %), and dried over anhydrous $MgSO_4$. The solvent was evaporated under reduced pressure to give a dark crude products **5a**–**d**. Purification by flash column chromatography (basic alumina, EtOAc/*n*-hexane, 1/1) afforded the target amines **5a**–**d**.

*General procedure for the synthesis of heterocyclic esters (**7a**–**h**).* A solution of ethyl 2--bromoacetate **6a** or ethyl 3-bromopropanoate **6b** (20 mmol) in DMF (15 mL) was added dropwise with efficient stirring over 10 min to a mixture of bicyclic amine **6a**–**d** (15 mmol) and milled K_2CO_3 (40 mol) in DMF (30 mL) at room temperature. The reaction mixture was refluxed for 8–10 h. After which TLC analysis (AcOEt/hexane, 1/2) showed the reaction was completed, the solvent was removed *in vacuo* and the residue was diluted with water (100 mL) and extracted with AcOEt (3×30 mL). The combined organic layer was washed with water, dried over $MgSO_4$, filtered and concentrated *in vacuo*. The residue was purified by flash chromatography column to afford crude ester **7a**–**h**.

*General procedure for cyclization of heterocyclic esters **8a**–**h***

*Method I: General procedure for $AlCl_3$/CH_3NO_2-mediated cyclizations of esters (**8a**–**h**).* To a solution of $AlCl_3$ (10 mmol) in CH_3NO_2 (100 mmol) was added a solution of ester **7a**–**h** (3 mmol) in DCM (10 mL) dropwise with constant stirring over 10–15 min at ambient temperature. The mixture was stirred for a certain time at the required temperature (Table I). Afterwards, the mixture was quenched with ice-cold HCl solution (30 mL, 10 %) and extracted with EtOAc (2×30 mL). The combined extract was washed with H_2O and Na_2CO_3 solution (30 mL, 5 %). After drying over $MgSO_4$, the solution was filtrated and evaporated under reduced pressure to give the crude products **8a**–**h**.

*Method II: General procedure for TfOH-mediated cyclizations of esters (**8a**–**h**).* To a cooled (0 °C) solution of esters **7a**–**h** (3 mmol) in DCM (15 mL) was added TfOH (12 mmol) dropwise over 10 min the mixture was stirred at the required temperature and time as shown in Table I. Thereafter, the mixture was cooled and then quenched cautiously by the slow addition of aqueous $NaHCO_3$ solution (40 ml, 30 %). The product was extracted with EtOAc (3×30 mL). The organic extracts were washed with water and Na_2CO_3 solution (30 mL, 5 %), dried over anhydrous Na_2SO_4 and then evaporated *in vacuo* to give the crude products **8a**–**h**.

*Method III: General procedure for PPA-mediated cyclizations of esters (**8a**–**h**).* To a solution of esters **7a**–**h** (3 mmol) in PhCl (15 mL), was added freshly prepared PPA (10 g) and the mixture was refluxed for the required time presented in Table I. Afterwards, the solvent was evaporated under reduced pressure. The cold mixture was made alkaline with $NaHCO_3$ solution (40 ml, 20 %) and then extracted with EtOAc (3×30 mL). The combined organics was washed with water and Na_2CO_3 solution (30 mL, 5 %). After drying over $MgSO_4$, the solution was filtered and concentrated *in vacuo* to afford the desired crude products **8a**–**h**. In all procedures, the completion of the reaction was monitored by TLC-analysis. The crude residue was subjected to flash chromatography (basic alumina, EtOAc/hexane, 1/2) to afford the pure cyclic products **8a**–**h**.

TABLE I. Optimization of Friedel–Crafts cyclizations of precursors **7a**–**h**; Method I: esters **7a**–**h** (3 mmol) in CH_2Cl_2 (10 ml), $AlCl_3$ (10 mmol), $MeNO_2$ (100 mmol), room temperature; Method II: esters **7a**–**h** (3 mmol), TfOH (1 ml, 12 mmol), 1,2-DCE (20 ml), reflux; Method III: esters **7a**–**h** (3 mmol), PPA (10 g), PhCl (15 mL), reflux

Entry	Substrate	Methods	Time, h	Product	Yield, %
1	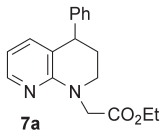 **7a**	Method I Method II Method III	12 8 8	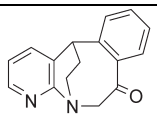 **8a**	82 75 71
2	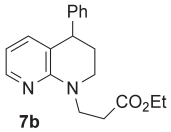 **7b**	I II III	15 5 7	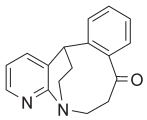 **8b**	80 73 70
3	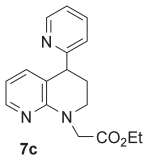 **7c**	I II III	18 6 10	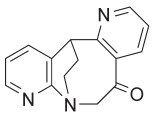 **8c**	84 77 74
4	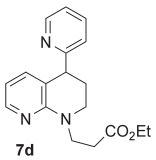 **7d**	I II III	11 8 12	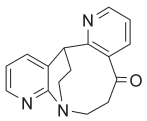 **8d**	88 81 71
5	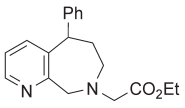 **7e**	I II III	16 10 10	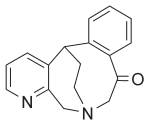 **8e**	84 80 72
6	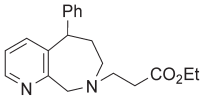 **7f**	I II III	18 7 10	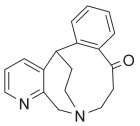 **8f**	91 78 68
7	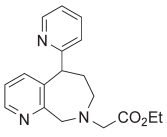 **7g**	I II III	18 6 8	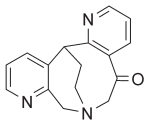 **8g**	90 87 72
8	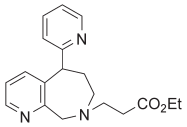 **7h**	I II III	15 6 10	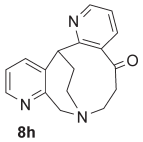 **8h**	89 86 74

RESULTS AND DISCUSSION

Chemistry

The reaction sequences employed for synthesis of polyheterocycles **8a**–**h** from heterocyclic esters **7a**–**h** are illustrated in Scheme 1. Firstly, the starting amides **3a** (n = 0; Ar = Ph), **3b** (n = 0; Ar = 2-pyridyl), **3c**[32] (n = 1; Ar = Ph), **3d** (n = 1; Ar = = 2-pyridyl), were obtained in good yields through the reaction of ary-substituted acryloyl chlorides (**2a**: Ar = Ph; **2b**: Ar = 2-pyridyl[33]) with pyridine amines **1a** and **b** in benzene for 7 h. Secondly, these amides were transformed to the corresponding bicyclic lactams **4a**–**d** by fusion with $AlCl_3$/NaCl at 80–90 °C for 1h following the standard literature procedure.[34] Thirdly, reduction of the latter lactams **4a**–**d** using $LiAlH_4$ in Et_2O/THF for 4–6 h under reflux conditions to furnish bicyclic amines **5a**–**d**. Various substituted esters **7a**–**h** were synthesized *via N*-alkylations of bicyclic amines **5a**–**d** with ethyl 2-bromoacetate **6a** or ethyl 3-bromopropanoate **6b** in the presence of K_2CO_3 in DMF.

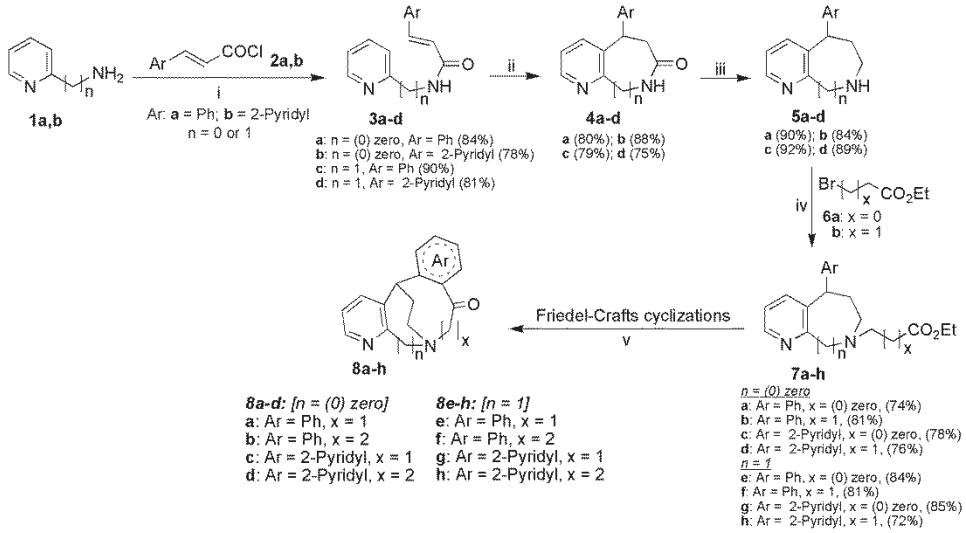

Scheme 1. Reagents and conditions: *i*) cinnamoyl chloride or 3-(pyridine-2-yl)acryloyl chloride/PhH, 7 h, reflux, *ii*) $AlCl_3$/NaCl, 1 h, 80–90 °C, *iii*) $LiAlH_4$/THF/Et_2O, reflux, 4–6 h, NaOH, *iv*) $BrCH_2CO_2Et$ or $BrCH_2CH_2CO_2Et$/K_2CO_3/DMF, reflux, 8–10 h, *v*) cycliacylations of esters **8a**–**h** mediated by $AlCl_3$/CH_3NO_2 or TfOH or PPA promoters (Table I).

Our synthetic approach allows easy access to fused medium-sized *N*-heterocycles **8a**–**h** namely, benzo-fused pyrido[2,3-*b*:2',3'-*e*]azocinones, pyrido[2,3--*b*]azoninones and pyrido[2,3-*c*:2',3'-*f*]azecinones (Table I). Initially, an investigation of $AlCl_3$/CH_3NO_2 or TfOH or PPA catalysts in cycliacylations of nitrogen-based esters **7a**–**h** was carried out under different reaction conditions. We focused on the screening of several variables including, mole ratio, catalyst type

and loading, solvent and temperature. Notably the choice of Brønsted and Lewis acids screened was based on the degree of oxophilicity, chemical yield as well as extent of their acidity.

Interestingly, in this type of electrophilic aromatic substitution reactions containing sufficiently electron rich nucleophiles, the appearance of catalytic inhibitions[35] by sp^2-and sp^3-hybridized nitrogens beside the presence of poor leaving –OEt group present in cyclization precursors **7a**–**h** is obvious. These coordination or protonation of basic nitrogen with acidic promoters leading to ring closure is less likely to occur or gave disappointingly low yields. Practically, low yields of tetracyclic amines **8a**–**h** were obtained on cyclization of precursors **7a**–**h** with less than equivalent of these catalysts at lower reaction time. It was observed that, cycliacylations of electron rich precursors and yield enhancements were attained under severe conditions with more than stoichiometric loading of oxophilic promoter for longer reaction times and high temperatures.

On the other hand, numerous studies on the intramolecular Friedel–Crafts acylation mechanisms have been carried out.[36–38] Thus, it can be concluded that, cyclization mechanism of highly electron-rich precursors diverges to two different pathways based on the nature of the acylating agent and the binding strength of acidic promoters on substrate heteroatoms. A possible mechanism for formation of the compound **8f** is shown in Scheme 2. The cycliacylation mechanism of this reaction is probably similar to that of the Okauchi acylation procedure.[36] It is presumably that, differential in cyclization pathways is due to whether heteroatoms on acyclic ester **7f** were protonated by Brønsted acid proton or the formation of a polarized Lewis acid-acylating agent complex. This coordination's were leading to either alteration in catalyst acidity or decreasing its reactivity beside deactivation of a nucleophilic substrate. It was hypothesized that, the nature of the acylating agent and the strength of the Lewis acid determine the electrophilicity of this complex while the regiochemistry is determined by the transition state.

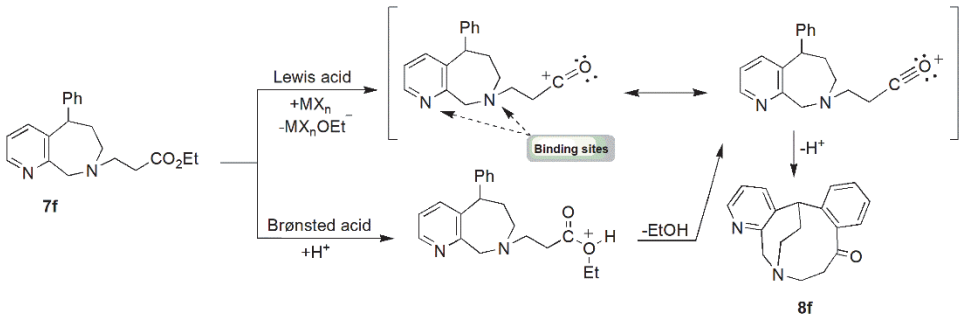

Scheme 2. Proposed mechanism for the cyclization of ester **7f** by Lewis or Brønsted acids.

Subsequently, that would lead to removal of EtOH molecule generating acyl--carbocation either free or as an ion pair.[39] The anticipated acyl-carbocation stabilizes both by resonance delocalizations and adjacent hyperconjugative interactions. Ultimately, ring closures of this carbocation may proceed *via* a single transition states concurrent with the removal of H^+ to give the product **8f** in a single regioisomer.

Further evidence for this result was confirmed by NMR spectroscopy. At closer look on the intermediates **7a**–**f** and cyclic structures **8a**–**h**, we observed that the benzylic-carbon (C-5) is a chiral center and the next methylene group (C-6) protons are diastereotopic[40] in nature. These protons are chemically inequivalent and will split each other resulting in complex overlapping signals with different multiplicities. In addition to diastereotopic protons and because of the flexibility of these ring systems, other constitutional conformers with inequivalent sets of cyclic methylene protons (pseudo-axial and equatorial hydrogens) emerged from a large number of low energy interconverting conformers. Interesting stereochemical outcomes were observed during this study. Since cyclization precursors and products were conformer mixtures with different chemical environments and chirality, NMR interpretation was difficult. Efforts were made to understand the reactivity profiles of these building blocks and to identify the configuration of unique structures and bonding characteristics of these ring systems. The assignment of all chemical structures of the cyclic products was made on the direct inspection of the ^{1}H-NMR spectrum.

For example, the ^{1}H-NMR spectrum of compounds **7f** and tetracyclic **8f** displayed complex signals of CH_2-group adjacent to the stereogenic center and bridged pseudo-axial and equatorial protons (Fig. 2). Moreover, the neighboring environment of bridged *N*-CH_2 group is very unsymmetrical due to the ring conformations. The expected downfield shifting signal for pseudo-equatorial could be explained in terms of shielding effect exerted by the magnetic anisotropic effect generated by heteroatoms of both carbonyl groups and *N*-heteroatoms incorporated in tetracyclic structures.

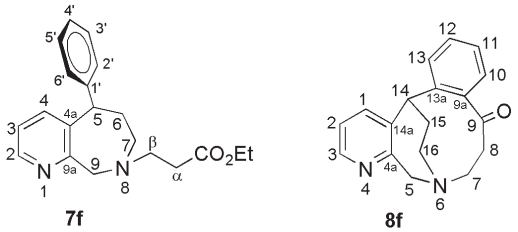

Fig. 2. Diastereotopic protons containing tetracyclic structure **8f** and its acid precursor **7f**.

Thus, the ^{1}H-NMR spectrum of **7f** showed three upfield triplet signals at δ 1.18, 2.48 and 2.93 ppm related to $\underline{CH_3}CH_2O$–, $C^{\alpha}H_2$ and $C^{\beta}H_2$ groups. The most

downfield quartet signal at δ 4.28 ppm was assigned to the $CH_3\underline{CH_2}O$-group. The complex overlapped multiplets at δ 2.05 ppm is assigned to the diastereotopic protons (Ha & Hb) of C^6H_2-group appeared as doublet of doublets of doublets of doublets (d*ddd*) with four vicinal coupling constants 13.9, 6.6, 4.7 and 2.6 Hz. Another upfield multiplet signal at δ 2.91 ppm assigned to C^7H_2 group appeared as doublet of doublets of doublets with coupling constants 7.8, 6.6 and 2.6 Hz. Two signals appearing at δ 4.01 and 4.17 ppm are assigned to C^7H and *N*-C^9H_2, respectively. These upfield shifts can be explained by shielding due to the magnetic anisotropic effect[49] generated by heteroatom or the carbonyl group. The remaining eight aromatic protons appeared in the range of δ 7.10–8.60 ppm with inner overlapping and different multiplicities.

In comparison with ester **7f**, the ^{1}H-NMR spectrum of tetracyclic skeleton **8f** displayed as several complex overlapped signals. The most upfield with multiplicity of doublet of doublets of doublets of doublets at δ 2.66 ppm is assigned to the bridged-$C^{15}H_2$ with couplings 11.1, 7.7, 6.3 and 2.2 Hz. The complex multiplet signals in the regions of δ 3.08–3.10, 3.32–3.41 and 3.48–3.50 ppm were assigned to C^8H_2, bridged-*N*$C^{16}H_2$ and C^7H_2 groups, respectively. Chemically inequivalent C^5H_2-protons are expected to appear in the range of δ 4.37–4.48 ppm as doublet of doublets with coupling constants 8.6 and 6.9 Hz. A doublet signal appeared at δ 4.45 ppm is assigned to bridged-$C^{14}H$ proton. The diagnostic signal in the ^{13}C--NMR spectrum of **8f** is that of the carbonyl carbon at δ 200.8 ppm. The upfield signals at δ 31.2, 32.9, 35.9, 51.4, 53.4 and 59.5 ppm are assigned to $C^{14}H$, bridged-CH_2, C^8H_2CO, C^7H_2, C^5H_2 and bridged-$C^{16}H_2$, respectively. Comparison of the fragmentation patterns of compounds ester **7f** with tetracyclic **8f** show some quantitative and qualitative differences attributed to the nature of both the substituents at the 5-position of the bicyclic ring system and at the nitrogen atom. The mass spectra of ester **7f** are much simpler and contain only molecular ion peaks *m*/*z* 324 with intensity 20 % and the base peak appeared at *m*/*z* 279. Whilst, the molecular ion peak of **8f** appeared at 278 as a base peak (100 %).

Evaluation of antimicrobial activity

The antimicrobial activity of the synthesized compounds **8a**–**h** was determined *in vitro* against a variety of bacteria and fungi. The antibacterial activity was investigated against Gram-positive bacteria *(Bacillus Subtilis*, *Micrococcus luteus*) and Gram-negative bacteria (*Escherichia coli*, *Pseudomonas aeruginosa*) using chloramphenicol (0.001 mol/ml) as standard. The antifungal activity was determined against *Aspergellius flavus*, *Candida albicans*, *Geotrichum candidum* and *Scopulariopsis brevicaulis* using clotrimazole (0.001 mol/ml) as standard. The tests were carried out using disc diffusion method.[41] The minimum inhibitory concentrations (*MICs*) for compounds were calculated in DMF/H_2O solution and activity mentioned on 1000 ppm.

The results are summarized in Table II. Amongst the compounds tested for antibacterial activity, compounds **8c**, **8d**, **8g** and **8h** possess good activity against all the bacteria, whereas compounds **8a**, **8b**, **8e** and **8f** were found to display moderate activity against *M. luteus*, *E. coli* and *P. aeruginosa* and low activity against Gram-positive bacteria (*B. cereus*).

TABLE II. Antimicrobial activity of the compounds **8a**–**h**

Compd.[a] no.	Antibacterial activity Zone of inhibition, mm[b]				Antifungal activity Zone of inhibition, mm			
	Gram positive		Gram negative					
	B. cereus	*M. luteus*	*E. coli*	*P. aeruginosa*	*A. flavus*	*C. albicans*	*G. candidum*	*S. brevicaulis*
8a	7	10	15	14	10	11	10	11
8b	5	16	12	13	11	10	13	16
8c	44	37	22	52	16	14	13	15
8d	25	16	19	26	10	17	12	12
8e	6	15	17	20	13	11	10	13
8f	9	17	20	18	15	13	14	10
8g	58	39	36	64	22	19	24	31
8h	37	28	38	45	13	26	15	36
Standard[c]	20	23	22	22	26	22	20	25

[a]Chemical compounds tested at 20 mg; [b]the minimal inhibitory concentrations (*MIC*, 50 μg/ml) for each pore in DMF/H_2O; [c]standard for antibacterial: chloramphenicol (0.001 mol/ml); standard for antifungal: clotrimazole (0.001 mol/ml)

From the data presented in Table II, it was observed that compounds **8c**, **8d**, **8g** and **8h** show good activity against all fungal strains as compared to standard chloramphenicol. Other compounds **8a**, **8b**, **8e** and **8f** showed moderate antifungal activity. Further, it could be concluded that, due to the increasing of ring size and the insertion of additional pyridine nucleus in a complex molecular structures, compounds **8g** and **8h** showed relatively better inhibitory activity towards all the tested microorganisms than compounds **8c** and **8d**.

CONCLUSIONS

In summary, the present work embodies a facile and concise synthesis of several benzo- and pyrido-fused azocinones, azoninones and azecinones incorporating 8-, 9- and 10-membered *N*-heterocyclic rings from easily assessable ester precursors in good to excellent yields *via* Friedel–Crafts cycliacylation methodology. The newly synthesized scaffolds **8a**–**h** have been assayed for their bactericidal and fungicidal activities. The combination of structural complexity and biological activity of tetracyclic skeletons **8a**–**h** has made these fused ring systems as important architectures for the promising drug discovery. The simplicity and wide variability of the methods make a good alternative to the literature lengthy multistep procedures usually employed.

SUPPLEMENTARY MATERIAL

Additional data and information are available electronically at the pages of journal website: https://www.shd-pub.org.rs/index.php/JSCS/article/view/13466, or from the corresponding author on request.

Acknowledgement. The authors are grateful for the financial support and all the facilities received while performing and writing this work by the Chemistry department, Faculty of science Assiut University, Assiut, Egypt.

ИЗВОД

СИНТЕЗА И ИСПИТИВАЊЕ БИОЛОШКЕ АКТИВНОСТИ НЕКИХ СТРУКТУРА СЛИЧНИХ ЛЕКОВИМА КОЈЕ САДРЖЕ БЕНЗО- И ПИРИДО-КОНДЕНЗОВАНЕ *N*-ХЕТЕРОЦИКЛЕ СРЕДЊЕ ВЕЛИЧИНЕ, ДОБИЈЕНИХ ИНТРАМОЛЕКУЛСКОМ РЕАКЦИЈОМ ФРИДЕЛ–КРАФТСОВОГ АЦИЛОВАЊА

HASSAN ABDOU KOTB ABD EL-AAL

Chemistry Department, Faculty of Science, Assiut University, Assiut, 71516, Egypt

Приказан је јединствен и еколошки прихватљив поступак за синтезу бензо- и пиридо--кондензованих азоцинона, азонинона и азецинона **8a**–**h** применом Фридел–Крафтсове реакције. Овај једноставан и ефикасан поступак, као кључни синтетички корак, има циклоацилување хетероцикличних естара **7a**–**h** у присуству каталитичке количине $AlCl_3$/ /CH_3NO_2, TfOH или PPA. Полазни амиди **3a**–**d** су лако добијени купловањем акрилоил--хлорида **2a** и **2b** са пиридин-2-аминима **1a** и **b**. Примењена стратегија нуди реакције високе селективности, благе реакционе услове и лак приступ сложеним *N*-хетероциклима средње величине, у средњем до добром приносу. Испитана је антимикробна активност свих тетрацикличних кондензованих једињења.

(Примљено 19. јула, ревидирано 17. новембра 2025, прихваћено 9. јануара 2026)

REFERENCES

1. J. Buckingham, K. H. Baggaley, A. D. Roberts, L. F. Szabó,*Dictionary of alkaloids*, 2nd ed., CRC Press, Boca Raton, FL, 2010 (ISBN 9780429145377)
2. D. Robaa, C. Enzensperger, S. E. AbulAzm, M. M. Hefnawy, H. I. E. Subbagh, T. A. Wani, J. Lehmann, *J. Med. Chem.* **54** (2011) 7422 (https://doi.org/10.1021/jm200676f)
3. M. J. Moerke, L. R. McMahon, J. L. Wilkerson, *Pharm. Rev.* **72** (2020) 527 (https://doi.org/10.1124/pr.119.018028)
4. N. Boden, R. Bissell, J. Clements, B. Movaghar, *Liq. Cryst. Today* **6** (1996) 1 (https://doi.org/10.1080/13583149608047629)
5. A. L. Ahmed, Y. Briseno, S. A. Xia, J. Jenekhe, *J. Am. Chem. Soc.* **130** (2008) 1118 (https://doi.org/10.1021/ja077444g)
6. C. E. Harding, J. G. R. Standford, *J. Org. Chem.* **54** (1989) 3054 (https://doi.org/10.1021/jo00274a018)
7. L. A. Paquette, R. E. Hartung, J. E. Hofferberth, I. Vilotijevic, J. Yang, *J. Org. Chem.* **69** (2004) 2454 (https://doi.org/10.1021/jo0358675)
8. N. Krause, C. Winter, *Chem. Rev.* **111** (2011) 1994 (https://doi.org/10.1021/cr1004088)
9. R. H. Grubbs, *Handbook of Metathesis*, Vol. 1, 1st ed., Wiley-VCH, Verlag GmbH, Weinheim, 2003, p. 204

10. A. T. Soldatenkov, S. V. Volkov, S. A. Soldatova, *Chem. Heterocycl. Compd.* **43** (2007) 508 (https://doi.org/10.1007/s10593-007-0076-z)
11. J. Marco-Contelles, E. De Opazo, *J. Org. Chem*. **67** (2002) 3705 (https://doi.org/10.1021/jo0111107)
12. H. Ishibashi, T. Sato, M. Ikeda, *Synthesis* **6** (2002) 695 (https://doi.org/10.1055/s-2002-25759)
13. M. A. Sierra, I. Fernández, F. P. Cossío, *Chem.Commun*. (2008) 4671 (https://doi.org/10.1039/B807806H)
14. D. L. Boger, S. M. Weinreb, *Hetero Diels-Alder Methodologyin Organic Synthesis*, Academic Press, New York, 1987
15. L. F. Tietze, G. Brasche, K. M. Gericke, *Domino Reactions in Organic synthesis*, Wiley--VCH Verlag GmbH & Co. KgaA, Weinheim, 2006 (ISBN:9783527290604)
16. J. Limanto, M. L. Snapper, *J. Am. Chem. Soc.* **122** (2000) 8071 (https://doi.org/10.1021/ja001946b)
17. T. Hudicky, in *Alkaloids: Chemical and Biological Perspectives*, S. W. Pelletier, Ed., Wiley-Interscience, New York, Vol. 5, Ch. 1, 1987, pp. 25–37
18. R. E. Gawley, *Org. React.* **35** (1987) 1 (https://doi.org/10.1002/0471264180.or035.01)
19. D. H. R. Barton, R. James, G. W. Kirby, D. W. Turner, D. A. Widdowson, *J. Chem. Soc., C* (1968) 1529 (https://doi.org/10.1039/J39680001529)
20. I. W. Elliott, M. J. Sloan, E. Tate, *Tetrahedron* **52** (1996) 8063 (https://doi.org/10.1016/0040-4020(96)00390-0)
21. M. Qadir, J. Cobb, P. W. Sheldrake, N. Whittall, A. J. P. White, K. K. Hii, P. N. Horton, M. B. Hursthouse, *J. Org. Chem.* **70** (2005) 1552 (https://doi.org/10.1021/jo048117j)
22. L. J. Dolby, D. L. Booth, *J. Amer. Chem. Soc*. **88** (1966) 1049 (https://doi.org/10.1021/ja00957a035)
23. N. J. Leonard, T. Sato, *J. Org. Chem.* **34** (1969) 1066 (https://doi.org/10.1021/jo01256a064)
24. S. Gerhard, H. Manfred, F. Edgar, B. Heinrich, G. Volker, W. Bernd, S. Wolfgang, European Patent, 0 035 360 B1, 1952
25. J. B. Bremner, D. F. Perkins, *Tetrahedron* **61** (2005) 2659 (https://doi.org/10.1016/j.tet.2005.01.061)
26. G. Kim, M. Y. Chu-Moyer, S. J. Danishefsky, *J. Am. Chem. Soc.* **112** (1990) 2003 (https://doi.org/10.1021/ja00161a059)
27. R. Frutos-Pedreño, P. González-Herrero, J. Vicente, P. G. Jones, *Organometallics* **32** (2013) 1892 (https://doi.org/10.1021/om4000192)
28. H. A. K. Abd El-Aal, A. A. Khalaf, *Arkivoc* **8** (2024) 202412254 (https://doi.org/10.24820/ark.5550190.p012.254)
29. H. A. K. Abd El-Aal, *Chem. Heterocycl. Comp*. **56** (2020) 1353 (https://doi.org/10.1007/s10593-020-02822-1)
30. H. A. K. Abd El-Aal, *Aus. J. Chem.* **76** (2023) 760 (https://doi.org/10.1071/CH23030)
31. R. M. Roberts, A. A. Khalaf, *Friedel-Crafts Chemistry: A Century of Discovery*, Marcel Dekker, New York, 1984
32. G. Pelletier, A. B. Charrette, *Org. Lett. **15*** (2013) 2290 (https://doi.org/10.1021/ol400870b)
33. L. Panizzon, *Helv. Chim. Acta* **24** (1941) 27 (https://doi.org/10.1002/hlca.19410240205)
34. L. T. Smith, W. W. Prichard, *J. Am. Chem. Soc.* **62** (1940) 778 (https://doi.org/10.1021/ja01861a024)

35. K. H. Yong, J. A. Lotoski, J. M. Chong, *J. Org. Chem.* **66** (2001) 8248 (https://doi.org/10.1021/jo015940w)
36. T. Okauchi, I. Masaaki, T. Minami, T. Owa, K. Kitoh, H. Yoshino, *Org. Lett.* **2** (2000) 1485 (https://doi.org/10.1021/ol005841p)
37. G. A. Olah, *Acc. Chem. Res.* **4** (1971) 240 (https://doi.org/10.1021/ar50043a002)
38. R. D. Shingare, R. Velayudham, J. R. Gawade, D. S. Reddy, *Org. Lett*. **15** (2013) 4556 (https://doi.org/10.1021/ol402110e)
39. G. A. Olah, M. Tashiro, S. Kobayashi, *J. Am. Chem. Soc.* **92** (1970) 6371 (https://doi.org/10.1021/ja00724a063)
40. R. M. Silverstein, F. X. Webster, D. J. Kiemle, *Spectrometric Identification of Organic Compounds*, 7th ed., Wiley, Hoboken, NJ, 2005
41. G. J. Collee, G. A. Fraser, P. B. Marmion, A. Simmons, *Practical Medical Microbiology*, 14th ed., Churchill Livingstone, Edinburgh, Vol. 11, 1996, p. 163.

Journal of the Serbian Chemical Society
JSCS@tmf.bg.ac.rs • www.shd.org.rs/JSCS
J. Serb. Chem. Soc. 91 (3) S66–S106 (2026) *Supplementary material*

SUPPLEMENTARY MATERIAL TO

Synthesis and biological evaluation of some drug-like scaffolds of benzo- and pyrido-fused medium-sized *N*-heterocycles obtained *via* intramolecular Friedel–Crafts acylation reactions

HASSAN ABDOU KOTB ABD EL-AAL*

Chemistry Department, Faculty of Science, Assiut University, Assiut, 71516, Egypt

J. Serb. Chem. Soc. 91 (3) (2026) 213–225

ANALYTICAL AND SPECTRAL DATA

(*E*)-*N*-(Pyridin-2-yl)cinnamamide (3a): Yellow plates; 85%; mp 148–150 ºC (ethanol); IR (KBr, ν, cm^{-1}): 3280, 3075, 2980, 1672, 1600, 1480, 1450, 1355, 1250, 1120, 765. ^{1}H NMR (400 MHz, $CDCl_3$, δ, ppm): 5.25 (1H, s, NH), 6.74 (1H, d, J = 15.7 Hz, =CH), 7.10 (1H, ddd, J_1 = 7.4, J_2 = 4.8, J_3 = 1.2 Hz), 7.43 (2H, dddd, J_1 = 8.1, J_2 = 7.2, J_3 = 2.0, J_4 = 0.5 Hz), 7.44 (1H, tt, J_1 = 7.2, J_2 = 1.6 Hz), 7.51 (2H, dddd, J_1 = 8.1, J_2 = 2.3, J_3 = 1.6, J_4 = 0.5 Hz), 7.62 (1H, d, J = 15.7 Hz, =CH), 7.65 (1H, ddd, J_1 = 7.9, J_2 = 1.2, J_3 = 0.5 Hz), 7.75 (1H, ddd, J_1 = 7.9, J_2 = 7.4, J_3 = 1.9 Hz), 8.40 (1H, ddd, J_1 = 4.8, J_2 = 1.9, J_3 = 0.5 Hz). ^{13}C NMR (100 MHz, $CDCl_3$, δ, ppm): 114.6 (1C, Ar., Py-C-6"), 117.6 (1C, Ar., Py-C-4"), 118.4 (1C, =C^{2}H-), 128.0 (2C, Ar., C-3', C-5'), 129.0 (2C, Ar., C-4', C-6'), 129.4 (1C, Ar.,C-2'), 135.8 (1C, Ar.,C-1'), 139.2 (1C, Ar., Py-C-5"), 141.0 (1C, =C^{3}H-), 148.1 (1C, Ar., Py-C-3"), 152.9 (1C, Ar., Py-C-1"), 164.9 (1C, C=O, C-1). MS (EI, 70 eV) m/z (%), 225 (M^++1, 32), 224 (M^+, 100), 216 (17), 203 (27), 188 (12), 175 (21), 147 (28), 134 (15), 119 (37), 106 (15), 91 (17), 90 (25), 67 (84), 54 (30). Anal. Calcd. for $C_{14}H_{12}N_2O$ (224); C, 75.00; H, 5.35; N, 12.50. Found: C, 75.12; H, 5.33; N, 12.47%.

(*E*)-*N*,3-di(pyridin-2-yl)acrylamide (3b): Yellow needles, 78%, mp 132-34 °C (AcOEt); IR (KBr, ν, cm^{-1}): 3247, 3077, 2973, 1670, 1600, 1480, 1384, 1275, 1182, 892. ^{1}H NMR (400 MHz, $CDCl_3$, δ, ppm): 5.72 (1H, s, NH), 6.85 (1H, d, J = 15.5 Hz, =CH), 7.10 (1H, ddd, J_1 = 7.9, J_2 = 4.8, J_3 = 1.2 Hz), 7.43 (1H, d, J = 15.5 Hz, =CH), 7.54 (1H, ddd, J_1 = 7.4, J_2 = 4.7, J_3 = 1.4 Hz), 7.65 (1H, ddd, J_1 = 7.9, J_2 = 1.2, J_3 = 0.5 Hz), 7.71 (1H, ddd, J_1 = 7.7, J_2 = 1.4, J_3 = 0.5 Hz), 7.75 1H, (td, J_1 = 7.9, J_2 = 1.9 Hz), 7.89 (1H, ddd, J_1 = 7.7, J_2 = 7.4, J_3 = 1.9 Hz), 8.40 (1H, ddd, J_1 = 4.8, J_2 = 1.9, J_3 = 0.5 Hz), 8.73 (1H, ddd, J_1 = 4.7, J_2 = 1.9, J_3 = 0.5 Hz). ^{13}C NMR (100 MHz, $CDCl_3$, δ, ppm): 115.2 (1C, Ar., C-6"), 118.4 (1C, Ar., C-4"), 122.8 (1C, Ar., C-6'), 123.3 (1C, =C^{2}H-), 127.2 (1C, Ar., C-4'), 139.2 (1C, Ar.,C-5'), 139.6 (1C, Ar.,C-5"), 139.8 (1C, =C^{3}H-), 148.1 (1C, Ar.,C-3'), 149.2 (1C, Ar.,C-3"), 152.9 (1C, Ar., C-1'), 155.3 (1C, Ar., C-1"), 168.4 (1C, C=O, C-1). MS (EI, 70 eV) m/z (%), 228 (M^++3, 3), 226 (M^++1, 32), 225 (M^+, 100), 190 (41), 188 (35), 176 (2), 166 (5), 153 (18), 141 (33), 118 (39), 106 (10), 94 (11), 90 (82), 71 (9), 47 (19). Anal. Calcd. for $C_{13}H_{11}N_3O$ (225); C, 69.33; H, 4.88; N, 18.66. Found: C, 69.30; H, 4.94; N, 18.58%.

* Correspondnce E-mail: hassankotb33@yahoo.com; hassankotb@aun.edu.eg

(*E*)-*N*-(Pyridin-2-ylmethyl)cinnamamide (3c): Pale pink plates; 90%; mp 104-6 ºC (Lit.[35] mp 100-101 (ethanol); IR (KBr, *v*, cm^{-1}): 3250, 2920, 1662, 1615, 1577, 1480, 1440, 1355, 1264, 1060, 779. ^{1}H NMR (400 MHz, $CDCl_3$, δ, ppm): 4.65 (2H, s, CH_2), 5.43 (1H, s, NH), 6.61 (1H, d, J = 15.6 Hz, =CH), 7.11 (1H, ddd, J_1 = 7.4, J_2 = 4.6, J_3 = 1.2 Hz), 7.25 (1H, ddd, J_1 = 7.6, J_2 = 1.2, J_3 = 0.5 Hz), 7.35 (m, 2H), 7.43 (1H, tt, J_1 = 7.2, J_2 = 1.3 Hz), 7.50 (m, 2H), 7.65 (1H, d, J = 15.6 Hz, =CH), 7.63 (1H, ddd, J_1 = 7.6, J_2 = 7.4, J_3 = 1.9 Hz), 8.55 (1H, ddd, J_1 = 4.6, J_2 = 1.9, J_3 = 0.5 Hz). ^{13}C NMR (100 MHz, $CDCl_3$, δ, ppm): 44.1 (1C, N-CH_2-), 120.0 (1C, =C^2H-), 120.5 (1C, Ar., Py-C-4"), 123.6 (1C, Ar., Py-C-6"), 128.0 (2C, Ar., C-2', C-6'), 129.0 (2C, Ar., C-3', C-5'), 129.4 (1C, Ar.,C-4'), 135.8 (1C, Ar.,C-1'), 139.1 (1C, Ar., Py-C-5"), 140.9 (1C, =C^3H-), 148.0 (1C, Ar., Py-C-3"), 157.3 (1C, Ar., Py-C-1"), 170.2 (1C, C=O, C-1). MS (EI, 70 eV) m/z (%), 239 (M^++1, 46), 238 (M^+, 71), 230 (12), 208 (7), 199 (16), 184 (5), 167 (11), 149 (11), 126 (13), 112 (32), 98 (100), 90 (53), 74 (55), 69 (27). Anal. Calcd. for $C_{15}H_{14}N_2O$ (238); C, 75.63; H, 5.88; N, 11.76. Found: C, 76.01; H, 5.80; N, 11.55%.

(*E*)-3-(Pyridin-2-yl)-*N*-((pyridin-2-yl)methyl)acrylamide (3d): Yellow crystals; 81%; mp 158–60 ºC (ethanol); IR (KBr, *v*, cm^{-1}): 3237, 3068, 2975, 1688, 1605, 1585, 1440, 1330, 1265, 1127, 790. ^{1}H NMR (400 MHz, $CDCl_3$, δ, ppm): 4.66 (2H, s, CH_2), 5.62 (1H, s, NH), 6.78 (1H, d, J = 15.2 Hz, =CH), 7.16 (1H, ddd, J_1 = 7.4, J_2 = 4.6, J_3 = 1.2 Hz), 7.29 (1H, ddd, J_1 = 7.6, J_2 = 1.2, J_3 = 0.5 Hz), 7.40 (1H, d, J = 15.2 Hz, =CH), 7.52 (1H, ddd, J_1 = 7.4, J_2 = 4.7, J_3 = 1.4 Hz), 7.63 (1H, ddd, J_1 = 7.6, J_2 = 7.4, J_3 = 1.9 Hz), 7.75 (1H, ddd, J_1 = 7.7, J_2 = 1.4, J_3 = 0.5 Hz), 7.89 (1H, ddd, J_1 = 7.7, J_2 = 7.4, J_3 = 1.9 Hz), 8.54 (1H, ddd, J_1 = 4.6, J_2 = 1.9, J_3 = 0.5 Hz), 8.77 (1H, ddd, J_1 = 4.7, J_2 = 1.9, J_3 = 0.5 Hz). ^{13}C NMR (100 MHz, $CDCl_3$, δ, ppm): 45.7 (1C, N-CH_2-), 120.4 (1C, Ar., C-4"), 122.8 (1C, Ar., C-6'), 123.3 (1C, Ar.,C-4'), 123.6 (1C, Ar., C-6"), 128.0 (1C, =C^2H-), 139.1 (1C, Ar.,C-5'), 139.8 (1C, Ar.,C-5"), 141.1 (1C, =C^3H-), 148.0 (1C, Ar., C-3"), 149.2 (1C, Ar., C-3'), 155.3 (1C, Ar.,C-1'), 157.3 (1C, Ar., C-1"), 175.2 (1C, C=O, C-1). MS (EI, 70 eV) m/z (%), 240 (M^++1, 4), 239 (M^+, 22), 238 (2), 208 (6), 199 (13), 184 (6), 167 (35), 149 (15), 126 (18), 112 (36), 106 (26), 98 (100), 93 (6), 84 (46), 74 (35), 69 (20), 55 (54). Anal. Calcd. for $C_{14}H_{13}N_3O$ (239); C, 70.29; H, 5.43; N, 17.57. Found: C, 70.24; H, 5.40; N, 17.63%.

3,4-Dihydro-4-phenyl-1,8-naphthyridin-2(1*H*)-one (4a): Yellowish brown plates; 80%; mp 170 ºC *dec.* (acetone); IR (KBr, *v*, cm^{-1}): 3345, 3047, 2945, 1677, 1600, 1585, 1480, 1480, 1474, 1340, 1255, 1140, 769. ^{1}H NMR (400 MHz, $CDCl_3$, δ, ppm): 2.84 (2H, dd, J_1 = 16.3, J_2 = 3.0 Hz, C^3H_2), 5.08 (1H, dd, J_1 = 4.1, J_2 = 1.8 Hz, C^4H), 6.66 (1H, dd, J_1 = 8.1, J_2 = 4.6 Hz), 7.15 (1H, tdd, J_1 = 7.7, J_2 = 1.5, J_3 = 1.3 Hz), 7.21 (2H, dddd, J_1 = 7.8, J_2 = 7.7, J_3 = 1.9, J_4 = 0.5 Hz), 7.27 (2H, dddd, J_1 = 7.8, J_2 = 1.4, J_3 = 1.3, J_4 = 0.5 Hz), 8.05 (1H, dd, J_1 = 4.6, J_2 = 1.9 Hz), 8.36 (1H, dd, J_1 = 8.1, J_2 = 1.9 Hz), 9.78 (1H, s, NH). ^{13}C NMR (100 MHz, $CDCl_3$, δ, ppm): 38.1 (1C, -CH_2-, C-3), 40.6 (1C, -CH-, C-4), 114.0 (1C, Ar., Py-C-6), 121.0 (1C, Ar.,C-4'), 126.8 (1C, Ar., Py-C-4a), 128.7 (2C, Ar., C-2', C-6'), 129.3 (2C, Ar., C-3', C-5'), 131.7 (1C, Ar., Py-C-5), 143.2 (1C, Ar.,C-1'), 144.3 (1C, Ar., Py-C-7), 151.2 (1C, Ar., Py-C-8a), 169.4 (1C, C=O, C-2). MS (EI, 70 eV) m/z (%), 224 (M^+, 12), 223 (71), 209 (4), 192 (2), 180 (3), 165 (34), 134 (24), 119 (2), 112 (3), 106 (100), 91 (44), 90 (17), 79 (14), 65 (9). Anal. Calcd. for $C_{14}H_{12}N_2O$ (224); C, 75.00; H, 5.35; N, 12.50. Found: C, 75.06; H, 5.40; N, 12.46%.

3,4-Dihydro-4-(pyridin-2-yl)-1,8-naphthyridin-2(1*H*)-one (4b): White crystals; 88%, mp 135-37 ºC (acetone); IR (KBr, *v*, cm^{-1}): 3405, 3030, 2965, 1678, 1600, 1490, 1450, 1260, 1145, 1080, 792. ^{1}H NMR (400 MHz, $CDCl_3$, δ, ppm): 2.82 (2H, dd, J_1 = 16.3, J_2 = 3.0 Hz, C^3H_2), 5.32 (1H, dd, J_1 = 4.1, J_2 = 1.8 Hz, C^4H), 6.67 (1H, dd, J_1 = 8.1, J_2 = 4.6 Hz), 7.18 (1H, ddd, J_1 = 7.4, J_2 = 4.9, J_3 = 1.2 Hz), 7.27 (1H, ddd, J_1 = 7.6, J_2 = 1.2, J_3 = 0.5 Hz), 7.68 (1H, ddd, J_1 = 7.6, J_2 = 7.4, J_3 = 1.9 Hz), 7.95 (1H, dd, J_1 = 8.1, J_2 = 1.9 Hz), 8.11 (1H, dd, J_1 = 4.6,

J_2 = 1.9 Hz), 8.55 (1H, ddd, J_1 = 4.9, J_2 = 1.9, J_3 = 0.5 Hz), 9.34 (1H, s, NH). ^{13}C NMR (100 MHz, $CDCl_3$, δ, ppm): 37.1 (1C, -CH-, C-4), 42.1 (1C, -CH_2-, C-3), 113.3 (1C, Ar., C-6), 120.0 (1C, Ar., C-4'), 120.3 (1C, Ar., C-5'), 126.4 (1C, Ar., C-6'), 130.9 (1C, Ar., C-4a), 139.6 (1C, Ar., C-5), 144.4 (1C, Ar., C-7), 146.5 (1C, Ar., C-8a), 152.2 (1C, Ar.,C-3'), 165.4 (1C, Ar.,C-1'), 173.4 (1C, C=O, C-2). MS (EI, 70 eV) m/z (%), 226 (M^++1, 9), 225 (M^+, 66), 208 (2), 194 (2), 181 (3), 165 (37), 148 (16), 133 (12), 120 (100), 105 (28), 91 (24), 77 (51), 68 (3). Anal. Calcd. for $C_{13}H_{11}N_3O$ (225); C, 69.33; H, 4.88; N, 18.66. Found: C, 69.28; H, 4.91; N, 18.70%.

5,6,8,9-Tetrahydro-5-phenylpyrido[2,3-*c*]azepin-7-one (4c): Yellow needles; 79%, m.p. 172-75 °C (AcOEt); IR (KBr, *v*, cm^{-1}): 3410, 3040, 2950, 1700, 1590, 1480, 1440 1375, 1280, 1176, 796. ^{1}H NMR (400 MHz, $CDCl_3$, δ, ppm): 3.08 (2H, dd, J_1 = 16.2, J_2 = 6.2 Hz, C^6H_2), 4.32 (1H, dd, J_1 = 10.2, J_2 = 2.3 Hz, C^5H), 4.89 (2H, d, J = 12.0 Hz, N-C^9H_2), 7.12 (1H, dd, J_1 = 7.4, J_2 = 4.6 Hz), 7.18 (1H, tdd, J_1 = 7.7, J_2 = 1.5, J_3 = 1.3 Hz), 7.25 (2H, dddd, J_1 = 7.8, J_2 = 7.7, J_3 = 1.9, J_4 = 0.5 Hz), 7.39 (2H, dddd, J_1 = 7.8, J_2 = 1.4, J_3 = 1.3, J_4 = 0.5 Hz), 7.66 (1H, dd, J_1 = 7.4, J_2 = 1.9 Hz), 8.49 (1H, dd, J_1 = 4.6, J_2 = 1.9 Hz), 9.63 (1H, s, NH). ^{13}C NMR (100 MHz, $CDCl_3$, δ, ppm): 42.7 (1C, -CH-, C-5), 46.6 (1C, -CH_2-, C-1), 50.7 (1C, -CH_2-, C-4), 122.0 (1C, Ar., Py-C-7), 127.0 (1C, Ar.,C-4'), 128.8 (2C, Ar., C-2', C-6'), 129.7 (2C, Ar., C-3', C-5'), 132.3 (1C, Ar., Py-C-6), 133.3 (1C, Ar., Py-C-5a), 143.4 (1C, Ar.,C-1'), 145.4 (1C, Ar., Py-C-8), 159.6 (1C, Ar., Py-C-9a), 175.8 (1C, C=O, C-3). MS (EI, 70 eV) m/z (%), 239 (M^++1, 6), 238 (M^+, 25), 203 (2), 194 (100), 180 (87), 165 (12), 151 (8), 137 (26), 109 (69), 95 (26), 90 (19), 67 (22). Anal. Calcd. for $C_{15}H_{14}N_2O$ (238); C, 75.63; H, 5.88; N, 11.76. Found: C, 75.58; H, 5.90; N, 11.79%.

5,6,8,9-Tetrahydro-5-(pyridin-2-yl)pyrido[2,3-*c*]azepin-7-one (4d): Yellow crystal; m.p. 180 ºC *dec.*, 75% (AcOEt); IR (KBr, *v*, cm^{-1}): 3180, 3040, 2975, 1677, 1600, 1590, 1447, 1375, 1240, 1160, 795. ^{1}H NMR: δ 3.15 (2H, dd, J_1 = 16.3, J_2 = 6.2 Hz, J_3 = C^6H_2), 4.65 (1H, dd, J_1 = 10.2, J_2 = 2.2 Hz, C^5H), 4.87 (2H, d, J = 12.0 Hz, N-C^9H_2), 7.14 (1H, dd, J_1 = 7.1, J_2 = 4.6 Hz), 7.20 (1H, ddd, J_1 = 7.4, J_2 = 4.9, J_3 = 1.2 Hz), 7.27 (1H, ddd, J_1 = 7.6, J_2 = 1.2, J_3 = 0.5 Hz), 7.68 (2H, ddd, J_1 = 7.6, J_2 = 7.4, J_3 = 1.9 Hz), 8.51 (1H, ddd, J_1 = 4.9, J_2 = 1.9, J_3 = 0.5 Hz), 8.58 (1H, dd, J_1 = 4.6, J_2 = 1.9 Hz), 9.81 (1H, s, NH). ^{13}C NMR (100 MHz, $CDCl_3$, δ, ppm): 40.1 (1C, -CH-, C-5), 46.6 (1C, -CH_2-, C-1), 49.3 (1C, -CH_2-, C-4), 119.9 (1C, Ar., C-6), 121.1 (1C, Ar., C-4'), 127.0 (1C, Ar., C-6'), 132.5 (1C, Ar., C-5), 132.7 (1C, Ar., C-5'), 139.8 (1C, Ar., C-5a), 146.7 (1C, Ar., C-8), 147.2 (1C, Ar., C-3'), 156.3 (1C, Ar., C-9a), 165.6 (1C, Ar.,C-1'), 172.7 (1C, C=O, C-3). MS (EI, 70 eV) m/z (%), 239 (M^++1, 3), 238 (M^+, 11), 223 (60), 210 (15), 206 (4), 197 (18), 181 (100), 165 (20), 152 (25), 139 (4), 115 (3), 90 (30), 76 (5), 69 (7). Anal. Calcd. for $C_{14}H_{13}N_3O$ (**239**); C, 70.29; H, 5.43; N, 17.57. Found: C, 70.35; H, 5.45; N, 17.49%.

1,2,3,4-Tetrahydro-4-phenyl-1,8-naphthyridine (5a): Yellow crystals; 90%; mp 115-17 ºC (benzene); IR (KBr, *v*, cm^{-1}): 3430, 3050, 2975, 1698, 1600, 1590, 1470, 1440, 1361, 1270, 1121, 779. ^{1}H NMR (400 MHz, $CDCl_3$, δ, ppm): 2.06 (2H, dddd, J_1 = 13.4, J_2 = 7.0, J_3 = 6.6, J_4 = 2.5 Hz, C^3H_2), 3.43 (2H, ddd, J_1 = 13.8, J_2 = 6.6, J_3 = 2.5 Hz, N-C^2H_2), 3.94 (1H, dd, J_1 = 10.1, J_2 = 3.9 Hz, C^4H), 7.12 (1H, dd, J_1 = 7.6, J_2 = 4.7 Hz), 7.16 (1H, tt, J_1 = 7.7, J_2 = 1.3 Hz), 7.20 (2H, dtd, J_1 = 7.8, J_2 = 1.2, J_3 = 0.5 Hz), 7.28 (2H, dddd, J_1 = 7.8, J_2 = 7.7, J_3 = 1.9, J_4 = 0.5 Hz), 8.07 (1H, dd, J_1 = 4.7, J_2 = 1.9 Hz), 8.23 (1H, dd, J_1 = 7.6, J_2 = 1.9 Hz), 9.57 (1H, s, NH). ^{13}C NMR (100 MHz, $CDCl_3$, δ, ppm): 30.8 (1C, -CH_2-, C-3), 36.9 (1C, -CH_2-, C-2), 39.9 (1C, -CH-, C-4), 111.2 (1C, Ar., Py-C-6), 117.7 (1C, Ar., Py-C-4a), 126.7 (1C, Ar., C-4'), 128.7 (2C, Ar., C-2', C-6'), 129.1 (2C, Ar., C-3', C-5'), 132.9 (1C, Ar., C-1'), 144.9 (1C, Ar., Py-C-5), 144.9 (1C, Ar., Py-C-7), 163.8 (1C, Ar., Py-C-8a). MS (EI, 70 eV) m/z (%), 212 (M^++2, 2), 211 (M^++1, 11), 210 (M^+, 64), 205 (2), 195 (100), 181 (32), 167 (12), 154 (8), 140 (5), 133 (21),

105 (8), 91 (15), 77 (29), 67 (2). Anal. Calcd. for $C_{14}H_{14}N_2$ (210); C, 80.00; H, 6.66; N, 13.33. Found: C, 80.11; H, 6.60; N, 13.27%.

1,2,3,4-Tetrahydro-4-(pyridin-2-yl)-1,8-naphthyridine (5b): Yellow crystals; 84%; mp 122-24 ºC (ethanol); IR (KBr, *v*, cm^{-1}): 3440, 3075, 2980, 1695, 1600, 1580, 1470, 1440, 1385, 1252, 1170, 794. ^{1}H NMR (400 MHz, $CDCl_3$, δ, ppm): 2.13 (2H, dddd, J_1 = 13.6, J_2 = 6.9, J_3 = 6.6, J_4 = 2.5 Hz, C^3H_2), 3.45 (2H, ddd, J_1 = 13.8, J_2 = 6.6, J_3 = 2.5 Hz, N-C^2H_2), 4.15 (1H, dd, J_1 = 10.1, J_2 = 3.8 Hz, C^4H), 7.17 (1H, dd, J_1 = 7.6, J_2 = 4.7 Hz), 7.20 (1H, ddd, J_1 = 7.4, J_2 = 4.5, J_3 = 1.2 Hz), 7.28 (1H, ddd, J_1 = 7.6, J_2 = 1.2, J_3 = 0.5 Hz), 7.68 (1H, ddd, J_1 = 7.6, J_2 = 7.4, J_3 = 1.9 Hz), 7.93 (1H, dd, J_1 = 7.6, J_2 = 1.9 Hz), 8.13 (1H, dd, J_1 = 4.7, J_2 = 1.9 Hz), 8.52 (1H, ddd, J_1 = 4.5, J_2 = 1.9, J_3 = 0.5 Hz), 9.48 (1H, s, NH). ^{13}C NMR (100 MHz, $CDCl_3$, δ, ppm): 28.3 (1C, -CH_2-, C-3), 36.9 (1C, -CH_2-, C-2), 39.6 (1C, -CH-, C-4), 110.3 (1C, Ar., C-6), 117.7 (1C, Ar., C-4a), 120.6 (1C, Ar., C-4'), 125.0 (1C, Ar., C-6'), 131.6 (1C, Ar., C-5'), 139.4 (1C, Ar., C-5), 145.5 (1C, Ar., C-3'), 146.0 (1C, Ar., C-7), 153.4 (1C, Ar., C-1'), 167.7 (1C, Ar., C-8a). MS (EI, 70 eV) m/z (%), 213 (M^++2, 2), 212 (M^++1, 13), 211 (M^+, 36), 195 (2), 183 (6), 170 (77), 153 (100), 141 (3), 135 (12), 125 (15), 107 (5), 90 (20), 79 (14), 68 (4). Anal. Calcd. for $C_{13}H_{13}N_3$ (211); C, 73.93; H, 6.16; N, 19.90. Found: C, 73.88; H, 6.21; N, 19.90%.

6,7,8,9-Tetrahydro-5-phenyl-5*H*-pyrido[2,3-*c*]azepine (5c): Yellow crystals; 92%; mp 138-140 ºC (ethanol); IR (KBr, *v*, cm^{-1}): 3390, 3020, 2956, 1690, 1600, 1590, 1470, 1440, 1375, 1240, 1122, 798. ^{1}H NMR (400 MHz, $CDCl_3$, δ, ppm): 2.18 (2H, dddd, J_1 = 13.9, J_2 = 6.6, J_3 = 4.7, J_4 = 2.6 Hz, C^6H_2), 2.89 (2H, ddd, J_1 = 11.3, J_2 = 6.6, J_3 = 2.6 Hz, C^7H_2), 3.97 (2H, d, J = 15.0 Hz, N-C^9H_2), 4.17 (1H, dd, J_1 = 8.1, J_2 = 1.4 Hz, C^5H), 7.12 (1H, dd, J_1 = 8.0, J_2 = 4.7 Hz), 7.18 (1H, tt, J_1 = 7.7, J_2 = 1.3 Hz), 7.21 (2H, dddd, J_1 = 7.8, J_2 = 7.7, J_3 = 1.9, J_4 = 0.5 Hz), 7.27 (2H, dtd, J_1 = 7.8, J_2 = 1.2, J_3 = 0.5 Hz), 8.31 (1H, dd, J_1 = 8.0, J_2 = 1.9 Hz), 8.67 (1H, dd, J_1 = 4.7, J_2 = 1.9 Hz), 9.41 (1H, s, NH). ^{13}C NMR (100 MHz, $CDCl_3$, δ, ppm): 35.7 (1C, -CH-, C-5), 50.4 (1C, -CH_2-, C-4), 54.5 (1C, -CH_2-, C-1), 56.9 (1C, -CH_2-, C-3), 122.6 (1C, Ar., Py-C-7), 126.9 (1C, Ar., C-4'), 128.9 (2C, Ar., C-2', C-6'), 129.5 (2C, Ar., C-3', C-5'), 132.8 (1C, Ar., Py-C-6), 134.4 (1C, Ar., Py-C-5a), 145.0 (1C, Ar., C-1'), 145.9 (1C, Ar., Py-C-8), 169.3 (1C, Ar., Py-C-9a). MS (EI, 70 eV) m/z (%), 225 (M^++1, 7), 224 (M^+, 100), 222 (40), 191 (3), 177 (2), 156 (2), 145 (44), 128 (2), 109 (25), 91 (39), 74 (25), 61 (2), 50 (7). Anal. Calcd. for $C_{15}H_{16}N_2$ (224); C, 80.35; H, 7.14; N, 12.50. Found: C, 80.42; H, 7.17; N, 12.40%.

6,7,8,9-Tetrahydro-5-(pyridin-2-yl)-5*H*-pyrido[2,3-*c*]azepine (5d): Yellow crystals; 89%; mp 158-61 ºC (ethanol); IR (KBr, *v*, cm^{-1}): 3420, 3040, 2985, 1700, 1605, 1580, 1475, 1440, 1374, 1248, 1127, 770. ^{1}H NMR (400 MHz, $CDCl_3$, δ, ppm): 2.17 (2H, dddd, J_1 = 13.9, J_2 = 6.6, J_3 = 4.7, J_4 = 2.6 Hz, C^6H_2), 2.95 (2H, ddd, J_1 = 10.1, J_2 = 6.6, J_3 = 2.6 Hz C^7H_2), 4.03 (2H, d, J = 15.0 Hz, N-C^9H_2), 4.41 (1H, dd, J_1 = 8.1, J_2 = 1.4 Hz, C^5H), 7.20 (2H, ddd, J_1 = 7.4, J_2 = 4.5, J_3 = 1.2 Hz), 7.25 (1H, ddd, J_1 = 7.6, J_2 = 1.2, J_3 = 0.5 Hz), 7.60 (1H, ddd, J_1 = 7.6, J_2 = 7.4, J_3 = 1.9 Hz), 7.95 (1H, dd, J_1 = 7.6, J_2 = 1.9 Hz), 8.58 (1H, ddd, J_1 = 4.5, J_2 = 1.9, J_3 = 0.5 Hz), 8.72 (1H, dd, J_1 = 4.7, J_2 = 1.9 Hz), 9.72 (1H, s, NH). ^{13}C NMR (100 MHz, $CDCl_3$, δ, ppm): 35.0 (1C, -CH-, C-5), 50.4 (1C, -CH_2-, C-4), 50.8 (1C, -CH_2-, C-1), 54.5 (1C, -CH_2-, C-3), 120.6 (1C, Ar., C-7), 121.5 (1C, Ar., C-4'), 125.6 (1C, Ar., C-6'), 133.3 (1C, Ar., C-5'), 133.5 (1C, Ar., C-6), 139.5 (1C, Ar., C-5a), 146.3 (1C, Ar., C-8), 147.6 (1C, Ar., C-3'), 155.4 (1C, Ar., C-9a), 168.1 (1C, Ar., C-1'). MS (EI, 70 eV) m/z (%), 226 (M^++1, 10), 224 (M^+, 53), 208 (2), 194 (2), 181 (12), 165 (2), 148 (30), 120 (100), 105 (31), 91 (17), 74 (52), 68 (3), 51 (16). Anal. Calcd. for $C_{14}H_{15}N_3$ (225); C, 74.66; H, 6.66; N, 18.66. Found: C, 74.64; H, 6.71; N, 18.64%.

Ethyl 2-(3,4-dihydro-4-phenyl-1,8-naphthyridin-1(2*H*)-yl)acetate (7a): Pale yellow needles; 74%, mp 115–17 ºC (ethanol); IR (KBr, *v*, cm^{-1}): 3060, 2975, 1730, 1600, 1580, 1470, 1445, 1354, 1271, 780. ^{1}H NMR (400 MHz, $CDCl_3$, δ, ppm): 1.17 (3H, t, J = 7.1 Hz, CH_3), 2.05 (2H, dddd, J_1 = 13.7, J_2 = 7.2, J_3 = 6.9, J_4 = 1.9 Hz, C^3H_2), 3.36 (2H, ddd, J_1 = 13.8, J_2 = 6.9, J_3 = 1.9 Hz, N-C^2H_2), 3.66 (2H, s, $C^{\alpha}H_2$), 3.86 (1H, dd, J_1 = 9.7, J_2 = 4.6 Hz, C^4H), 4.14 (2H, q, J = 7.1 Hz, CH_2), 7.10 (1H, dd, J_1 = 7.6, J_2 = 4.7 Hz), 7.14 (1H, tt, J_1 = 7.7, J_2 = 1.3 Hz), 7.19 (2H, dtd, J_1 = 7.8, J_2 = 1.2, J_3 = 0.5 Hz), 7.31 (1H, dddd, J_1 = 7.8, J_2 = 7.7, J_3 = 1.9, J_4 = 0.5 Hz), 8.12-8.35 (2H, m). ^{13}C NMR (100 MHz, $CDCl_3$, δ, ppm): 14.7 (1C, -OCH$_2$*CH$_3$*), 29.7 (1C, -CH_2-, C-3), 39.9 (1C, -$C^{\alpha}H_2$CO), 47.5 (1C, -CH-, C-4), 50.7 (1C, -O*CH$_2$*CH_3), 61.1 (1C, -CH_2-, C-2), 113.6 (1C, Ar., Py-C-6), 124.9 (1C, Ar., Py-C-4a), 126.7 (1C, Ar., C-4'), 128.7 (2C, Ar., C-2', C-6'), 129.1 (2C, Ar., C-3', C-5'), 134.3 (1C, Ar., Py-C-5), 144.9 (1C, Ar., C-1'), 145.1 (1C, Ar., Py-C-7), 156.7 (1C, Ar., Py-C-8a), 171.0 (1C, C=O). MS (EI, 70 eV) m/z (%), 297 (M^++1, 4), 296 (M^+, 31), 275 (27), 251 (M^+-COEt, 100), 218 (7), 189 (4), 143 (72), 115 (60), 91 (11), 77 (26). Anal. Calcd. for $C_{18}H_{20}N_2O_2$ (296); C, 72.97; H, 6.75; N, 9.45. Found: C, 73.05; H, 6.73; N, 9.38%.

Ethyl 3-(3,4-dihydro-4-phenyl-1,8-naphthyridin-1(2*H*)-yl)propanoate (7b): Buff crystals; 81%, mp 129–31 ºC (acetone); IR (KBr, *v*, cm^{-1}): 3065, 2979, 1735, 1605, 1590, 1480, 1445, 1370, 1185, 789. ^{1}H NMR (400 MHz, $CDCl_3$, δ, ppm): 1.14 (3H, t, J = 7.1 Hz, CH_3), 2.03 (2H, dddd, J_1 = 13.7, J_2 = 7.2, J_3 = 6.9, J_4 = 1.9 Hz, C^3H_2), 2.50 (2H, t, J = 6.7 Hz, $C^{\alpha}H_2$), 3.39 (t, J = 6.7 Hz, $C^{\beta}H_2$), 3.44 (ddd, J_1 = 13.7, J_2 = 6.9, J_3 = 1.9 Hz, N-C^2H_2), 3.86 (1H, dd, J_1 = 9.7, J_2 = 4.6 Hz, C^4H), 4.10 (2H, q, J = 7.1 Hz, CH_2), 7.18 (2H, m), 7.15 (2H, dtd, J_1 = 7.8, J_2 = 1.2, J_3 = 0.5 Hz), 7.28 (2H, dddd, J_1 = 7.8, J_2 = 7.7, J_3 = 1.9, J_4 = 0.5 Hz), 8.08 (dd, J_1 = 4.7, J_2 = 1.9 Hz), 8.31 (dd, J_1 = 7.6, J_2 = 1.9 Hz). ^{13}C NMR (100 MHz, $CDCl_3$, δ, ppm): 14.5 (1C, -OCH$_2$*CH$_3$*), 29.7 (1C, -CH_2-, C-3), 35.5 (1C, -$C^{\alpha}H_2$CO), 39.9 (1C, -CH-, C-4), 47.9 (1C, N-$C^{\beta}H_2$), 48.1 (1C, -O*CH$_2$*CH_3), 61.8 (1C, -CH_2-, C-2), 112.5 (1C, Ar., Py-C-6), 122.4 (1C, Ar., Py-C-4a), 126.7 (1C, Ar., C-4'), 128.7 (2C, Ar., C-2', C-6'), 129.1 (2C, Ar., C-3', C-5'), 134.4 (1C, Ar., Py-C-5), 144.9 (1C, Ar., C-1'), 145.9 (1C, Ar., Py-C-7), 156.2 (1C, Ar., Py-C-8a), 172.8 (1C, C=O). MS (EI, 70 eV) m/z (%), 310 (M^+, 33), 271 (6), 265 (M^+-OEt, 100), 224 (5), 186 (38), 170 (21), 153 (61), 117 (82), 106 (40), 89 (35), 90 (23), 77 (68). Anal. Calcd. for $C_{19}H_{22}N_2O_2$ (310); C, 73.54; H, 7.09; N, 9.03. Found: C, 73.50; H, 7.03; N, 9.12%.

Ethyl 2-(3,4-dihydro-4-(pyridin-2-yl)-1,8-naphthyridin-1(2*H*)-yl)acetate (7c): Pale yellow needles; 78%, mp 140–42 ºC (acetone); IR (KBr, *v*, cm^{-1}): 3030, 2965, 1732, 1600, 1580, 1460, 1485, 1330, 1277, 770. ^{1}H NMR (400 MHz, $CDCl_3$, δ, ppm): 1.16 (3H, t, J = 7.1 Hz, CH_3), 2.09 (2H, dddd, J_1 = 13.6, J_2 = 7.2, J_3 = 6.9, J_4 = 1.9 Hz, C^3H_2), 3.36 (2H, ddd, J_1 = 14.6, J_2 = 6.9, J_3 = 1.9 Hz, N-C^2H_2), 3.68 (2H, s, $C^{\alpha}H_2$), 3.99 (dd, J_1 = 9.7, J_2 = 4.6 Hz, C^4H), 4.19 (2H, q, J = 7.1 Hz, CH_2), 7.07 (1H, dd, J_1 = 7.6, J_2 = 4.7 Hz), 7.18 (1H, ddd, J_1 = 7.4, J_2 = 4.5, J_3 = 1.2 Hz), 7.28 (1H, ddd, J_1 = 7.6, J_2 = 1.2, J_3 = 0.5 Hz), 7.61 (1H, ddd, J_1 = 7.6, J_2 = 7.4, J_3 = 1.9 Hz), 7.95 (1H, dd, J_1 = 7.6, J_2 = 1.9 Hz), 8.20 (1H, dd, J_1 = 4.7, J_2 = 1.9 Hz), 8.58 (1H, ddd, J_1 = 4.5, J_2 = 1.9, J_3 = 0.5 Hz). ^{13}C NMR (100 MHz, $CDCl_3$, δ, ppm): 15.0 (1C, -OCH$_2$*CH$_3$*), 27.9 (1C, -CH_2-, C-3), 39.9 (1C, -CH-, C-4), 47.5 (1C, -CH_2-, C-2), 50.7 (1C, -$C^{\alpha}H_2$CO), 61.9 (1C, -O*CH$_2$*CH_3), 113.0 (1C, Ar., C-6), 120.6 (1C, Ar., C-4'), 124.7 (1C, Ar., C-4a), 125.0 (1C, Ar., C-6'), 132.6 (1C, Ar., C-5'), 139.4 (1C, Ar., C-5), 146.0 (1C, Ar., C-7), 146.1 (1C, Ar., C-3'), 156.0 (1C, Ar., C-8a), 167.7 (1C, Ar., C-1'), 175.5 (1C, C=O). MS (EI, 70 eV) m/z (%), 298 (M^++1 7), 297 (M^+, 62), 274 (42), 252 (M^+-OEt, 100), 225 (88), 197 (37), 181 (50), 152 (24), 104 (17), 93 (13), 90 (8), 77 (17). Anal. Calcd. for $C_{17}H_{19}N_3O_2$ (297); C, 68.68; H, 6.39; N, 14.14. Found: C, 68.74; H, 6.42; N, 14.10%.

Ethyl 3-(3,4-dihydro-4-(pyridin-2-yl)-1,8-naphthyridin-1(2*H*)-yl)propanoate (7d): Brownish needles; 76%, mp 104–6 ºC (ethanol); IR (KBr, *v*, cm^{-1}): 3064, 2982, 1730, 1600, 1580, 1470, 1440, 1375, 1285, 1134, 789. ^{1}H NMR (400 MHz, $CDCl_3$, δ, ppm): 1.18 (3H, t, J = 7.1 Hz, CH_3), 2.14 (2H, dddd, J_1 = 13.6, J_2 = 7.2, J_3 = 6.9, J_4 = 1.9 Hz, C^3H_2), 2.50 (2H, t, J = 6.7 Hz, $C^{\alpha}H_2$), 3.34 (2H, ddd, J_1 = 13.8, J_2 = 6.9, J_3 = 1.9 Hz, N-C^2H_2), 3.38 (2H, t, J = 6.7 Hz, $C^{\beta}H_2$), 4.02 (1H, dd, J_1 = 9.7, J_2 = 4.6 Hz C^4H), 4.15 (2H, q, J = 7.1 Hz, CH_2), 7.12 (1H, dd, J_1 = 7.6, J_2 = 4.7 Hz), 7.24 (1H, ddd, J_1 = 7.4, J_2 = 4.5, J_3 = 1.2 Hz), 7.30 (1H, ddd, J_1 = 7.6, J_2 = 1.2, J_3 = 0.5 Hz), 7.61 (1H, ddd, J_1 = 7.6, J_2 = 7.4, J_3 = 1.9 Hz), 7.85 (1H, dd, J_1 = 7.6, J_2 = 1.9 Hz), 8.19 (1H, dd, J_1 = 4.7, J_2 = 1.9 Hz), 8.50 (1H, ddd, J_1 = 4.5, J_2 = 1.9, J_3 = 0.5 Hz). ^{13}C NMR (100 MHz, $CDCl_3$, δ, ppm): 15.8 (1C, -$OCH_2\underline{CH_3}$), 27.9 (1C, -CH_2-, C-3), 35.5 (1C, -$C^{\alpha}H_2CO$), 39.9 (1C, -CH-, C-4), 47.9 (1C, -CH_2-, C-2), 48.1 (1C, N-$C^{\beta}H_2$), 63.5 (1C, -$O\underline{CH_2}CH_3$), 111.8 (1C, Ar., C-6), 120.6 (1C, Ar., C-4'), 121.7 (1C, Ar., C-4a), 125.0 (1C, Ar., C-6'), 132.7 (1C, Ar., C-5'), 139.4 (1C, Ar., C-5), 146.0 (1C, Ar., C-7), 146.9 (1C, Ar., C-3'), 155.8 (1C, Ar., C-8a), 167.7 (1C, Ar., C-1'), 178.5 (1C, C=O). MS (EI, 70 eV) m/z (%), 312 (M^++1, 13), 311 (M^+, 34), 275 (20), 266 (M^+-OEt, 14), 265 (100), 249 (48), 187 (14), 165 (18), 148 (24), 121 (43), 105 (11), 92 (47), 77 (57). Anal. Calcd. for $C_{18}H_{21}N_3O_2$ (311); C, 69.45; H, 6.75; N, 13.50. Found: C, 69.42; H, 6.80; N, 13.45%.

Ethyl 2-(6,7-dihydro-5-phenyl-5*H*-pyrido[2,3-*c*]azepin-8(9*H*)-yl)acetate (7e): Yellow crystals; 84%, mp 134-36 ºC (AcOEt); IR (KBr, *v*, cm^{-1}): 3060, 2971, 1740, 1605, 1590, 1480, 1445, 1363, 1250, 1185, 790. ^{1}H NMR (400 MHz, $CDCl_3$, δ, ppm): 1.24 (3H, t, J = 7.1 Hz, CH_3), 2.03 (2H, dddd, J_1 = 13.9, J_2 = 6.6, J_3 = 4.7, J_4 = 2.6 Hz, C^6H_2), 2.85 (2H, ddd, J_1 = 6.6, J_2 = 5.8, J_3 = 2.6 Hz, C^7H_2), 3.51 (2H, s, $C^{\alpha}H_2$), 4.02 (1H, dd, J_1 = 8.1, J_2 = 1.4 Hz, C^5H), 4.13 (2H, d, J = 12.6 Hz, N-C^9H_2), 4.17 (2H, q, J = 7.1 Hz, CH_2), 7.10-7.18 (2H, m), 7.24 (2H, dddd, J_1 = 7.8, J_2 = 7.7, J_3 = 1.9, J_4 = 0.5 Hz), 7.31 (2H, dtd, J_1 = 7.8, J_2 = 1.2, J_3 = 0.5 Hz), 8.38 (1H, dd, J_1 = 7.6, J_2 = 1.9 Hz), 8.64 (1H, dd, J_1 = 4.7, J_2 = 1.9 Hz). ^{13}C NMR (100 MHz, $CDCl_3$, δ, ppm): 14.7 (1C, -$OCH_2\underline{CH_3}$), 34.2 (1C, -CH-, C-5), 55.0 (1C, -CH_2-, C-4), 56.5 (1C, -CH_2-, C-1), 57.3 (1C, -CH_2-, C-3), 60.3 (1C, -$C^{\alpha}H_2CO$), 61.7 (1C, -$O\underline{CH_2}CH_3$), 121.9 (1C, Ar., Py-C-7), 126.9 (1C, Ar., C-4'), 128.9 (2C, Ar., C-2', C-6'), 129.5 (2C, Ar., C-3', C-5'), 133.6 (1C, Ar., Py-C-6), 136.1 (1C, Ar., Py-C-5a), 145.0 (1C, Ar., C-1'), 146.0 (1C, Ar., Py-C-8), 157.7 (1C, Ar., Py-C-9a), 171.4 (1C, C=O). MS (EI, 70 eV) m/z (%), 311 (M^++1, 12), 310 (M^+, 26), 275 (27), 265 (M^+-OEt, 100), 246 (10), 218 (5), 189 (41), 171 (23), 143 (54), 151 (76), 105 (9), 89 (13), 77 (38). Anal. Calcd. for $C_{19}H_{22}N_2O_2$ (310); C, 73.54; H, 7.09; N, 9.03. Found: C, 73.60; H, 7.12; N, 8.95%.

Ethyl 3-(6,7-dihydro-5-phenyl-5*H*-pyrido[2,3-*c*]azepin-8(9*H*)-yl)propanoate (7f): Pale yellow crystals; 81%, mp 172-75 ºC (benzene); IR (KBr, *v*, cm^{-1}): 3072, 2964, 1740, 1600, 1590, 1475, 1440, 1392, 1277, 1170, 795. ^{1}H NMR (400 MHz, $CDCl_3$, δ, ppm): 1.18 (3H, t, J = 7.1 Hz, CH_3), 2.05 (2H, dddd, J_1 = 13.9, J_2 = 6.6, J_3 = 4.7, J_4 = 2.6 Hz, C^6H_2), 2.48 (2H, t, J = 3.9 Hz, $C^{\alpha}H_2$), 2.91 (2H, ddd, J_1 = 7.8, J_2 = 6.6, J_3 = 2.6 Hz, C^7H_2), 2.93 (2H, t, J = 3.9 Hz, $C^{\beta}H_2$), 4.01 (1H, d, J = 11.9 Hz, C^5H), 4.17 (2H, dd, J_1 = 8.1, J_2 = 1.4 Hz, N-C^9H_2), 4.28 (2H, q, J = 7.1 Hz, CH_2), 7.10 (1H, dd, J_1 = 7.6, J_2 = 4.7 Hz), 7.20 (1H, tt, J_1 = 7.7, J_2 = 1.3 Hz), 7.25 (m, 2H), 7.31 (2H, dtd, J_1 = 7.8, J_2 = 1.2, J_3 = 0.5 Hz), 8.32 (1H, dd, J_1 = 7.6, J_2 = 1.9 Hz), 8.60 (1H, dd, J_1 = 4.7, J_2 = 1.9 Hz). ^{13}C NMR (100 MHz, $CDCl_3$, δ, ppm): 14.2 (1C, -$OCH_2\underline{CH_3}$), 34.2 (1C, -CH-, C-5), 34.2 (1C, -$C^{\alpha}H_2CO$), 51.6 (1C, -CH_2-, C-4), 54.3 (1C, N-$C^{\beta}H_2$), 56.5 (1C, -CH_2-, C-3), 61.1 (1C, -CH_2-, C-1), 62.5 (1C, -$O\underline{CH_2}CH_3$), 121.9 (1C, Ar., Py-C-7), 126.9 (1C, Ar., C-4'), 128.9 (2C, Ar., C-2', C-6'), 129.5 (2C, Ar., C-3', C-5'), 133.6 (1C, Ar., Py-C-6), 136.1 (1C, Ar., Py-C-5a), 145.0 (1C, Ar., C-1'), 146.0 (1C, Ar., Py-C-8), 157.7 (1C, Ar., Py-C-9a), 175.4 (1C, C=O). MS (EI, 70 eV) m/z (%), 325 (M^++1, 6), 324 (M^+,

20), 287 (18), 279 (M^+-OEt, 100), 240 (11), 223 (18), 196 (54), 169 (64), 109 (12), 105 (9), 97 (75), 89 (11), 76 (8). Anal. Calcd. for $C_{20}H_{24}N_2O_2$ (324); C, 74.07; H, 7.40; N, 8.64. Found: C, 74.05; H, 7.45; N, 8.71%.

Ethyl 2-(6,7-dihydro-5-(pyridin-2-yl)-5*H*-pyrido[2,3-*c*]azepin-8(9*H*)-yl)acetate (7g): Yellow needles; 85%, mp 158–60 ºC (acetone); IR (KBr, *v*, cm^{-1}): 3040, 2975, 1737, 1600, 1580, 1470, 1440, 1376, 1273, 1145, 768. ^{1}H NMR (400 MHz, $CDCl_3$, δ, ppm): 1.17 (3H, t, J = 7.1 Hz, CH_3), 2.06 (2H, dddd, J_1 = 13.6, J_2 = 6.6, J_3 = 4.7, J_4 = 2.6 Hz, C^6H_2), 2.83 (2H, ddd, J_1 = 7.4, J_2 = 6.6, J_3 = 2.6 Hz C^7H_2), 3.51 (2H, s, $C^{\alpha}H_2$), 4.15 (2H, d, J = 12.6 Hz, N-C^9H_2), 4.18 (2H, q, J = 7.1 Hz, CH_2), 4.48 (1H, dd, J_1 = 8.1, J_2 = 1.4 Hz, C^5H), 7.11 (1H, dd, J_1 = 7.5, J_2 = 4.7 Hz), 7.20 (1H, ddd, J_1 = 7.4, J_2 = 4.5, J_3 = 1.2 Hz), 7.31 (1H, ddd, J_1 = 7.6, J_2 = 1.2, J_3 = 0.5 Hz), 7.62 (1H, ddd, J_1 = 7.6, J_2 = 7.4, J_3 = 1.9 Hz), 7.80 (1H, dd, J_1 = 7.5, J_2 = 1.9 Hz), 8.52 (1H, ddd, J_1 = 4.5, J_2 = 1.9, J_3 = 0.5 Hz), 8.65 (1H, dd, J_1 = 4.7, J_2 = 1.9 Hz). ^{13}C NMR (100 MHz, $CDCl_3$, δ, ppm): 15.7 (1C, -$OCH_2\underline{CH_3}$), 33.7 (1C, -CH-, C-5), 49.7 (1C, -CH_2-, C-4), 55.0 (1C, -CH_2-, C-1), 57.3 (1C, -CH_2-, C-3), 60.3 (1C, -$C^{\alpha}H_2CO$), 62.2 (1C, -$O\underline{CH_2}CH_3$), 120.2 (1C, Ar., C-7), 121.5 (1C, Ar., C-4'), 125.6 (1C, Ar., C-6'), 133.5 (1C, Ar., C-5'), 135.2 (1C, Ar., C-6), 139.5 (1C, Ar., C-5a), 146.3 (1C, Ar., C-8), 147.5 (1C, Ar., C-3'), 153.0 (1C, Ar., Py-C-9a), 167.8 (1C, Ar., C-1'), 171.4 (1C, C=O). MS (EI, 70 eV) m/z (%), 312 (M^++1, 12), 311 (M^+, 100), 290 (11), 275 (19), 266 (M^+-OEt, 29), 265 (55), 249 (38), 187 (12), 165 (14), 115 (24), 92 (45), 77 (18). Anal. Calcd. for $C_{18}H_{21}N_3O_2$ (311); C, 69.45; H, 6.75; N, 13.50. Found: C, 69.52; H, 6.71; N, 13.47%.

Ethyl 3-(6,7-dihydro-5-(pyridin-2-yl)-5*H*-pyrido[2,3-*c*]azepin-8(9*H*)-yl)propanoate (7h): Greenish crystals; 72%, mp 151-53 ºC (acetone); IR (KBr, *v*, cm^{-1}): 3074, 2967, 1740, 1600, 1590, 1480, 1440, 1378, 1280, 1195, 788. ^{1}H NMR (400 MHz, $CDCl_3$, δ, ppm): 1.13 (3H, t, J = 7.1 Hz, CH_3), 2.10 (2H, dddd, J_1 = 13.6, J_2 = 6.6, J_3 = 4.7, J_4 = 2.6 Hz, C^6H_2), 2.48 (2H, t, J = 3.9 Hz, $C^{\alpha}H_2$), 2.88 (2H, ddd, J_1 = 7.6, J_2 = 6.6, J_3 = 2.6 Hz, C^7H_2), 2.90 (2H, t, J = 3.9 Hz, $C^{\beta}H_2$), 4.04 (2H, d, J = 11.9 Hz, N-C^9H_2), 4.15 (2H, q, J = 7.1 Hz, CH_2), 4.48 (1H, dd, J_1 = 8.1, J_2 = 1.4 Hz, C^5H), 7.11 (1H, dd, J_1 = 7.5, J_2 = 4.7 Hz), 7.22 (1H, ddd, J_1 = 7.4, J_2 = 4.5, J_3 = 1.2 Hz), 7.29 (1H, ddd, J_1 = 7.6, J_2 = 1.2, J_3 = 0.5 Hz), 7.61 (1H, ddd, J_1 = 7.6, J_2 = 7.4, J_3 = 1.9 Hz), 7.90 (1H, dd, J_1 = 7.5, J_2 = 1.9 Hz), 8.55 (1H, ddd, J_1 = 4.5, J_2 = 1.9, J_3 = 0.5 Hz), 8.68 (1H, dd, J_1 = 4.7, J_2 = 1.9 Hz). ^{13}C NMR (100 MHz, $CDCl_3$, δ, ppm): 16.1 (1C, -$OCH_2\underline{CH_3}$), 33.7 (1C, -CH-, C-5), 34.2 (1C, -$C^{\alpha}H_2CO$), 49.7 (1C, -CH_2-, C-4), 51.6 (1C, -CH_2-, C-3), 54.3 (1C, -CH_2-, C-1), 61.3 (1C, N-$C^{\beta}H_2$), 62.4 (1C, -$O\underline{CH_2}CH_3$), 120.2 (1C, Ar., C-7), 121.5 (1C, Ar., C-4'), 125.6 (1C, Ar., C-6'), 133.5 (1C, Ar., C-5'), 135.2 (1C, Ar., C-6), 139.5 (1C, Ar., C-5a), 146.3 (1C, Ar., C-8), 147.5 (1C, Ar., C-3'), 153.0 (1C, Ar., Py-C-9a), 167.8 (1C, Ar., C-1'), 180.6 (1C, C=O). MS (EI, 70 eV) m/z (%), 326 (M^++1, 7), 325 (M^+, 36), 303 (46), 280 (M^+-OEt, 100), 267 (36), 230 (39), 196 (18), 184 (22), 145 (14), 91 (20), 77 (21). Anal. Calcd. for $C_{19}H_{23}N_3O_2$ (325); C, 70.15; H, 7.07; N, 12.92. Found: C, 70.20; H, 7.11; N, 12.95%.

5,12-Ethano-6*H*-benzo[*e*]pyrido[2,3-*b*]azocin-7(12*H*)-one (8a): Yield 0.61 g (81%, method I), 0.56 g (75%, method II), 0.53 g (71%, method III), Pale yellow crystals; mp 137-40 ºC (acetone); IR (KBr, *v*, cm^{-1}): 3030, 2975, 1693, 1600, 1580, 1480, 1440, 1376, 1255, 1184, 792. ^{1}H NMR (400 MHz, $CDCl_3$, δ, ppm): 2.03 (2H, dddd, J_1 = 13.3, J_2 = 8.0, J_3 = 4.1, J_4 = 3.6 Hz, *bridged-*CH_2), 3.51 (2H, ddd, J_1 = 11.9, J_2 = 8.0, J_3 = 3.6 Hz, *bridged-*NCH_2), 4.30 (1H, dd, J_1 = 6.7, J_2 = 1.4 Hz $C^{12}H$), 4.92 (2H, d, J = 16.1 Hz, N-C^6H_2CO), 7.14 (1H, dd, J_1 = 7.6, J_2 = 4.7 Hz), 7.28 (1H, ddd, J_1 = 8.0, J_2 = 1.4, J_3 = 0.4 Hz), 7.30-7.42 (2H, m), 7.94 (1H, ddd, J_1 = 7.9, J_2 = 1.3, J_3 = 0.4 Hz), 8.02 (1H, dd, J_1 = 7.6, J_2 = 1.9 Hz), 8.17 (1H, dd, J_1 = 4.7, J_2 = 1.9 Hz). ^{13}C NMR (100 MHz, $CDCl_3$, δ, ppm): 28.4 (1C, bridged-CH_2-, C-13), 32.9 (1C,

-CH-, C-12), 40.0 (1C, bridged-CH_2-, C-14), 50.0 (1C, -CH_2CO, C-6), 121.2 (1C, Ar., Py-C-2), 122.7 (1C, Ar., Py-C-12a), 124.6 (1C, Ar., C-9), 126.1 (1C, Ar., C-11a), 126.7 (2C, Ar., C-8, C-11), 127.8 (2C, Ar., C-10, C-7a), 128.7 (1C, Ar., Py-C-1), 151.7 (1C, Ar., Py-C-3), 156.4 (1C, Ar., Py-C-4a), 203.5 (1C, C=O, C-7). MS (EI, 70 eV) m/z (%), 252 (M^++2, 5), 251 (M^++1, 31), 250 (M^+, 100), 222 (36), 209 (15), 197 (6), 185 (66), 165 (33), 147 (18), 108 (17), 92 (28), 77 (26). Anal. Calcd. for $C_{16}H_{14}N_2O$ (250); C, 76.80; H, 5.60; N, 11.20. Found: C, 76.85; H, 5.57; N, 11.24%.

6,7-Dihydro-5,13-ethanobenzo[*e*]pyrido[2,3-*b*]azonin-8(13*H*)-one (8b): Yield 0.63 g (80%, method I), 0.57 g (73%, method II), 0.55 g (70%, method III), Yellow solid; mp 168-71 ºC (acetone); IR (KBr, *v*, cm^{-1}): 3060, 2974, 1700, 1600, 1585, 1480, 1440, 1393, 1284, 1178, 782. ^{1}H NMR (400 MHz, $CDCl_3$, δ, ppm): 2.11 (2H, dddd, J_1 = 14.4, J_2 = 7.2, J_3 = 3.3, J_4 = 3.1 Hz, *bridged-*CH_2), 2.84 (2H, ddd, J_1 = 15.7, J_2 = 6.4, J_3 = 2.8 Hz, C^7H_2), 3.57 (2H, ddd, J_1 = 14.4, J_2 = 6.9, J_3 = 3.6 Hz, *bridged-*NCH_2), 3.85 (2H, ddd, J_1 = 14.4, J_2 = 6.6, J_3 = 2.5 Hz, C^6H_2), 4.50 (1H, dd, J_1 = 4.5, J_2 = 1.7 Hz, C^{13}H), 7.09 (1H, dd, J_1 = 7.5, J_2 = 4.7 Hz), 7.31 (1H, ddd, J_1 = 11.5, J_2 = 1.8, J_3 = 0.5 Hz), 7.33 (1H, ddd, J_1 = 7.8, J_2 = 7.5, J_3 = 1.8 Hz), 7.45 (1H, ddd, J_1 = 11.5, J_2 = 7.5, J_3 = 1.2 Hz), 7.98 (1H, ddd, J_1 = 7.8, J_2 = 1.2, J_3 = 0.5 Hz), 8.09 (1H, dd, J_1 = 7.5, J_2 = 1.9 Hz), 8.18 (1H, dd, J_1 = 4.7, J_2 = 1.9 Hz). ^{13}C NMR (100 MHz, $CDCl_3$, δ, ppm): 26.4 (1C, bridged-CH_2-, C-14), 35.9 (1C, -CH_2CO, C-7), 40.0 (1C, -CH-, C-13), 50.9 (1C, bridged-CH_2-, C-15), 51.7 (1C, N-CH_2-, C-6), 121.2 (1C, Ar., Py-C-2), 122.7 (1C, Ar., Py-C-13a), 124.6 (1C, Ar., C-10), 126.1 (1C, Ar., C-12a), 126.7 (2C, Ar., C-9, C-12), 127.8 (2C, Ar., C-11, C-8a), 128.7 (1C, Ar., Py-C-1), 151.7 (1C, Ar., Py-C-3), 156.4 (1C, Ar., Py-C-4a), 210.8 (1C, C=O, C-8). MS (EI, 70 eV) m/z (%), 265 (M^++1, 12), 264 (M^+, 60), 246 (53), 236 (100), 219 (6), 207 (31), 193 (10), 178 (3), 165 (45), 152 (63), 134 (33), 92 (20), 77 (32). Anal. Calcd. for $C_{17}H_{16}N_2O$ (264); C, 77.27; H, 6.06; N, 10.60. Found: C, 77.32; H, 6.09; N, 10.55%.

6,12-Dihydro-5*H*-7,12-ethanodipyrido[2,3-*b*:2',3'-*e*]azocin-5-one (8c): Yield 0.63 g (84%, method I), 0.57 g (77%, method II), 0.55 g (74%, method III), Yellow crystals, mp 184-86 °C (benzene); IR (KBr, ν, cm^{-1}): 3034, 2979, 1692, 1600, 1580, 1500, 1440, 1322, 1275, 1153, 794. ^{1}H NMR (400 MHz, $CDCl_3$, δ, ppm): 2.14 (2H, dddd, J_1 = 13.4, J_2 = 7.9, J_3 = 4.1, J_4 = 3.6 Hz, *bridged-*CH_2), 3.49 (2H, ddd, J_1 = 12.4, J_2 = 7.9, J_3 = 3.6 Hz, *bridged-*NCH_2), 4.83 (2H, dd, J_1 = 6.7, J_2 = 1.4 Hz, N-C^6H_2CO), 4.95 (1H, d, J = 16.2 Hz, C^{12}H), 7.11 (1H, dd, J_1 = 7.6, J_2 = 4.7 Hz), 7.25 (1H, dd, J_1 = 7.8, J_2 = 4.5 Hz), 7.80 (1H, dd, J_1 = 7.8, J_2 = 1.9 Hz), 7.97 (1H, dd, J_1 = 7.6, J_2 = 1.9 Hz), 8.12 (1H, dd, J_1 = 4.7, J_2 = 1.9 Hz), 8.70 (1H, dd, J_1 = 4.5, J_2 = 1.9 Hz). ^{13}C NMR (100 MHz, $CDCl_3$, δ, ppm): 27.4 (1C, bridged-CH_2-, C-13), 32.9 (1C, -CH-, C-12), 45.4 (1C, bridged-CH_2-, C-14), 56.2 (1C, -$\underline{CH_2}$CO, C-6), 121.1 (1C, Ar., C-10), 121.2 (1C, Ar., C-11a), 124.6 (1C, Ar., C-3), 126.7 (1C, Ar., C-4a), 127.8 (1C, Ar., C-4), 128.7 (1C, Ar., C-11), 149.2 (1C, Ar., C-9), 151.7 (1C, Ar., C-2), 154.6 (1C, Ar., C-7a), 156.4 (1C, Ar., C-12a), 206.4 (1C, C=O, C-5). MS (EI, 70 eV) m/z (%), 252 (M^++1, 11), 251 (M^+, 100), 223 (30), 192 (2), 162 (12), 145 (39), 135 (55), 117 (20), 108 (19), 92 (46), 77 (24). Anal. Calcd. for $C_{15}H_{13}N_3O$ (251); C, 71.71; H, 5.17; N, 16.73. Found: C, 71.68; H, 5.22; N, 16.71%.

6,7-Dihydro-8,13-ethanodipyrido[2,3-*b*:2',3'-*e*]azonin-5(13*H*)-one (8d): Yield 0.69 g (88%, method I), 0.63 g (81%, method II), 0.56 g (71%, method III), Yellow needles, mp 154-56 °C (AcOEt); IR (KBr, *v*, cm^{-1}): 3018, 2945, 1700, 1605, 1585, 1470, 1440, 1394, 1241, 1179, 794. ^{1}H NMR (400 MHz, $CDCl_3$, δ, ppm): 2.19 (2H, dddd, J_1 = 14.3, J_2 = 7.2, J_3 = 3.3, J_4 = 3.1 Hz, *bridged-*CH_2), 2.82 (2H, ddd, J_1 = 15.7, J_2 = 6.4, J_3 = 2.8 Hz, C^6H_2), 3.47 (2H, ddd, J_1 = 14.5, J_2 = 6.9, J_3 = 3.5 Hz, *bridged-*NCH_2), 3.83 (2H, ddd, J_1 = 14.4, J_2 = 6.6, J_3 = 2.5 Hz C^7H_2), 4.76 (1H, dd, J_1 = 4.4, J_2 = 1.7 Hz, C^{13}H), 6.95 (1H, dd, J_1 = 7.9, J_2 = 4.5 Hz), 7.14 (1H,

dd, J_1 = 7.5, J_2 = 4.7 Hz), 7.85 (1H, dd, J_1 = 7.9, J_2 = 1.9 Hz), 7.92 (1H, dd, J_1 = 7.5, J_2 = 1.9 Hz), 8.15 (1H, dd, J_1 = 4.7, J_2 = 1.9 Hz), 8.92 (1H, dd, J_1 = 4.5, J_2 = 1.9 Hz). ^{13}C NMR (100 MHz, $CDCl_3$, δ, ppm): 31.2 (1C, bridged-CH_2-, C-14), 35.9 (1C, *C*H_2CO, C-6), 45.4 (1C, -CH-, C-13), 49.1 (1C, bridged-CH_2-, C-15), 50.44 (1C,N-*C*H_2, C-7), 121.1 (1C, Ar., C-11), 121.2 (1C, Ar., C-12a), 124.6 (1C, Ar., C-3), 126.7 (1C, Ar., C-4a), 127.8 (1C, Ar., C-4), 128.7 (1C, Ar., C-12), 149.2 (1C, Ar., C-10), 151.7 (1C, Ar., C-2), 154.6 (1C, Ar., C-8a), 156.4 (1C, Ar., C-13a), 215.8 (1C, C=O, C-5). MS (EI, 70 eV) m/z (%), 267 (M^++2, 15), 266 (M^++1, 20), 265 (M^+, 57), 237 (47), 230 (100), 195 (25), 167 (10), 154 (29), 139 (22), 126 (13), 111 (15), 90 (36), 75 (17). Anal. Calcd. for $C_{16}H_{15}N_3O$ (265); C, 72.45; H, 5.66; N, 15.84. Found: C, 72.50; H, 5.71; N, 15.79%.

7,13-Dihydro-6,13-ethanobenzo[*f*]pyrido[2,3-*c*]azonin-8(5*H*)-one (8e): Yield 0.66 g (84%, method I), 0.63 g (80%, method II), 0.56 g (72%, method III), Creamy powder; mp 139-41 ºC (acetone); IR (KBr, *v*, cm^{-1}): 3052, 2973, 1695, 1600, 1480, 1440, 1392, 1240, 1186, 775. ^{1}H NMR (400 MHz, $CDCl_3$, δ, ppm): 2.17 (2H, dddd, J_1 = 13.3, J_2 = 7.0, J_3 = 3.4, J_4 = 1.7 Hz, *bridged-CH*$_2$), 2.86 (2H, ddd, J_1 = 7.0, J_2 = 6.5, J_3 = 1.7 Hz, *bridged-NCH*$_2$), 4.03 (2H, d, J = 11.9 Hz, *C*^{5}*H*$_2$), 4.27-4.41 (3H, dd, J_1 = 5.5, J_2 = 1.4 Hz, N-C^{7}H$_2$CO), 4.35 (d, J = 12.9 Hz, C^{13}H), 7.08 (1H, dd, J_1 = 7.6, J_2 = 4.7 Hz), 7.24 (1H, ddd, J_1 = 10.3, J_2 = 1.8, J_3 = 0.4 Hz), 7.34 (1H, ddd, J_1 = 7.9, J_2 = 7.3, J_3 = 1.8 Hz), 7.46 (1H, ddd, J_1 = 10.3, J_2 = 7.3, J_3 = 1.3 Hz), 7.85 (1H, ddd, J_1 = 7.9, J_2 = 1.3, J_3 = 0.4 Hz), 8.35 (1H, dd, J_1 = 7.6, J_2 = 1.9 Hz), 8.72 (1H, dd, J_1 = 4.7, J_2 = 1.9 Hz). ^{13}C NMR (100 MHz, $CDCl_3$, δ, ppm): 31.7 (1C, -CH-, C-13), 32.9 (1C, bridged-CH_2-, C-14), 51.4 (1C, -CH_2-, C-5), 53.4 (1C, bridged-CH_2-, C-15), 59.2 (1C, N-CH_2CO, C-7), 123.4 (1C, Ar., Py-C-2), 124.6 (1C, Ar., C-10), 124.9 (1C, Ar., C-11), 128.0 (1C, Ar., C-8a), 128.7 (1C, Ar., Py-C-13a), 128.9 (2C, Ar., C-9, C-12), 135.6 (2C, Ar., Py-C-1, C-12a), 149.2 (1C, Ar., Py-C-3), 149.9 (1C, Ar., Py-C-4a), 202.2 (1C, C=O, C-8). MS (EI, 70 eV) m/z (%), 264 (M^+, 19), 263 (100), 262 (43), 236 (32), 221 (20), 200 (68), 184 (3), 170 (2), 165 (12), 147 (20), 108 (16), 92 (31), 77 (24). Anal. Calcd. for $C_{17}H_{16}N_2O$ (264); C, 77.27; H, 6.06; N, 10.60. Found: C, 77.29; H, 5.98; N, 10.67%.

7,8-Dihydro-5*H*-6,14-ethanobenzo[*f*]pyrido[2,3-*c*]azecin-9(14*H*)-one (8f): Yield 0.75 g (91%, method I), 0.64 g (78%, method II), 0.56 g (68%, method III), Yellow solid; mp 164-66 ºC (acetone); IR (KBr, *v*, cm^{-1}): 3060, 2935, 1700, 1600, 1575, 1470, 1440, 1359, 1235, 1170, 798. ^{1}H NMR (400 MHz, $CDCl_3$, δ, ppm): 2.66 (2H, dddd, J_1 = 11.1, J_2 = 7.7, J_3 = 6.3, J_4 = 2.2 Hz, *bridged-C*^{15}*H*$_2$), 3.09 (2H, ddd, J_1 = 10.1, J_2 = 6.3, J_3 = 2.2 Hz, C^{8}H$_2$), 3.34 (2H, ddd, J_1 = 10.6, J_2 = 7.5, J_3 = 2.5 Hz, *bridged-NC*^{16}*H*$_2$), 3.50 (2H, ddd, J_1 = 11.1, J_2 = 7.5, J_3 = 2.5 Hz, C^{7}H$_2$), 4.37-4.48 (2H, dd, J_1 = 8.6, J_2 = 6.9 Hz, C^{5}H$_2$), 4.45 (1H, d, J = 15.8 Hz, C^{14}H), 7.06 (1H, dd, J_1 = 7.6, J_2 = 4.6 Hz), 7.19 (1H, ddd, J_1 = 11.5, J_2 = 1.1, J_3 = 0.5 Hz), 7.41 (1H, ddd, J_1 = 11.5, J_2 = 10.2, J_3 = 1.3 Hz), 7.57 (1H, ddd, J_1 = 10.2, J_2 = 8.9, J_3 = 1.1 Hz), 7.77 (1H, ddd, J_1 = 8.9, J_2 = 1.3, J_3 = 0.5 Hz), 8.05 (1H, dd, J_1 = 4.6, J_2 = 2.0 Hz), 8.37 (1H, dd, J_1 = 7.6, J_2 = 2.0 Hz). ^{13}C NMR (100 MHz, $CDCl_3$, δ, ppm): 31.2 (1C, -CH-, C-14), 32.9 (1C, bridged-CH_2-, C-15), 35.9 (1C, CH_2CO, C-8), 51.4 (1C, -CH_2-, C-7), 53.4 (1C, -CH_2-, C-5), 59.5 (1C, bridged-CH_2-, C-16), 123.4 (1C, Ar., Py-C-2), 124.6 (1C, Ar., C-11), 124.9 (1C, Ar., C-12), 128.0 (1C, Ar., C-9a), 128.7 (1C, Ar., Py-C-14a), 128.9 (2C, Ar., C-10, C-13), 135.6 (2C, Ar., Py-C-1, C-13a), 149.2 (1C, Ar., Py-C-3), 149.9 (1C, Ar., Py-C-4a), 200.8 (1C, C=O, C-8). MS (EI, 70 eV) m/z (%), 280 (M^++2, 7), 279 (M^++1, 16), 278 (M^+, 100), 250 (19), 244 (9), 214 (3), 196 (9), 184 (13), 167 (5), 154 (27), 140 (18), 108 (76), 92 (48), 77 (25). Anal. Calcd. for $C_{18}H_{18}N_2O$ (278); C, 77.69; H, 6.47; N, 10.07. Found: C, 77.74; H, 6.50; N, 9.99%.

8,13-Dihydro-7,13-ethanodipyrido[2,3-*c*:2',3'-*f*]azonin-5(6*H*)-one (8g): Yield 0.71 g (90%, method I), 0.68 g (87%, method II), 0.56 g (72%, method III), Brownish crystals; mp

170-173 ºC (ethanol); IR (KBr, *v*, cm^{-1}): 3070, 2985, 1694, 1600, 1590, 1470, 1440, 1360, 1284, 1132, 774. ^{1}H NMR (400 MHz, $CDCl_3$, δ, ppm): 2.09 (2H, dddd, J_1 = 13.5, J_2 = 7.0, J_3 = 3.5, J_4 = 1.7 Hz, *bridged-*CH_2), 2.89 (2H, ddd, J_1 = 7.0, J_2 = 5.9, J_3 = 1.7 Hz, *bridged-*NCH_2), 4.05 (2H, d, J = 11.9 Hz, C^6H_2), 4.36 (2H, d, J = 13.1 Hz, C^8H_2), 4.54 (1H, dd, J_1 = 5.5, J_2 = 1.4 Hz, $C^{13}H$), 7.12 (1H, dd, J_1 = 7.5, J_2 = 4.7 Hz), 7.29 (1H, dd, J_1 = 7.8, J_2 = 4.5 Hz), 7.71 (1H, dd, J_1 = 7.5, J_2 = 1.9 Hz), 7.91 (1H, dd, J_1 = 7.8, J_2 = 1.9 Hz), 8.64 (1H, dd, J_1 = 4.7, J_2 = 1.9 Hz), 8.76 (1H, dd, J_1 = 4.5, J_2 = 1.9 Hz). ^{13}C NMR (100 MHz, $CDCl_3$, δ, ppm): 31.2 (1C, -CH-, C-13), 32.9 (1C, bridged-CH_2-, C-14), 51.4 (1C, -$\underline{CH_2}$, C-8), 53.4 (1C, bridged-CH_2-, C-15), 60.2 (1C, -$\underline{CH_2}$CO, C-6), 123.6 (1C, Ar., C-11), 124.6 (1C, Ar., C-3), 124.9 (1C, Ar., C-4a), 128.7 (1C, Ar., C-12a), 128.9 (1C, Ar., C-4), 135.6 (1C, Ar., C-12), 149.2 (2C, Ar., C-2, C-10), 149.9 (1C, Ar., C-8a), 151.6 (1C, Ar., C-13a), 212.5 (1C, C=O, C-5). MS (EI, 70 eV) m/z (%), 266 (M^++1, 6), 248 (5), 230 (49), 201 (4), 195 (25), 184 (2), 167 (10), 154 (29), 139 (23), 111 (16), 90 (8), 77 (18). Anal. Calcd. for $C_{16}H_{15}N_3O$ (265); C, 72.45; H, 5.66; N, 15.84. Found: C, 72.44; H, 5.70; N, 15.77%.

6,7,9,14-Tetrahydro-5*H*-8,14-ethanodipyrido[2,3-*c*:2',3'-*f*]azecin-5-one (8h): Yield 0.73 g (89%, method I), 0.71 g (86%, method II), 0.61 g (74%, method III), Gray crystals; mp 180 *dec.*°C (EtOAc); IR (KBr, *v*, cm^{-1}): 3046, 2972, 1705, 1600, 1580, 1480, 1440, 1362, 1235, 1170, 789. ^{1}H NMR (400 MHz, $CDCl_3$, δ, ppm): 2.68 (2H, dddd, J_1 = 11.2, J_2 = 7.7, J_3 = 6.3, J_4 = 2.2 Hz, *bridged-*CH_2), 3.09 (2H, ddd, J_1 = 6.8, J_2 = 6.3, J_3 = 2.2 Hz, C^6H_2), 3.36 (2H, ddd, J_1 = 10.6, J_2 = 7.5, J_3 = 2.6 Hz, *bridged-*NCH_2), 3.49 (2H, ddd, J_1 = 11.1, J_2 = 7.5, J_3 = 2.6 Hz, C^7H_2), 4.42 (2H, d, J = 15.8 Hz, C^9H_2), 4.64 (1H, dd, J_1 = 8.7, J_2 = 6.8 Hz, $C^{14}H$), 7.02 (1H, dd, J_1 = 7.6, J_2 = 4.6 Hz), 7.28 (1H, dd, J_1 = 7.8, J_2 = 4.6 Hz), 7.71 (1H, dd, J_1 = 7.6, J_2 = 2.0 Hz), 7.93 (1H, dd, J_1 = 7.8, J_2 = 1.9 Hz), 8.12 (1H, dd, J_1 = 4.6, J_2 = 2.0 Hz), 8.49 (1H, dd, J_1 = 4.6, J_2 = 1.9 Hz). ^{13}C NMR (100 MHz, $CDCl_3$, δ, ppm): 30.7 (1C, -CH-, C-14), 32.6 (1C, bridged-CH_2-, C-15), 35.9 (1C, -$\underline{CH_2}$CO, C-6), 51.4 (1C, -$\underline{CH_2}$, C-7), 53.4 (1C, -$\underline{CH_2}$, C-9), 63.3 (1C, bridged-CH_2-, C-16), 123.7 (1C, Ar., C-12), 124.6 (1C, Ar., C-3), 124.9 (1C, Ar., C-4a), 128.7 (1C, Ar., C-13a), 128.9 (1C, Ar., C-4), 135.6(1C, Ar., C-13), 149.2 (2C, Ar., C-2, C-11), 149.9 (1C, Ar., C-9a), 151.6 (1C, Ar., C-14a), 214.6 (1C, C=O, C-5). MS (EI, 70 eV) m/z (%), 280 (M^++1, 18), 279 (M^+, 100), 268 (12), 253 (25), 225 (23), 211 (17), 197 (4), 165 (5), 159 (38), 134 (45), 119 (62), 107 (42), 91 (47), 77 (20). Anal. Calcd. for $C_{17}H_{17}N_3O$ (279); C, 73.11; H, 6.09; N, 15.05. Found: C, 73.14; H, 6.15; N, 15.02%.

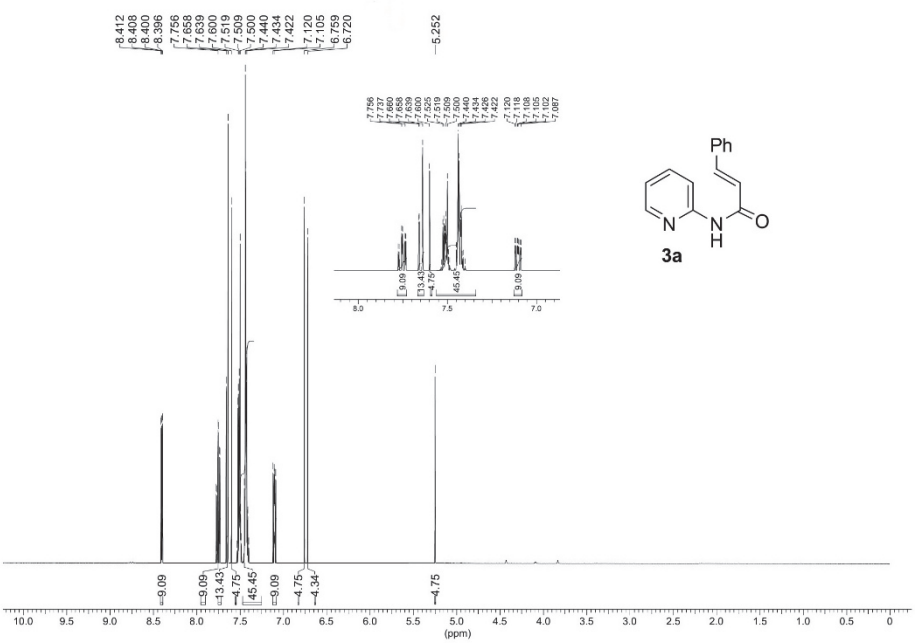

Fig. S-1. ^{1}H-NMR spectrum of compound **3a**

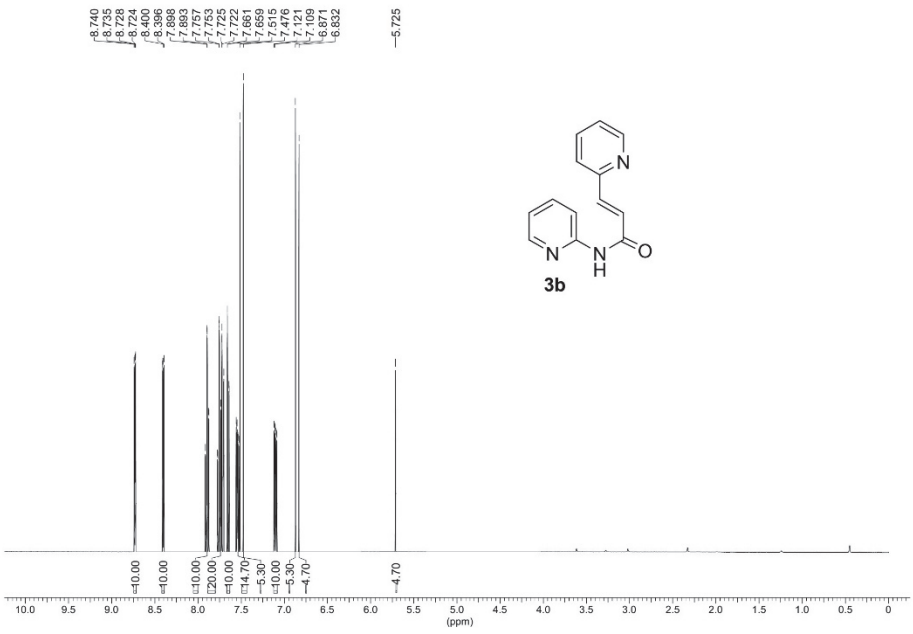

Fig. S-2. ^{1}H-NMR spectrum of compound **3b**

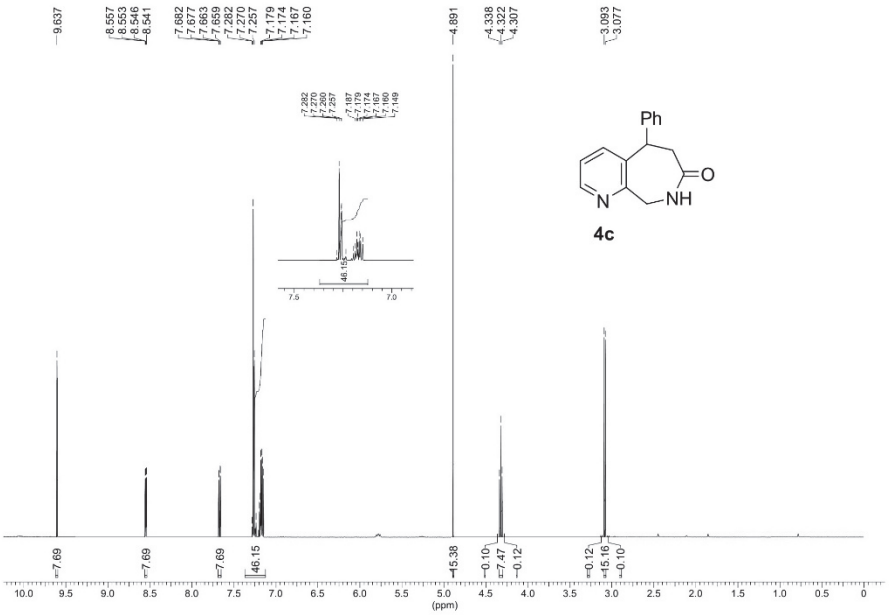

Fig. S-3. ^{1}H-NMR spectrum of compound **4c**

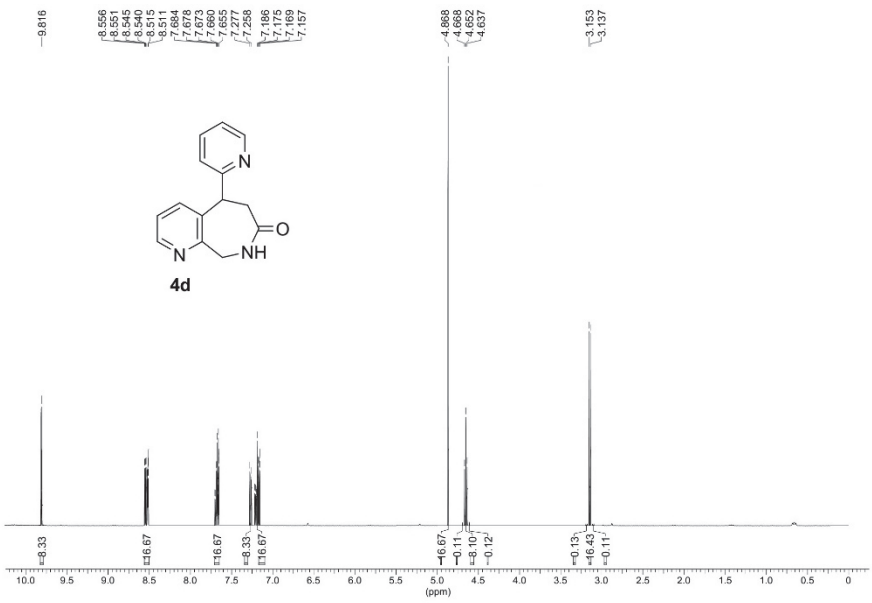

Fig. S-4. ^{1}H-NMR spectrum of compound **4d**

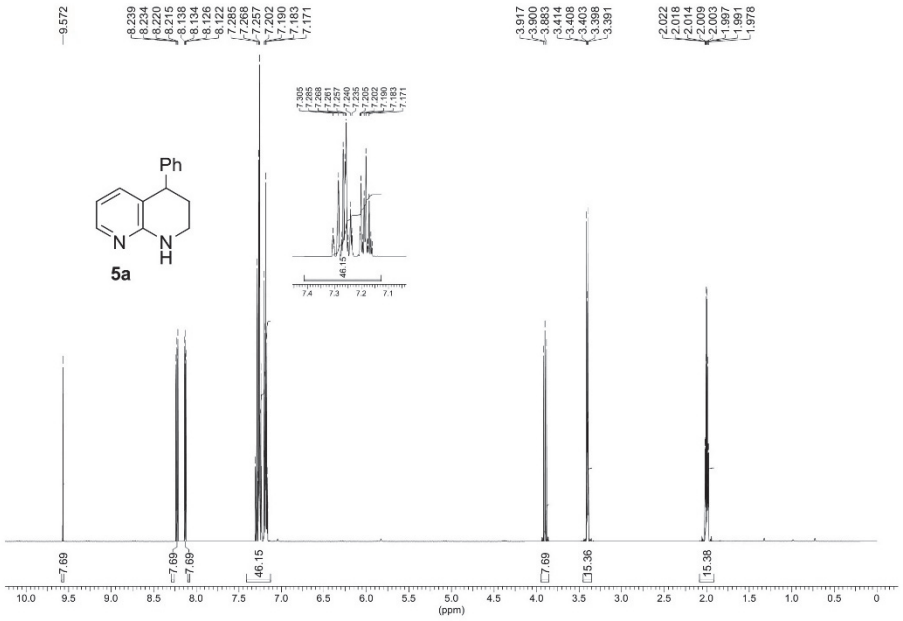

Fig. S-5. ^{1}H-NMR spectrum of compound 5a

Fig. S-6. ^{1}H-NMR spectrum of compound 5b

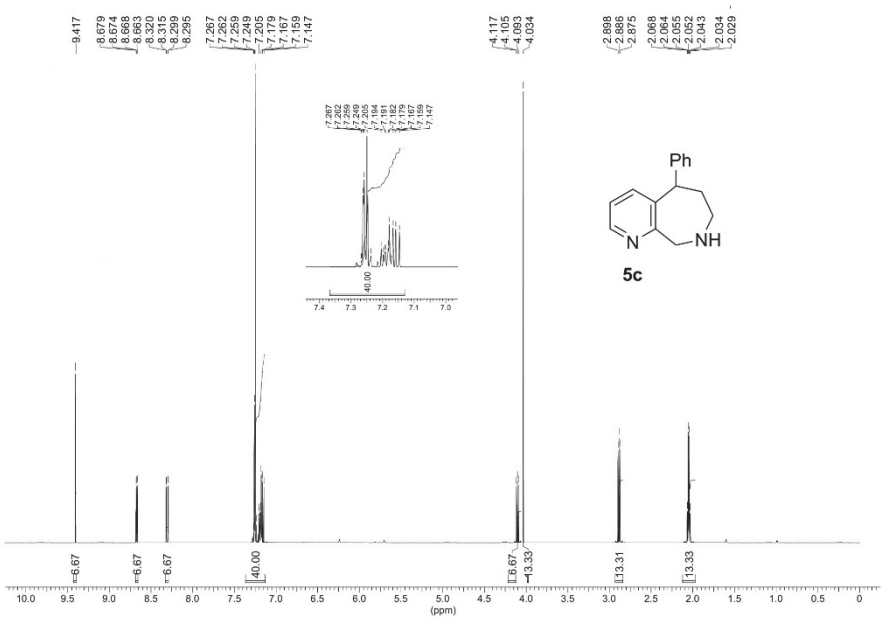

Fig. S-7. ^{1}H-NMR spectrum of compound **5c**

Fig. S-8. ^{1}H-NMR spectrum of compound **5d**

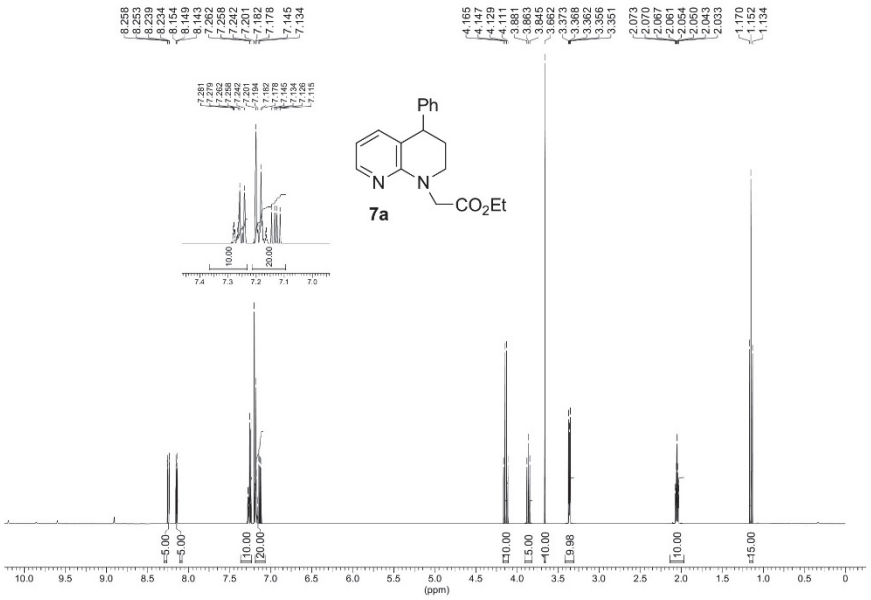

Fig. S-9. ^{1}H-NMR spectrum of compound **7a**

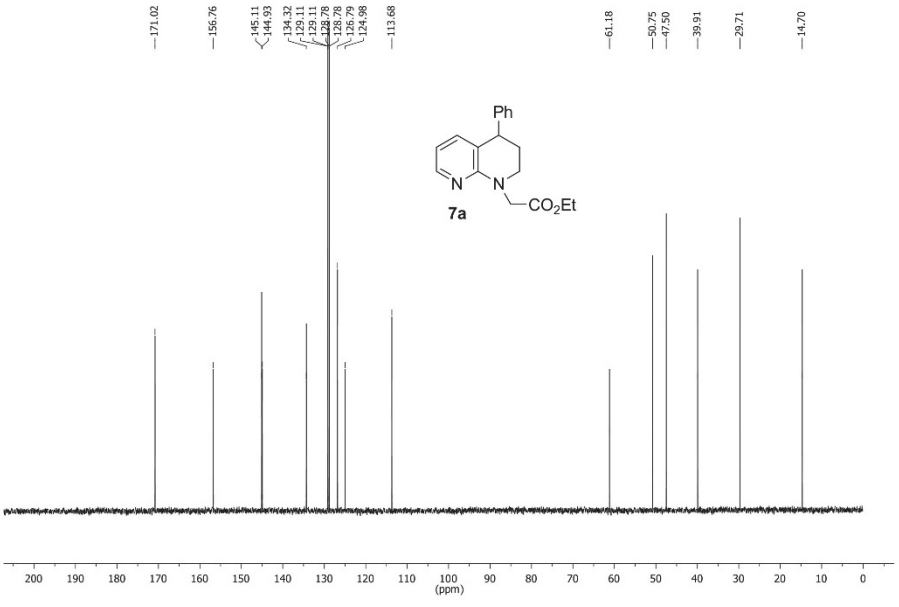

Fig. S-10. ^{13}C-NMR spectrum of compound **7a**

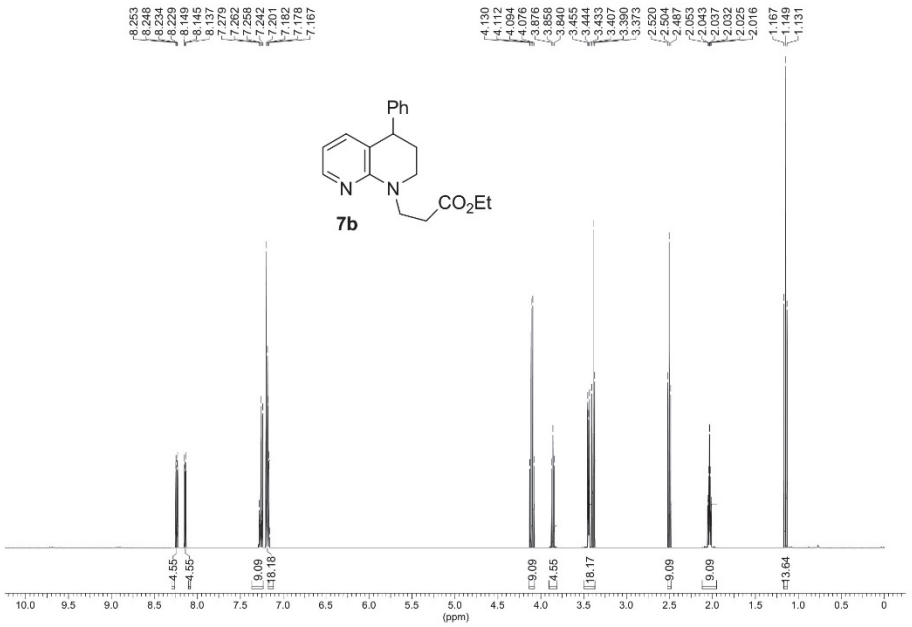

Fig. S-11. ^{1}H-NMR spectrum of compound **7b**

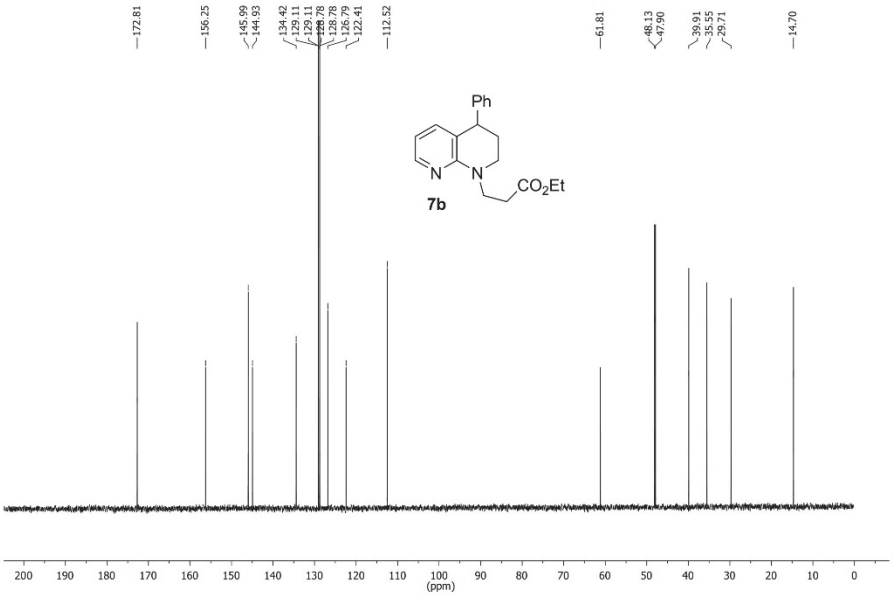

Fig. S-12. ^{13}C-NMR spectrum of compound **7b**

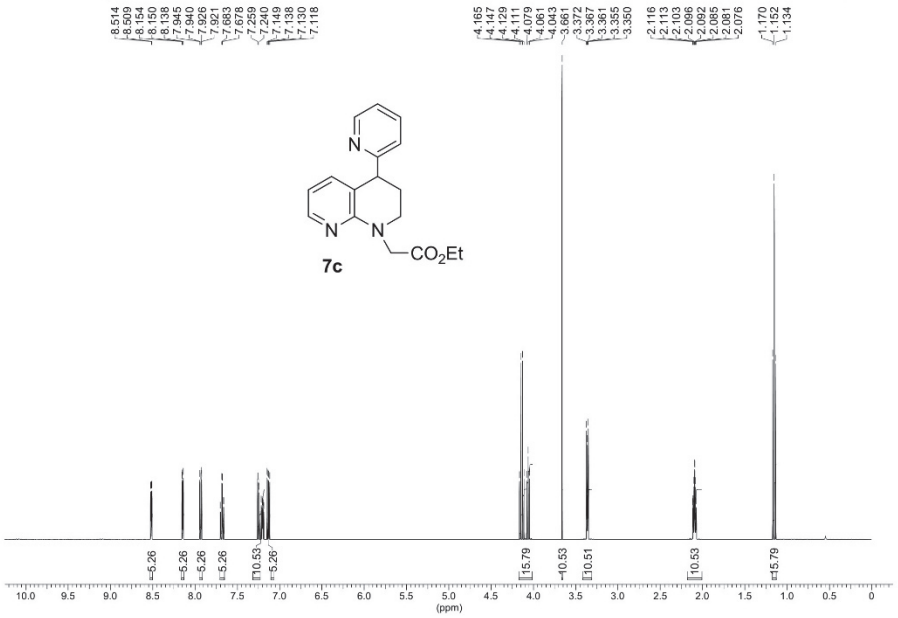

Fig. S-13. ^{1}H-NMR spectrum of compound **7c**

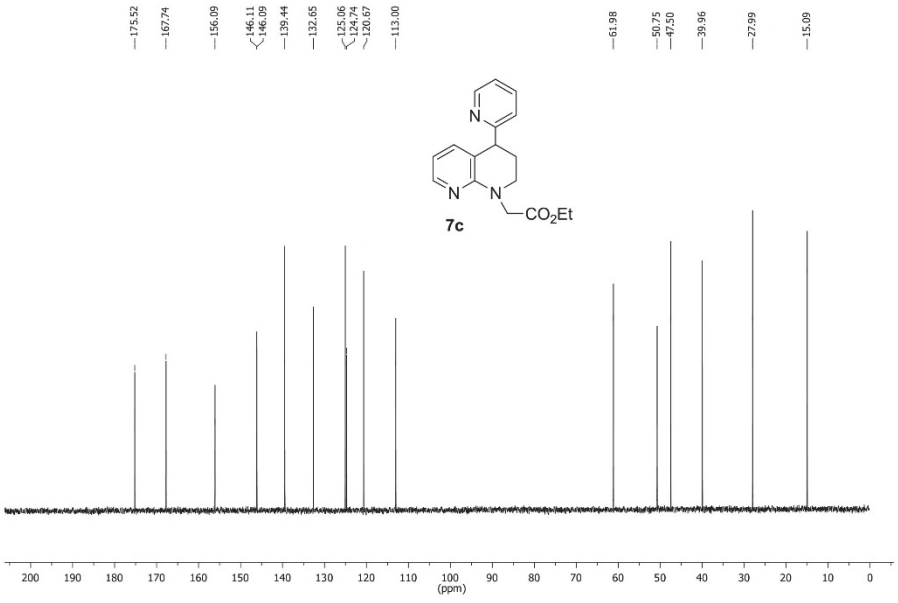

Fig. S-14. ^{13}C-NMR spectrum of compound **7c**

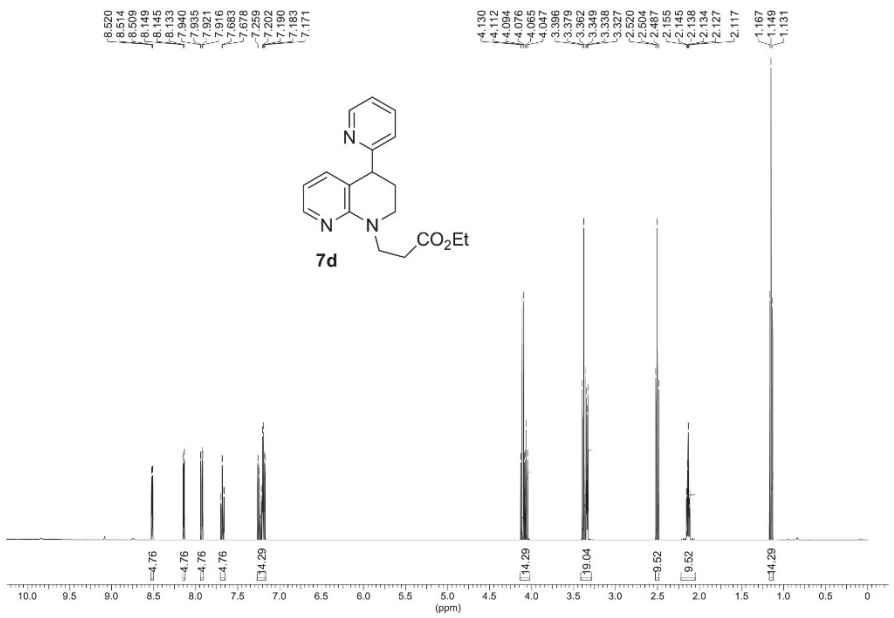

Fig. S-15. ^{1}H-NMR spectrum of compound **7d**

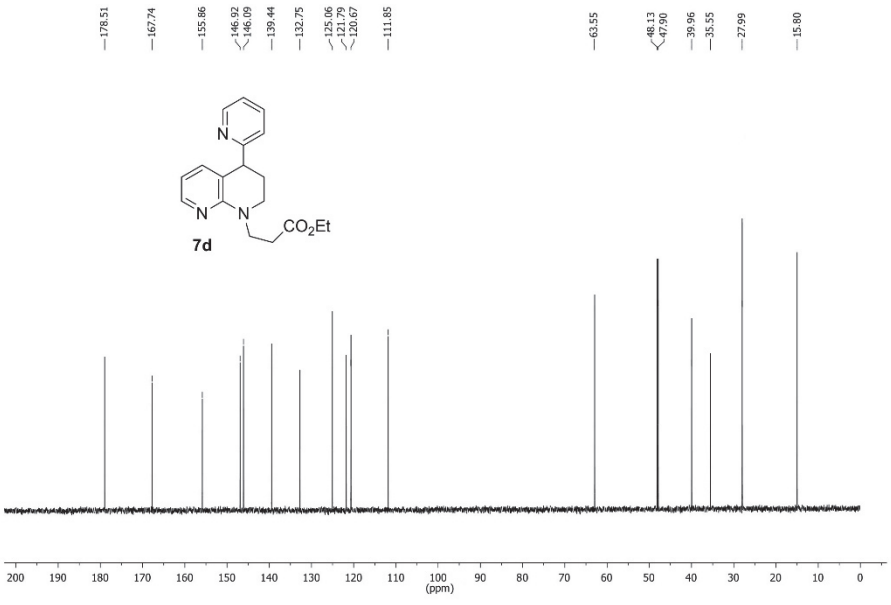

Fig. S-16. ^{13}C-NMR spectrum of compound **7d**

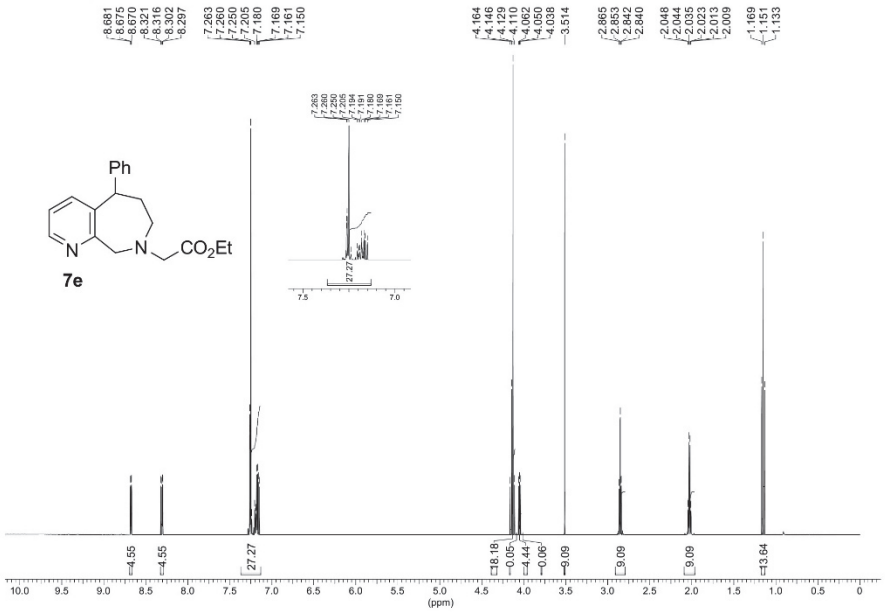

Fig. S-17. ^{1}H-NMR spectrum of compound **7e**

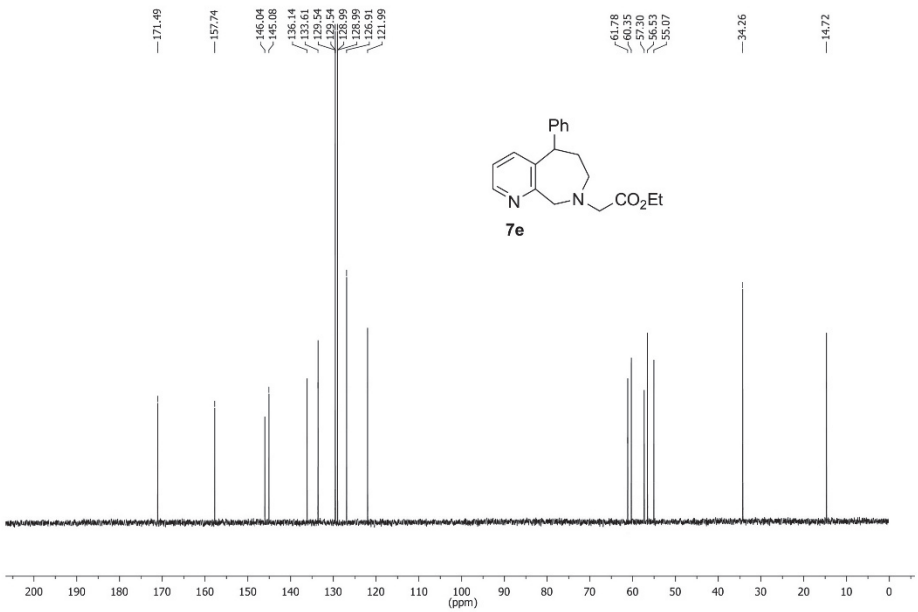

Fig. S-18. ^{13}C-NMR spectrum of compound **7e**

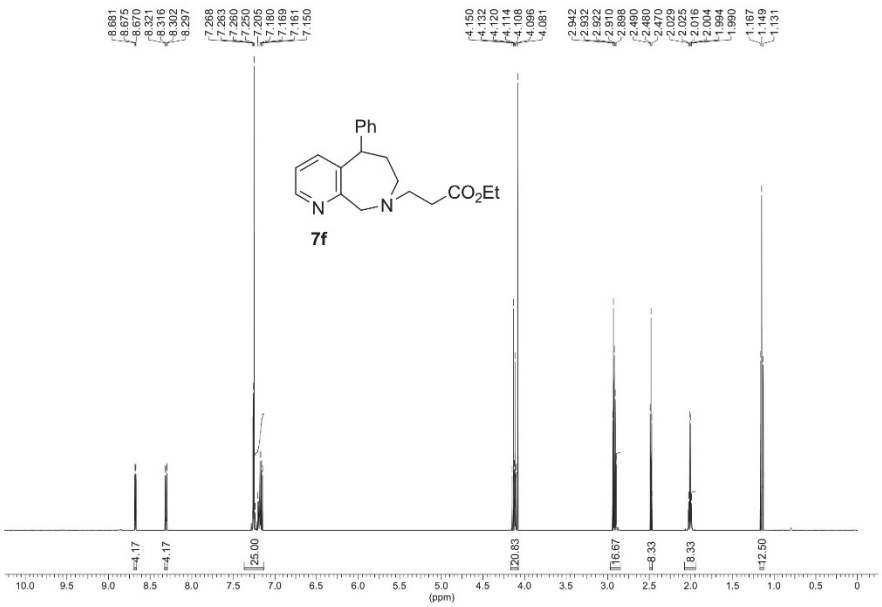

Fig. S-19. ^{1}H-NMR spectrum of compound **7f**

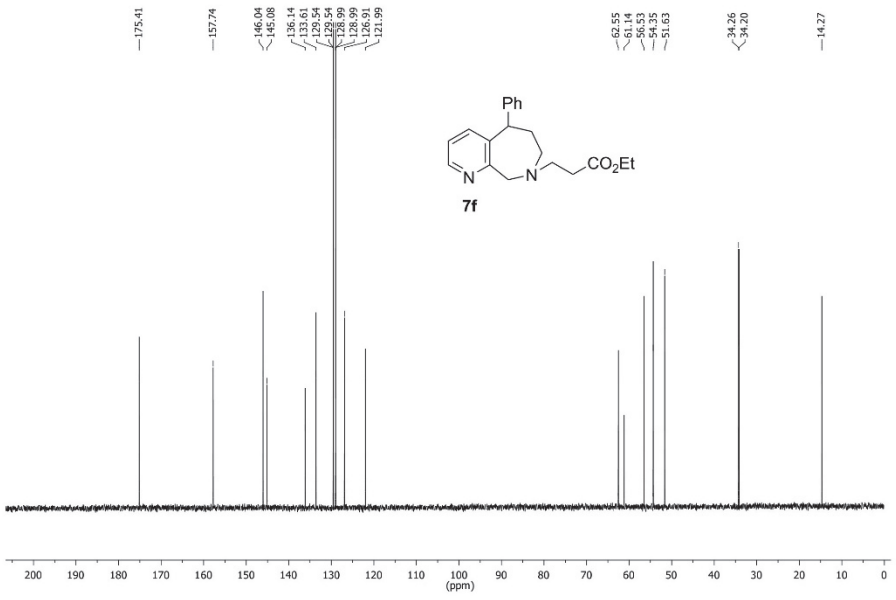

Fig. S-20. ^{13}C-NMR spectrum of compound **7f**

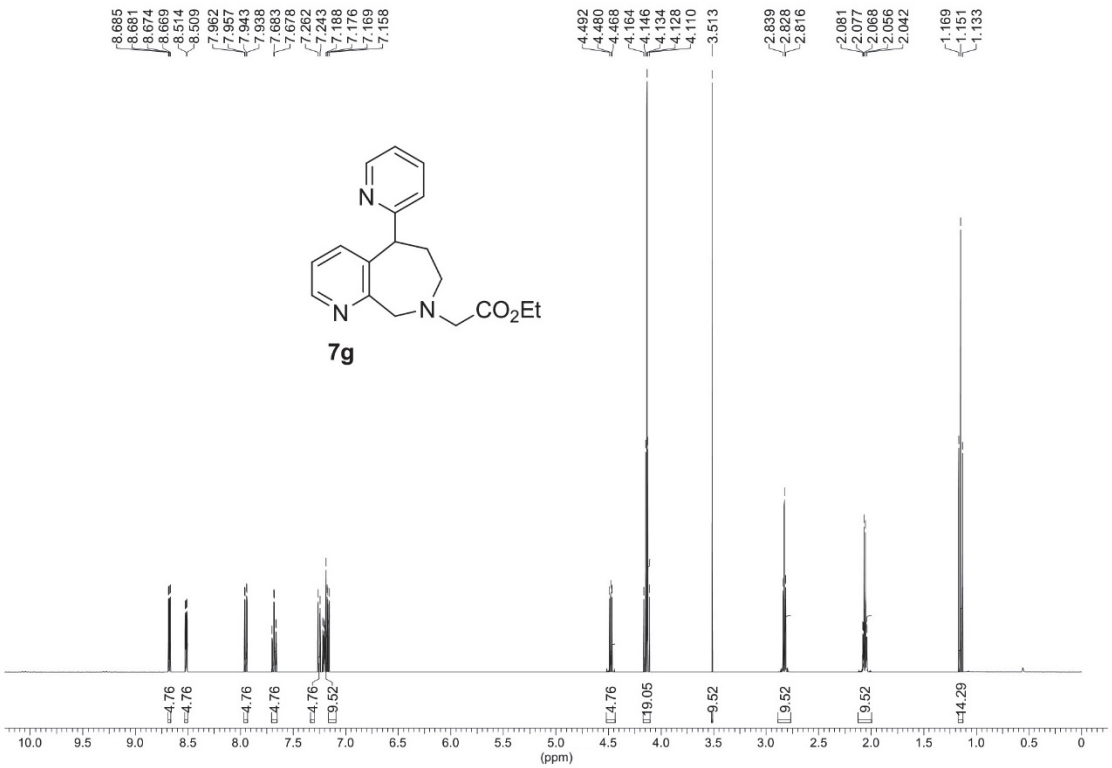

Fig. S-21. ^{1}H-NMR spectrum of compound **7g**

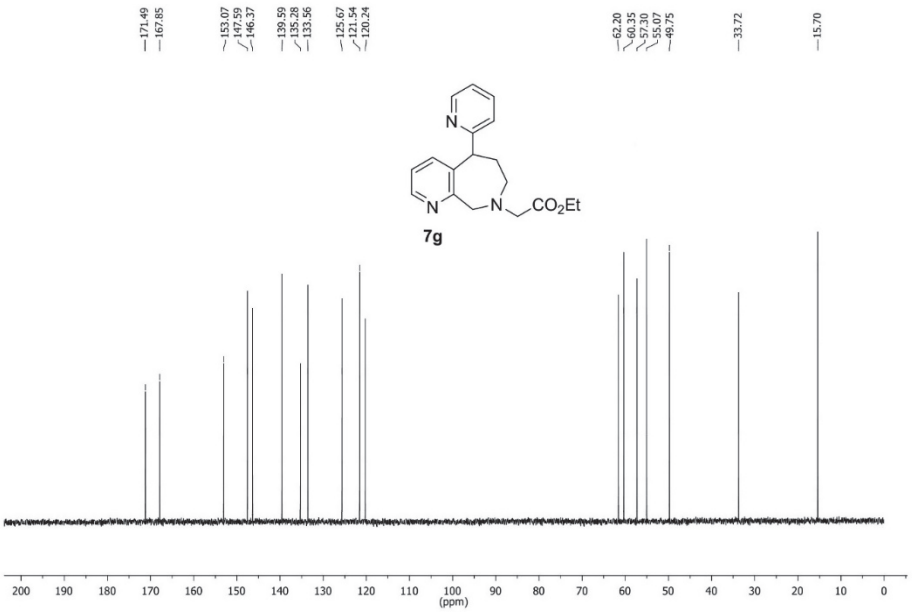

Fig. S-22. ^{13}C-NMR spectrum of compound **7g**

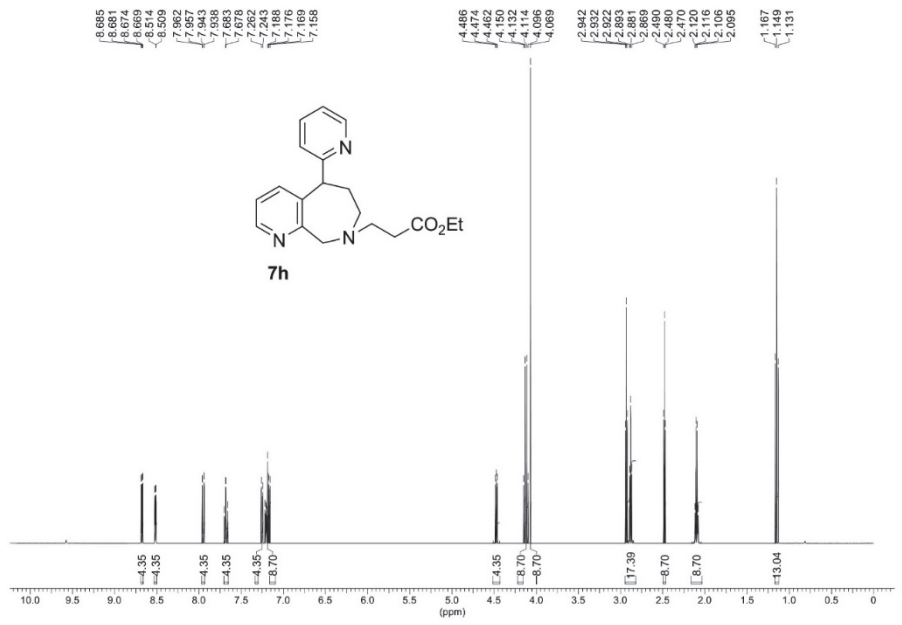

Fig. S-23. ^{1}H-NMR spectrum of compound **7h**

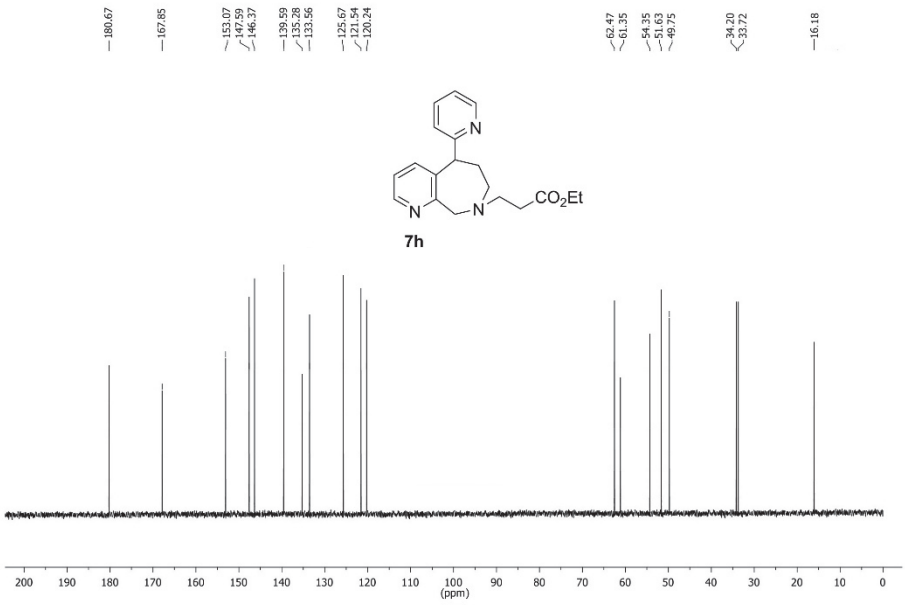

Fig. S-24. ^{13}C-NMR spectrum of compound **7h**

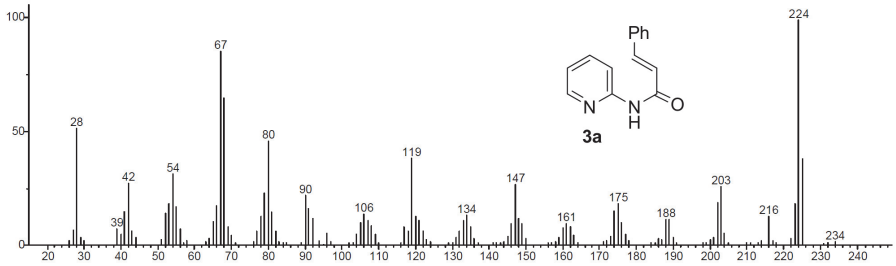

Fig. S-25. Mass spectrum of compound **3a**

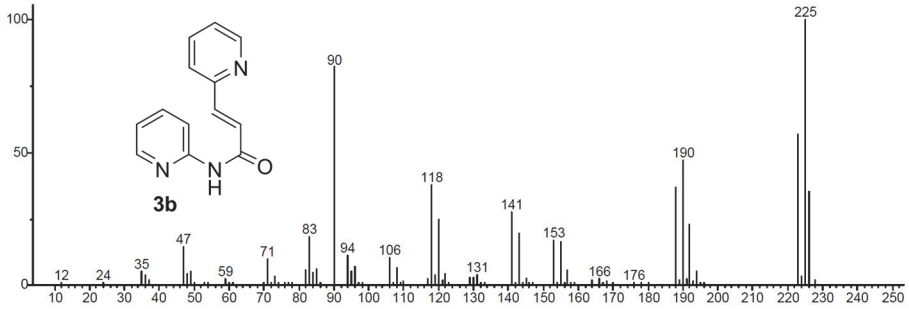

Fig. S-26. Mass spectrum of compound **3b**

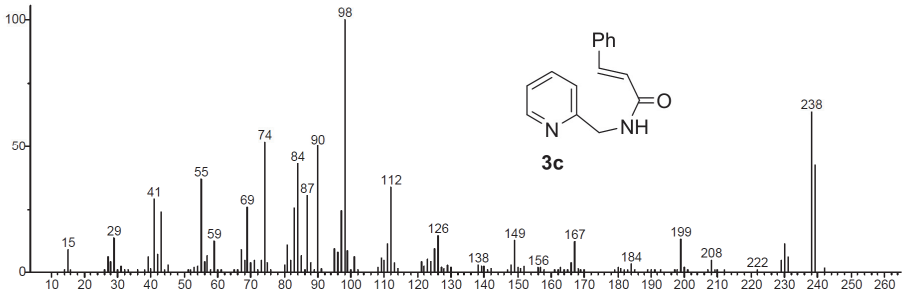

Fig. S-27. Mass spectrum of compound **3c**

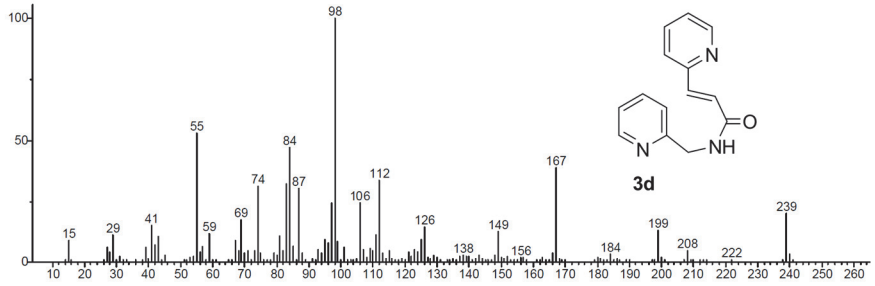

Fig. S-28. Mass spectrum of compound **3d**

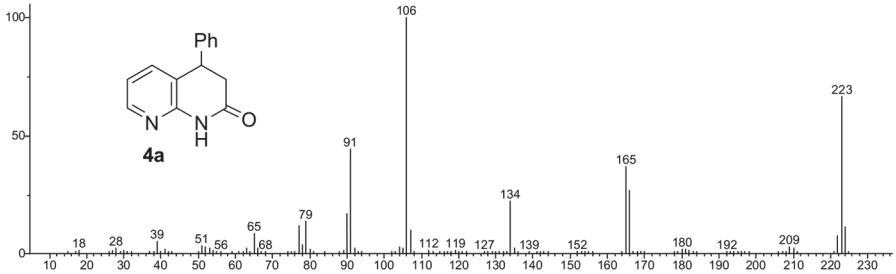

Fig. S-29. Mass spectrum of compound **4a**

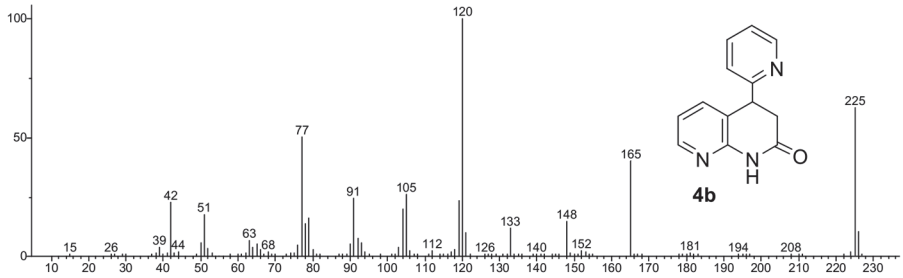

Fig. S-30. Mass spectrum of compound **4b**

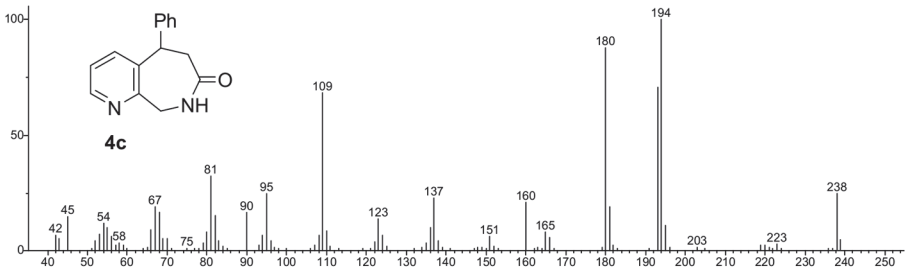

Fig. S-31. Mass spectrum of compound **4c**

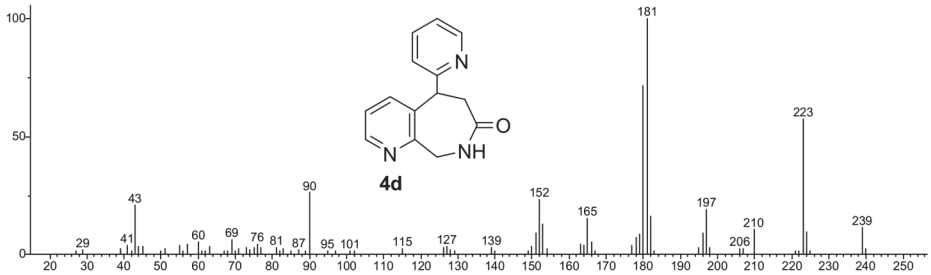

Fig. S-32. Mass spectrum of compound **4d**

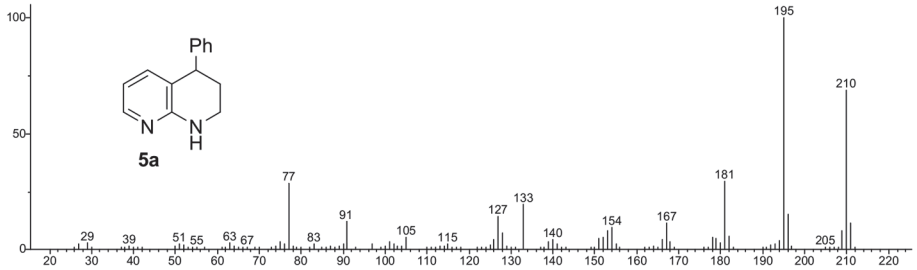

Fig. S-33. Mass spectrum of compound **5a**

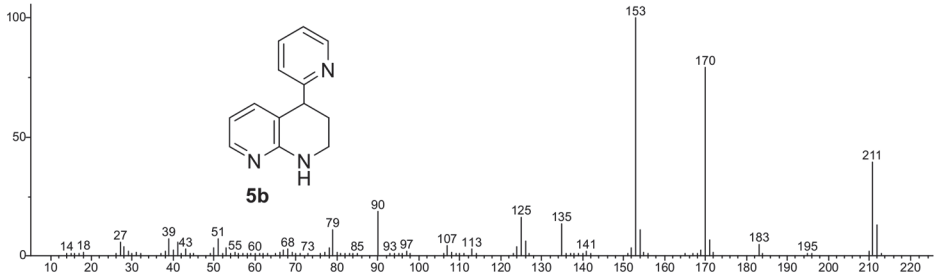

Fig. S-34. Mass spectrum of compound **5b**

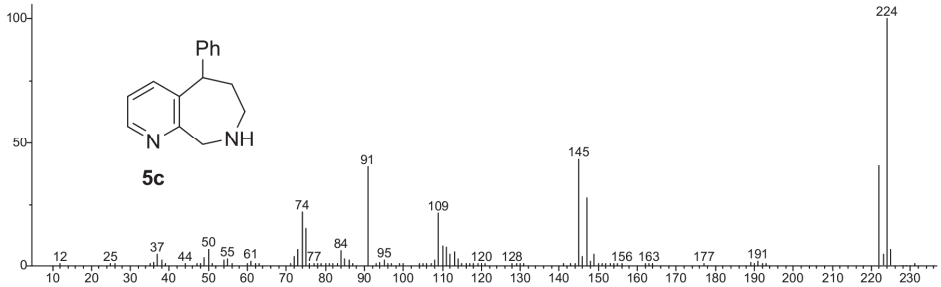

Fig. S-35. Mass spectrum of compound **5c**

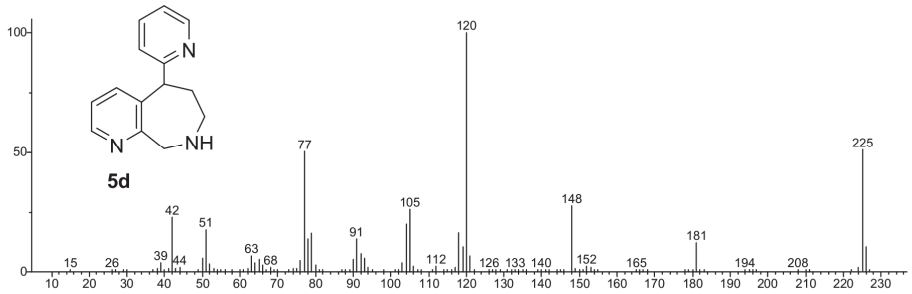

Fig. S-36. Mass spectrum of compound **5d**

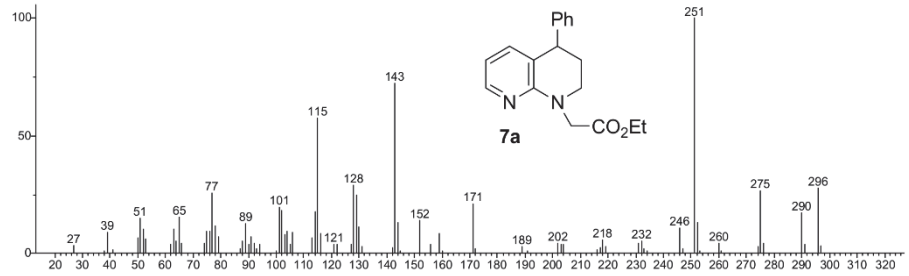

Fig. S-37. Mass spectrum of compound **7a**

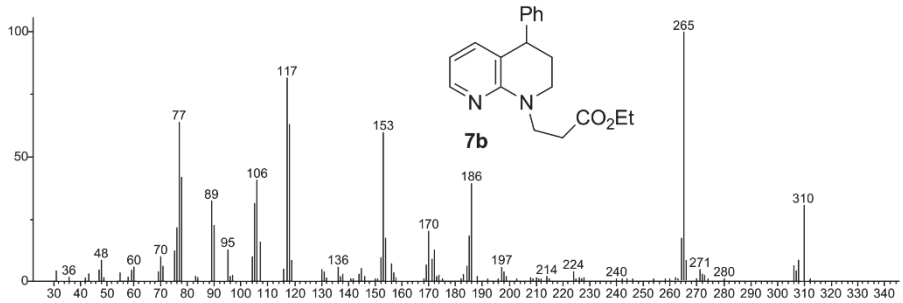

Fig. S-38. Mass spectrum of compound **7b**

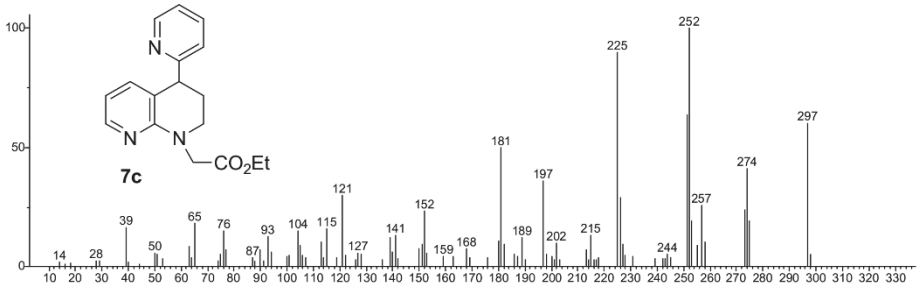

Fig. S-39. Mass spectrum of compound **7c**

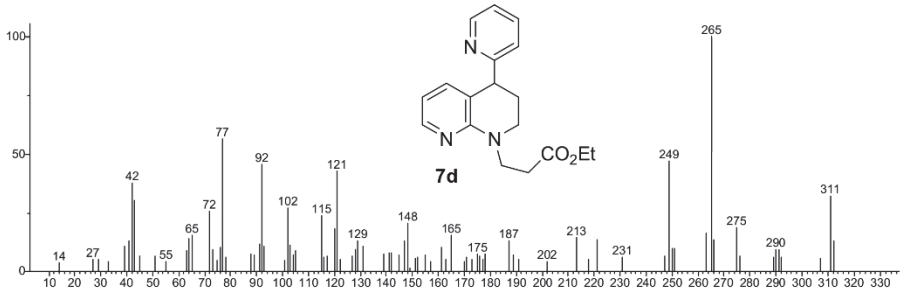

Fig. S-40. Mass spectrum of compound **7d**

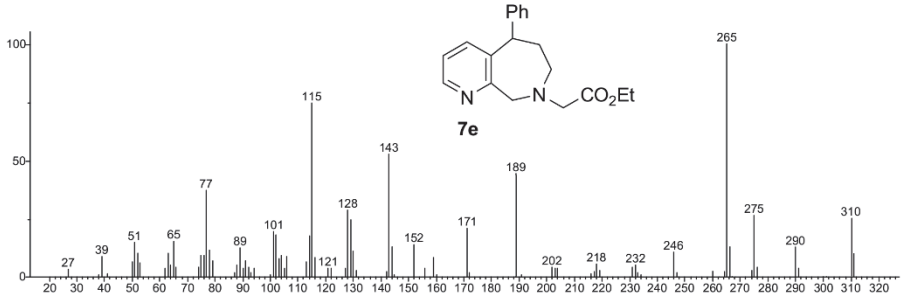

Fig. S-41. Mass spectrum of compound **7e**

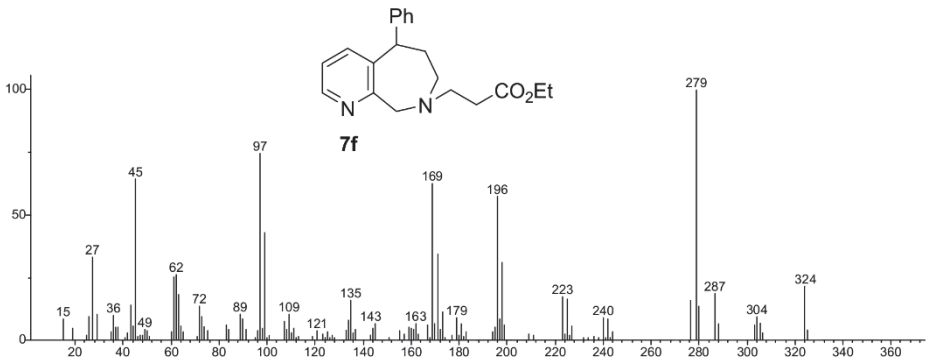

Fig. S-42. Mass spectrum of compound **7f**

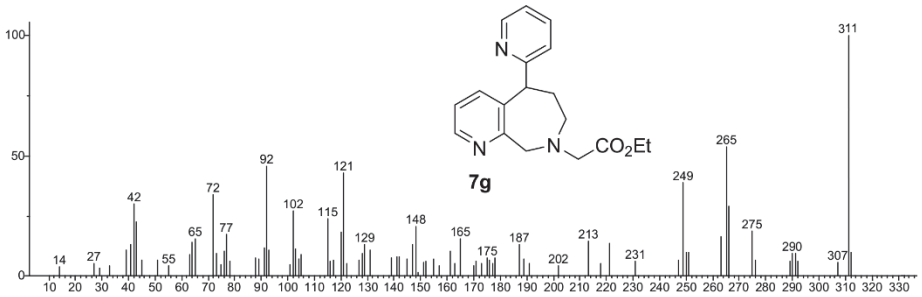

Fig. S-43. Mass spectrum of compound **7g**

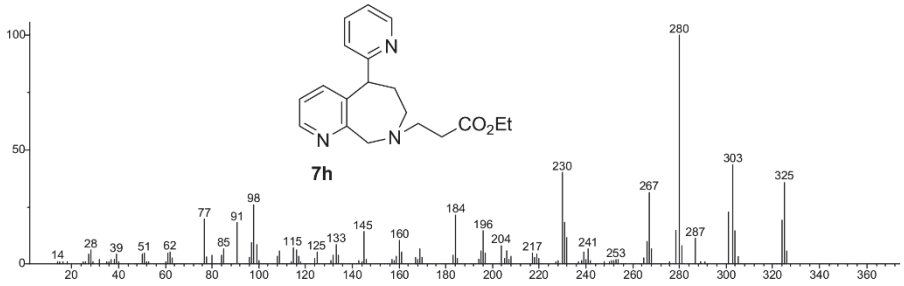

Fig. S-44. Mass spectrum of compound **7h**

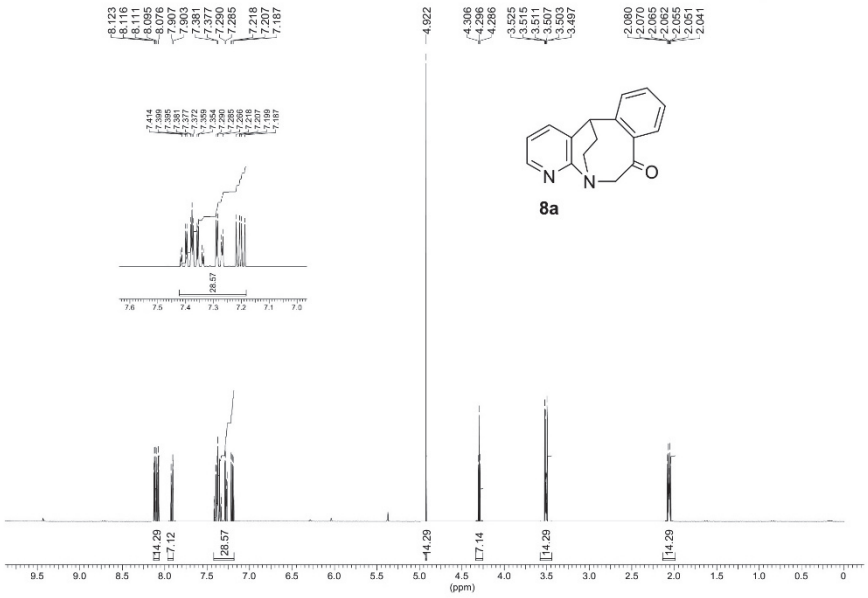

Fig. S-45. ^{1}H-NMR spectrum of compound **8a**

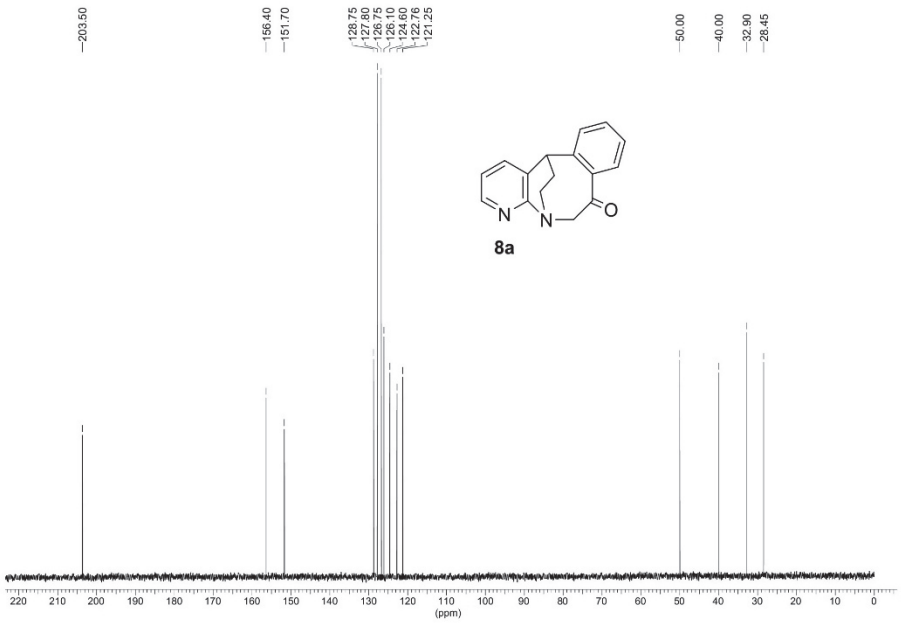

Fig. S-46. ^{13}C-NMR spectrum of compound **8a**

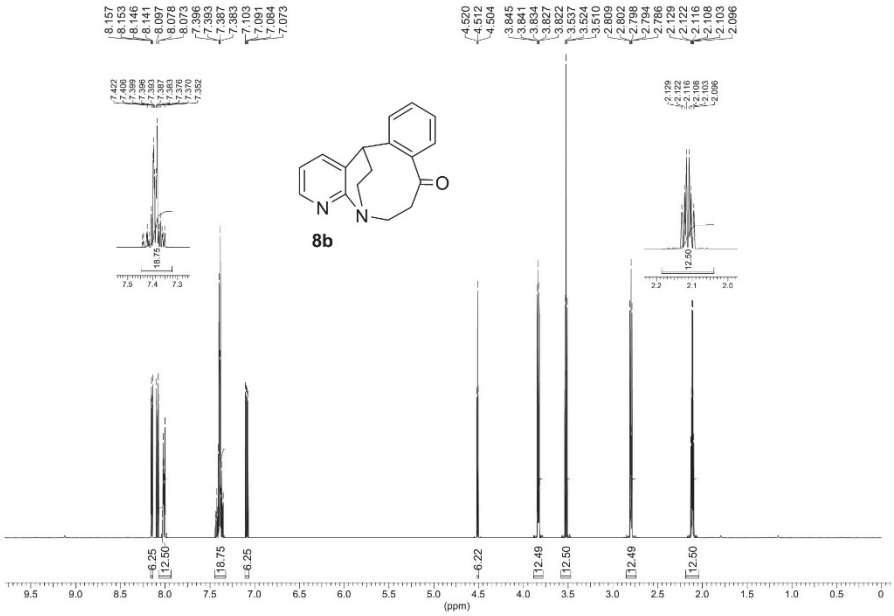

Fig. S-47. ^{1}H-NMR spectrum of compound **8b**

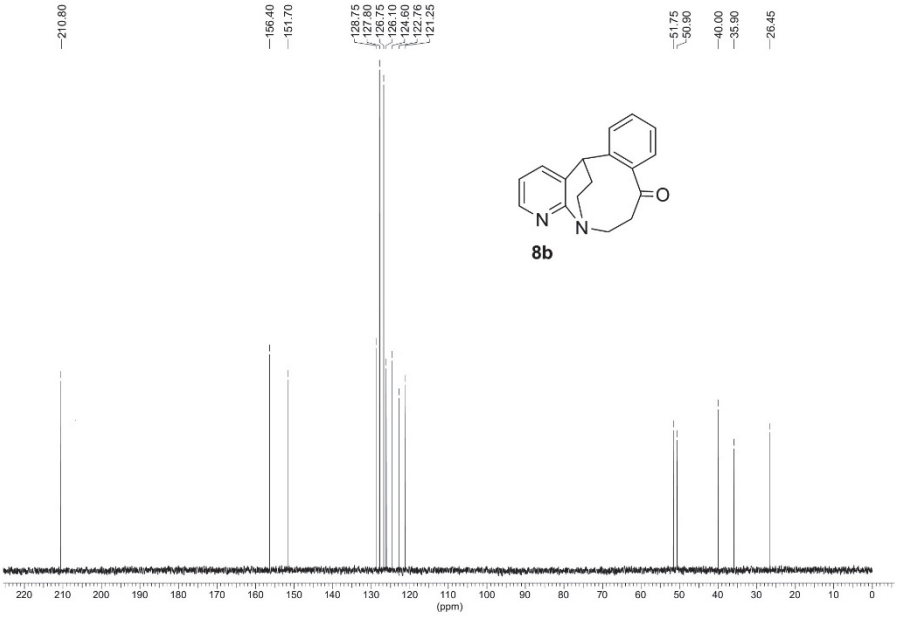

Fig. S-48. ^{13}C-NMR spectrum of compound **8b**

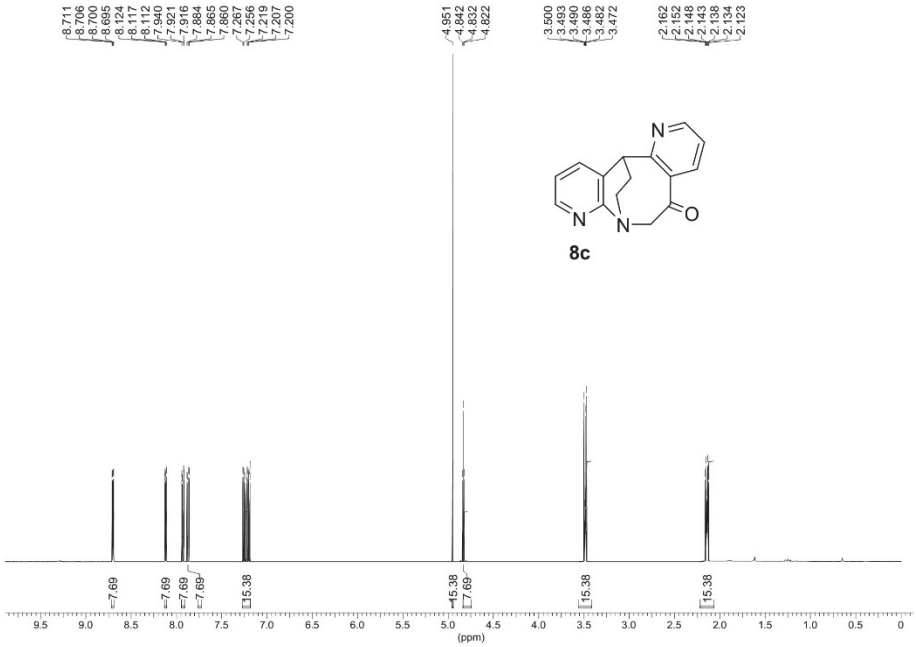

Fig. S-49. ^{1}H-NMR spectrum of compound **8c**

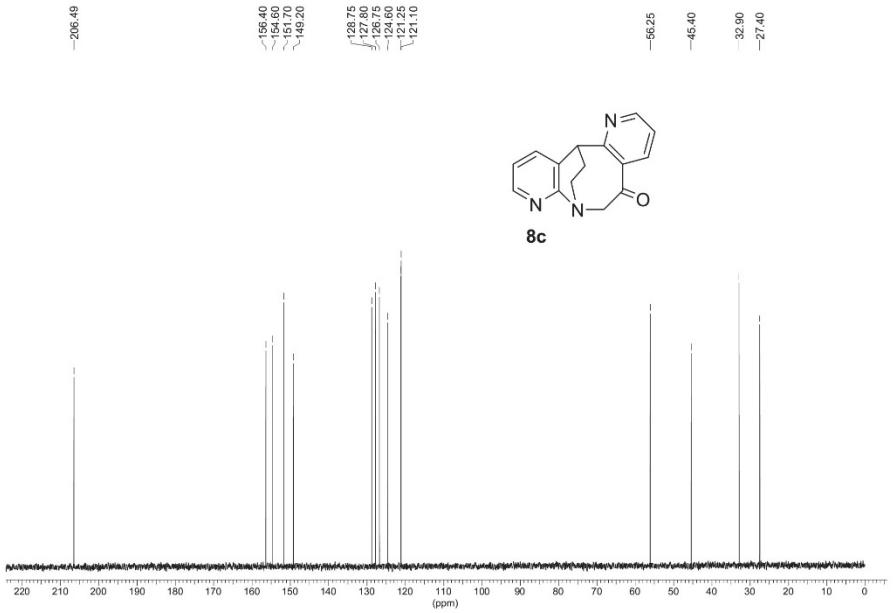

Fig. S-50. ^{13}C-NMR spectrum of compound **8c**

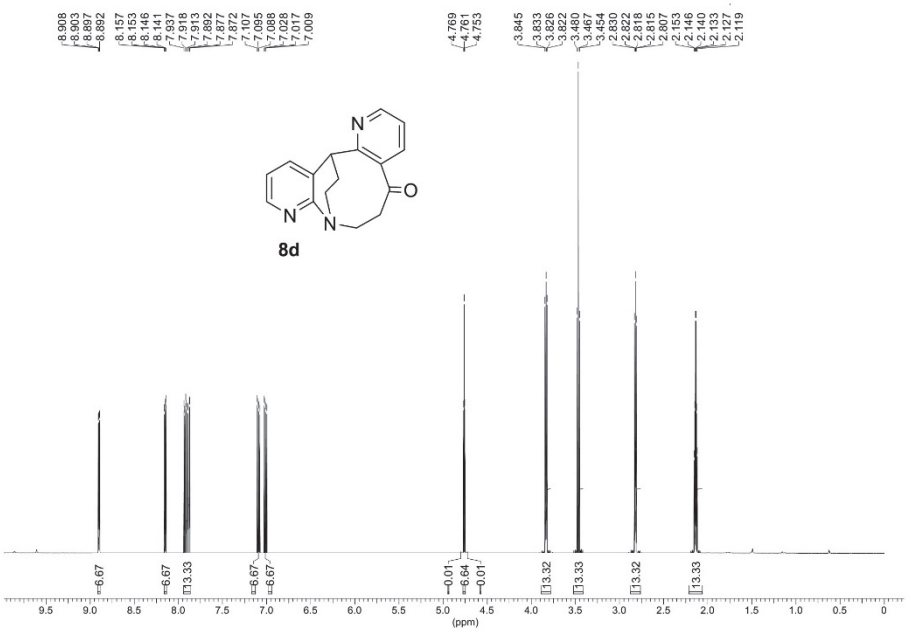

Fig. S-51. ^{1}H-NMR spectrum of compound **8d**

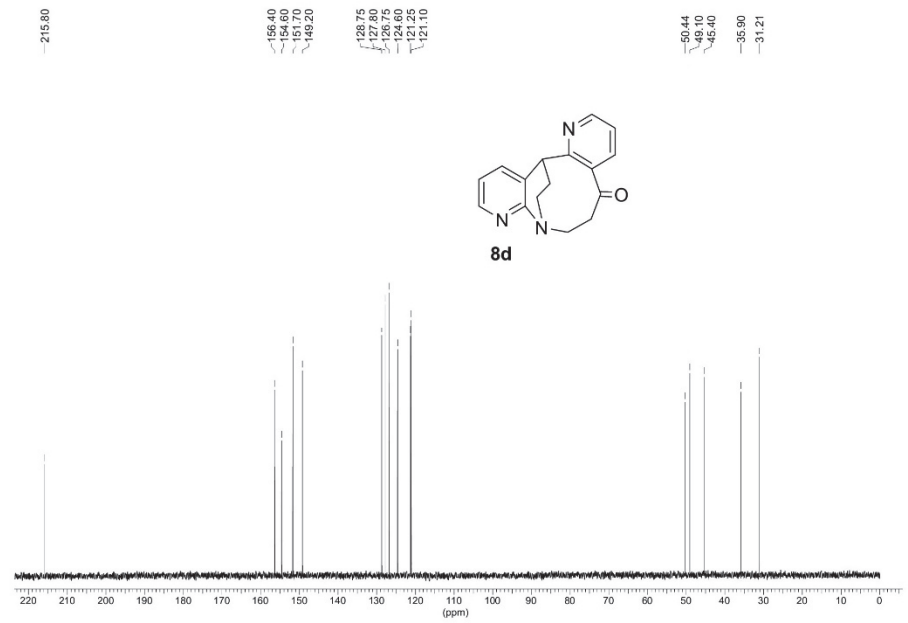

Fig. S-52. ^{13}C-NMR spectrum of compound **8d**

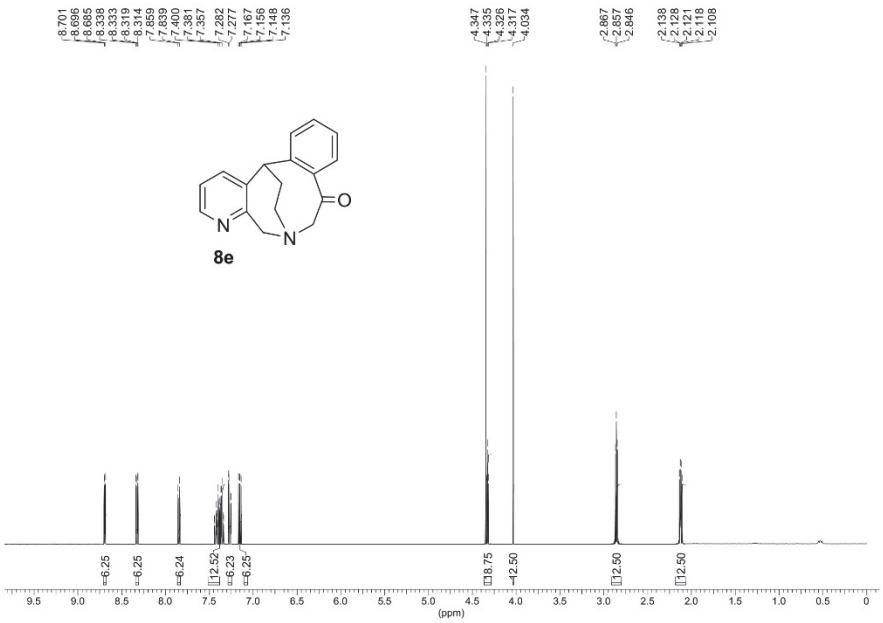

Fig. S-53. ^{1}H-NMR spectrum of compound **8e**

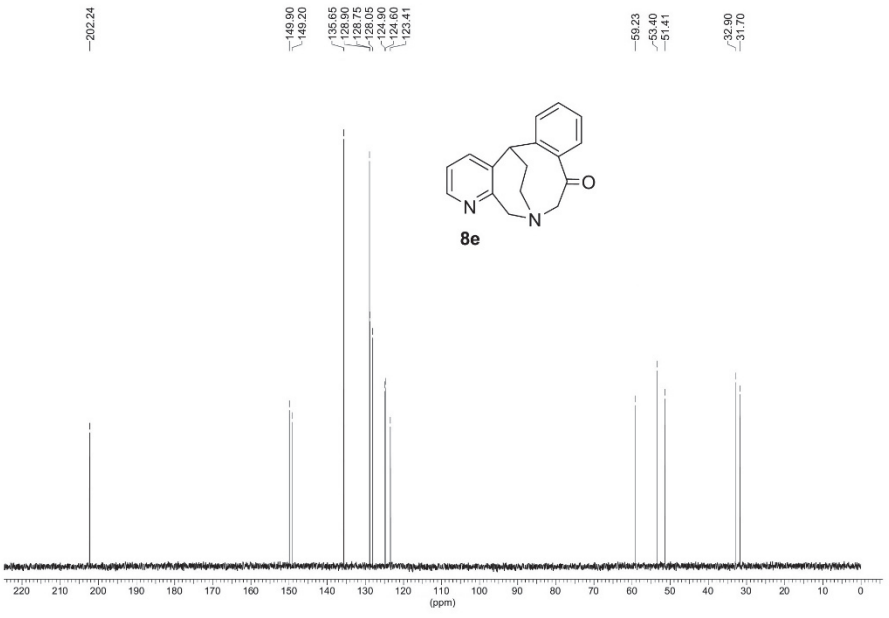

Fig. S-54. ^{13}C-NMR spectrum of compound **8e**

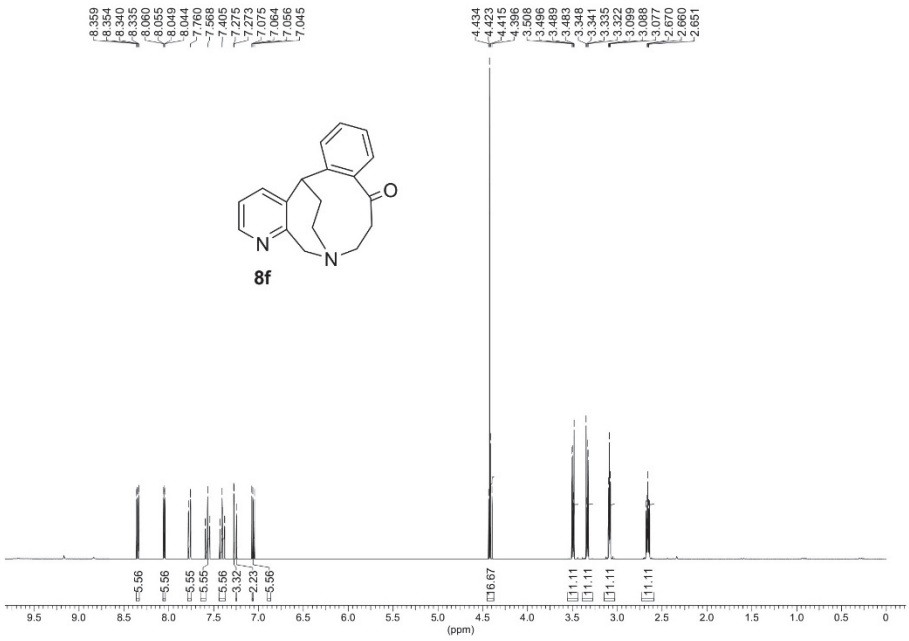

Fig. S-55. ^{1}H-NMR spectrum of compound **8f**

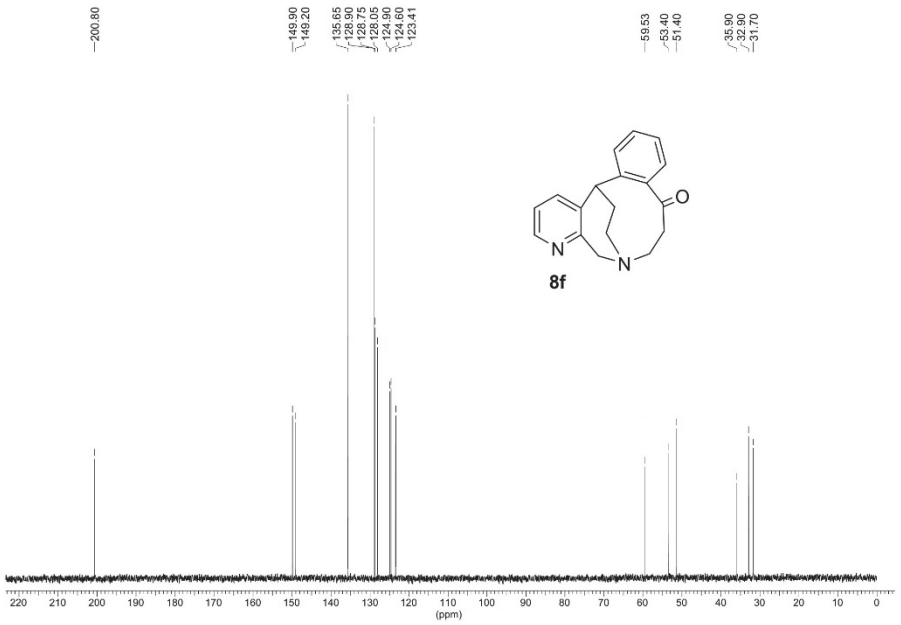

Fig. S-56. ^{13}C-NMR spectrum of compound **8f**

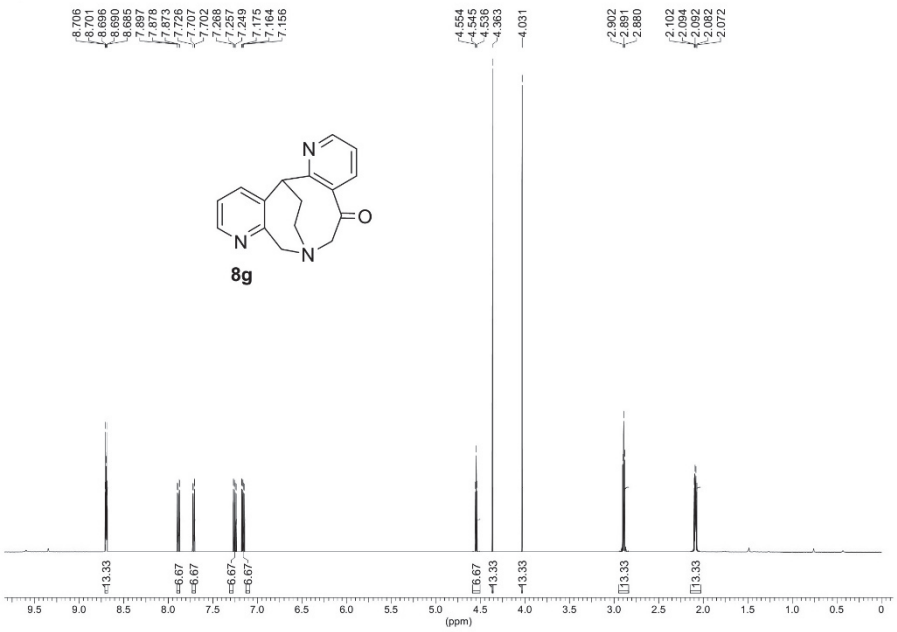

Fig. S-57. ^{1}H-NMR spectrum of compound **8g**

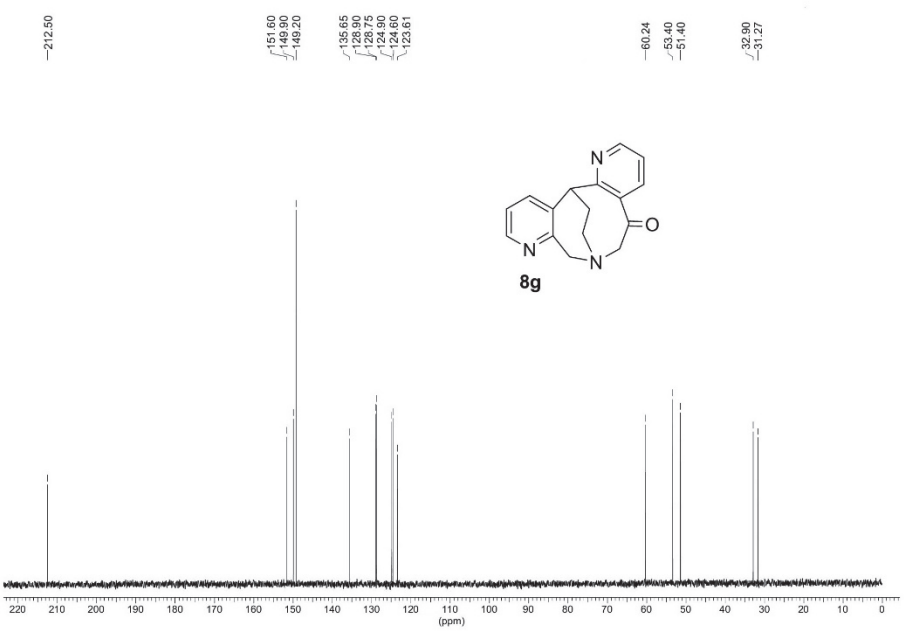

Fig. S-58. ^{13}C-NMR spectrum of compound **8g**

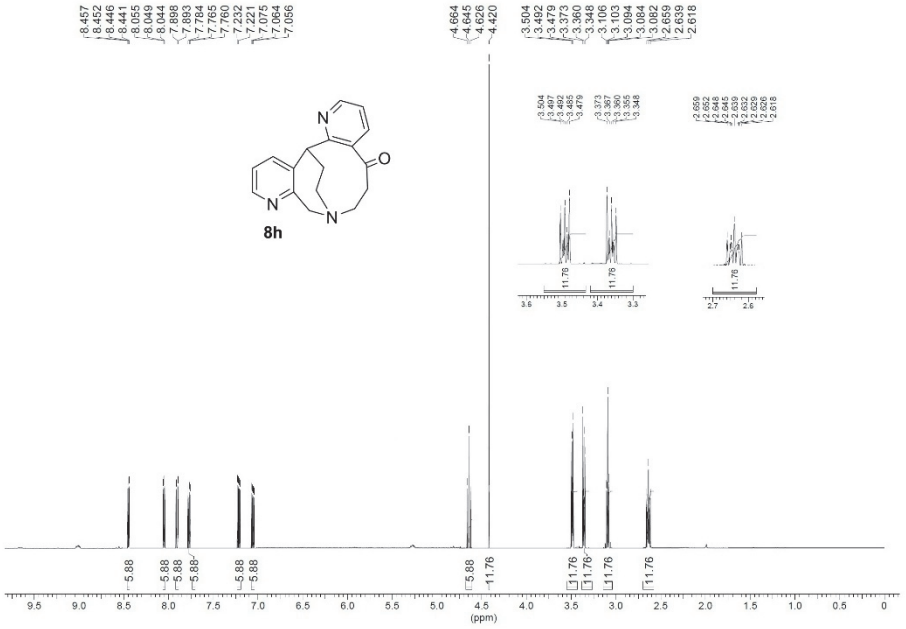

Fig. S-59. ^{1}H-NMR spectrum of compound **8h**

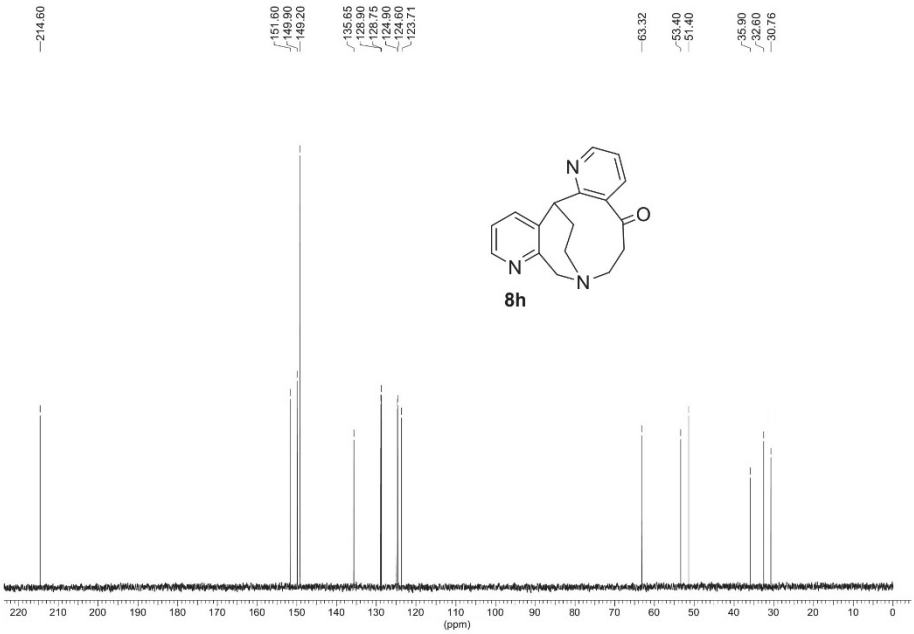

Fig. S-60. ^{13}C-NMR spectrum of compound **8h**

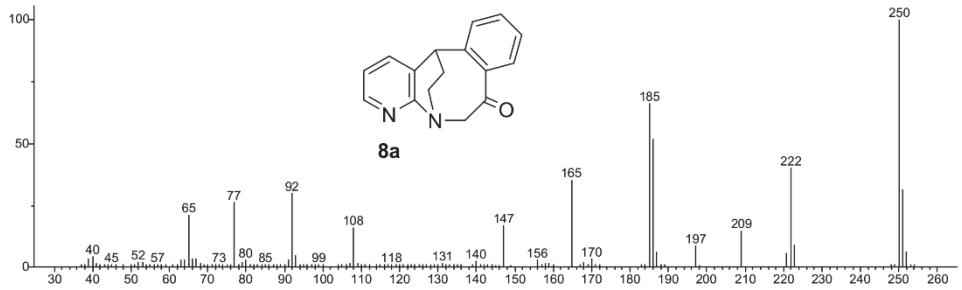

Fig. S-61. Mass spectrum of compound **8a**

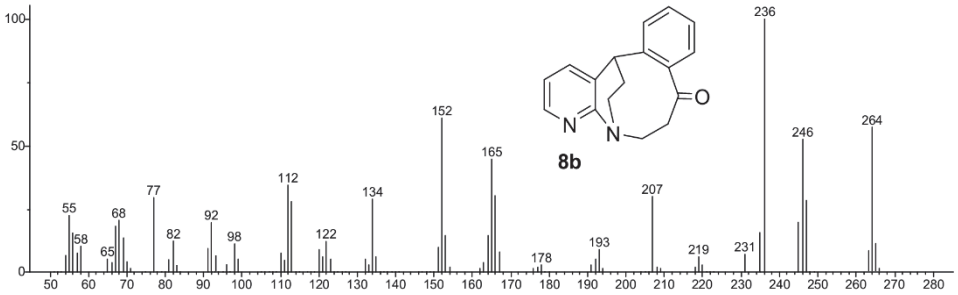

Fig. S-62. Mass spectrum of compound **8b**

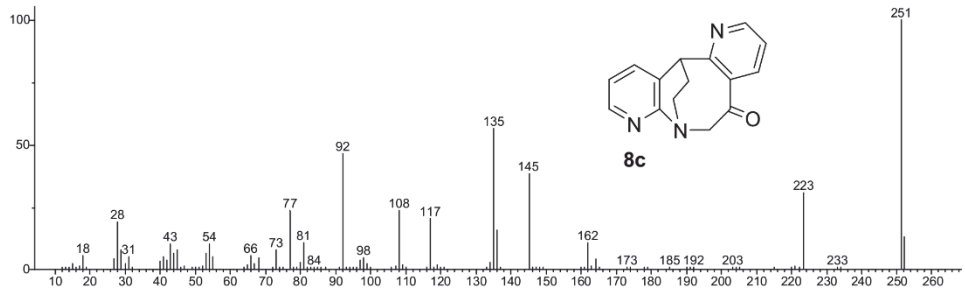

Fig. S-63. Mass spectrum of compound **8c**

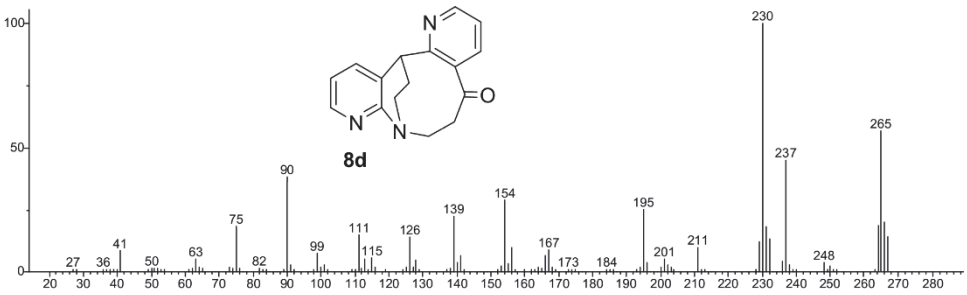

Fig. S-64. Mass spectrum of compound **8d**

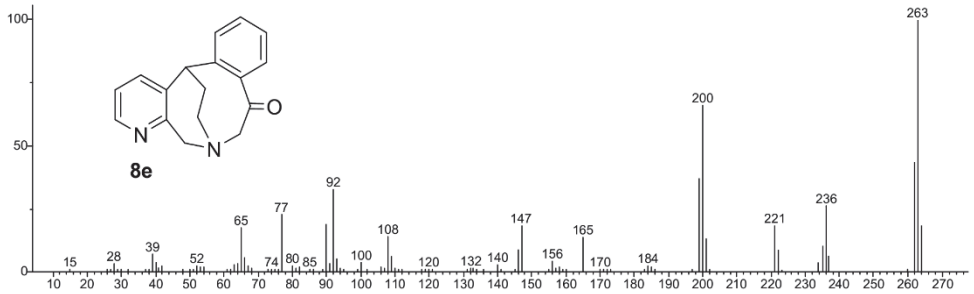

Fig. S-65. Mass spectrum of compound **8e**

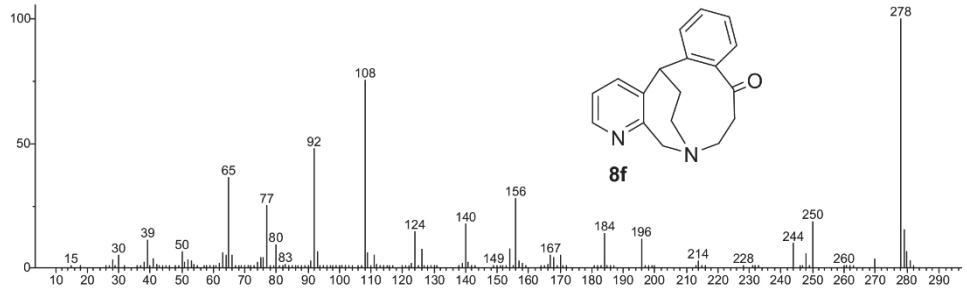

Fig. S-66. Mass spectrum of compound **8f**

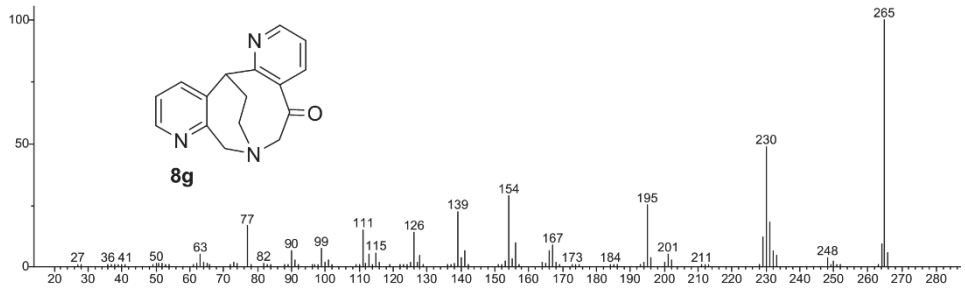

Fig. S-67. Mass spectrum of compound **8g**

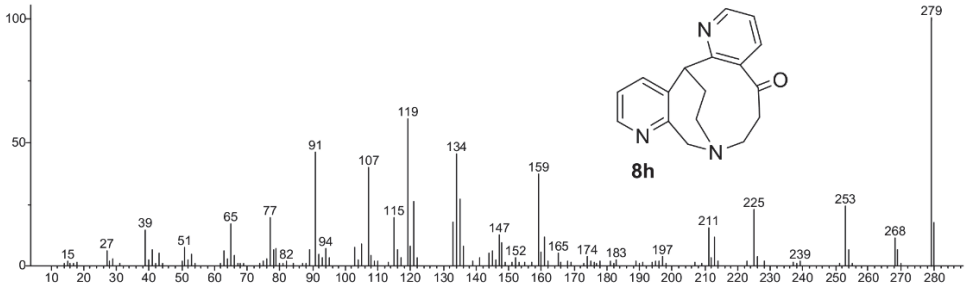

Fig. S-68. Mass spectrum of compound **8h**.

Journal of the Serbian Chemical Society
JSCS@tmf.bg.ac.rs • www.shd.org.rs/JSCS
J. Serb. Chem. Soc. *91* (3) 227–244 (2026)
JSCS–5488
Original scientific paper
Published 23 February, 2026

Le Chatelier's principle and metabolism: Biothermodynamic analysis of the metabolic pathway for synthesis of glucagon

MARKO E. POPOVIĆ[1]*, DONG PEI[2] and MARIJA MIHAILOVIĆ[1]

[1]*University of Belgrade, Institute of Chemistry, Technology and Metallurgy, Njegoševa 12, 11000 Belgrade, Serbia and* [2]*Research Center for Natural Medicine and Chemical Metrology, Lanzhou Institute of Chemical Physics, Chinese Academy of Sciences, Lanzhou 730000, China*

(Received 22 September, revised 11 November, accepted 26 November 2025)

Abstract: Glucagon is the main catabolic hormone in the human organism. Glucagon has been well studied from the aspect of life and biomedical sciences. However, no analysis of glucagon based on chemical thermodynamics can be found in the literature. The approach of biothermodynamics would allow to study the driving force of glucagon production, as well as provide an understanding of the process from the aspect of the fundamental laws of nature. This research reports an analysis of glucagon with the methodology of biothermodynamics. Based on the protein sequences, chemical and thermodynamic characterization of glucagon, proglucagon, preproglucagon and related peptides is performed, with the atom counting method and Patel–Erickson–Battley model. Reactions of translation at the ribosomes and post-translational processing are formulated and their driving force (Gibbs energy change) is calculated. The process of translation at the ribosomes that produces preproglucagon is studied from the aspect of chemical thermodynamics. Based on Gibbs energy, an analysis is performed of the metabolic pathway for production of glucagon. The role of Le Chatelier's principle in coupling of the reactions in the metabolic pathway is studied. Finally, a discussion is made of applications of the biothermodynamic methodology in omics research for determination of feasibility of metabolic pathways.

Keywords: enthalpy; entropy; Gibbs energy; mechanistic model; omics; post-translational processing.

INTRODUCTION

Glucagon is produced in the alpha cells of the islets of Langerhans in the endocrine part of the pancreas. The physiological effects of glucagon are opposite to those of insulin. Glucagon and insulin control the blood glucose level. Insulin is the main anabolic hormone in the organism, which stimulates absorption of glucose into cells, where it can be used for anabolic processes or as an energy source.

* Corresponding author. E-mail: marko.popovic@ihtm.bg.ac.rs
https://doi.org/10.2298/JSC250922087P

Glucagon is the main catabolic hormone in the organism. Glucagon increases the concentration of glucose in the blood, by stimulation of glycogenolysis and gluconeogenesis. Glucose is stored in the liver in form of the polysaccharide glycogen. Glucagon stimulates liver cells to degrade glycogen and produce glucose, which is released into the blood. This process is called glycogenolysis. Also, glucagon inhibits formation of glycogen by glycogenesis in liver cells. Glycogen represents the short-term energy storage of the organism. When it becomes depleted, glucagon promotes production of glucose in liver and kidney cells through gluconeogenesis. Gluconeogenesis is a metabolic process in which glucose is produced from substances that are not carbohydrates, like lactate, glycerol, alanine or glutamine. Also, glucagon inhibits glucose degradation by glycolysis in liver cells. Moreover, glucagon stimulates lipolysis in the adipose tissue and liver. Lipolysis leads to release of fatty acids into the blood, which can be used in catabolism to provide energy.

Glucagon is a polypeptide hormone that consists of 29 amino acid residues. It is produced by translation at the ribosomes based on the mRNA transcribed from the human glucagon gene.[1] The translation process produces the precursor molecule preproglucagon,[1] which is schematically presented in Fig. 1. Preproglucagon consists of seven domains: signal peptide, glicentin-related pancreatic peptide (GRPP), glucagon, hexapeptide or spacer peptide 1 (SP-1), glucagon-like peptide 1 (GLP-1), spacer peptide 2 (SP-2) and glucagon-like peptide 2 (GLP-2).[2] The domains are connected by Lys-Arg (KR), Arg-Arg (RR) or Arg-Lys (RK) dibasic sites.[2]

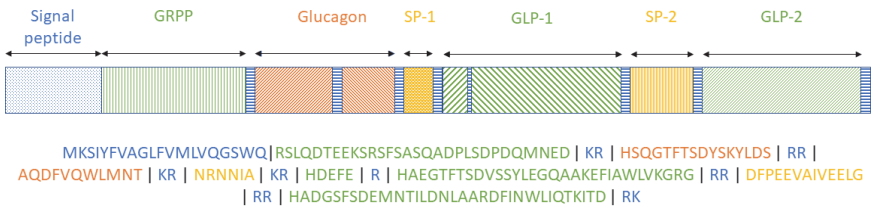

Fig. 1. Domains of preproglucagon. Preproglucagon consists of seven domains: signal peptide, glicentin-related pancreatic peptide (GRPP), glucagon, hexapeptide or spacer peptide 1 (SP-1), glucagon-like peptide 1 (GLP-1), spacer peptide 2 (SP-2) and glucagon-like peptide 2 (GLP-2). Each domain consists of one or more segments, which are marked by patterns and colors. The lower part of the figure shows the amino acid sequence of preproglucagon. The vertical lines separate the segments shown in the upper part of the figure by patterns and colors.

After production at the ribosomes, preproglucagon is converted into glucagon by post-translational processing, as shown in Fig. 2. The signal peptide domain (Fig. 1) targets preproglucagon to the endoplasmic reticulum for excretion.[3,4]

Inside the endoplasmic reticulum the signal peptide is cleaved to produce proglucagon.[5] After that, proglucagon is cleaved by a prohormone convertase enzyme (PC2) to produce glicentin-KR (glicentin with a Lys-Arg extension at the C-terminus) and major proglucagon fragment (MPGF).[2,6,7] Then glicentin-KR is cleaved to produce oxyntomodulin-KR (oxyntomodulin with a Lys-Arg extension at the C-terminus).[2] Oxyntomodulin is then transformed into glucagon-KR (glucagon with a Lys-Arg extension at the C-terminus).[2] After that, glucagon-KR is converted into glucagon.[2] Finally, glucagon is excreted from the cells into the blood.[8]

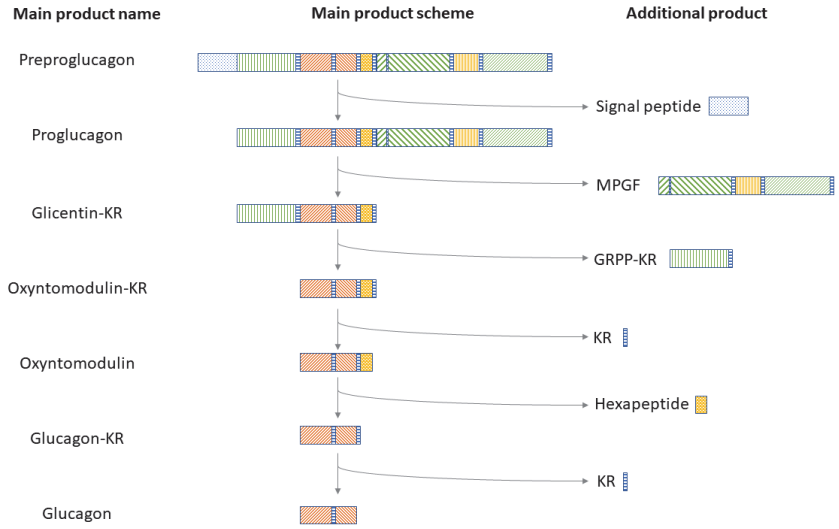

Fig. 2. Metabolic pathway for production of glucagon from preproglucagon. After production at the ribosomes, preproglucagon is targeted to the reticulum by the signal peptide. At the reticulum, preproglucagon is transformed into glucagon, which is excreted into the blood. The figure presents the chemical reactions that transform preproglucagon into glucagon. The process is catalyzed by a prohormone convertase enzyme.

Glucagon has been extensively studied from the aspect of life and biomedical sciences. However, chemical and thermodynamic analysis of glucagon cannot be found in the literature. Biothermodynamics applies the methodology of chemical and nonequilibrium thermodynamics to study biological structures and processes.[31,36] Biothermodynamic analysis has been applied to study microbial growth,[37,38] metabolism[39,40] and interactions,[41–43] as well as multicellular organisms.[35,44,45] Moreover, biothermodynamic methodology has been applied to biological molecules and metabolic reactions.[23,24,46,47]

Organisms are open nonequilibrium thermodynamic systems.[36,48] This is why the methodology of nonequilibrium thermodynamics is very important in analysis of organisms.[36,48] A cell is an open thermodynamic system out of equilibrium, which means that it exchanges matter and energy with its environment.[36,51] The

cell takes nutrients from the environment.[35,36,51] A part of the nutrients is degraded into simple products in catabolism to provide energy.[35,36,51] The rest of the nutrients is used in anabolic processes to produce more complex products.[35,36,51] For example, amino acids are taken by the cells of the pancreas as nutrients, which are transformed by anabolic processes into glucagon. To perform metabolic processes, a cell dissipates usable (Gibbs) energy released by degradation of nutrients in catabolism.[35,36,51] For example, during the process of translation amino acids are activated by hydrolysis of ATP, which is obtained from catabolism.[32–34] The activated amino acids are in the form of aminoacyl-tRNAs, which react at the ribosomes to produce polypeptides.[32–34]

Le Chatelier's principle states that when a system at equilibrium is subjected to an external perturbation, the composition of the system adjusts to minimize its effect.[14,50] For example, if there is a chemical reaction in the system, removal of products will make the reaction proceed towards formation of more products. Le Chatelier's principle has been extended to systems under nonequilbrium conditions.[48–50]

Biothermodynamic models allow calculation of thermodynamic properties of biological matter, based on chemical composition.[31,52,53] Biothermodynamic models include the Patel–Erickson–Battley,[25-27] Roels,[53] Sandler–Orbey,[54] Hurst–Harrison[30,31] models, *etc*. Biothermodynamic models have been extensively used in analysis of viruses, cellular microorganisms and multicellular organisms.[35,44,52,53,55] They give results for enthalpy and entropy in good agreement with experiment.[56–58] Moreover, biothermodynamic models have been applied in analysis of macromolecules and macromolecular assemblies.[23,24,58,59]

The aim of this paper is to perform a chemical and thermodynamic characterization of human glucagon, proglucagon and preproglucagon, as well as to make a biothermodynamic analysis of metabolic synthesis of glucagon. Empirical formulas and thermodynamic properties of glucagon, proglucagon and preproglucagon will be determined with the atom counting method and Patel–Erickson–Battley model. Moreover, the chemical reaction of translation will be formulated, in which preproglucagon is synthetized from amino acids at the ribosomes. Thermodynamic properties of the translation reaction will be calculated. Thermodynamic properties will also be calculated for the chemical reactions in the post-translational processing of preproglucagon into glucagon. Furthermore, the driving force for biosynthesis of glucagon will be determined. Based on the determined thermodynamic properties, an analysis will be made of the metabolic pathway for production of glucagon in the alpha cells of the pancreas.

METHODS

Data sources

The amino acid sequences of human glucagon, proglucagon, preproglucagon and related peptides were taken from.[2,9-12] The amino acid sequence of preproglucagon can be found under

the UniProt access number P01275 (section Sequence)[9] and NCBI access number NP_002045.1 (Ref. 11).[11] The amino acid sequence of glucagon can be found under the UniProt access number P01275 (section PTM/Processing),[9] PubChem CID 16132283.[2,10,12] The amino acid sequences of proglucagon and related peptides can be found under the UniProt access number P01275 (section PTM/Processing).[2,9] More information can be found in the Supplementary material to this paper (Table S-I).

Thermodynamic properties of ATP, AMP, Pi and amino acids were taken from.[13-21]

Atom counting method

Molecular formulas, empirical formulas and molar masses of glucagon, proglucagon and preproglucagon and related peptides were calculated with the atom counting method, based on amino acid sequences.[22,23] Atom counting method is a computational approach for calculation of chemical properties of macromolecules and macromolecular assemblies. The inputs are genetic sequences, protein sequences and morphology. The program goes along the nucleic acid and protein sequences and adds atoms that come from the monomer residues to find molecular formulas. Empirical formulas are obtained when numbers of atoms of all constituent elements are divided by the number of carbon atoms.[22,23]

Patel–Erickson–Battley model

Changes in enthalpy, entropy and Gibbs energy of glucagon, proglucagon, preproglucagon and related peptides were calculated with the Patel–Erickson–Battley model, based on molecular and empirical formulas.[24-27] Empirical formula weas used to calculate the degree of reduction, E:

$$E = 4n_{\mathrm{C}} + n_{\mathrm{H}} - 2n_{\mathrm{O}} - 0n_{\mathrm{N}} + 5n_{\mathrm{P}} + 6n_{\mathrm{S}} \tag{1}$$

where n_{C}, n_{H}, n_{O}, n_{N}, n_{P} and n_{S} are the numbers of C, H, O, N, P and S atoms, respectively, in the empirical formula.[25,27] Based on E, the change in enthalpy of combustion, $\Delta_C H$, was calculated with the Patel–Erickson equation:[25,27]

$$\Delta_{\mathrm{C}} H(\mathrm{bio}) = -111.14 \frac{\mathrm{kJ}}{\mathrm{C\text{-}mol}} E \tag{2}$$

$\Delta_C H$ was used to find the change in enthalpy of formation, $\Delta_{\mathrm{f}} H$, with Hess's law:[23,25]

$$\begin{aligned} \Delta_{\mathrm{f}} H(\mathrm{bio}) = n_{\mathrm{C}} \Delta_{\mathrm{f}} H(\mathrm{CO_2}) + \frac{n_{\mathrm{H}}}{2} \Delta_{\mathrm{f}} H(\mathrm{H_2O}) + \frac{n_{\mathrm{P}}}{4} \Delta_{\mathrm{f}} H(\mathrm{P_4O_{10}}) + \\ + n_{\mathrm{S}} \Delta_{\mathrm{f}} H(\mathrm{SO_3}) - \Delta_{\mathrm{C}} H(\mathrm{bio}) \end{aligned} \tag{3}$$

Molar entropy, S_{m}, was calculated with the Battley equation:

$$S_{\mathrm{m}}(\mathrm{bio}) = 0.187 \sum\nolimits_J \frac{S_{\mathrm{m}}(J)}{\mathrm{a}_J} n_J \tag{4}$$

where $S_{\mathrm{m}}(J)$ is standard molar entropy of element J, a_J number of atoms of element J in its standard state elemental form, and n_J the number of atoms of element J in the empirical formula of live matter.[26,28] The summation is over all J elements that form the analyzed macromolecules.[26,28] Change in entropy of formation, $\Delta_{\mathrm{f}} S$, was calculated with the modified Battley equation:[26,28]

$$\Delta_{\mathrm{f}} S(\mathrm{bio}) = -0.813 \sum\nolimits_J \frac{S_{\mathrm{m}}(J)}{\mathrm{a}_J} n_J \tag{5}$$

Change in Gibbs energy of formation, $\Delta_f G$, was calculated as:

$$\Delta_f G(\text{bio}) = \Delta_f H(\text{bio}) - T\Delta_f S(\text{bio}) \quad (6)$$

where T is temperature.[14,29]

Hurst–Harrison model

Heat capacities of glucagon, proglucagon, preproglucagon and related peptides were calculated with the Hurst–Harrison model, based on molecular and empirical formulas, as described.[30,31] The Hurst–Harrison model calculates molar heat capacity at constant pressure, $C_{p,\text{m}}$ as:

$$C_{p,\text{m}} = \sum_J C_J n_J \quad (7)$$

where C_J is the contribution of element J to heat capacity.[30,31]

Translation reaction

Translation is a chemical process in which amino acids activated by ATP hydrolysis polymerize into a polypeptide.[32-34] Amino acids are activated by ATP hydrolysis to AMP and Pi ($H_2PO_4^-$) and are loaded onto tRNAs to form aminoacyl-tRNAs.[32-34] The aminoacyl-tRNAs react at the ribosomes to extend the growing polypeptide chain and the tRNAs are regenerated.[32-34] For each peptide bond formed, an ATP molecule is hydrolyzed to AMP. Therefore, the overall reaction of translation is

$$x(\text{Amino acids}) + (x\text{–}1)\text{ATP} + (x\text{–}1)\ \text{H}_2\text{O} \rightarrow (\text{Polypeptide}) + (x\text{–}1)\text{AMP} + 2(x\text{–}1)\text{Pi} \quad (8)$$

where x is the number of amino acids in the polypeptide.

Reaction thermodynamic properties at room temperature

Changes in thermodynamic properties during chemical reactions in the metabolic pathway of production of glucagon were calculated with the methodology of thermochemistry.[14,23] The determined reaction thermodynamic properties include: reaction enthalpy change at 25 °C, $\Delta_r H$, reaction entropy change at 25 °C, $\Delta_r S$, reaction Gibbs energy change at 25 °C, $\Delta_r G$, reaction heat capacity change at constant pressure and 25 °C, $\Delta_r C_p$. They were calculated with Hess's law:

$$\Delta_r H = \sum_{\text{products}} \nu \Delta_f H - \sum_{\text{reactants}} \nu \Delta_f H \quad (9)$$

$$\Delta_r S = \sum_{\text{products}} \nu S_{\text{m}} - \sum_{\text{reactants}} \nu S_{\text{m}} \quad (10)$$

$$\Delta_r G = \sum_{\text{products}} \nu \Delta_f G - \sum_{\text{reactants}} \nu \Delta_f G \quad (11)$$

$$\Delta_r C_p = \sum_{\text{products}} \nu C_{p,\text{m}} - \sum_{\text{reactants}} \nu C_{p,\text{m}} \quad (12)$$

where ν represents a stoichiometric coefficient.[14,29]

Reaction thermodynamic properties at physiological temperature

Changes in thermodynamic properties at the physiological temperature (37 °C) were calculated as described.[14,29,35] reaction enthalpy change at 37 °C, $\Delta_r H'$, at physiological temperature was calculated with Kirchhoff's law:

$$\Delta_r H' = \Delta_r H + (T_2 - T_1)\Delta_r C_p \quad (13)$$

where $\Delta_r H$ is the reaction enthalpy change at room temperature, $\Delta_r C_p$ reaction heat capacity at constant pressure, T_2 is the physiological temperature (37 °C) and T_1 is room temperature (25 °C).[14,29,35] Reaction entropy change at 37 °C, $\Delta_r S'$, was calculated as:

$$\Delta_r S' = \Delta_r S + \Delta_r C_p \ln \frac{T_2}{T_1} \quad (14)$$

where $\Delta_r S$ is the reaction entropy change at room temperature.[14,29,35] Reaction Gibbs energy change at 37 °C, $\Delta_r G'$, was calculated as:[14,29,35]

$$\Delta_r G' = \Delta_r H' - T\Delta_r S' \quad (15)$$

RESULTS AND DISCUSSION

Glucagon is the antagonist of insulin. Both represent peptide hormones. Chemical and thermodynamic properties of insulin are given elsewhere.[23] Chemical and thermodynamic properties of glucagon have not been reported. The dynamics of synthesis of glucagon depends on the driving force of the biosynthesis process and occurs in the alpha cells in the pancreas. The driving force of the biosynthesis reactions of glucagon is Gibbs energy. Therefore, to understand the physiology and pathophysiology of regulation of the blood glucose level, it is necessary to know the chemical and thermodynamic parameters that characterize and regulate insulin and glucagon. The empirical formula of glucagon is reported.[10]

Glucagon is produced by translation at the ribosomes in the form of preproglucagon, the structure of which is shown in Fig. 1. Preproglucagon is transformed into glucagon in a series of reactions, which are presented in Fig. 2. Chemical and thermodynamic properties of glucagon and related peptides are presented in Tables I and II, and in the Supplementary material (Tables S-II and S-III).Thermodynamic properties of the chemical reactions of production of preproglucagon at the ribosomes and post-translational processing into glucagon are shown in Tables III and IV, and in the Supplementary material (Table S-IV).

TABLE I. Molecular formulas and molar masses of glucagon, proglucagon, preproglucagon and related peptides. The molecular formulas have the general form $C_{m_C}H_{m_H}O_{m_O}N_{m_N}S_{m_S}$, where m_C, m_H, m_O, m_N and m_S represent the numbers of carbon, hydrogen, oxygen, nitrogen and sulfur atoms in the molecular formula, respectively. The table also gives the molecular formula of the entire molecules, *Mr*(tot) in Da

Name	m_C	m_H	m_O	m_N	m_S	*Mr*(tot) / Da
Preproglucagon	914	1414	287	268	5	20909
Proglucagon	804	1250	262	244	3	18622
GRPP	136	215	58	41	1	3384
GRPP-KR	148	239	60	47	1	3669
Glicentin-KR	352	556	121	114	2	8385
Glicentin	340	532	119	108	2	8101
Oxyntomodulin-KR	204	319	62	67	1	4734
Oxyntomodulin	192	295	60	61	1	4450
Glucagon-KR	165	249	51	49	1	3767
Glucagon	153	225	49	43	1	3483
Mini-glucagon	61	89	18	15	1	1352
Hexapeptide	27	48	10	12	0	701

TABLE I. Continued

Name	m_C	m_H	m_O	m_N	m_S	Mr(tot) / Da
GLI9000	301	462	108	90	2	7133
MPGF	452	696	142	130	1	10255
GLP-1	186	275	59	51	0	4169
t-GLP-1	151	228	47	40	0	3356
GLP-2	171	266	56	48	1	3922
Signal peptide	110	166	26	24	2	2305
KR	12	26	3	6	0	302

TABLE II. Thermodynamic properties of entire molecules of glucagon, proglucagon, preproglucagon and related peptides. Symbols: change in enthalpy of formation, $\Delta_f H$, molar entropy, S_m, change in Gibbs energy of formation, $\Delta_f G$, molar heat capacity at constant pressure, $C_{p,m}$, change in entropy of formation, $\Delta_f S$, change in enthalpy of combustion, $\Delta_C H$. The properties in this table are for the entire molecules and are given per mole

Name	$\Delta_f H$ kJ/mol	S_m J/(mol K)	$\Delta_f G$ kJ/mol	$C_{p,m}$ J/(mol K)	$\Delta_f S$ kJ/mol	$\Delta_C H$ kJ/mol
Preproglucagon	–60708.91	28555.26	–23694.58	29578.96	–124146.67	–503019.64
Proglucagon	–56098.55	25516.57	–23023.07	26331.24	–110935.70	–440114.4
GRPP	–12509.95	4620.18	–6521.10	4665.5	–20086.68	–72129.86
GRPP-KR	–13104.51	5071.65	–6530.45	5116.9	–22049.48	–79687.38
Glicentin-KR	–26050.94	11531.54	–11103.35	11821.54	–50134.47	–192716.76
Glicentin	–25456.38	11080.08	–11094.00	11370.14	–48171.68	–185159.24
Oxyntomodulin-KR	–13232.27	6503.51	–4802.18	6733.18	–28274.63	–113029.38
Oxyntomodulin	–12637.71	6052.05	–4792.83	6281.78	–26311.83	–105471.86
Glucagon-KR	–10553.89	5074.55	–3976.07	5294.33	–22062.08	–90356.82
Glucagon	–9959.33	4623.08	–3966.72	4842.93	–20099.29	–82799.3
Mini-glucagon	–3443.85	1770.30	–1149.12	1872.15	–7696.55	–33675.42
Hexapeptide	–2369.65	1021.11	–1046.05	1015.99	–4439.39	–15115.04
GLI9000	–22778.00	9651.12	–10267.88	9931.29	–41959.13	–162486.68
MPGF	–30333.44	14028.65	–12149.01	14538.24	–60990.86	–247397.64
GLP-1	–12357.35	5597.16	–5102.11	5852.06	–24334.18	–100137.14
t-GLP-1	–9983.31	4559.58	–4073.03	4748.41	–19823.18	–82021.32
GLP-2	–11899.16	5366.44	–4942.99	5536.55	–23331.10	–93802.16
Signal peptide	–4896.19	3082.31	–900.80	3276.26	–13400.61	–62905.24
KR	–880.39	495.09	–238.64	479.94	–2152.43	–7557.52

Chemical and thermodynamic properties of glucagon

Based on protein sequences, chemical and thermodynamic properties of glucagon, proglucagon, preproglucagon and related peptides were calculated with the atom counting method, Patel–Erickson–Battley model and Hurst–Harrison model. Table I presents molecular formulas and molar masses. Table II presents thermodynamic properties of entire molecules. For empirical formulas and thermodynamic properties per C-mole please see the Supplementary material (Tables S-II and S-III).

Change in enthalpies of formation, $\Delta_f H$, of all the analyzed molecules are negative. The reason for the negative standard enthalpies of formation is energy released by the attraction of valence electrons of less electronegative C, H and S by more electronegative O and N atoms. Molar entropies, S_m, and molar heat capacities at constant pressure, $C_{p,m}$, are positive for all the analyzed molecules, due to the third law of thermodynamics. Change in Gibbs energies of formation, $\Delta_f G$, are negative for all the analyzed molecules. The negative $\Delta_f G$ values originate from the negative standard enthalpies of formation, $\Delta_f H$, through the equation $G = H - TS$.

Change in entropies of formation, $\Delta_f S$, are negative for all the analyzed molecules. $\Delta_f S$ is the entropy change of the hypothetical reaction where the analyzed molecules are formed from elements in their standard state: $C + H_2 + O_2 + N_2 + S \rightarrow$ (molecule). The reason for the negative $\Delta_f S$ values is formation of compact and ordered live matter from simple gaseous molecules like H_2, O_2 and N_2. Change in enthalpies of combustion, $\Delta_C H$, are negative for all the analyzed molecules. The reason for the negative $\Delta_C H$ values is energy released by the acceptance of valence electrons of less electronegative elements, (C, H and S) by oxygen during the combustion process.

Biothermodynamic analysis of translation at the ribosomes

Fig. 3 and Table III show an analysis of changes in thermodynamic properties (enthalpy, entropy, Gibbs energy) during the chemical reaction of translation at the ribosomes that produces preproglucagon from amino acids. Table III shows changes in thermodynamic properties for the entire process, while Fig. 3 shows changes in thermodynamic properties per peptide bond formed (there are 179 peptide bonds in preproglucagon).

The translation process can be divided into sub-processes: assembly of amino acids into a polypeptide and activation of amino acids by hydrolysis of ATP. The assembly part represents the changes in thermodynamic properties during polymerization of amino acids into a polypeptide without ATP. The activation part represents hydrolysis of ATP into AMP and Pi to provide energy. The sum of the subprocesses represents the entire reaction of polymerization where amino acids activated by ATP polymerize to produce a polypeptide.

The reaction of assembly of amino acids into a polypeptide without ATP hydrolysis has a positive enthalpy change. This means that the enthalpy change is unfavorable. The assembly process also has a positive entropy change. The positive entropy change originates from the release of a water molecule during the reaction in which the peptide bond is formed: $R_1–COOH + H_2N–R_2 \rightarrow R_1–CO–NH–R_2 + H_2O$, where $R_1–COOH$ and $H_2N–R_2$ are the carboxyl and amino ends of the amino acids that react and $R_1–CO–NH–R_2$ is the newly formed peptide. Release of the water molecule makes the entropy of the reaction positive.

The positive entropy change contributes favorably to the feasibility of the process. However, the enthalpy change is dominant, which makes Gibbs energy change positive for the assembly part. Therefore, assembly of amino acids into the polypeptide (preproglucagon) without activation of amino acids by ATP hydrolysis is not favorable and will not occur spontaneously.

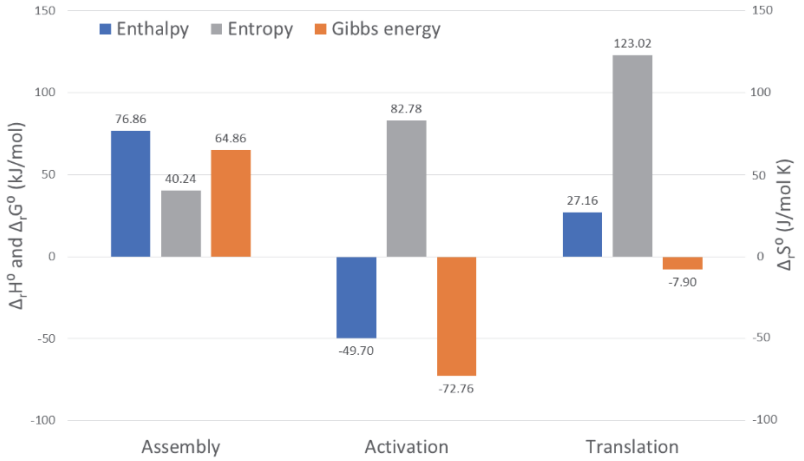

Fig. 3. Thermodynamic analysis of translation at the ribosomes. This graph shows standard reaction thermodynamic properties at 25 °C, for polymerization of amino acids into a polypeptide (assembly), hydrolysis of ATP into AMP and Pi (activation), and total translation reaction. The blue columns represent enthalpy change, gray columns entropy change and orange columns Gibbs energy change. Changes in all thermodynamic properties are presented per peptide bond formed.

The activation sub-process with ATP hydrolysis has a negative enthalpy change, which is favorable. Moreover, it has a highly positive entropy change. The positive entropy change originates from hydrolysis of pyrophosphate. During ATP hydrolysis to AMP, ATP reacts with water to produce AMP and pyrophosphate PPi, in the reaction ATP + H_2O → AMP + PPi. The pyrophosphate then spontaneously hydrolyzes into phosphates Pi in the reaction PPi + H_2O → 2Pi. This makes the entire reaction ATP + $2H_2O$ → AMP + 2Pi have a highly positive entropy change. The positive entropy change contributes favorably to the feasibility of the reaction. Due to the negative enthalpy and positive entropy changes, the Gibbs energy change of the ATP hydrolysis reaction is highly negative. This means that the ATP hydrolysis reaction has a large driving force and is highly favorable.

The translation process is the sum of assembly of amino acids into the polypeptide and their activation by ATP hydrolysis. The enthalpy change of the translation process is positive, which is unfavorable. However, the entropy change is highly positive. The reason is that entropy changes of the sub-processes (amino acid assembly and ATP hydrolysis) are positive. The positive entropy contributes

favorably towards feasibility of the translation reaction. The favorable entropy dominates over the unfavorable enthalpy and makes the Gibbs energy change negative and the translation process feasible.

TABLE III. Thermodynamic properties of translation. This table shows changes in thermodynamic properties (enthalpy, entropy and Gibbs energy) during the translation process, in which amino acids form preproglucagon. Thermodynamic properties are shown for assembly of amino acids into preproglucagon without ATP, hydrolysis of ATP that activates the amino acids and entire translation process in which preproglucagon is formed from amino acids activated by ATP hydrolysis. Symbols: change in reaction enthalpy at 25 °C, $\Delta_r H$, change in reaction entropy at 25 °C, $\Delta_r S$, change in reaction Gibbs energy at 25 °C, $\Delta_r G$

Name	Reaction	$\Delta_r H$ kJ/mol	$\Delta_r S$ J/(mol K)	$\Delta_r G$ kJ/mol
Assembly (of amino acids into preproglucagon)	13Ala + 16Arg + 8Asn + 16Asp + 13Glu + 10Gln + 9Gly + 4His + 8Ile + 12Leu + 10Lys + 5Met + 11Phe + 3Pro + 17Ser + 9Thr + 4Trp + 4Tyr + 8Val → (Preproglucagon) + 179H_2O	13757.55	7202.25	11609.96
Activation (by energy from ATP hydrolysis)	179ATP + 358H_2O → 179AMP + 358$H_2PO_4^-$	–8896.3	14817.62	–13024.04
Total translation with ATP	13Ala +16 Arg + 8Asn + 16Asp + 13Glu + 10Gln + 9Gly + 4His + 8Ile + 12Leu + 10Lys + 5Met + 11Phe + 3Pro + 17Ser + 9Thr + 4Trp + 4Tyr + 8Val + 179ATP + 179H_2O → (Preproglucagon) + 179AMP + 358$H_2PO_4^-$	4861.25	22019.87	–1414.08

The favorable positive entropy change and unfavorable positive enthalpy change imply that the translation process is overall entropy driven. The positive entropy originates from release of a water molecule during polymerization of amino acids and hydrolysis of the pyrophosphate released during ATP hydrolysis. Therefore, even though many small amino acids polymerize into a large polypeptide molecule, the release of the small H_2O and Pi particles allows the entropy change of the process to be positive. The positive entropy change makes the Gibbs energy change favorable, which provides the driving force for the translation process.

Biothermodynamic analysis of post-translational processing

Table IV presents thermodynamic properties of the reactions of post-translational processing. Fig. 4 shows Gibbs energy changes of the reactions in the metabolic pathway for production of glucagon. Reaction A is translation at the ribosomes, where amino acids activated by ATP hydrolysis polymerize to produce

preproglucagon (blue column in Fig. 4a). Reactions B–G represent post-translational processing of preproglucagon into glucagon (green columns in Fig. 4a). Gibbs energy change of the translation reaction is highly negative. The reason for the highly negative Gibbs energy change of the translation reaction is hydrolysis of ATP that activates amino acids that are loaded to tRNAs before they react at the ribosomes to produce the polypeptide. The highly negative Gibbs energy change means that the translation reaction has a large driving force and is highly favorable. On the other hand, the reactions of post-translational processing (B–G) have slightly positive Gibbs energy changes. This means that these reactions alone are not favorable and will not occur unless they are coupled with reactions with negative Gibbs energy change.

TABLE IV. Stoichiometry and thermodynamic properties of the reactions in the metabolic pathway for production of glucagon from amino acids at the physiological temperature of 37 °C. Symbols: change in reaction enthalpy at 37 °C, $\Delta_r H'$, change in reaction entropy at 37 °C, $\Delta_r S'$, and change in reaction Gibbs energy at 37 °C, $\Delta_r G'$

Name	Reaction	$\Delta_r H'$ kJ/mol	$\Delta_r S'$ J/(mol K)	$\Delta_r G'$ kJ/mol
A	13Ala + 16Arg + 8Asn + 16Asp + 13Glu + 10Gln + 9Gly + 4His + 8Ile + 12Leu + 10Lys + 5Met + 11Phe + 3Pro + 17Ser + 9Thr + 4Trp + 4Tyr + 8Val + 179ATP + 179H_2O → (Preproglucagon) + 179AMP + 358$H_2PO_4^-$	–	–	-1666.65
B	(Preproglucagon) + H_2O → (Proglucagon) + (Signal peptide)	-0.56	-28.14	8.17
C	(Proglucagon) + H_2O → (Glicentin-KR) + MPGF	-0.56	-28.14	8.17
D	(Glicentin-KR) + H_2O → (Oxyntomodulin-KR) + GRPP-KR	-0.56	-28.14	8.17
E	(Oxyntomodulin-KR) + H_2O → Oxyntomodulin + KR	-0.56	-28.14	8.17
F	(Oxyntomodulin) + H_2O → (Glucagon-KR) + (Hexapeptide)	-0.56	-28.14	8.17
G	(Glucagon-KR) + H_2O → (Glucagon) + KR	-0.56	-28.14	8.17

The initial reactant of the post-translational processing reactions is preproglucagon, while their final product is glucagon (Fig. 4b). Preproglucagon is the product of the translation reaction, which has a highly negative Gibbs energy change. This means that the translation reaction is highly favorable and will continuously produce preproglucagon, which is the reactant of the post-translational processing reactions. Therefore, the reactant of the post-translational processing reactions is continuously produced by the translation reaction with its great driving force. Moreover, the final product of the post-translational processing reactions is glucagon, which is excreted from the cell into the blood. This means the product of the post-translational processing reactions is continuously removed from the system (cell). The continuous input of reactant (preproglucagon) and removal of product (glucagon) shifts the post-translational processing reactions towards production of more products, in accordance with the Le Chatelier's principle. Therefore, the Le Chatelier's principle allows the coupling of the translation reaction

that has a highly negative Gibbs energy change with the post-translational processing reactions that alone are not favorable, which makes the entire metabolic pathway for production of glucagon feasible. Indeed, the total Gibbs energy change of the metabolic pathway is highly negative (grey column in Fig. 4a).

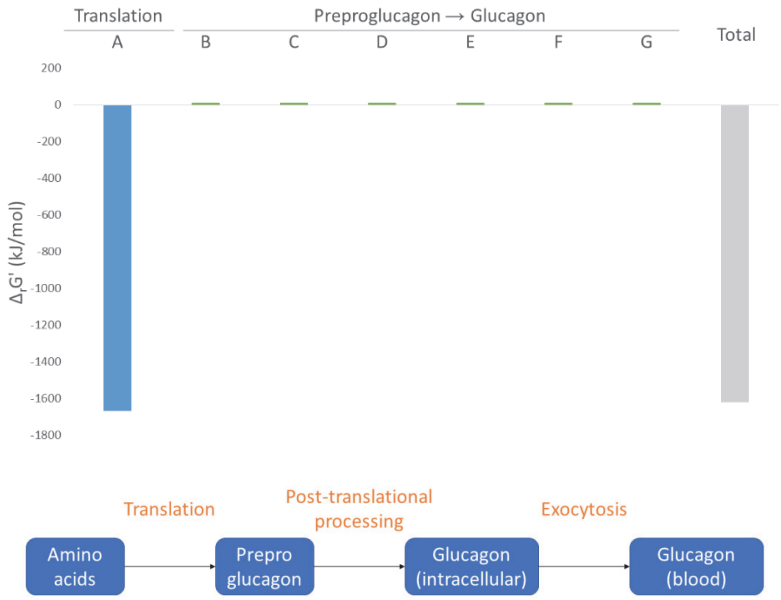

Fig. 4. Driving force of glucagon synthesis. This figure shows standard reaction Gibbs energy at physiological temperature, $\Delta_r G'$, of the reactions in the metabolic pathway for synthesis of glucagon. Reaction A (blue column) is translation at the ribosomes, where preproglucagon is synthetized from amino acids activated by ATP. Reactions B–G (green columns) represent post-translational processing of preproglucagon to produce glucagon. The last (grey) column gives the total Gibbs energy change for the entire metabolic pathway.

In summary, the translation reaction A that produces preproglucagon from amino acids at the ribosomes has a highly negative Gibbs energy change, due to hydrolysis of ATP during activation of amino acids, which means that it has a large driving force and is highly favorable. The post-translational processing reactions B–G have slightly positive Gibbs energy changes and are not feasible unless coupled with a reaction with a negative Gibbs energy change. The initial reactant of the post-translational processing reactions is preproglucagon, which is continuously produced by the highly favorable translation reaction. Moreover, the final product of the post-translational processing reactions is glucagon, which is continuously removed from the cell (system) by excretion into the blood. The continuous input of reactant (preproglucagon) and removal of product (glucagon)

makes the post-translational processing reactions proceed towards formation of more product, due to the Le Chatelier's principle.

In this research, the methodology of biothermodynamics was used to calculate changes in Gibbs energy during the reactions of the metabolic pathway for production of glucagon, based on protein sequences. Gibbs energy change represents the driving force of chemical reactions and allows to determine their feasibility. Based on the determined Gibbs energies, the feasibility of the metabolic pathway for production of glucagon was analyzed. This approach could be useful in omics research, where a lot of data on biomolecules is collected and based on it many potential metabolic pathways can be proposed. The biothermodynamic methodology described in this research allows to determine which potential metabolic pathways are feasible and can occur in the cell. This makes the biothermodynamic approach presented in this paper useful for omics research.

CONCLUSIONS

Chemical and thermodynamic characterization was performed of glucagon, proglucagon, preproglucagon and related peptides. The determined properties include molecular formulas, empirical formulas, molar masses, enthalpies of formation, $\Delta_f H$, molar entropies, S_m, Gibbs energies of formation, $\Delta_f G$, molar heat capacities at constant pressure, $C_{p,m}$, entropies of formation, $\Delta_f S$, and enthalpies of combustion, $\Delta_C H$.

Biothermodynamic analysis was made of the translation process where amino acids activated with ATP polymerize at the ribosomes to produce a polypeptide (preproglucagon). The translation process is made feasible by ATP hydrolysis during activation of amino acids. The translation process has a positive enthalpy and positive entropy change, which means that the process is entropy driven.

The metabolic pathway for the production of glucagon was analyzed with the methodology of biothermodynamics. The driving forces (Gibbs energy changes) of the reactions in the metabolic pathway were determined. The reaction of translation has a highly negative Gibbs energy change and is favorable. The reactions of post-translational processing have slightly positive Gibbs energy changes and are not feasible unless they are coupled with a process with a negative Gibbs energy change. The initial reactant of the post-translational processing reactions is preproglucagon, while their final product is glucagon. Preproglucagon is continuously produced by translation at the ribosomes, which has a large driving force – highly negative Gibbs energy change. Moreover, glucagon is continuously removed by excretion into the blood. The continuous introduction of reactant and removal of product allows the post-translational processing reactions to proceed in accordance with the Le Chatelier's principle. Therefore, the Le Chatelier's principle makes the entire metabolic pathway feasible, because it provides coupling

between the highly favorable translation process and slightly unfavorable post-translational processing reactions.

The biothermodynamic methodology used in this study can be applied in omics research for metabolic pathway analysis. Based on protein sequences, driving forces of metabolic pathways were calculated. The driving forces were used to find the feasibility of the metabolic pathway. Therefore, the methodology presented in this paper can be used in omics research to find feasibility of metabolic pathways.

NOMENCLATURE

GRPP, glicentin-related pancreatic peptide, GRPP-KR, glicentin-related pancreatic peptide with a Lys-Arg extension at the C-terminus, glicentin-KR, glicentin with a Lys-Arg extension at the C-terminus, oxyntomodulin-KR, oxyntomodulin with a Lys-Arg extension at the C-terminus, glucagon-KR, glucagon with a Lys-Arg extension at the C-terminus, MPGF, major proglucagon fragment, GLP-1, glucagon-like peptide 1, t-GLP-1, truncated glucagon-like peptide 1, GLP-2, glucagon-like peptide 2, KR, Lys-Arg dipeptide.

SUPPLEMENTARY MATERIAL

Additional data and information are available electronically at the pages of journal website: https://www.shd-pub.org.rs/index.php/JSCS/article/view/13558, or from the corresponding author on request.

Acknowledgements. This work was supported by the Ministry of Science, Technological Development and Innovation of the Republic of Serbia (Grant No. 451-03-136/2025-03/200026).

И З В О Д

ЛЕ ШАТЕЉЕОВ ПРИНЦИП И МЕТАБОЛИЗАМ: БИОТЕРМОДИНАМИЧКА АНАЛИЗА МЕТАБОЛИЧКОГ ПУТА ЗА СИНТЕЗУ ГЛУКАГОНА

МАРКО Е. ПОПОВИЋ[1], ДОНГ ПЕИ[2] и МАРИЈА МИХАИЛОВИЋ[1]

[1]Универзитет у Београду, Институт за хемију, технологију и металургију, Његошева 12, 11000 Београд и [2]Research Center for Natural Medicine and Chemical Metrology, Lanzhou Institute of Chemical Physics, Chinese Academy of Sciences, Lanzhou 730000, China

Глукагон је основни катаболички хормон у људском организму. Глукагон је добро проучен са аспекта биолошких и медицинских наука. Међутим, у литератури се не може наћи анализа глукагона заснована на хемијској термодинамици. Приступ биотермодинамике би омогућио да се одреди погонска сила за производњу глукагона, као и разумевање процеса са аспекта фундаменталних закона природе. У овом истраживању извршена је анализа глукагона помоћу методологије биотермодинамике. На основу протеинских секвенци, извршена је хемијска и термодинамичка карактеризација глукагона, проглукагона, препроглукагона и повезаних пептида, помоћу метода пребројавања атома и *Patel–Erickson–Battley* модела. Формулисане су реакције транслације на рибозомима као и посттранслационе обраде и израчуната је њихова погонска сила (промена Гибсове енергије). Процес транслације на рибозомима који производи препроглукагон изучен је са аспекта хемијске термодинамике. На основу Гибсове енергије, извршена је анализа метаболичког пута за производњу глукагона. Изучена је улога Ле Шатељеовог принципа

у спрезању реакција у метаболичком путу. На крају, разматрана је примена биотермодинамичке методологије у омици за одређивање изводљивости метаболичких путева.

(Примљено 22. септембра, ревидирано 11. новембра, прихваћено 26. новембра 2025)

REFERENCES

1. J. Philippe, in: *Glucagon III. Handbook of Experimental Pharmacology*, Vol. 123, P.J. Lefèbvre, Ed., Springer, Berlin, 1996 (https://doi.org/10.1007/978-3-642-61150-6_2)
2. D. Bataille, in: *Glucagon III. Handbook of Experimental Pharmacology,* Vol. 123, P.J. Lefèbvre, Ed., Springer, Berlin, 1996 (https://doi.org/10.1007/978-3-642-61150-6_3)
3. S. Lang, D. Nguyen, P. Bhadra, M. Jung, V. Helms, R. Zimmermann, *Front. Physiol.* **13** (2022) 833540 (https://doi.org/10.3389/fphys.2022.833540)
4. K. Ono, *Int. J. Mol. Sci.* **25** (2024) 13534 (https://doi.org/10.3390/ijms252413534)
5. P. Lindquist, J. S. Madsen, H. Bräuner-Osborne, M. M. Rosenkilde, A. S. Hauser, *Front. Endocrin.* **12** (2021) 698511 (https://doi.org/10.3389/fendo.2021.698511)
6. R. C. Moffett, N. G. Docherty, C. W. le Roux, *Appetite* **156** (2021) 104807 (https://doi.org/10.1016/j.appet.2020.104807)
7. R. D. Wideman, S. D. Covey, G. C. Webb, D. J. Drucker, T. J. Kieffer, *Diabetes* **56** (2007) 2744 (https://doi.org/10.2337/db07-0563)
8. I. Rix, C. Nexøe-Larsen, N.C. Bergmann *et al.*, in: *Endotext*, K.R. Feingold, S.F. Ahmed, B. Anawalt *et al*., Eds., MDText.com Inc., South Dartmouth, 2019. Available from: https://www.ncbi.nlm.nih.gov/books/NBK279127/ (accessed on August 9, 2025)
9. *UniProt: P01275 GLUC_HUMAN*, Available at: https://www.uniprot.org/uniprotkb/P01275/entry (accessed on August 9, 2025)
10. *PubChem: Compound summary: Glucagon*, Available at: https://pubchem.ncbi.nlm.nih.gov/compound/Glucagon (accessed on August 9, 2025)
11. *NCBI: Pro-glucagon preproprotein (Homo sapiens)*, Available at: https://www.ncbi.nlm.nih.gov/protein/NP_002045.1?report=genbank&log$=protalign&blast_rank=6&RID=7J5YEGKW014 (accessed on August 9, 2025)
12. J. Thomsen, K. Kristiansen, K. Brunfeldt, F. Sundby, *FEBS Lett.* **21** (1972) 315 (https://doi.org/10.1016/0014-5793(72)80192-3)
13. R. A. Alberty, R. N. Goldberg, *Biochemistry* **31** (1992) 10610 (https://doi.org/10.1021/bi00158a025)
14. P. W. Atkins, J. de Paula. *Physical Chemistry for the Life Sciences (2nd ed.)*, W. H. Freeman and Company, New York, 2011 (ISBN-13: 978-1429231145)
15. S. Perisanu, D. Gheorghe, A. Neacsu, *Ins. Chem. Biochem.* **1** (2020) 1 (https://doi.org/10.33552/ICBC.2020.01.000515)
16. V. Pokorný, V. Štejfa, J. Havlín, M. Fulem, K. Růžička, *Molecules* **29** (2024) 5366 (https://doi.org/10.3390/molecules29225366)
17. V. Pokorný, V. Štejfa, J. Havlín, M. Fulem, K. Růžička, *Molecules* **28** (2023) 451 (https://doi.org/10.3390/molecules28010451)
18. V. Pokorný, E. Lieberzeitová, V. Štejfa J. Havlín, M. Fulem, K. Růžička, *Int. J. Thermophys*. **42** (2021) 160 (https://doi.org/10.1007/s10765-021-02911-z)
19. V. Pokorný, V. Štejfa, J. Havlín, K. Růžička, M. Fulem, *Molecules* **26** (2021) 4298 (https://doi.org/10.3390/molecules26144298)
20. V. Pokorný, C. Červinka, V. Štejfa, J. Havlín, K. Růžička, M. Fulem, *J. Chem. Eng. Data* **65** (2020) 1833 (https://doi.org/10.1021/acs.jced.9b01086)
21. P. Vieillard, Y. Tardy, in: *Phosphate Minerals*, J.O. Nriagu, P.B. Moore, Eds., Springer, Berlin, 1984 (https://doi.org/10.1007/978-3-642-61736-2_4)

22. M. Popovic, *Comp. Biol. Chem.* **96** (2022) 107621 (https://doi.org/10.1016/j.compbiolchem.2022.107621)
23. M. Popovic, V. Tadić, M. Mihailović, *J. Biomol. Struct. Dyn.* **42** (2024) 10388 (https://doi.org/10.1080/07391102.2023.2256880)
24. M. E. Popović, M. Stevanović, M. Pantović Pavlović, *J. Mol. Evol.* **92** (2024) 776 (https://doi.org/10.1007/s00239-024-10205-9)
25. E. H. Battley, *Thermochim. Acta* **309** (1998) 17 (https://doi.org/10.1016/S0040-6031(97)00357-2)
26. E. H. Battley, *Thermochim. Acta* **326** (1999) 7 (https://doi.org/10.1016/S0040-6031(98)00584-X)
27. S. A. Patel, L. E. Erickson, *Biotechnol. Bioeng.* **23** (1981) 2051 (https://doi.org/10.1002/bit.260230910)
28. E. H. Battley, J. R. Stone, *Thermochim. Acta* **349** (2000) 153 (https://doi.org/10.1016/S0040-6031(99)00509-2)
29. P. W. Atkins, J. de Paula, *Physical Chemistry: Thermodynamics, Structure, and Change, 10th ed*., W. H. Freeman and Company, New York, 2014 (ISBN-13: 978-1429290197)
30. J. E. Hurst, B. K. Harrison, *Chem. Eng. Comm.* **112** (1992) 21 (https://doi.org/10.1080/00986449208935989)
31. M. Ozilgen, E. Sorguven Oner, *Biothermodynamics: Principles and Applications (1st ed.)*, CRC Press, Boca Raton, FL, 2016 (https://doi.org/10.1201/9781315374147)
32. J. Stenesh, in: *Biochemistry*, Springer, Boston, MA, 1998 (https://doi.org/10.1007/978-1-4757-9427-4_19)
33. B. Alberts, A. Johnson, J. Lewis *et al*., in: *Molecular Biology of the Cell, 4th ed.*, Garland Science, New York, 2002. Available from: https://www.ncbi.nlm.nih.gov/books/NBK26829/ (accessed on August 9, 2025)
34. J. M. Berg, J. L. Tymoczko, L. Stryer, *Biochemistry, 5th ed.*, Freeman, New York, 2002 (ISBN-13: 978-0716746843)
35. M. E. Popović, M. Popović, D. Pei, *Biophysica* **5** (2025) 19 (https://doi.org/10.3390/biophysica5020019)
36. U. Von Stockar, in *Biothermodynamics: The Role of Thermodynamics in Biochemical Engineering*, U. von Stockar, L. A. M. van der Wielen, Eds., EPFL Press, Lausanne, 2013, pp. 399–421 (https://doi.org/10.1201/b15428)
37. T. Cossetto, J. Rodenfels, P. Sartori, *Nat. Comm.* **16** (2025) 8543 (https://doi.org/10.1038/s41467-025-62975-5)
38. S. Calabrese, A. Chakrawal, S. Manzoni, P. Van Cappellen, *PNAS* **118** (2021) e2107668118 (https://doi.org/10.1073/pnas.2107668118)
39. V. Piñeiro, Y. Lestido-Cardama, C. Pérez-Cruzado, N. Barros, *Soil Biol. Biochem.* **206** (2025) 109812 (https://doi.org/10.1016/j.soilbio.2025.109812)
40. U. Lucia, G. Grisolia, *Inventions* **10** (2025) 47 (https://doi.org/10.3390/inventions10040047)
41. M. E. Popović, M. Stevanović, V. Tadić, *Virology* **614** (2025) 110742 (https://doi.org/10.1016/j.virol.2025.110742)
42. M. E. Popović, M. Stevanović, M. P. Pavlović, *Microb. Risk Anal.* **26** (2024) 100292 (https://doi.org/10.1016/j.mran.2024.100292)
43. M. Özilgen, B. Yilmaz, *Int. J. Energy Res.* **45** (2021) 1157 (https://doi.org/10.1002/er.5883)
44. M. E. Popović, *Zoology* **163** (2024) 126158 (https://doi.org/10.1016/j.zool.2024.126158)

45. V. Dragičević, in: *Recent Advances in Thermo and Fluid Dynamics*, M. Gorji-Bandpy, Ed., InTech, Rijeka, 2015 (https://doi.org/10.5772/60990)
46. O. Ebenhöh, J. Ebeling, R. Meyer, F. Pohlkotte, T. Nies, *Life* **14** (2024) 247 (https://doi.org/10.3390/life14020247)
47. M. Corrao, H. He, W. Liebermeister, E. Noor, A. Bar-Even, *PLoS Comp. Bio.* **21** (2025) e1013564 (https://doi.org/10.1371/journal.pcbi.1013564)
48. Y. Demirel, *Nonequilibrium Thermodynamics: Transport and Rate Processes in Physical, Chemical and Biological Systems, 3rd ed.*, Elsevier, Amsterdam, 2014 (ISBN: 9780444595812)
49. O. Shpielberg, E. Akkermans, *Phys. Rev. Lett.* **116** (2016) 240603 (https://doi.org/10.1103/PhysRevLett.116.240603)
50. A. E. Allahverdyan, A. Galstyan, P*hys. Rev., E* **84** (2011) 041117 (https://doi.org/10.1103/PhysRevE.84.041117)
51. R. T. Balmer, *Modern Engineering Thermodynamics*, Academic Press, Cambridge, MA, 2010 (https://doi.org/10.1016/C2009-0-20199-1)
52. M.E. Popović, V. Tadić, M. Popović, *Virology* **603** (2025) 110319 (https://doi.org/10.1016/j.virol.2024.110319)
53. U. von Stockar, J. Liu, *Biochim. Biophys Acta* **1412** (1999) 191 (https://doi.org/10.1016/s0005-2728(99)00065-1)
54. S. I. Sandler, H. Orbey, *Biotech. Bioeng.* **38** (1991) 697 (https://doi.org/10.1002/bit.260380704)
55. U. von Stockar, in: *Biothermodynamics: The Role of Thermodynamics in Biochemical Engineering*, U. von Stockar, L. A. M. van der Wielen, Eds., EPFL Press, Lausanne, 2013, pp. 475–534 (https://doi.org/10.1201/b15428)
56. M. Popovic, G. B. G. Stenning, A. Göttlein, M. Miniceva, *J. Biotech.* **331** (2021) 99 (https://doi.org/10.1016/j.jbiotec.2021.03.006)
57. M. Popovic, *Helyon* **5** (2019) e01950 (https://doi.org/10.1016/j.heliyon.2019.e01950)
58. N. Barros, M. Popovic, J. Molina-Valero, Y. Lestido-Cardama, C. Pérez-Cruzado*, Sci. Rep.* **14** (2024) 16644 (https://doi.org/10.1038/s41598-024-67590-w)
59. B. Şimşek, M. Özilgen, F. Ş. Utku, *Energy Storage* **4** (2022) e298 (https://doi.org/10.1002/est2.298).

Journal of the Serbian Chemical Society
JSCS@tmf.bg.ac.rs • www.shd.org.rs/JSCS
J. Serb. Chem. Soc. 91 (3) S107–S113 (2026) *Supplementary material*

SUPPLEMENTARY MATERIAL TO

Le Chatelier's principle and metabolism: Biothermodynamic analysis of the metabolic pathway for synthesis of glucagon

MARKO E. POPOVIĆ[1]*, DONG PEI[2] and MARIJA MIHAILOVIĆ[1]

[1]*University of Belgrade, Institute of Chemistry, Technology and Metallurgy, Njegoševa 12, 11000 Belgrade, Serbia and* [2]*Research Center for Natural Medicine and Chemical Metrology, Lanzhou Institute of Chemical Physics, Chinese Academy of Sciences, Lanzhou 730000, China*

J. Serb. Chem. Soc. 91 (3) (2026) 227–244

Table S-I presents the amino acid sequences of glucagon, proglucagon, preproglucagon and related peptides. The sequences were taken from [UniProt, 2025; PubChem, 2025; NCBI, 2025; Bataille, 1996; Thomsen et al., 1972]. The amino acid sequence of preproglucagon can be found under the UniProt access number P01275 (section *Sequence*) [UniProt, 2025] and NCBI access number NP_002045.1 [NCBI, 2025]. The amino acid sequence of preproglucagon is: MKSIYFVAGLFVMLVQGSWQRSLQDTEEKSRSFSASQADPLSDPDQMNE DKRHSQGTFTSDYSKYLDSRRAQDFVQWLMNTKRNRNNIAKRHDEFER HAEGTFTSDVSSYLEGQAAKEFIAWLVKGRGRRDFPEEVAIVEELGRRH ADGSFSDEMNTILDNLAARDFINWLIQTKITDRK [UniProt, 2025; NCBI, 2025]. The amino acid sequence of glucagon can be found under the UniProt access number P01275 (section *PTM/Processing*) [UniProt, 2025], PubChem CID 16132283 [PubChem, 2025] and in references [Bataille, 1996; Thomsen et al., 1972]. The amino acid sequence of glucagon is HSQGTFTSDYSKYLDSRRAQDFVQWLMNT [UniProt, 2025; PubChem, 2025; Bataille, 1996; Thomsen et al., 1972]. The amino acid sequences of proglucagon and related peptides can be found under the UniProt access number P01275 (section *PTM/Processing*) [UniProt, 2025] and in reference [Bataille, 1996].

Table S-II shows the empirical formulas of glucagon, proglucagon, preproglucagon and related peptides. Empirical formulas express the numbers of atoms present in a molecule per carbon atom. The empirical formulas have the general form $CH_{nH}O_{nO}N_{nN}S_{nS}$, where n_H, n_O, n_N and n_S represent the numbers of hydrogen, oxygen, nitrogen and sulfur atoms in the empirical formula,

* Corresponding author. E-mail: marko.popovic@ihtm.bg.ac.rs

respectively. They were determined with the atom counting method, based on protein sequences, as described in [Popovic et al., 2024a; Popovic, 2022].

Table S-II gives thermodynamic properties of empirical formulas of glucagon, proglucagon, preproglucagon and related peptides. The determined thermodynamic properties of entire molecules include standard enthalpy of formation, $\Delta_f H^o$, standard molar entropy, $S_m{}^o$, standard Gibbs energy of formation, $\Delta_f G^o$, standard molar heat capacity at constant pressure, $C^o{}_{p,m}$, standard entropy of formation, $\Delta_f S^o$, and standard enthalpy of combustion, $\Delta_C H^o$. Thermodynamic properties of empirical formulas are expressed per mole of carbon (C-mol). They were determined with the Patel-Erickson-Battley and Hurst-Harrison models, based on empirical formulas, as described in [Popovic et al., 2024b; Ozilgen and Sorguven Oner, 2016].

Table S-IV shows the stoichiometry and changes in thermodynamic properties of the chemical reactions in the metabolic pathway for synthesis of glucagon at room temperature (25°C). The determined properties include standard reaction enthalpy at 25°C, $\Delta_r H^o$, standard reaction entropy at 25°C, $\Delta_r S^o$, standard reaction Gibbs energy at 25°C, $\Delta_r G^o$, standard reaction heat capacity at constant pressure at 25°C, $\Delta_r C_p{}^o$. They were determined based on the molecular formulas and thermodynamic properties of the analyzed molecules, with the methodology of thermochemistry, as described in [Popovic et al., 2024a; Atkins and de Paula, 2011].

Table S-I: Amino acid sequences of glucagon, proglucagon, preproglucagon and related peptides. All peptides in this table are derived by post-translational processing of preproglucagon. For every sequence, the start and end amino acid within preproglucagon is given, as well as its length. Abbreviations: GRPP glicentin-related pancreatic peptide, GRPP-KR glicentin-related pancreatic peptide with a Lys-Arg extension at the C-terminus, Glicentin-KR glicentin with a Lys-Arg extension at the C-terminus, Oxyntomodulin-KR oxyntomodulin with a Lys-Arg extension at the C-terminus, Glucagon-KR glucagon with a Lys-Arg extension at the C-terminus, MPGF major proglucagon fragment, GLP-1 glucagon-like peptide 1, t-GLP-1 truncated glucagon-like peptide 1, GLP-2 glucagon-like peptide 2, KR Lys-Arg dipeptide. Data taken from taken from [UniProt, 2025; PubChem, 2025; NCBI, 2025; Bataille, 1996; Thomsen et al., 1972].

Name	Start	End	Sequence	Length
Preproglucagon	1	180	MKSIYFVAGLFVMLVQGSWQRSLQDTEEKSRSFSASQADP LSDPDQMNEDKRHSQGTFTSDYSKYLDSRRAQDFVQWLM NTKRNRNNIAKRHDEFERHAEGTFTSDVSSYLEGQAAKEFI AWLVKGRGRRDFPEEVAIVEELGRRHADGSFSDEMNTILD NLAARDFINWLIQTKITDRK	180
Proglucagon	21	180	RSLQDTEEKSRSFSASQADPLSDPDQMNEDKRHSQGTFTSD YSKYLDSRRAQDFVQWLMNTKRNRNNIAKRHDEFERHAE GTFTSDVSSYLEGQAAKEFIAWLVKGRGRRDFPEEVAIVEE LGRRHADGSFSDEMNTILDNLAARDFINWLIQTKITDRK	160
GRPP	21	50	RSLQDTEEKSRSFSASQADPLSDPDQMNED	30
GRPP-KR	21	52	RSLQDTEEKSRSFSASQADPLSDPDQMNEDKR	32
Glicentin-KR	21	91	RSLQDTEEKSRSFSASQADPLSDPDQMNEDKRHSQGTFTSD YSKYLDSRRAQDFVQWLMNTKRNRNNIAKR	71
Glicentin	21	89	RSLQDTEEKSRSFSASQADPLSDPDQMNEDKRHSQGTFTSD YSKYLDSRRAQDFVQWLMNTKRNRNNIA	69
Oxyntomodulin-KR	53	91	HSQGTFTSDYSKYLDSRRAQDFVQWLMNTKRNRNNIAKR	39
Oxyntomodulin	53	89	HSQGTFTSDYSKYLDSRRAQDFVQWLMNTKRNRNNIA	37
Glucagon-KR	53	83	HSQGTFTSDYSKYLDSRRAQDFVQWLMNTKR	31
Glucagon	53	81	HSQGTFTSDYSKYLDSRRAQDFVQWLMNT	29
Mini-glucagon	71	81	AQDFVQWLMNT	11
Hexapeptide	84	89	NRNNIA	6
GLI9000	21	81	RSLQDTEEKSRSFSASQADPLSDPDQMNEDKRHSQGTFTSD YSKYLDSRRAQDFVQWLMNT	61
MPGF	92	180	HDEFERHAEGTFTSDVSSYLEGQAAKEFIAWLVKGRGRRD FPEEVAIVEELGRRHADGSFSDEMNTILDNLAARDFINWLI QTKITDRK	89
GLP-1	92	128	HDEFERHAEGTFTSDVSSYLEGQAAKEFIAWLVKGRG	37
t-GLP-1	98	128	HAEGTFTSDVSSYLEGQAAKEFIAWLVKGRG	31
GLP-2	145	178	RHADGSFSDEMNTILDNLAARDFINWLIQTKITD	34
Signal peptide	1	20	MKSIYFVAGLFVMLVQGSWQ	20
KR			KR	2

Table S-II: Empirical formulas of glucagon, proglucagon, preproglucagon and related peptides. The empirical formulas have the general form $CH_{nH}O_{nO}N_{nN}S_{nS}$, where n_H, n_O, n_N and n_S represent the numbers of hydrogen, oxygen, nitrogen and sulfur atoms in the empirical formula, respectively. The table also gives the molar masses of empirical formulas, *Mr* in grams per mole of carbon (C-mole).

Name	n_H	n_O	n_N	n_S	Mr (g/C-mol)
Preproglucagon	1.5470	0.3140	0.2932	0.0055	22.88
Proglucagon	1.5547	0.3259	0.3035	0.0037	23.16
GRPP	1.5809	0.4265	0.3015	0.0074	24.89
GRPP-KR	1.6149	0.4054	0.3176	0.0068	24.79
Glicentin-KR	1.5795	0.3438	0.3239	0.0057	23.82
Glicentin	1.5647	0.3500	0.3176	0.0059	23.83
Oxyntomodulin-KR	1.5637	0.3039	0.3284	0.0049	23.21
Oxyntomodulin	1.5365	0.3125	0.3177	0.0052	23.18
Glucagon-KR	1.5091	0.3091	0.2970	0.0061	22.83
Glucagon	1.4706	0.3203	0.2810	0.0065	22.76
Mini-glucagon	1.4590	0.2951	0.2459	0.0164	22.17
Hexapeptide	1.7778	0.3704	0.4444	0.0000	25.95
GLI9000	1.5349	0.3588	0.2990	0.0066	23.70
MPGF	1.5398	0.3142	0.2876	0.0022	22.69
GLP-1	1.4785	0.3172	0.2742	0.0000	22.42
t-GLP-1	1.5099	0.3113	0.2649	0.0000	22.22
GLP-2	1.5556	0.3275	0.2807	0.0058	22.94
Signal peptide	1.5091	0.2364	0.2182	0.0182	20.95
KR	2.1667	0.2500	0.5000	0.0000	25.20

Table S-III: Thermodynamic properties of empirical formulas of glucagon, proglucagon, preproglucagon and related peptides. Symbols: standard enthalpy of formation, $\Delta_f H^o$, standard molar entropy, $S_m{}^o$, standard Gibbs energy of formation, $\Delta_f G^o$, standard molar heat capacity at constant pressure, $C^o{}_{p,m}$, standard entropy of formation, $\Delta_f S^o$, standard enthalpy of combustion, $\Delta_C H^o$. The properties in this table are for the empirical formulas and are given per mole of carbon (C-mol).

Name	$\Delta_f H^o$ (kJ/C-mol)	$S^o{}_m$ (J/C-mol K)	$\Delta_f G^o$ (kJ/C-mol)	$C^o{}_{p,m}$ (J/C-mol K)	$\Delta_f S^o$ (kJ/C-mol)	$\Delta_C H^o$ (kJ/C-mol)
Preproglucagon	-66.42	31.24	-25.92	32.36	-135.83	-550.35
Proglucagon	-69.77	31.74	-28.64	32.75	-137.98	-547.41
GRPP	-91.98	33.97	-47.95	34.31	-147.70	-530.37
GRPP-KR	-88.54	34.27	-44.12	34.57	-148.98	-538.43
Glicentin-KR	-74.01	32.76	-31.54	33.58	-142.43	-547.49
Glicentin	-74.87	32.59	-32.63	33.44	-141.68	-544.59
Oxyntomodulin-KR	-64.86	31.88	-23.54	33.01	-138.60	-554.07
Oxyntomodulin	-65.82	31.52	-24.96	32.72	-137.04	-549.33
Glucagon-KR	-63.96	30.75	-24.10	32.09	-133.71	-547.62
Glucagon	-65.09	30.22	-25.93	31.65	-131.37	-541.17
Mini-glucagon	-56.46	29.02	-18.84	30.69	-126.17	-552.06
Hexapeptide	-87.76	37.82	-38.74	37.63	-164.42	-559.82
GLI9000	-75.67	32.06	-34.11	32.99	-139.40	-539.82
MPGF	-67.11	31.04	-26.88	32.16	-134.94	-547.34
GLP-1	-66.44	30.09	-27.43	31.46	-130.83	-538.37
t-GLP-1	-66.11	30.20	-26.97	31.45	-131.28	-543.19
GLP-2	-69.59	31.38	-28.91	32.38	-136.44	-548.55
Signal peptide	-44.51	28.02	-8.19	29.78	-121.82	-571.87
KR	-73.37	41.26	-19.89	40.00	-179.37	-629.79

Table S-IV: Stoichiometry and thermodynamic properties of the reactions in the metabolic pathway for production of glucagon from amino acids at 25°C. Symbols: standard reaction enthalpy at 25°C, $\Delta_r H^o$, standard reaction entropy at 25°C, $\Delta_r S^o$, standard reaction Gibbs energy at 25°C, $\Delta_r G^o$, standard reaction heat capacity at constant pressure at 25°C, $\Delta_r C_p{}^o$.

Name	Reaction	$\Delta_r H^o$ (kJ/mol)	$\Delta_r S^o$ (J/mol K)	$\Delta_r G^o$ (kJ/mol)	$\Delta_r C_p{}^o$ (J/mol K)
A	13 Ala + 16 Arg + 8 Asn + 16 Asp + 13 Glu + 10 Gln + 9 Gly + 4 His + 8 Ile + 12 Leu + 10 Lys + 5 Met + 11 Phe + 3 Pro + 17 Ser + 9 Thr + 4 Trp + 4 Tyr + 8 Val + 179 ATP + 179 H_2O → (Preproglucagon) + 179 AMP + 358 $H_2PO_4^-$	4861.25	21047.55	-1414.08	
B	(Preproglucagon) + H_2O → (Proglucagon) + (Signal peptide)	0.00	-26.29	7.84	-46.75
C	(Proglucagon) + H_2O → (Glicentin-KR) + MPGF	0.00	-26.29	7.84	-46.75
D	(Glicentin-KR) + H_2O → (Oxyntomodulin-KR) + GRPP-KR	0.00	-26.29	7.84	-46.75
E	(Oxyntomodulin-KR) + H_2O → Oxyntomodulin + KR	0.00	-26.29	7.84	-46.75
F	(Oxyntomodulin) + H_2O → (Glucagon-KR) + (Hexapeptide)	0.00	-26.29	7.84	-46.75
G	(Glucagon-KR) + H_2O → (Glucagon) + KR	0.00	-26.29	7.84	-46.75

REFERENCES

1. Atkins, P. W., & de Paula, J. (2011). *Physical Chemistry for the Life Sciences (2nd edition)*, W. H. Freeman and Company. ISBN-13: 978-1429231145
2. Bataille, D. (1996). Preproglucagon and Its Processing. In: Lefèbvre, P.J. (eds) Glucagon III. Handbook of Experimental Pharmacology, vol 123. Springer, Berlin, Heidelberg. https://doi.org/10.1007/978-3-642-61150-6_3
3. NCBI (2025). Pro-glucagon preproprotein (Homo sapiens) [Online] National Center for Biotechnology Information. Available at: https://www.ncbi.nlm.nih.gov/protein/NP_002045.1?report=genbank&log$=protalign&blast_rank=6&RID=7J5YEGKW014 (Accessed on August 9, 2025)
4. Ozilgen, M., & Sorguven Oner, E. (2016). Biothermodynamics: Principles and Applications (1st ed.). CRC Press. https://doi.org/10.1201/9781315374147
5. Popovic, M., Tadić, V., & Mihailović, M. (2024a). From genotype to phenotype with biothermodynamics: empirical formulas, biosynthesis reactions and thermodynamic properties of preproinsulin, proinsulin and insulin molecules. *Journal of biomolecular structure & dynamics*, *42*(19), 10388–10400. https://doi.org/10.1080/07391102.2023.2256880
6. Popović, M. E., Stevanović, M., & Pantović Pavlović, M. (2024b). Biothermodynamics of Hemoglobin and Red Blood Cells: Analysis of Structure and Evolution of Hemoglobin and Red Blood Cells, Based on Molecular and Empirical Formulas, Biosynthesis Reactions, and Thermodynamic Properties of Formation and Biosynthesis. *Journal of molecular evolution*, *92*(6), 776–798. https://doi.org/10.1007/s00239-024-10205-9
7. Popovic M. (2022). Atom counting method for determining elemental composition of viruses and its applications in biothermodynamics and environmental science. *Computational biology and chemistry*, *96*, 107621. https://doi.org/10.1016/j.compbiolchem.2022.107621
8. PubChem (2025). Compound summary: Glucagon [Online] Available at: https://pubchem.ncbi.nlm.nih.gov/compound/Glucagon (Accessed on August 9, 2025)
9. Thomsen, J., Kristiansen, K., Brunfeldt, K., & Sundby, F. (1972). The amino acid sequence of human glucagon. *FEBS letters*, *21*(3), 315–319. https://doi.org/10.1016/0014-5793(72)80192-3
10. UniProt (2025). P01275 GLUC_HUMAN [Online] Available at: https://www.uniprot.org/uniprotkb/P01275/entry (Accessed on August 9, 2025).

Journal of the Serbian Chemical Society
JSCS-info@shd.org.rs • www.shd.org.rs/JSCS
J. Serb. Chem. Soc. *91* (3) 245–258 (2026)
JSCS–5489
Original scientific paper
Published 23 February, 2026

Enhanced photocatalytic performance of ZnO/Cu_2O composite for the degradation of methylene blue under the synergy effect

HONGYING LI[1,2], LUWEN MA[1], ZHENYANG WU[1] and CHENGLI YAO[1]*

[1]*School of Chemistry and Pharmaceutical Engineering, Hefei Normal University, Hefei, Anhui, China and* [2]*Hefei National Research Center for Physical Sciences at the Microscale, University of Science and Technology of China, Hefei, Anhui, China*

(Received 15 November, revised 27 November 2025, accepted 29 January 2026)

Abstract: In order to investigate the catalytic degradation efficiency of ZnO/ /Cu_2O composite, the nanocomposite was synthesized v*ia* one-pot method and the template of SDS. The crystal structure, microscopic morphology, chemical composition, specific surface area, pore size distribution and optical absorption property of the composite were characterized. Under the irradiation of xenon lamp, the photocatalytic performance of the composite was evaluated by degrading methylene blue (MB). The aforementioned characterization showed that the synthesized composite consisted of ZnO (hexagonal wurtzite) and Cu_2O (cubic crystal). Due to the mediation of SDS template, the particles were nanoscale with uniform distribution of Cu, Zn and O elements and contained abundant mesopores. The photo-response range of the composite expanded to the visible region because of the combination of ZnO and Cu_2O. Degradation ratio of MB catalyzed by ZnO/Cu_2O maintained about 92 % within 100 min after five recycling, demonstrating promising potentiality for photocatalytic applications. The enhanced photocatalytic performance maybe related to the mediation of SDS during the preparation process and the synergy effect between ZnO and Cu_2O.

Keywords: SDS; template; ZnO/Cu_2O; photocatalytic degradation.

INTRODUCTION

In recent years, wastewater pollution has increasingly become serious with the rapid development of industrialization. Dyes, pesticides, antibiotics and other organic pollutants which are difficult to degrade in wastewater critically threaten the safety of water ecosystem and human health. Photocatalytic degradation, as a high-efficiency and environment-friendly wastewater treatment technology, has attracted much attention in recent years.[1–4] ZnO,[5,6] CdS,[7] WO_3,[8] TiO_2,[9] Cu_2O,[10] SnO_2,[11] *etc*., have once been selected as semiconductor photocatalysts to degrade organic

* Corresponding author. E-mail: yaochengli@hfnu.edu.cn
https://doi.org/10.2298/JSC251115005L

pollutants in wastewater; however, the photocatalytic performance of a single catalyst is not good. Taking Cu_2O as an example, as a p-type semiconductor with a narrow band gap (E_g = 2.1 eV), it was once considered as a potential photocatalyst because of its low price, environmental friendliness and absorption of most visible light.[10] However, the electron-hole pairs generated in Cu_2O, after absorbing light energy, were easy to recombine quickly. Moreover, Cu_2O was easy oxidized in humid environment, so its photocatalytic performance was unsatisfactory.[12] To improve the photocatalytic performance of Cu_2O, the deposition of metals,[12] doping of nonmetallic elements,[13] recombination with other materials[14] or construction of heterojunction[15] were selected.

As an n-type semiconductor with wide band gap (E_g = 3.37 eV), ZnO has attracted significant attention in recent years by virtue of good chemical stability, convenient preparation method, non-toxicity and low price.[5,6,16] However, as a photocatalyst, ZnO can only be excited by ultraviolet light with high energy, which results in the low utilization efficiency for sunlight and limits its wide application in photocatalytic field. Relevant literature suggested that the photocatalytic property of the composite through combining ZnO with Cu_2O was improved significantly. On one hand, the absorption spectrum of the composite declared a red shift, which significantly improved the availability of sunlight. On the other hand, the separation of photo-generated e^- and h^+ was effectively promoted due to the energy level matching of two semiconductor materials.[17,18]

Surfactants were often used as soft templates to effectively control the morphology and enhance the dispersibility of materials.[19,20] Up to now, the preparation and photocatalytic performance of ZnO/Cu_2O composite have been studied,[17,18,21–23] but it is rarely reported that surfactants are used as templates to regulate the formation of ZnO/Cu_2O. So, it is worth exploring sodium dodecyl sulfate (SDS) mediating the morphology and structure of ZnO/Cu_2O as well as its properties. Here, ZnO/Cu_2O composite was prepared via one-pot method with the template of SDS. The molecules of SDS self-assembled to form ordered aggregates with specific structures, its hydrophilic groups attracted metal ions, thereby changed the distribution of metal ions in the reaction system. Due to the mediation of SDS template, the composite composed of flower-like nano-ZnO and Cu_2O nano-spheres was prepared, which exhibited satisfactory photocatalytic degradation performance of MB under simulated sunlight. This provided a facile way for the preparation of economical and efficient photocatalysts for wastewater treatment.

EXPERIMENTAL

Chemicals

Sodium hydroxide (NaOH, AR), glucose ($C_6H_{12}O_6$, AR), sodium dodecyl sulfate (SDS) ($C_{12}H_{25}SO_4Na$, AR), zinc acetate dihydrate ($Zn(CH_3COO)_2{\cdot}2H_2O$, AR), copper acetate monohydrate ($Cu(CH_3COO)_2{\cdot}H_2O$, AR), methylene blue ($C_{16}H_{18}N_3ClS$, AR) and absolute ethanol (C_2H_5OH, AR). Deionized water was used in the whole experiment.

Preparation of ZnO/Cu_2O with SDS as a template

1.5 g SDS was added into a beaker containing the mixed solution of $Zn(CH_3COO)_2$ (0.5 mol/L, 50 mL), $Cu(CH_3COO)_2$ (0.5 mol/L, 50 mL) and glucose (1 mol/L, 25 mL). The beaker was placed in a water bath (60 °C) and kept magnetic stirring for 30 min. Later, NaOH solution (2 mol/L, 50 mL) was added into it drop by drop. The mixing process was assisted by magnetic stirring and lasted for 30 min. The sediment at the bottom of the beaker was collected by centrifugation. It was washed alternately by water and ethanol three times each, and dried under vacuum at 60 °C. The desired sample was prepared and named as S1.

Preparation of ZnO/Cu_2O, ZnO and Cu_2O

For comparison, ZnO/Cu_2O, ZnO and Cu_2O without SDS were also synthesized. The following procedure described the synthesis steps. The preparation of ZnO/Cu_2O composite without SDS mediating was similar as S1, except that SDS was not added. The obtained sample was labeled as S2. 50 mL of $Zn(CH_3COO)_2$ solution (0.5 mol/L) was placed in the water bath (60 °C). Then 25 mL of NaOH solution (2 mol/L) was added into it drop by drop with magnetic stirring for 30 min. Then, the white precipitation was centrifuged, washed, and dried in an oven (60 °C) for 24 h. The obtained sample was named as ZnO (S3). 50 mL of $Cu(CH_3COO)_2$ (0.5 mol/L) and 25 mL of glucose (1 mol/L) were mixed with a water bath (60 °C). After 10 min of magnetic stirring, 25 mL of NaOH solution (2 mol/L) was added into the mixture drop by drop with a continuous stirring. 30 min later, the brick red precipitation was centrifuged, washed and dried under vacuum. Then, it was collected and named as Cu_2O (S4).

Characterization

The crystal structure was characterized using an X-ray powder diffractometer (XRD, TD--3500). The morphology and elemental mapping of the samples were examined using scanning electron microscope (SEM, SU1510; Zeiss Sigma 360) coupled with an energy dispersive spectrometer (EDS). The X-ray photoelectron spectroscopy (XPS) was analyzed by Thermo Scientific K-Alpha spectrometer. The specific surface area was measured by automated surface area and porosimetry analyzer (Micromeritics ASAP 2460). The UV–Vis-DRS absorption spectra were performed using spectrometer (U3900).

Photocatalytic degradation of MB

Using methylene blue (MB) as a model organic pollutant and a xenon lamp as a simulated sunlight source, photocatalytic degradation experiments were carried out according to the procedure.[6] In short, 150 mg of photocatalysts were put into MB solution (150 mL, 2.0×10^{-5} mol/L) with magnetic stirring continuously for 1 h in dark environment. After that, the mixed solution was irradiated by a xenon lamp with the light intensity of 100 mW/cm^2. The distance of lamp and solution was 15 cm. The degradation solution (1 mL) was taken out every 20 min and centrifuged in the dark. The absorbance of supernatant was monitored by an UV–Vis spectrophotometer in the wavelength range of 550–750 nm. The total illumination time was 100 min. The degradation ratio R was calculated as:

$$R(\%) = 100\frac{A_0 - A_t}{A_0} \quad (1)$$

A_0 and A_t represent the initial and time-dependent absorbance of MB at 664 nm, respectively.

RESULTS AND DISCUSSION

Material characterizations

The XRD patterns of the four samples are shown in Fig. 1. For comparison, the standard powder diffraction files of Cu_2O with cubic crystal structure (PDF#65-3288) and ZnO with hexagonal wurtzite structure (PDF#36-1451) were also presented. Fig. 1a is the XRD pattern of S4 sample. The diffraction peaks (marked with *) matched well with those of cubic Cu_2O (PDF#65-3288), indicating that sample S4 was Cu_2O with cubic crystal structure. The XRD pattern of sample S3 is displayed in Fig. 1b. Comparison with the standard powder diffraction file for hexagonal wurtzite ZnO (PDF#36-1451) indicated that the diffraction peaks (marked with ♦) corresponded to hexagonal wurtzite ZnO in sample S3.

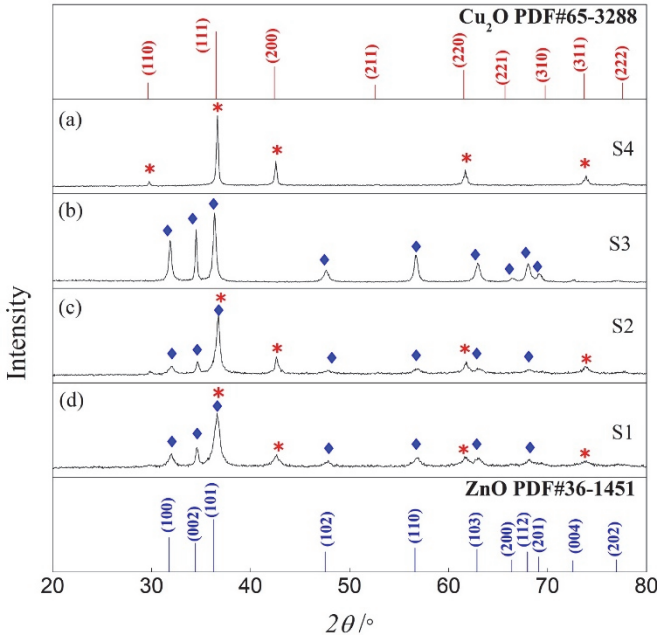

Fig. 1. The XRD patterns of samples: S4 (a), S3 (b), S2 (c) and S1 (d).

Fig. 1c and d are the XRD patterns of S1 and S2 samples. The characteristic diffraction peaks (marked with ♦) corresponded to the (100), (002), (101), (102), (110), (103) and (112) crystal planes of ZnO with wurtzite structure, respectively. At the same time, the peaks at 2θ 36.6, 42.5, 61.6 and 73.9° (marked with *) matched with (111), (200), (220) and (311) crystal planes of cubic Cu_2O. These evidences confirmed that the samples of S1 and S2 were the composite of ZnO/ /Cu_2O. Moreover, the crystal structure of the component was unchanged under the

mediation of SDS. In addition, there were no other diffraction peaks in Fig. 1a–d, and the sharp peaks declared the synthesized samples were with good crystallinity.

Fig. 2 is the XPS spectra of the ZnO/Cu_2O (S1) composite. The survey spectrum (Fig. 2a) indicated that Zn, O and Cu elements existed in the composite. In the line spectrum of Zn 2p (Fig. 2b), two dominant peaks at 1021.8 and 1044.7 eV, were attributed to the Zn $2p_{3/2}$ and Zn $2p_{1/2}$ of Zn^{2+}, respectively.[24] In the XPS data of O 1s (Fig. 2c), the first peak located at 530.4 eV, corresponding to the lattice oxygen in ZnO and Cu_2O,[13,25] the second peak appeared at the binding energy of 531.7 eV might be attributed to hydration.[25,26] As shown in Fig. 2d, two binding energy peaks of Cu 2p were observed at 932.4 and 952.3 eV, and ascribed to those of Cu $2p_{3/2}$ and Cu $2p_{1/2}$ from Cu^+ in Cu_2O, respectively.[13,27,28] In addition, two satellite peaks located at 942.3 and 962.1 eV of Cu(II) were identified, indicating the existence of CuO.[29] However, it is worth mentioning that no characteristic peaks of CuO were detected in the XRD pattern of sample S1, demonstrating that not much Cu_2O was oxidized to CuO on the surface of the composite. It might be due to the surface sensitivity of the XPS characterization technique. In summary, the characterization of XPS demonstrated the successful synthesis of ZnO/Cu_2O (S1) composite.

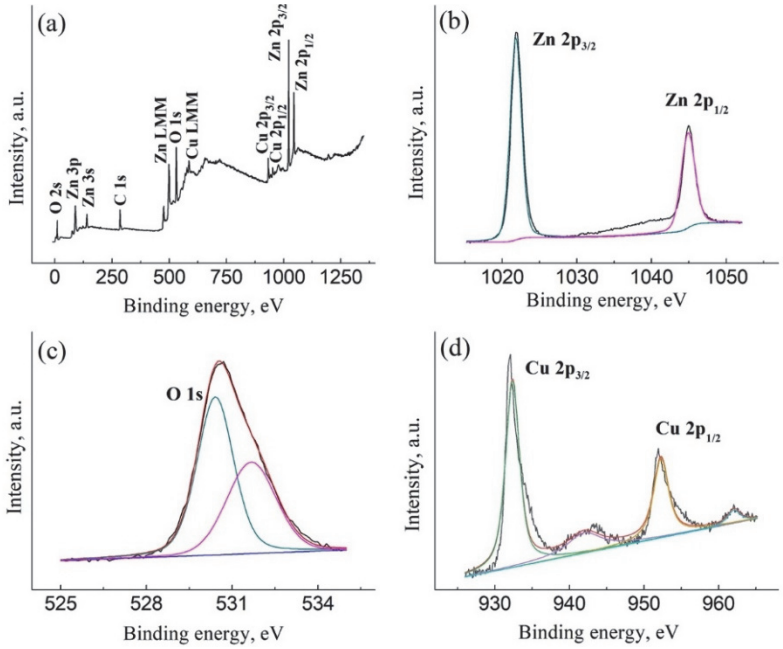

Fig. 2. The XPS spectra of ZnO/Cu_2O (S1): survey spectrum (a), Zn 2p (b), O 1s (c), Cu 2p (d).

Fig. 3 revealed the SEM images of ZnO, Cu_2O, ZnO/Cu_2O(S2) and ZnO/ /Cu_2O (S1), together with the EDS spectra and elemental mapping images of

ZnO/Cu_2O (S1). It can be observed that the morphologies of ZnO particles were irregular, which sizes were in the range of 0.2–1 μm (Fig.3a). Cu_2O particles, ranging from 0.5 to 2.5 μm, exhibited polyhedral or spherical shapes with smooth surfaces (Fig.3b). For ZnO/Cu_2O(S2) composite (Fig.3c), it could be seen that ZnO particles adhered to the surface of Cu_2O, in which, the morphology and size of Cu_2O particles showed little change compared to the pure Cu_2O particles (Fig. 3b). Fig. 3d–f displayed that the composite of ZnO/Cu_2O (S1) was consisted of nano-spherical Cu_2O aggregates and flower-like ZnO particles. The aggregates of Cu_2O were formed by the self-assembly of Cu_2O particles with a size of 50–100 nm. The size of nano-spherical Cu_2O aggregates was obviously smaller than that of Cu_2O shown in Fig. 3b. Moreover, the size and morphologies of ZnO particles underwent significant changes comparing with pure ZnO (Fig.3a). Through Fig. 3d–f, it could be found that the particle size of ZnO with flower morphology was about 200 nm.

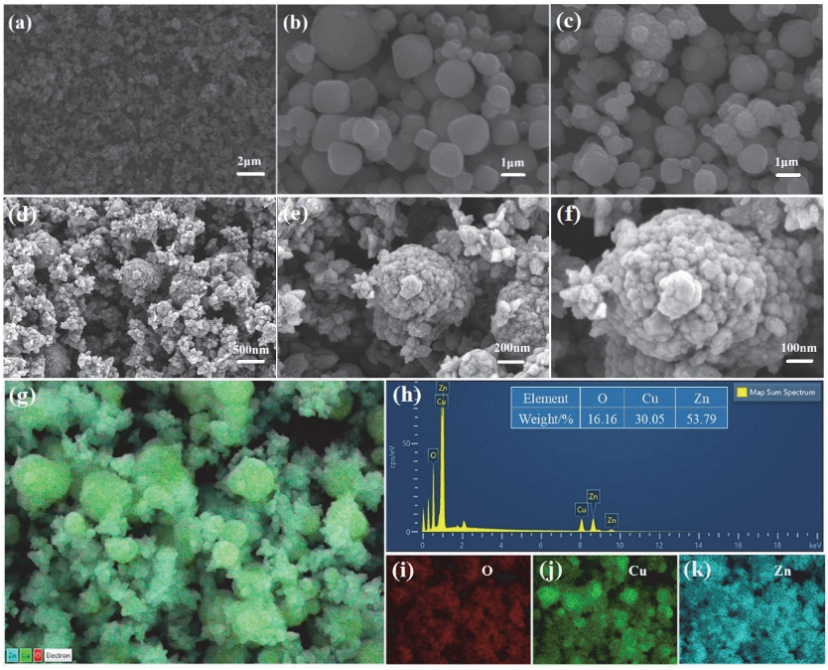

Fig. 3. SEM images of ZnO (a), Cu_2O (b), ZnO/Cu_2O (S2) (c), ZnO/Cu_2O (S1) (d–f); EDS spectra (g–h) and elemental mapping images (i–k) of ZnO/Cu_2O (S1).

From the EDS spectra (Fig. 3g–h), the elements of Cu, Zn, and O were detected, and no other additional elements were found, which confirmed the composition of ZnO/Cu_2O (S1) composite. Additionally, it could be seen that Cu, Zn and

O elements (Fig. 3i–k) were uniformly distributed which further verified the successful synthesis of ZnO/Cu_2O (S1) composite with high purity.

The change of particle size and morphology of ZnO/Cu_2O (S1) composite was closely related to the regulation of SDS. As a surfactant, the molecules of SDS could form self-assembly aggregates with unique spatial structure when its concentration reached a specific value. These aggregates with obvious structural interfaces could act as soft template to induce the formation of the materials with specific structures, morphologies, and properties. The hydrophilic group of SDS were negatively charged and attracted Zn^{2+} and Cu^{2+} to gather around them by electrostatic attraction.[30,31] Then, the distributions of metal cations in the solution were changed, and the crystal nucleation sites were regulated. Due to the template effect, the crystal underwent a controlled growth. The structure and morphology of the obtained sample were shaped and the desired property was endowed.

Fig. 4a displayed the N_2 adsorption–desorption isotherm of ZnO/Cu_2O (S1) composite. The curve accorded with typical type IV isotherm and displayed an obvious hysteresis loop of type H3, indicating the presence of a large number of mesopores.[32] The specific surface area measured by BET method was 17.15 m^2/g. The pore size distribution calculated by BJH method was shown in Fig. 4b. The average pore diameter was 11.98 nm. The mesoporous channels can facilitate the diffusion of reactant molecules into the interior of the material, which endow the composite with the advantage of adsorption for pollutants and then enhance its photocatalytic performance.

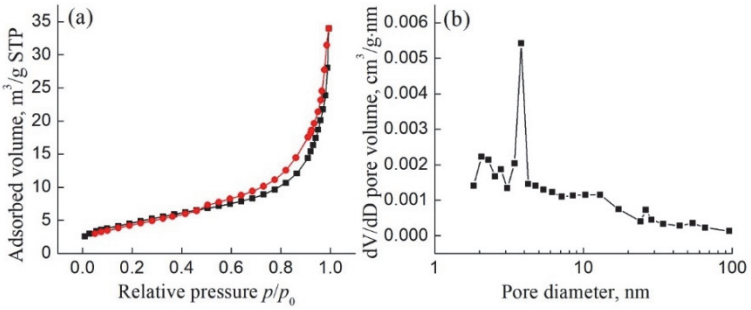

Fig. 4. N_2 adsorption–desorption isotherm (a) and pore size distribution (b) of ZnO/Cu_2O (S1).

Fig. 5a showed the UV–Vis-DRS absorption spectra of ZnO, Cu_2O and ZnO/Cu_2O (S1). It can be observed that ZnO/Cu_2O (S1) exhibited strong adsorption in the region from 400 to 800 nm. Comparing with ZnO, the photo-response range expanded to the visible region. According to the Kubelka–Munk transformation and Tauc formulas,[33–35] the band gap energies (E_g) of ZnO, Cu_2O and ZnO/Cu_2O(S1) were calculated and displayed in Fig. 5b. The E_g value of Cu_2O and ZnO were approximately 1.99 and 3.25 eV, respectively, which were basically

consistent with previous reports.[27,32] Two E_g values of 2.06 and 3.22 eV existed for ZnO/Cu_2O (S1) composite. The E_g value of Cu_2O in the composite was 2.06 eV, which was larger than that of pure Cu_2O (1.99 eV), it lowered the recombination rate of e^-/h^+.[33] At the same time, the E_g value of ZnO in the composite was 3.22 eV, instead of 3.25 eV of pure ZnO, the narrowing of the band gap induced the red-shift of the absorption edge.[32] The changes of band gap energy were attributed to successful incorporation of ZnO and Cu_2O in the composite, which resulted in the enhancement of photocatalytic properties.

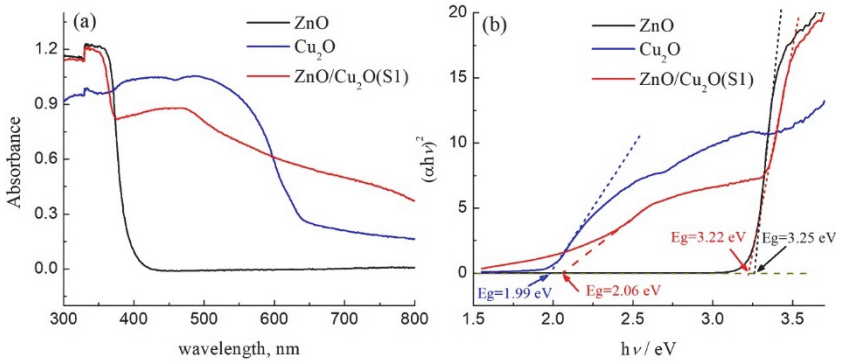

Fig. 5. The UV–Vis-DRS absorption spectra (a) and Tauc plot (b) to calculate the band gap energy.

Photocatalytic activity and stability analysis

Fig. 6 presented the UV–Vis spectra of MB solution which underwent photocatalytic degradation by the photocatalysts of ZnO/Cu_2O (S1), ZnO/Cu_2O (S2), ZnO and Cu_2O after different times, respectively. The absorbance values of the solution decreased at the wavelength of 664 nm (the maximum absorption peak of MB[36–38]) with the elapse of illumination time, which suggested that MB was degraded gradually.

To present the photocatalytic performance more intuitively, the degradation ratio R was calculated and shown in Fig. 7a. The results showed the relationship of R: R(ZnO/Cu_2O (S1)) > R(ZnO/Cu_2O (S2)) > R(ZnO) > R(Cu_2O). Taking 100 min as an example, the degradation ratio R of MB by ZnO/Cu_2O (S1) reached 98.1 %, while R of MB by ZnO/Cu_2O (S2), ZnO and Cu_2O were only 80.8, 70.0 and 36.0 %, respectively. Therefore, the photocatalytic efficiency of ZnO/Cu_2O (S1) was the best among the four photocatalysts.

In order to evaluate the degradation kinetics of MB by the synthesized photocatalysts, the curves of ln (A_0/A_t)–t were plotted and shown in Fig. 7b. There was a good linear relationship between ln (A_0/A_t) and the time of t, which accorded with the kinetic characteristics of pseudo first-order. The kinetic parameters of the fitting curves were summarized in Table I. From the data, it was demonstrated that

the *k* value of the degradation reaction using ZnO/Cu_2O (S1) as the photocatalyst was about 2.4, 3.2 and 8.3 times that of ZnO/Cu_2O (S2), ZnO and Cu_2O, respectively. Therefore, the ZnO/Cu_2O (S1) nanocomposite presented an ideal degradation efficiency under the same conditions, demonstrating promising potentiality for photocatalytic applications.

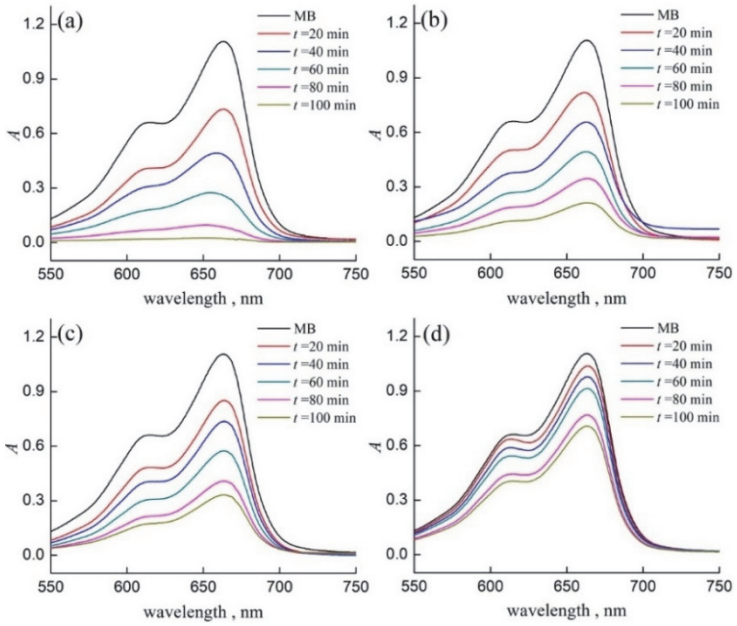

Fig. 6. The UV–Vis spectra of MB solution degraded by ZnO/Cu_2O (S1) (a), ZnO/Cu_2O (S2) (b), ZnO (c) and Cu_2O (d).

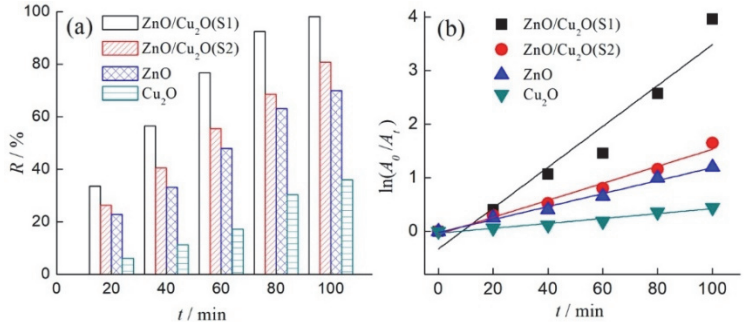

Fig. 7. *R*–*t* histogram (a) and the kinetic curves (b) of photocatalytic degradation of MB.

The enhanced photocatalytic performance of ZnO/Cu_2O (S1) may be attributed to the mediation of SDS and the synergistic effect of ZnO and Cu_2O components in the composite. The results of SEM suggested that the morphology of both

TABLE I. Parameters of kinetic curves

Sample	Rate constant k / min^{-1}	R^2
ZnO/Cu_2O (S1)	0.03814	0.92797
ZnO/Cu_2O (S2)	0.01585	0.97676
ZnO	0.01210	0.98707
Cu_2O	0.00457	0.94903

ZnO and Cu_2O changed in shape as in size and became smaller. The BET characterization revealed that the average pore diameter was 11.98 nm. The changes of morphology and particle size, as well as the abundant presence of meso--pores in the composite were closely related to the template effect of SDS. It might make it easier to contact with the molecules of MB and offer more surface adsorption sites, and then facilitate the further occurrence of oxidative decomposition. In addition, another important factor could not be ignored. The energy level matching of Cu_2O and ZnO in the composite promoted the separation of photo--generated charge carriers electron(e^-)/hole(h^+) pairs,[17,33,38] and then improved its catalytic ability. The possible mechanism was described,[17,23,33,39] and the corresponding mechanism diagram was shown in Fig. 8. The e^- in the valence band (VB) of Cu_2O and ZnO transferred to the conduction band (CB) under the irradiation of light, and the h^+ was left in the VB. Because the CB position of Cu_2O is higher than that of ZnO, the photo-generated e^- in the CB of Cu_2O transferred to the surface of ZnO; at the same time, the h^+ in the VB of ZnO transferred to the surface of Cu_2O, thus effectively avoiding the recombination of e^- and h^+ on the catalyst surface. h^+ and e^- with strong oxidation and reduction ability react with H_2O and O_2, respectively, to form reactive hydroxide radicals ($^\bullet$OH) and super oxide radical anion ($O_2^{-\bullet}$), in which, O_2^- can further turn into $^\bullet$OH.[13,24,27,33,39] The $^\bullet$OH has perfect oxidation ability to degrade MB molecules into CO_2 and H_2O.

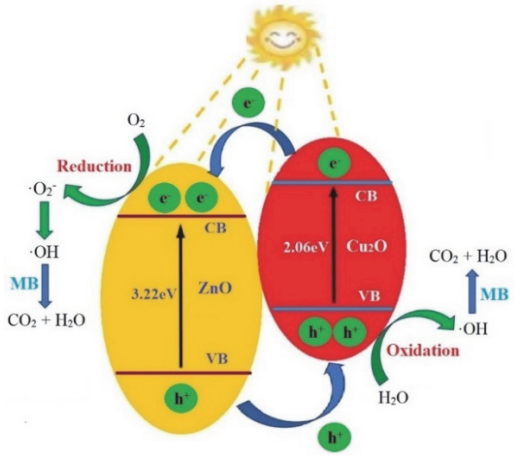

Fig. 8. Possible mechanism of photocatalytic degradation of MB by ZnO/Cu_2O (S1).

The stability of ZnO/Cu_2O (S1) was tested by recycling the sample in the photocatalytic degradation experiment of MB. As shown in Fig. 9, after 5 times cycling of photocatalytic degradation, *R* only decreased from 98.1 to 92.1 %, indicating that ZnO/Cu_2O (S1) has good photocatalytic stability.

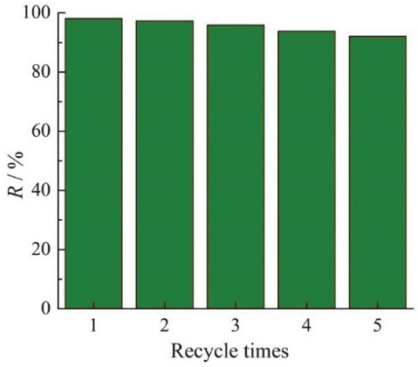

Fig. 9 Recycling experiments of ZnO/Cu_2O (S1) composite.

CONCLUSION

In summary, ZnO/Cu_2O (S1) nanocomposite was prepared by one-pot method. During the process of preparation, SDS served an effective template. The characterizations confirmed that flower-like ZnO nanoparticles (hexagonal wurtzite) grew on the Cu_2O nanospheres (cubic crystal) self-assembled from single Cu_2O particles, and Cu, Zn and O elements were uniformly distributed in the composite. Abundant mesopores were in ZnO/Cu_2O (S1) and the photo-response range expanded to the visible region. The photocatalytic degradation tests indicated that the degradation ratio *R* of MB by ZnO/Cu_2O (S1) reached 98.1 % after 100 min illumination, significantly larger than that of ZnO (70.0 %), Cu_2O (36.0 %) and ZnO/Cu_2O (S2) (80.8 %), and *R* did not obviously decrease after 5 recycling, demonstrating high photocatalytic degradation ability and good photocatalytic stability. The enhanced photocatalytic property maybe attributed to the inducement of SDS and the synergy effect of ZnO and Cu_2O. The advantages of smaller particle sizes, larger amount of meso-pores, more surface adsorption sites, stronger absorption in the visible light range and easier separation of photo-generated carriers (e^-/h^+) will help to improve its catalytic degradation ability. The ZnO/Cu_2O nanocomposite assisted by SDS shows a good application prospect for sewage treatment.

Acknowledgements. This work is supported by Anhui Province Young Teacher Training Action: Discipline (Major) Leader Cultivation Project (DTR2023037), Anhui Provincial Teaching Innovation Team (2023cxtd073), Natural Science Foundation of the Department of Education of Anhui Province (2025AHGXZK31414, 2022AH052139), Anhui Engineering Laboratory for Medicinal and Food Homologous Natural Resources Exploration (2025KYPT04) and National/Provincial College Students Innovation Training (202514098035/S202514098176).

The authors extend their gratitude to Mr. Yangjin Zhang (from Scientific Compass www.shiyanjia.com) for providing invaluable assistance with the SEM, XPS and BET analysis.

ИЗВОД

ПОБОЉШАНА ФОТОКАТАЛИТИЧКА АКТИВНОСТ ZnO/Cu_2O КОМПОЗИТА ЗА РАЗГРАДЊУ МЕТИЛЕН ПЛАВОГ УСЛЕД СИНЕРГИСТИЧКОГ ЕФЕКТА

HONGYING LI,[1,2] LUWEN MA,[1] ZHENYANG WU[1] и CHENGLI YAO[1]

[1]*School of Chemistry and Pharmaceutical Engineering, Hefei Normal University, Hefei, Anhui, China u* [2]*Hefei National Research Center for Physical Sciences at the Microscale, University of Science and Technology of China, Hefei, Anhui, China*

У циљу испитивања каталитичке ефикасности разградње ZnO/Cu_2O композита, синтетисан је нанокомпозит применом „*one-pot*“ методе и SDS једињења. Кристална структура, микроскопска морфологија, хемијски састав, специфична површина, расподела величине пора и оптичка апсорпциона својства композита су детаљно окарактерисани. Испитивана је фотокаталитичка активност композита према разградњи метилен плавог (MB) у присуству зрачења ксенонске лампе. Резултати карактеризације су показали да се синтетисани композит састоји од ZnO (хексагонална вурцитна структура) и Cu_2O (кубна кристална структура). Захваљујући посредовању SDS једињења, добијене честице су нанометарских димензија, са равномерном расподелом елемената Cu, Zn и O, као и са великим бројем мезопора. Опсег фотокаталитичке активности композита је проширен на видљиви део спектра услед комбинације ZnO и Cu_2O. Степен разградње MB једињења у присуству ZnO/Cu_2O композита износио је приближно 92 % за 100 min након пет поновљених циклуса, што указује на значајан потенцијал за фотокаталитичке примене. Побољшана фотокаталитичка активност може бити повезана са посредовањем SDS једињења током процеса припреме и синергистичким ефектом између ZnO и Cu_2O.

(Примљено 15. новембра, ревидирано 27. новембра 2025, прихваћено 29. јануара 2026)

REFERENCES

1. C. Ashina, N. Pugazhenthiran, R. V. Mangalaraja, P. Sathishkumar, *Renew. Sustain. Energy Rev.* **214** (2025) 115490 (https://doi.org/10.1016/j.rser.2025.115490)
2. C. Vanlalhmingmawia, H. Moradi, Y. J. Kim, D. S. Kim, J. K. Yang, *Chem. Eng. J.* **509** (2025) 161335 (https://doi.org/10.1016/j.cej.2025.161335)
3. C. Q. Shen, X. Y. Li, B. Xue, D. J. Feng, Y. P. Liu, F. Yang, M. Y. Zhang, S. J. Li, *Appl. Surf. Sci*. **679** (2025) 161303 (https://doi.org/10.1016/j.apsusc.2024.161303)
4. H. Tu, B. H. Tian, Z. C. Zhao, R. J. Guo, Y. Wang, S. H. Chen, J. Wu, *Water Res.* **28** (2025) 100315 (https://doi.org/10.1016/j.wroa.2025.100315)
5. M. Y. Areeshi, *Luminescence* **38** (2023) 1111 (https://doi.org/10.1002/bio.4432)
6. H. Y. Li, X. X. Liu, J. Q. Huang, W. J. Zhu, A. M. Ding, C. L. Yao, J. M. Zhu, *Crystallogr. Rep*. **67** (2022) 1231 (https://doi.org/10.1134/S1063774522070082)
7. H. Zhao, Z. H. Zhan, W. C. Li, N. Zhang, X. Ma, P. K. Yan, Y. J. Gao, H. L. Cong, Q. Zhang, *J. Alloy. Compd*. **1002** (2024) 175197 (https://doi.org/10.1016/j.jallcom.2024.175197)
8. L. Nadjia, A. Chakib, K. Mohamed, T. Mohamed, E. Abdelkader, *Appl. Phys., A* **131** (2025) 154 (https://doi.org/10.1007/s00339-024-08223-x)
9. D. Xu, H. L. Ma, *J. Clean. Prod*. **313** (2021) 127758 (https://doi.org/10.1016/j.jclepro.2021.127758)

10. A. L. Yang, L. L. Wang, *Curr. Nanosci*. **18** (2022) 94 (https://doi.org/10.2174/1573413717666210129115305)
11. R. Rathinabala, R. Thamizselvi, D. Padmanabhan, S. F. Alshahateet, I. Fatimah, A. K. Sibhatu, G. K. Weldegebrieal, S. I. A. Razak, S. Sagadevan, *Inorg. Chem. Commun*. **143** (2022) 109783 (https://doi.org/10.1016/j.inoche.2022.109783)
12. P. Attri, S. Garg, J. K. Ratan, A. S. Giri, *Korean J. Chem. Eng*. **41** (2024) 3191 (https://doi.org/10.1007/s11814-024-00283-2)
13. J. K. Nie, X. J. Yu, Z. B. Liu, J. Zhang, Y. Ma, Y. Y. Chen, Q. G. Ji, N. N. Zhao, Z. Chang, *J. Clean. Prod*. **363** (2022) 132593 (https://doi.org/10.1016/j.jclepro.2022.132593)
14. T. Bekele, G. Mebratie, A. Girma, G. Alamnie, *Colloids Surfaces, A* **685** (2024) 133271 (https://doi.org/10.1016/j.colsurfa.2023.133271)
15. X. J. Yu, Z. Y. Li, Z. B. Liu, K. Wang, *Appl. Surf. Sci*. **665** (2024) 160285 (https://doi.org/10.1016/j.apsusc.2024.160285)
16. P. Liang, W. Y. Yang, H. Y. Peng, S. H. Zhao, *Molecules* **29** (2024) 5584 (https://doi.org/10.3390/molecules29235584)
17. X. S. Wang, Y. D. Zhang, Q. C. Wang, B. Dong, Y. J. Wang, W. Feng, *Sci. Eng. Compos. Mater*. **26** (2019) 104 (https://doi.org/10.1515/secm-2018-0170)
18. X. S. Jiang, Q. B. Lin, M. Zhang, G. He, Z. Q. Sun, *Nanoscale Res. Lett*. **10** (2015) 30 (https://doi.org/10.1186/s11671-015-0755-0)
19. C. L. Yao, C. Chen, Y. J. Yuan, W. J. Zhu, W. Q. Tai, C. Ding, H. Y. Li, *Cryst. Res. Technol.* **59** (2024) 2300233 (https://doi.org/10.1002/crat.202300233)
20. M. Amano, K. Hashimoto, H. Shibata, *J. Oleo. Sci*. **71** (2022) 927 (https://doi.org/10.5650/jos.ess22061)
21. J. Cui, L. Ye, X. X. Chen, J. N. Li, B. Yang, M. Yang, Q. Yang, D. Q. Yun, S. D. Sun, *Appl. Surf. Sci*. **638** (2023) 158046 (https://doi.org/10.1016/j.apsusc.2023.158046)
22. A. Norouzi, A. Nezamzadeh-Ejhieh, *Mater. Res. Bull*. **164** (2023) 112237 (https://doi.org/10.1016/j.materresbull.2023.112237)
23. K. Chitalkar, D. Hase, S. Gurav, S. Musmade, R. Gaikar, M. Sillanpää, V. Murade, H. Aher, *J. Inorg. Organomet. Polym*. **35** (2025) 6961 (https://doi.org/10.1007/s10904-025-03705-8)
24. X. J. Yu, J. Zhang, J. Zhang, J. F. Niu, J. Zhao, Y. C. Wei, B. H. Yao, *Chem. Eng. J.* **374** (2019) 316 (https://doi.org/10.1016/j.cej.2019.05.177)
25. F. Liu, Y. L. Che, Q. W. Chai, M. F. Zhao, Y. Lv, H. Sun, Y. Q. Wang, J. Sun, C. C. Zhao, *Environ. Sci. Pollut. R.* **26** (2019) 25286 (https://doi.org/10.1007/s11356-019-05814-7)
26. Y. W. Lu, F. Yu, J. Hu, J. Liu, *Appl. Catal., A* **429** (2012) 48 (https://doi.org/10.1016/j.apcata.2012.04.005)
27. J. K. Nie, X. J. Yu, Z. B. Liu, Y. C. Wei, J. Zhang, N. N. Zhao, Z. Yu, B. H. Yao, *Appl. Surf. Sci.* **576** (2022) 151842 (https://doi.org/10.1016/j.apsusc.2021.151842)
28. J. K. Nie, X. J. Yu, Y. C. Wei, Z. B. Liu, J. Zhang, Z. Yu, Y. Ma, B. H. Yao, *Process Saf. Environ*. **170** (2023) 241 (https://doi.org/10.1016/j.psep.2022.12.002)
29. T. Nesavi, L. Balu, R. Ezhil Pavai, *Ionics* **31** (2025) 12027 (https://doi.org/10.1007/s11581-025-06697-0)
30. J. H. Cao, L. P. Ding, W. T. Hu, X. L. Chen, X. Chen, Y. Fang, *Langmuir* **30** (2014) 15364 (https://doi.org/10.1021/la5039798)

31. C. L. Yao, A. J. Xie, Y. H. Shen, W. N. Zhu, J. M. Zhu, *Cryst. Res. Technol*. **49** (2014) 982 (https://doi.org/10.1002/crat.201400300)
32. Y. F. Wang, J. Gao, X. Z. Wang, L. P. Jin, L. L. Fang, M. Zhang, G. He, Z. Q. Sun, J. *Sol-Gel Sci. Technol*. **88** (2018) 172 (https://doi.org/10.1007/s10971-018-4786-8)
33. N. Akter, T. Ahmed, I. Haque, M. K. Hossain, G. Ray, M. M. Hossain, M. S. Islam, M. A. A. Shaikh, U. S. Akhtar, *Heliyon* **10** (2024) e30802 (https://doi.org/10.1016/j.heliyon.2024.e30802)
34. Z. B. Liu, X. J. Yu, K. Wang, J. Zhang, J. F. Niu, *Sep. Purif. Technol*. **356** (2025) 129810 (https://doi.org/10.1016/j.seppur.2024.129810)
35. B. Simović, Ž. Radovanović, G. Branković, A. Dapčević, *Mat. Sci. Semicon. Proc*. **162** (2023) 107542 (https://doi.org/10.1016/j.mssp.2023.107542)
36. X. J. Yu, J. Zhang, Y. Y. Chen, Q. G. Ji, Y. C. Wei, J. F. Niu, Z. Yu, B. H. Yao, *J. Environ. Chem. Eng.* **9** (2021) 106161 (https://doi.org/10.1016/j.jece.2021.106161)
37. H. Usui, *J. Colloid Interface Sci*. **336** (2009) 667 (https://doi.org/10.1016/j.jcis.2009.04.060)
38. X. J. Yu, Q. G. Ji, Y. C. Wei, Z. B. Liu, N. N. Zhao, M. Yang, Q. Yang, *J. Electrochem. Soc.* **168** (2021) 126513 (https://doi.org/10.1149/1945-7111/ac3e79)
39. S. Y. Gao, J. J. Zhang, W. Q. Li, S. J. Jiao, Y. G. Nie, H. Y. Fan, Z. Zeng, Q. J. Yu, J. Z. Wang, X. T. Zhang, *Chem. Phys. Lett*. **692** (2018) 14 (https://doi.org/10.1016/j.cplett.2017.11.062).

Journal of the Serbian Chemical Society
JSCS-info@shd.org.rs • www.shd.org.rs/JSCS
J. Serb. Chem. Soc. *91* (3) 259–270 (2026)
JSCS–5490
Original scientific paper
Published 26 February, 2026

Removal of nickel(II) ions during water purification with ferrous sulfate. Part 2. Structure and composition of iron(III) hydroxide precipitates

OLEG D. LINNIKOV*, IRINA V. RODINA, GALINA S. ZAKHAROVA, INNA V. BAKLANOVA, YULIA V. KUZNETSOVA, ALEXANDER P. TYUTYUNNIK and ZILARA A. FATTAKHOVA

Institute of Solid State Chemistry, Ural Branch of the Russian Academy of Sciences, Pervomayskaya St., 91, 620990, Ekaterinburg, Russia

(Received 7 April, revised 28 April, accepted 30 October 2025)

Abstract: A comparative analysis of the composition and structure of freshly precipitated iron(III) hydroxide precipitates obtained from a solution of iron(II) sulfate in the presence of sodium sulfate (400 mg L^{-1}) at pH 7 and 8, before and after the sorption of nickel ions onto them, was carried out. Using IR and Raman spectroscopy, X-ray phase and thermogravimetric analysis, it was shown that the precipitates have the general (gross) formula $Fe_2O_3 \cdot 2H_2O$ and contain small amounts of goethite (α-FeOOH) and lepidocrocite (γ-FeOOH). It has been established that the sorption of nickel ions onto these precipitates is not accompanied by chemisorption, *i.e.*, no mixed compounds between iron and nickel are formed. The point of zero charge of the precipitate particles is at pH 5.4, with a positive zeta potential below and a negative zeta potential above this pH. The introduction of nickel ions into the solution leads to the appearance of a second zero charge point at pH 10.2.

Keywords: iron(III) hydroxide; iron(II) sulfate; nickel ions; IR and Raman spectroscopy; X-ray and thermogravimetric methods of analysis; zeta potential.

INTRODUCTION

In the first part of this work, it was shown that iron(III) hydroxide, formed during the hydrolysis of the $FeSO_4$ coagulant in the presence of sodium sulfate (400 mg L^{-1}) at pH 7 and 8, has a high sorption capacity with respect to divalent nickel ions.[1] However, the structure and composition of the resulting precipitate were not studied in detail. Therefore, it remained unclear which iron(III) compound was acting as the sorbent in this case. The fact is that the precipitation of iron(III) hydroxide from solutions of divalent iron salts occurs due to the oxidation of the

* Corresponding author. E-mail: linnikov@mail.ru
https://doi.org/10.2298/JSC250407081L

latter by atmospheric oxygen present in dissolved form in the solution and, at low concentrations of iron(II) ions, can be described by a generalizing reaction equation:

$$4Fe^{2+} + O_2 + 2H_2O + 8OH^- \rightarrow 4Fe(OH)_3\downarrow$$

However, according to the literature data, the precipitate of iron(III) hydroxide formed in this case does not always correspond to the general (gross) formula $Fe(OH)_3$.[2–6] For example, previous studies of iron(III) hydroxide precipitates formed by the hydrolysis of the coagulant $FeCl_3$ in the presence of sodium sulfate (400 mg L^{-1}) at pH 7 and 8 showed the formation of two-line ferrihydrite with the general (gross) formula $Fe_2O_3 \cdot 3H_2O$.[7] At the same time, these precipitates also have a high sorption capacity with respect to nickel ions.[7]

The purpose of this part of the work is to study the physicochemical properties, composition and structure of the iron(III) hydroxide precipitate formed during the hydrolysis of the $FeSO_4$ coagulant.

EXPERIMENTAL

Iron(III) hydroxide precipitates with adsorbed nickel ions were obtained in coagulation experiments according to the technique described earlier.[1] The studies were carried out under laboratory conditions at room temperature (25±2 °C) using a model solution containing 400 mg L^{-1} of sodium sulfate. Nickel ions were introduced into the solution in the form of a $NiSO_4$ solution with a concentration of 10 mg L^{-1}. Iron(III) hydroxide precipitates were obtained at pH 7 and 8 by adding a 10 g L^{-1} NaOH solution to the model solution. The mixture was continuously stirred on a magnetic stirrer to maintain the resulting iron(III) hydroxide precipitate in suspension. After 30 min, the stirrer was turned off and the formed precipitate of iron(III) hydroxide was separated from the solution by filtration through blue ribbon filter paper (Russia). The next step was the washing of the iron(III) hydroxide precipitate several times on the filter with distilled water, followed by drying at room temperature.

Iron(III) hydroxide precipitates without nickel ions adsorbed on them were obtained in a similar manner without the introduction of nickel ions into the model solution.

Analysis and characterization

The morphology of the precipitates was studied using a scanning electron microscope (SEM) JSM-6309LA from JEOL (Japan).

The zeta potential of iron(III) hydroxide precipitate particles was determined using electrophoretic light scattering with a Zetasizer Nano ZS device (Malvern Panalytical Ltd.) during the precipitation reaction by taking aliquots at different pH values. To prepare the test solution, the required amount of a $FeSO_4$ solution (13.57 g L^{-1}) was introduced into a given volume of the model solution with continuous stirring on a magnetic stirrer. After that, the solution was slowly alkalized with a NaOH solution (10 g L^{-1}). After each alkalinization and establishment of equilibrium in the solution, an aliquot was taken and used for the zeta potential measurements. The initial concentration of iron(II) ions in the solution was 12.5 mg L^{-1}.

Another similar experiment was carried out in the presence of nickel ions in the solution, which were introduced into the model solution before adding the $FeSO_4$ solution. The concentration of nickel ions in the solution before alkalization was 10 mg L^{-1}.

The IR absorption spectrum of iron (III) hydroxide precipitates in the wavenumber range of 4000–400 cm^{-1} was recorded using a Vertex 80 infrared-Fourier spectrometer (Brooker),

using an attenuated total internal reflection (ATR) MVP-Pro attachment (Harrick, prism material diamond).

Raman spectra were recorded in the wavenumber range of 4000–50 cm^{-1} at room temperature using an InVia Reflex RENISHAW dispersive Raman spectrometer (λ = 532 nm wavelength, P, 1–5 mW laser power).

Thermogravimetric analysis of iron(III) hydroxide precipitates was performed using a STA 449 F3 Jupiter thermal analyzer (Netzsch), combined with a QMS 403 quadrupole mass spectrometer, in an air atmosphere at a heating rate of 10 °C min^{-1}.

X-ray phase analysis of the precipitates was carried out using a STOE STADI-P X-ray powder diffractometer.

RESULTS AND DISCUSSION

SEM images of the iron(III) hydroxide precipitates formed in the model solution are shown in Fig. 1. All iron(III) hydroxide precipitates obtained in this study consisted of very small particles that aggregated into larger structures. Externally, they appear as loose, dark-brown formations. After filtration, washing with distilled water and air drying at room temperature, the precipitates compacted, became more solid, and they significantly reduced in volume.

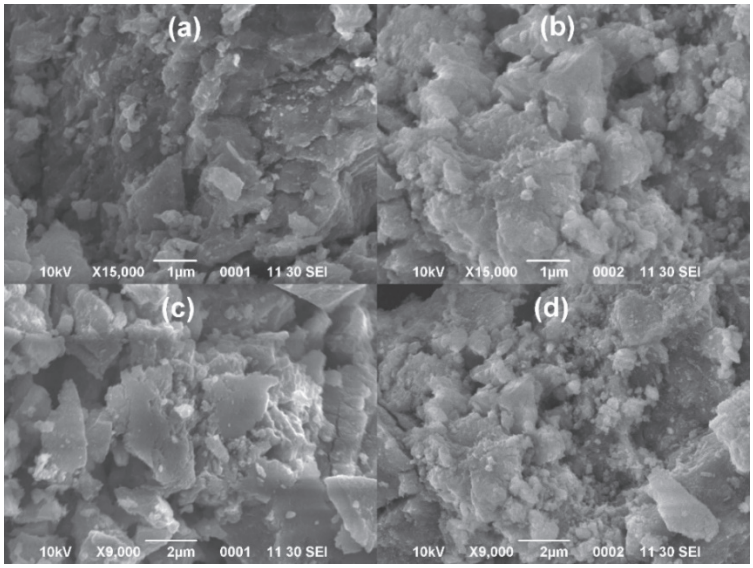

Fig. 1. SEM image of the iron(III) hydroxide precipitate obtained from the model solution: a and b – precipitation at pH 7 and 8, respectively; c and d – precipitation in the presence of nickel ions in solution at pH 7 and 8, respectively.

The diffraction patterns of iron(III) hydroxide precipitates are shown in Fig. 2 and indicate a similar structure of the precipitates. The blurred appearance of the peaks in the diffraction patterns indicates the nanometer size of the precipitate particles and their weak crystallinity.

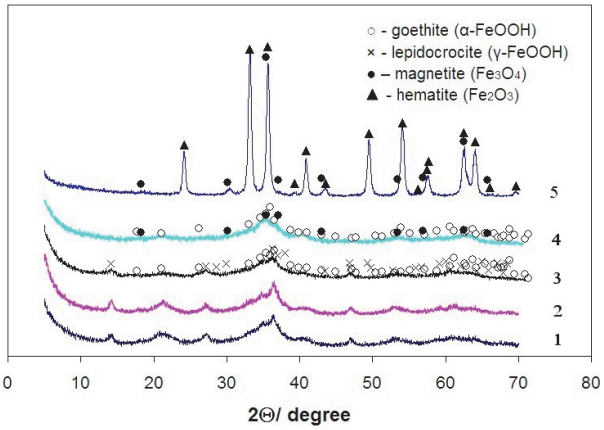

Fig. 2. X-ray powder diffraction patterns of iron(III) hydroxide precipitates after drying in air at room temperature (25±2 °C): 1 and 2 – precipitation at pH 7 and 8, respectively; 3 and 4 – precipitation in the presence of nickel ions in solution at pH 7 and 8, respectively; 5 – precipitate after thermal analysis obtained at pH 7 in the presence of nickel ions in solution.

XRD patterns analysis showed that when iron(III) hydroxide is precipitated at pH 7 and 8 without nickel ions in the model solution, the resulting precipitates consist of a mixture of two phases: goethite (α-FeOOH) and lepidocrocite (γ-FeOOH) (Fig. 2, curves 1 and 2). The ratio of these phases depends on the pH of the solution. Thus, at pH 7, goethite comprises approximately 62 wt. % of the precipitate, while lepidocrocite accounts for 38 wt. %. At pH 8, the proportion of goethite increases to 81 wt. %, with lepidocrocite decreasing to 19 wt. %. In the presence of nickel ions during precipitation, the phase composition of the resulting precipitates changes insignificantly (Fig. 2, curves 3 and 4). At pH 7, the precipitate still contains approximately 62 wt. % goethite and 38 wt. % lepidocrocite. However, at pH 8, lepidocrocite is replaced by magnetite (Fe_3O_4), which appears in an amount of about 38 wt. %, while the goethite content remains unchanged at approximately 62 wt. %. This formation of magnetite may be facilitated by the higher pH of the solution. None of the diffraction patterns indicated the presence of a new phase containing nickel ions. Subsequent thermal analysis (see below) resulted in the decomposition of the precipitates, and the samples consisted of hematite and magnetite. An example of such a diffraction pattern is shown in Fig. 2 (curve 5).

Raman spectra of the iron(III) hydroxide precipitates obtained at pH 7 and 8 and at different powers of the irradiating laser are shown in Fig. 3. It can be seen from Fig. 3 that with increasing laser power (P), a change in the shape of the obtained Raman spectrum is observed. If at P = 1 mW the spectrum is a curve in which not a single line is fixed (Fig. 3, curves 1), then at a laser power of 5 mW (Fig. 3, curves 2) the shape of the spectrum changes, and lines corresponding to hematite (α-Fe_2O_3) appear in it: 211–215 (A_{1g}), 272–283, 379–389, 457–476,

568–588 and 616–689 cm^{-1} (E_g), ~1300 cm^{-1} (second harmonic). This indicates the destruction of the precipitate at a given power of the irradiating laser. The observed rise in the background is most likely associated with fluctuations in CO_3^{2-} and their overtones. It should be noted that thermogravimetric analysis (see below) also showed the presence of small amounts of carbonates in the precipitates. The observed decomposition of iron(III) hydroxide precipitate with an increase in the power of the irradiating laser is in good agreement with the data,[7,8] where a similar destruction of ferrihydrite was recorded during the recording Raman spectra, as well as the transformation of magnetite into maghemite and hematite.[9]

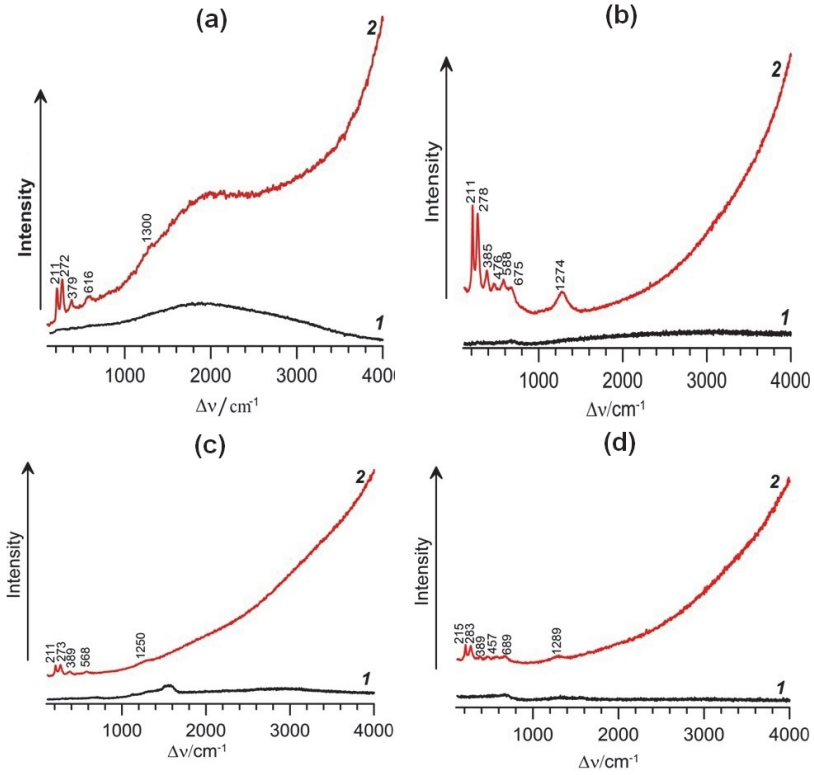

Fig. 3. Raman spectra of iron(III) hydroxide precipitate obtained at pH 7 and 8: a and c – precipitation at pH 7 and 8, respectively; b and d – precipitation in the presence of nickel ions in solution at pH 7 and 8, respectively; 1 – survey at P = 1 mW; 2 – survey at P = 5 mW (survey duration in all cases is 10 s).

Thus, recording the Raman spectrum at low laser power (1 mW) did not record lines characteristic of OH groups, which should be part of the precipitate if it corresponds to the general (gross) formula FeOOH (or $Fe(OH)_3$). In addition, the

spectrum does not contain lines characteristic of goethite (α-FeOOH) and lepidocrocite (γ-FeOOH),[8–10] which indicates the absence of these phases in the precipitate. This result does not agree with the X-ray phase analysis data (see above).

The IR spectra of the obtained iron(III) hydroxide precipitates are shown in Fig. 4, from which it can be seen that they are close to each other. On all IR spectra of iron(III) hydroxide precipitates, an intense wide band is present in the frequency range of stretching vibrations of water molecules $\nu(H_2O)$ at 3139–3209 cm^{-1}. At 1628–1635 cm^{-1}, the bending mode of water molecules $\delta(H_2O)$ is recorded. The bands at 1100–1122 cm^{-1} can be attributed to the stretching asymmetric vibrations of $\nu_3(SO_4^{2-})$. The presence of these bands indicates the presence of traces of unwashed sodium sulfate in the precipitates. The asymmetric and symmetric stretching vibrations $\nu(CO_3^{2-})$ appear as broad bands at 1493–1500, 1333–1359 and 1018––1093 cm^{-1}, and the deformation vibrations $\delta(CO_3^{2-})$ appear at 883–887 cm^{-1}. These bands are probably caused by the presence of carbonates in the formed precipitates, the presence of which was mentioned above. The stretching asymmetric and symmetric vibrations of the C–H bond are manifested at 2887–2890 cm^{-1} and 2817–2925 cm^{-1}, respectively. The appearance of these bands in the IR spectra of the precipitates can be attributed, as the analysis indicates, to the presence of small organic impurities in the initial NaOH reagent used to prepare a solution of sodium hydroxide (10 g L^{-1}) for alkalizing the model solution during experiments. In addition, a small impurity of iron(III) hydroxocarbonate ($FeOHCO_3$) may also be present in the precipitate. This compound could have formed during the precipitation of iron(III) hydroxide with NaOH solution, as the latter typically contains sodium carbonate (Na_2CO_3) as an impurity. Moreover, the absorption of carbon dioxide from the air by the solution during the experiment may have contributed to its formation.

For all samples, the bands from bending vibrations of C–H bonds are superimposed on modes with frequencies 883–885 cm^{-1} belonging to the CO_3^{2-}. Bands 786–787 cm^{-1} and 618–651 cm^{-1} can be attributed to bending vibrations of C–H and C–C bonds. Frequencies below 600 cm^{-1} can be attributed to Fe–O vibrations. The region below 1100 cm^{-1} contains mainly bands belonging to CO_3^{2-} and organic impurities. The observed differences in the IR spectra of the samples in the region below 1100 cm^{-1} are apparently explained by the different adsorption values of these impurities on the formed iron(III) hydroxide precipitate. None of the IR spectra, as well as earlier Raman spectra, showed intense absorption bands characteristic of OH groups that are not part of water and belong to the iron(III) hydroxide precipitate, if it corresponded to the general (gross) formula FeOOH or $Fe(OH)_3$.

Fig. 5 shows the results of thermogravimetric analysis of the formed iron(III) hydroxide precipitated at pH 7 and 8 in the absence (Fig. 5a and c) and presence (Fig. 5b and d) of nickel ions (10 mg L^{-1}). As can be seen, thermograms of all

precipitates demonstrate similar trends. Already with slight heating, water (MS curves m/z = 18 a.u.m.) and carbon dioxide (MS curves m/z = 44 a.u.m.) begin to be removed from precipitates. Moreover, much more carbon dioxide is released from the precipitates obtained in the presence of nickel ions in solution (Fig. 5b and d). This may be due to the higher content of organic impurities in these samples.

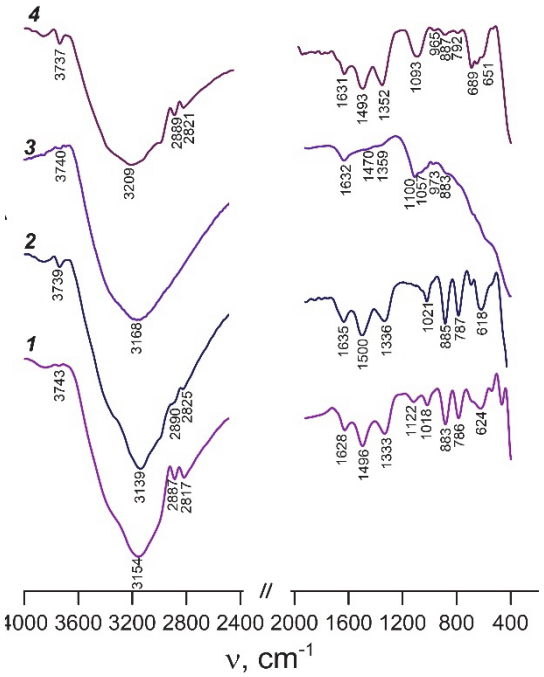

Fig. 4. IR spectra of iron(III) hydroxide precipitates: 1 and 2 – precipitation at pH 7 and 8, respectively; 3 and 4 – precipitation in the presence of nickel ions (10 mg L^{-1}) in solution at pH 7 and 8, respectively.

The mass loss of the precipitates occurs in a stepwise manner. Approximately 9–12 % of the mass is lost at the first stage, followed by an additional loss of about 9% in the second stage, resulting in a total mass decrease of around 18 %. It should be noted that several peaks in carbon dioxide release are observed, indicating the sequential decomposition of carbon-containing compounds into CO_2. The process is accompanied for all samples by weak exoeffects at temperatures 231–242, 281––295, 330–339 °C. The exoeffects observed at 365–423, 504 and 514 °C likely correspond to the crystallization process of hematite (α-Fe_2O_3) and magnetite (Fe_3O_4), as confirmed by X-ray phase analysis. Thus, after thermogravimetric analysis, the precipitate corresponding to Fig. 5a consisted of hematite, whereas the precipitate corresponding to Fig. 5b contained approximately 86.3 wt. % hematite and 13.7 wt. % magnetite (Fig. 2, curve 5). The formation and stability of the mag-

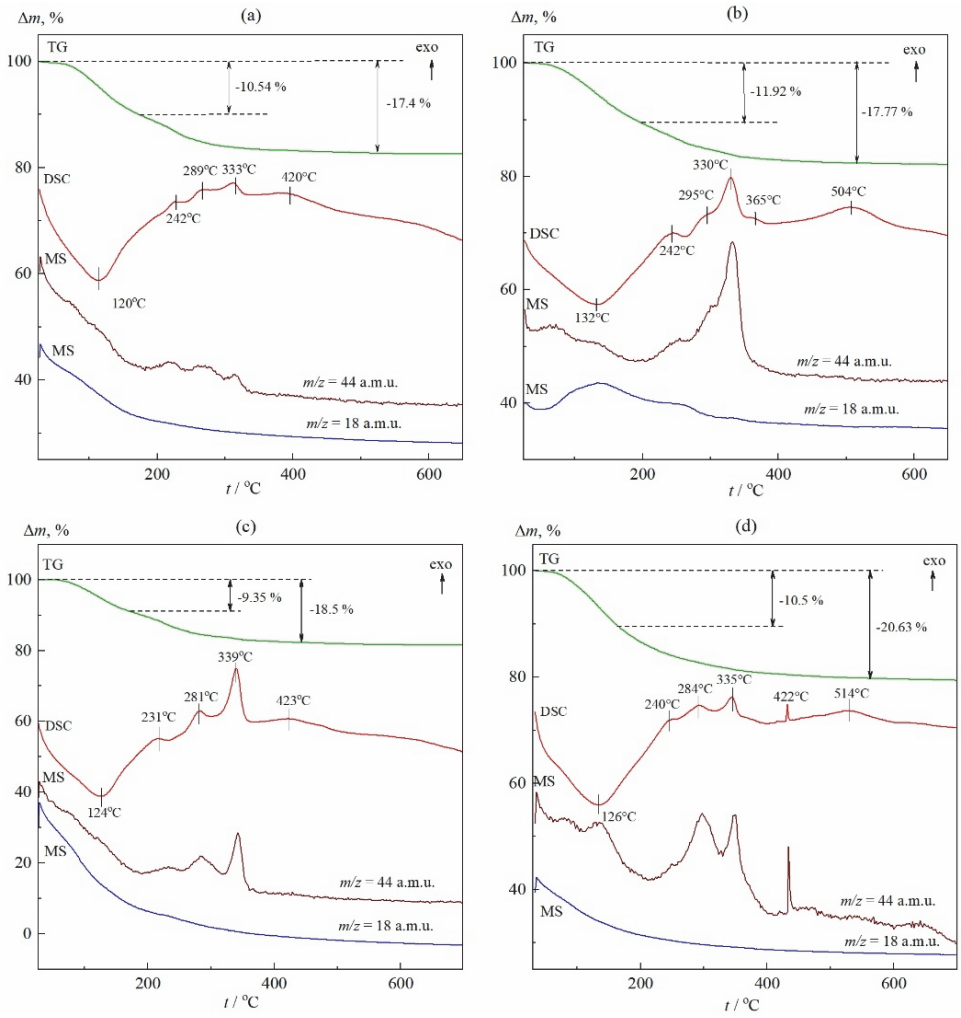

Fig. 5. Thermogravimetric (TG, green), DSC (red), and mass spectroscopy (MS, brown, blue) curves of iron(III) hydroxide precipitated from the model solution at pH 7 (a and b) and 8 (c and d): a, c – there are no nickel ions in the solution; b, d – precipitation in the presence of nickel ions (10 mg L^{-1}) in the solution. Δm is the change in the mass of the precipitate; t is the temperature, °C.

netite during thermal analysis is probably attributed to the presence of carbonates and organic compounds in the precipitates. The observed release of carbon dioxide is probably due to both its desorption from the samples and the gradual thermal decomposition of organic and carbonate impurities, the presence of which is recorded by IR spectra (Fig. 4). Analysis revealed a total carbon content in the samples ranging from 0.73 to 1.2 wt. %. Therefore, the mass loss during heating was mainly

due to dehydration. Considering that Raman and IR spectra did not confirm the presence of non-aqueous OH groups in the samples, and also taking into account the observed mass loss of about 18 %, we assign them the general (gross) formula $Fe_2O_3 \cdot 2H_2O$. It should be noted that if the precipitates consisted of goethite and lepidocrocite, then, given the absence of non-aqueous OH groups in their structure, they would have a general (gross) formula $Fe_2O_3 \cdot H_2O$, and the loss of precipitate mass during thermogravimetric analysis would be about 10 %. Furthermore, published data indicate that the TG curves for dehydrating goethite or lepidocrocite differ from those observed in our experiments.[11,12] Typically, when heated to 200 °C, there is an initial mass loss of no more than 5 % due to the loss of adsorbed water, followed by a sharp inflection in the TG curve and a total mass loss of about 10 %. Moreover, dehydration, in contrast to the iron(III) hydroxide precipitates obtained in this work, occurs in a single step.[11,12] Taking the above into account, it can be concluded that in the present experiments, iron(III) hydroxide was formed with the general (gross) formula $Fe_2O_3 \cdot 2H_2O$ with a minor admixture of goethite, lepidocrocite, and magnetite.

The formation of iron(III) hydroxide with the general (gross) formula $Fe_2O_3 \cdot 2H_2O$ was previously found in the works.[13,14] At the same time, the precipitate obtained in[14] was X-ray amorphous. The absence of OH groups in iron(III) hydroxide precipitates obtained from ammonia solutions at pH 10 and 13 was established by IR spectroscopy.[13]

Thus, since the resulting iron(III) hydroxide precipitates ($Fe_2O_3 \cdot 2H_2O$) are amorphous and cannot be detected by X-ray diffraction analysis, the diffraction patterns (Fig. 2) contain lines characteristic of goethite (α-FeOOH) and lepidocrocite (γ-FeOOH), which are present in the precipitates in small quantities and are probably impurities. Consequently, calculations of the phase composition of the precipitates based solely on X-ray diffraction data are incorrect. The low content of goethite (α-FeOOH) and lepidocrocite (γ-FeOOH) in the precipitates apparently explains the absence of bands characteristic of these compounds in the Raman spectra. The modes observed at 3740 cm^{-1} in Fig. 4 can be attributed to goethite and lepidocrocite. The low intensity of these modes further confirms that these phases are present in the precipitates in small quantities.

Fig. 6 shows the effect of pH on the zeta potential of iron(III) hydroxide precipitate particles formed in the solution. It is evident that the zeta potential of the iron(III) hydroxide precipitate particles formed in our experiments at pH < 5.4 has a positive value, and at pH > 5.4 it becomes negative (curve 1). The point of zero charge corresponds to pH 5.4. This finding aligns with data[7] reported for iron(III) hydroxide in the form of two-line ferrihydrite but significantly differs from results reported in previous studies,[15,16] where the pH of the point of zero charge for ferrihydrite particles was found to be 8.4[15] and 8.8[16]. This discrepancy is attributed, as noted previously,[7] to the presence of sulfate ions in the model solution.

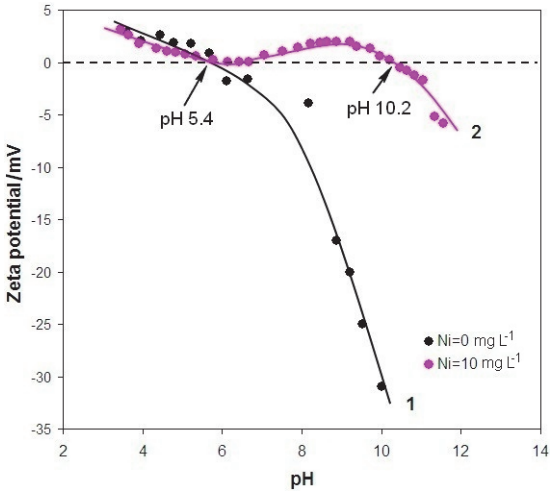

Fig. 6. Dependences of zeta potential of iron(III) hydroxide particles on the pH of the solution and the concentration of nickel ions in it.

Fig. 6 also shows that at pH < 5.4, the introduction of nickel ions into the solution has an insignificant effect on the zeta potential of iron(III) hydroxide particles (please see curves 1 and 2). This may indicate weak adsorption of nickel ions on the precipitate particles surface in this pH range. In contrast, at pH > 5.4, the adsorption of nickel ions on the surface of iron(III) hydroxide precipitate particles increases, as indicated by the rise in zeta potential (curve 2). At pH > 10, the adsorption of hydroxide ions begins to predominate, and the zeta potential of precipitate particles decreases (curve 2). This results in a shift of the point of zero charge to the alkaline region, reaching a value of 10.2.

It is noteworthy that a similar relationship was previously discovered in the work.[7] The study found an increase in the zeta potential of iron(III) hydroxide precipitate particles in the form of two-line ferrihydrite upon the introduction of nickel ions, accompanied by a corresponding shift in the pH of the zero charge point to the alkaline region.[7] Moreover, the pH shift of the zero charge point of iron(III) hydroxide particles when arsenic anions were introduced into the solution was also found in the work.[17] At the same time, due to the negative charge of arsenic anions, the zeta potential of the precipitate particles decreased, and the pH of the zero charge point shifted, respectively, to the acidic region.[17]

CONCLUSION

The studies of iron(III) hydroxide precipitates obtained at pH 7 and 8 from a solution of iron(II) sulfate in the presence of sodium sulfate (400 mg L^{-1}) indicate that they have the general (gross) formula $Fe_2O_3 \cdot 2H_2O$, along with small amounts of goethite (α-FeOOH) and lepidocrocite (γ-FeOOH). This is supported by data from X-ray and thermogravimetric analyses, as well as Raman and IR spectroscopy.

The zeta potential of the precipitate particles shows a positive value at pH < 5.4, transitioning to a negative value at pH > 5.4, indicating that the point of zero charge occurs at pH 5.4. Notably, the introduction of nickel ions into the solution results in a second point of zero charge at pH 10.2.

Furthermore, the sorption of nickel ions onto the iron(III) hydroxide precipitates does not involve chemisorption. Thus, no mixed compounds between iron and nickel are formed during precipitation.

Acknowledgements. This work was carried out in accordance with the assignment by the Ministry of Science and Higher Education of the Russian Federation (theme No. 124020600024-5) and also supported by Government of the Sverdlovsk region and the grant of Russian Fund for Basic Research (Project No. 20-48-660038).

ИЗВОД

УКЛАЊАЊЕ НИКЛ(II) ЈОНА ТОКОМ ПРЕЧИШЋАВАЊА ВОДЕ ГВОЖЂЕ(II) СУЛФАТОМ. 2. ДЕО. СТРУКТУРА И САСТАВ ПРЕЦИПИТАТА ГВОЖЂЕ(III) ХИДРОКСИДА

OLEG D. LINNIKOV, IRINA V. RODINA, GALINA S. ZAKHAROVA, INNA V. BAKLANOVA, YULIA V. KUZNETSOVA, ALEXANDER P. TYUTYUNNIK и ZILARA A. FATTAKHOVA

Institute of Solid State Chemistry, Ural Branch of the Russian Academy of Sciences, Pervomayskaya St., 91, 620990, Ekaterinburg, Russia

Спроведена је упоредна анализа састава и структуре свеже исталожених преципитата гвожђе(III)-хидроксида добијених из раствора гвожђе(II)-сулфата у присуству натријум-сулфата (400 mg L^{-1}) на pH 7 и 8, пре и после сорпције јона никла. Коришћењем IC и раманске спектроскопије, фазне рендгенске и термогравиметријске анализе показано је да талози имају општу (бруто) формулу $Fe_2O_3 \cdot 2H_2O$ и садрже малу количину гетита (α-FeOOH) и лепидокрокита (γ-FeOOH). Утврђено је да сорпција јона никла на овим талозима није праћена хемисорпцијом, тј. не долази до формирања мешовитих једињења гвожђа и никла. Тачка нултог наелектрисања честица талога налази се на pH 5,4, при чему је зета потенцијал позитиван испод, а негативан изнад ове вредности pH. Увођење јона никла у раствор доводи до појаве друге тачке нултог наелектрисања на pH 10,2.

(Примљено 7. априла, ревидирано 28. априла, прихваћено 30. октобра 2025)

REFERENCES

1. O. D. Linnikov, I. V. Rodina, *J. Serb. Chem. Soc*. **91** (2026) 39 (https://doi.org/10.2298/JSC250407080L)
2. M. Kiyama, T. Takada, *Bull. Chem. Soc. Japan* **45** (1972) 1923
3. T. Misawa, K. Yashimoto, S. Shimodaira, *Corros. Sci.* **14** (1974) 131
4. Y. Deng, *Water Res.* **31** (1997) 1347 (https://doi.org/10.1016/s0043-1354(96)00388-0)
5. R. R. Kleshcheva, D. A. Zherebtsov, V. Sh. Mirasov, D. G. Kleshchev, *Bull. South Ural State Univ.* **1** (2012) 17
6. E. V. Petrova, A. F. Dresvyannikov, M. A. Tsyganova, A. M. Gubaidullina, D. V. Wasserman, N. I. Naumkina, *Bull. Kazan Technol. Univ*. **2** (2009) 24

7. O. D. Linnikov, I. V. Rodina, G. S. Zakharova, K. N. Mikhalev, I. V. Baklanova, Yu. V. Kuznetsova, A. Yu. Germov, B. Yu. Goloborodskii, A. P. Tyutyunnik, Z. A. Fattakhova, *Water Environ. Res*. **94** (2022) e10827 (https://doi.org/10.1002/wer.10827)
8. M. Hanesch, *Geophys. J. Int.* **177** (2009) 941 (https://doi.org/10.1111/j.1365-246X.2009.04122.x)
9. D. L. de Faria, S. S. Venâncio, M. T. de Oliveira, *J. Raman Spectrosc*. 2**8** (1997) 873 (https://doi.org/10.1002/(SICI)1097-4555(199711)28:11<873::AID-JRS177>3.0.CO;2-B)
10. M. A. Legodi, D. de Waal, *Dyes Pigments* **74** (2007) 161 (https://doi.org/10.1016/j.dyepig.2006.01.038)
11. M. Kosmulski, S. Durand-Vidal, E. Mazcka, J. B. Rosenholm, *J. Col. Interface Sci*. **271** (2004) 261 (https://doi.org/10.1016/j.jcis.2003.10.032)
12. E. Paterson, R. Swaffield, *J. Therm. Anal.* **18** (1980) 161 (https://doi.org/10.1007/bf01909464)
13. M. V. Akhmanova, G. I. Malofeeva, N. P. Andreeva, *J. Anal. Chem*. **31** (1976) 447
14. L. G. Berg, K. P. Pribylov, V. P. Egunov, R. A. Abdurakhmanov, *Russ. J. Inorg. Chem*. **14** (1969) 2303
15. J. Liu, R. Zhu, L. Ma, H. Fu, X. Lin, S. C. Parker, M. Molinari, *Geoderma* **383** (2021) 114799 (https://doi.org/10.1016/j.geoderma.2020.114799)
16. M. Villalobos, J. Antelo, *Rev. Intern. Contam. Amb.* **27** (2011) 139 (https://doi.org/10.20937/RICA.25013)
17. M. A. Inam, R. Khan, K-H. Lee, Y-M. Wie, *Int. J. Environ. Res. Pub. Health* **18** (2021) 9812 (https://doi.org/10.3390/ijerph18189812).

Journal of the Serbian Chemical Society
JSCS-info@shd.org.rs • www.shd.org.rs/JSCS
J. Serb. Chem. Soc. *91* (3) 271–289 (2026)
JSCS–5491
Original scientific paper
Published 26 February, 2026

Inclusion of $H_3PW_{12}O_{40}$ in cyclodextrin as a catalyst for oleic acid esterification

FERIEL TOUMI[1], YASMINA IDRISSOU[2,4], TASSADIT MAZARI[1]*, NICOLAS KANIA[3], ANNE PONCHEL[3], ABDENOUR BOUMACHHOUR[5], NOUARA LAMRANI[1] and CHERIFA RABIA[2]

[1]*Laboratory of Applied Chemistry and chemical engineering (LCAGC), Faculty of chemistry, University of Mouloud Mammeri Tizi Ouzou (UMMTO),Tizi Ouzou, Algeria,* [2]*Laboratory of Natural Gas Chemistry (LCGN), Faculty of Chemistry (USTHB), BP 32, 16111, Algiers, Algeria,* [3]*Jean Perrin Faculty of Sciences, University of Artois, UCCS-UMR CNRS 8181, Lens, France,* [4]*Ecole Normale Supérieure Kouba (ENS), Alger, Algeria and* [5]*Centre de Recherche Scientifique et Technique en Analyses Physico–Chimiques, Bou Ismail, Algeria*

(Received 27 August, revised 14 October, accepted 6 December 2025)

Abstract: This study focuses on the use of cyclodextrins (*β*-CD and HP-*β*-CD) as host materials to immobilize 20 wt. % tungstophosphoric acid, $H_3PW_{12}O_{40}$ (HPW), and their application as catalysts for the esterification of oleic acid, a fatty acid commonly found in many vegetable oils and frequently used as a biodiesel feedstock, into methyl oleate using methanol, the most commonly preferred alcohol for this reaction. The catalytic performances of these hybrid materials were compared with those of HPW incorporated into polyacrylamide hydrogel (20 wt. % HPW/PAAm) and HPW supported on silica (20 wt. % HPW/SiO_2), a conventional inorganic support. All materials were characterized by various techniques. For all supports, the Keggin structure of $H_3PW_{12}O_{40}$ was retained after immobilization, as confirmed by FT-IR and Raman spectroscopies. XRD and SEM analyses suggested the formation of inclusion complexes in the HPW/*β*-CD and HPW/HP-*β*-CD systems, as well as the successful incorporation of HPW into the PAAm matrix. In the esterification reaction carried out at 60 °C for 3 h, bulk HPW, HPW/PAAm and HPW/*β*-CD exhibited high catalytic activity, achieving methyl oleate yields of 97, 94 and 69 %, respectively, significantly higher than that obtained with the silica-supported catalyst (41 %).

Keywords: tungstophosphoric acid; polymer; cyclodextrin; esterification; methanol; methyl oleate.

* Corresponding author. E-mail: tassadit.mazari@ummto.dz
https://doi.org/10.2298/JSC250827095T

INTRODUCTION

The transition from fossil fuels to renewable energy sources has become a necessity if current environmental challenges are to be met. Among the viable alternatives, biodiesel has emerged as a promising candidate, alongside wind, solar, hydrothermal and photovoltaic energy. Biodiesel is not only non-toxic and biodegradable, but it also has similar physicochemical properties to those of conventional diesel fuel, with the advantage of reducing emissions of hazardous substances, thereby minimizing health risks.[1] Biodiesel, composed of fatty acid methyl esters, is produced by homogeneous or heterogeneous catalytic processes, involving the esterification or transesterification of renewable feedstocks such as vegetable oils and animal fats.

In the heterogeneous phase, various catalysts have been investigated for this purpose, including strontium-zinc bifunctional oxides[1] basic or acidic oxides,[2] *β*-zeolite-supported sulphated metal oxide[3] and silica supported tungsten oxide.[4] The methanolysis of oils using catalysts such as SiO_2/Al_2O_3 incorporated in BEA zeolite frameworks with alkaline earth oxides (MgO, CaO, SrO) has also been studied.[5]

In the homogeneous phase, alkaline catalysts such as sodium or potassium hydroxides, carbonates and alkoxides,[2,5] mineral acids (*e.g.*, phosphoric, sulfuric)[4] and heteropolyacids (HPAs[6,7] were found to be effective for fatty acids transesterification. However, although base-catalysed transesterification is generally more cost-effective than acid catalysis, it is still very sensitive to the presence of water and free fatty acids, and is also subject to undesirable side reactions such as hydrolysis and saponification,[8] which make it difficult to recover the desired product.

In acid catalysis, Keggin-type tungstophosphoric acid $H_3PW_{12}O_{40}$ (HPW), is particularly preferred due to its high Brønsted acidity and lower toxicity compared with conventional mineral acids. However, its high solubility in polar media complicates catalyst recovery and raises concerns about equipment corrosion and environmental impact, similar to those encountered with mineral acids.[9] To address these limitations, HPW has been immobilized on various solid supports, including zirconia,[10] alumina,[11]mesoporous silica[7] and activated carbon.[12] In oleic acid esterification in the presence of 30 wt. % HPW supported on biomass-derived activated carbon[12] and 20 wt. % HPW on KIT-6 mesoporous silica, a maximum conversion of 86 % was obtained. However, leaching is frequently observed with these conventional supports, which limits the long-term efficiency and reusability of the catalytic systems. The present study aims to reduce this drawback by incurporating HPW into polymeric matrices such as polyacrylamide (PAAm) hydrogels and cyclodextrins (CD).

Hydrogels are cross-linked, three-dimensional, superabsorbent polymer networks capable of retaining large volumes of water without dissolving.[13] Their

functional groups, including carboxylic, amide, amino, sulphonic acid and hydroxyl groups, provide active sites for molecular interactions.[14,15] Due to their high absorbency and interactive surface chemistry, hydrogels have been widely employed in biomedicine, biotechnology and catalysis. For example, Dharmapriya *et al.*[16] have demonstrated the efficiency of hybrid systems composed of hydrogels and catalytic species in the conversion of carbohydrates to 5-hydroxymethylfurfural. In order to improve the efficiency of hydrogels in acid reactions, several studies have suggested incorporating $H_3PW_{12}O_{40}$ (HPW), a heteropolyacid stronger than $H_3PW_{12}O_{40}$, into the polymer matrix. Thus, catalytic membranes constituted of HPW embedded in PVA polyvinyl alcohol (HPW@PVA), tested in glycerol acetalization with acetone, showed high conversion (95 %) and high selectivity and remained effective after ten reuse cycles without performance loss.[17] HPW encapsulated inside microporous polymeric nanospheres (H-MPNs) using a hyper-crosslinked PLA-b-PS polymer exhibits excellent catalytic activity and stability thanks to its hollow and permeable structure.[18] A series of composite materials (PLMTPA) synthesized by incorporating HPW into a polyacrylamide matrix at different ratios proved to be effective, recyclable and non-corrosive for the synthesis of 2-benzazepines under mild conditions and reusable over six cycles without loss of activity.[19] The HPW/polymer hydrogel system synthesized from a triethylene glycol monomer and a cross-linking agent, trapping heteropolyacid in the network through hydrogen bonds, effectively catalyses the hydrolysis of ethyl esters in an aqueous medium. It has been shown that HPW does not leach in water, allowing it to be used as a stable heterogeneous catalyst.[20]

Cyclodextrins (CDs), in particular *β*-CD and its derivatives, have attracted attention in pharmaceutical studies due to their ability to form host-guest inclusion complexes.[21] *β*-CD, composed of D-glucose units, has a hydrophobic internal cavity and a hydrophilic external surface, allowing it to encapsulate a variety of guest molecules. Its low water solubility, unique truncated cone shape, cost-effectiveness and ease of functionalization make it highly suitable for catalytic applications.[22–25] In addition to its pharmaceutical interest, *β*-CD has shown catalytic potential in various organic transformations.[26] For example, Wu *et al.* synthesized a hybrid complex $[La(H_2O)_9]\{[PM_{O_{12}}O_{40}]\subset[\beta\text{-CD}]_2\}$ (CD-POM-2), highlighting its catalytic, photocatalytic and biomedical utility.[27] Polyoxometalates (POMs) adsorbed in γ-cyclodextrin-based polymers (PVW_{11}@CD–EPI) through the chaotropic effect have been shown to form supramolecular hybrid materials exhibiting rapid and efficient adsorption behaviour as well as excellent catalytic performance. In the oxidation of benzyl alcohol, these hybrids achieved high conversion, selectivity and recyclability under mild reaction conditions.[28] Computational investigations based on density functional theory (DFT) and molecular dynamics simulations have revealed that POMs, such as $H_3PW_{12}O_{40}$ (HPW), can spontaneously penetrate the hydrophobic cavity of *γ*-cyclodextrin (*γ*-CD) to form stable host–

–guest complexes. This encapsulation significantly influences the electronic properties, reactivity and electron transfer behaviour of POMs, while the nanoconfinement effect contributes to the spatial isolation and stabilisation of the catalytic species.[29] In addition to Keggin-type POMs, the immobilization of Wells–Dawson-type POMs within cyclodextrin-based nanosponges (WD@CDNS) has also been reported to yield robust and durable catalytic systems. When applied to the Knoevenagel condensation reaction in aqueous media, the WD@CDNS catalyst demonstrated enhanced reusability and excellent structural integrity, confirming its potential for sustainable heterogeneous catalysis.[28] To our knowledge, the HPW/cyclodextrin system has not been tested in esterification or transesterification reactions.

In previous work, a 20 wt. % HPW/PAA catalyst system was tested for the esterification of oleic acid, a fatty acid commonly found in vegetable oils and frequently used as a biodiesel precursor. Methanol was chosen because of its low cost, small molecular size and wide availability.[30–32] Under an oleic acid:methanol:catalyst mole ratio of 1:29:0.025, a high conversion of 95 % was obtained with a reaction temperature and time of 60 °C and 3 h, respectively.[31] In the present study, the quantities of alcohol and catalyst were significantly reduced, and the oleic acid:methanol:catalyst molar ratio was adjusted to 1:9:0.008. Under these conditions, the catalytic performance of 20 wt. % HPW/PAAm was re-evaluated and compared with that of bulk HPW and three other catalytic systems: 20 wt. % HPW/SiO_2 (with silica as a conventional support), 20 wt. % HPW/β-CD and 20 wt. % HPW/HP-β-CD. The HP-β-CD derivative was obtained by substituting the hydroxyl groups of β-CD with hydroxypropyl functionalities.

EXPERIMENTAL

Material synthesis

All chemical reagents and solvents (from Biochem Chemopharma, Sigma–Aldrich and Riedel-De Haen) were used without further purification.

Tungstophosphoric acid ($H_3PW_{12}O_{40}$, HPW) was synthesized following a conventional method previously described in the literature.[33,34]

HPW (20 wt. %) was immobilized on silica (SiO_2), incorporated into a polyacrylamide hydrogel (PAAm), and included in β-cyclodextrin (β-CD) and hydroxypropyl-β-cyclodextrin (HP-β-CD). For the cyclodextrin-based systems, a stoichiometric ratio of five cyclodextrin units per Keggin unit was used.

Preparation of HPW/SiO_2

In a 100 mL two-neck flask, 1 g of HPW was dissolved in 15 mL of distilled water. The solution was heated in a sand bath (60–80 °C). Then, 4 g of silica (60–200 mesh) were gradually added under stirring. The suspension was refluxed at 110 °C for 5 h, followed by drying using a rotary evaporator. The resulting solid was placed in a vacuum oven at 50 °C for 6–7 h to remove residual moisture.[35]

Preparation of HPW/PAAm

Polyacrylamide hydrogel synthesis. In a three-neck round-bottom flask, 1 g of acrylamide monomer (C_3H_5NO) and 1×10^{-3} g of potassium persulfate ($K_2S_2O_8$) as an initiator were dissolved in ~3 mL of distilled water. After dissolution, 3×10^{-3} g of *N*,*N*′-methylenebisacrylamide ($C_7H_{10}N_2O_2$) was added as the crosslinker. The mixture was stirred at 250 rpm and purged with nitrogen (N_2) for 30 min to eliminate oxygen. The flask was then immersed in a water bath preheated to 60 °C and stirred for 20 min. A transparent PAAm formed at the bottom of the flask. The hydrogel was cut into small pieces, washed three times with distilled water to remove residual reagents and air-dried.[31]

HPW/PAAm preparation. dried PAAm was immersed in an aqueous solution of HPW (corresponding to 20 wt. % HPW). After complete absorption and air drying, the HPW-loaded hydrogel (HPW/PAAm) was recovered.

HPW/β-CD preparation

The HPW/*β*-CD system was prepared by physical impregnation, following a method similar to that used for HPW/SiO_2. In a 100 mL two-neck flask, 0.4 g of HPW was dissolved in 20 mL of water and heated in a sand bath maintained at 50–60 °C. Then, 1.6 g of *β*-cyclodextrin was gradually added. The suspension was refluxed at 80 °C for 5 h, followed by drying with a rotary evaporator.

HPW/HP-β-CD preparation

A mixture of 0.4 g of HPW and 1.6 g of HP-*β*-CD was stirred in ethanol for 24 h. The solvent was then evaporated using a rotary evaporator. The resulting white powder corresponded to the HPW/HP-*β*-CD system.

Characterization

The FT-IR spectra of the prepared catalysts were recorded on a Fourier transform spectrometer model IRAffinity-1S, Shimadzu, including an ATR module.

X-ray diffractograms of the catalytic materials were recorded on a Siemens D5000 powder diffractometer at room temperature over an angular range (2θ) of 0 to 70°, with CuKα radiation (λ = 1.5406 Å) at 45 kV and 40 mA. The step size and scanning speed were 0.026° and 2°/min, respectively.

The microstructural observations were performed using a Hitachi SU3800 scanning electron microscope (SEM) operated in backscattered electron (BSE) mode, under partial vacuum, at an accelerating voltage of 15 kV and a working distance (WD) of 10 mm. Energy-dispersive X-ray spectroscopy (EDS) analyses were conducted using a Bruker Quantax EDS system equipped with an XFlash detector.

Catalytic testing

The catalytic activities of bulk HPW and supported HPW systems (HPW/SiO_2, HPW/PAAm, HPW/*β*-CD, HPW/HP-*β*-CD) containing 20 wt. % HPW were evaluated for the esterification of oleic acid with methanol. Reactions were carried out at 60 °C under atmospheric pressure and reflux, with constant stirring at 300 rpm. The molar ratio of oleic acid:methanol:catalyst was 1:9:0.008. The detailed description of the sample preparation was presented in Table I. In a glass reactor, oleic acid and methanol were heated to 60 °C before adding the catalyst. After 3 h, the condenser was rinsed with minimal distilled water to recover the entire reaction mixture. The catalyst was separated by filtration (for supported catalysts), and the mixture was transferred to a separating funnel. Chloroform was added to facilitate phase separation. The organic (chloroformic) phase containing methyl oleate was collected, and the aqueous phase was

washed twice with chloroform to extract any remaining ester. The methyl oleate was recovered by evaporating the chloroform using a rotary evaporator.

TABLE I. Material weight and volumes of methanol and oleic acid used in sample preparation

Material	$W_{(catalyst)}$ / g	$V_{(oleic\ acid)}$ / ml	$V_{(methanol)}$ / ml
HPW	0.25	3	3.5
HPW/SiO_2	1.25	3	3.5
HPW/PAAm	0.0993	1.2	1.4
HPW/*β*-CD	0.625	1.5	1.75
HPW/Hp-*β*-CD	1.25	1.5	1.75
SiO_2	0.25	3	3.5
PAAm	0.0882	1.0584	1.2348
β-CD	0.25	3	3.5
HP-*β*-CD	0.25	3	3.5

The methyl oleate content was analyzed using gas chromatography (Agilent Technologies 7890A GC) equipped with a flame ionization detector (FID). The separation was performed on a capillary column (Carbowax, 30 m×0.25 mm) with nitrogen as the carrier gas (flow rate: 1 mL/min). The injector temperature was set at 260 °C. The oven temperature program was: 120––180 °C at 10 °C/min, followed by 180–260 °C at 7 °C/min, then held at 260 °C for final separation.

The yield of methyl oleate, the only product of the oleic acid esterification, considered in this study, was calculated from the following equation:[36]

$$R = 100\frac{C_{\text{methyl oleate}} \times F_d \times Q_{\text{methyl oleate}}}{m_{\text{oleic acid}}} \quad (1)$$

where $C_{\text{methyl oleate}}$: methyl oleate concentration (mg/μl), F_d: dilution factor, $Q_{\text{methyl oleate}}$: methyl oleate quantity (ml), $m_{\text{oleic acid}}$: oleic acid quantity (g).

RESULTS AND DISCUSSION

Characterizations

FT-IR and Raman spectroscopies. The FT-IR spectra of HPW, SiO_2 and HPW/SiO_2 are shown in Fig. 1a. The Keggin structure of HPW is identified by characteristic vibrational bands: asymmetric P–O_a stretching at 1072 cm^{-1}, asymmetric W=O_d at 964 cm^{-1}, asymmetric W–O_b–W at 887 cm^{-1} and W–Oc–W at 786 cm^{-1}.[37] The FT-IR spectrum of HPW/SiO_2 shows that the asymmetric stretching of Si–O in the 1200–1000 cm^{-1} region envelops the P–O_a vibration band (1072 cm^{-1}). Furthermore, the Si–O– band at 800 cm^{-1} merges with those corresponding to W–O_b–W (887 cm^{-1}) and W–Oc–W (786 cm^{-1}). IR spectroscopy does not allow the vibration bands of the heteropoly anion to be clearly distinguished from those of silica. It should be noted that the preparation method is impregnation, so the acid can only be fixed to the support after a strong interaction between the basic sites of the silica and the protons of the acid.

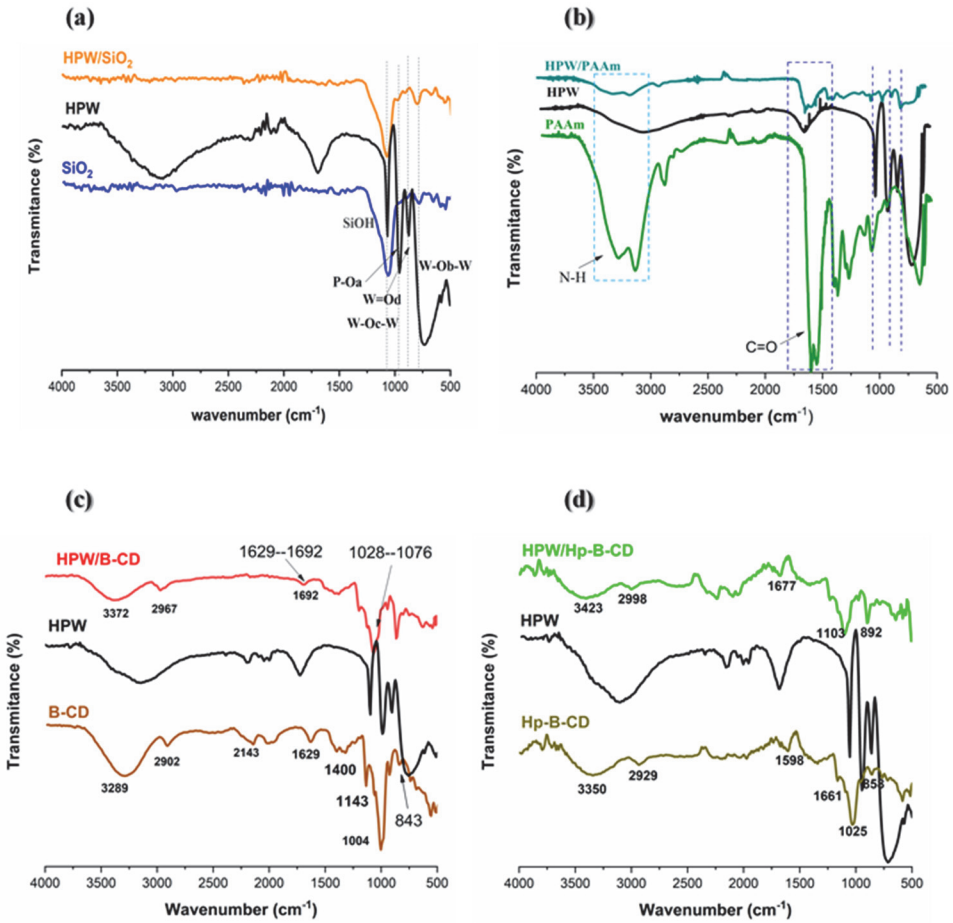

Fig. 1. FT-IR spectra of SiO_2, HPW and HPW/SiO_2 (a), PAAm, HPW and HPW/PAAm (b), β-CD, HPW and HPW/β-CD (c) and Hp-β-CD, HPW and HPW/Hp-β-CD (d).

Fig. 1b displays the FT-IR spectra of PAAm and HPW/PAAm. The spectrum of PAAm shows a strong band at 3334 cm^{-1}, characteristic of N–H stretching of primary amines, with two components at 3332 and 3189 cm^{-1} corresponding to asymmetric and symmetric N–H stretching, respectively. The intense band at 1640 cm^{-1} is assigned to C=O stretching, and the band at 1322 cm^{-1} to C–N bending vibrations of primary amides.[31] After incorporation of HPW into the hydrogel network, the FT-IR spectrum of HPW/PAAm shows the metal-oxygen vibrations of the heteropolyanion with reduced intensity, indicating that the structure of the Keggin unit is preserved.

The FT-IR spectra of β-CD (Fig. 1c) and HP-β-CD (Fig. 1d) are similar, displaying a broad band in the 3400–3200 cm^{-1} range, associated with O–H stretching

of primary alcohols in cyclodextrin, and a band near 2900 cm^{-1} corresponding to aliphatic C–H stretching. In the 1000–1150 cm^{-1} region, the observed bands are characteristic of C–O–C and C–C stretching.[24] Upon complexation with HPW, the FT-IR spectra of HPW/*β*-CD and HPW/HP-*β*-CD show the appearance of characteristic Keggin unit vibrational bands corresponding to the tungsten–oxygen and phosphorus–oxygen bonds, in the 1200–500 cm^{-1} region, with a slight shift towards high frequencies. Thus, the P–O_a vibration band shifts from 1072 to 1135 and 1063 cm^{-1}; the W=O_d band from 964 to 998 and 974 cm^{-1}; W–O_b–W from 887 to 917 and 888 cm^{-1}, and W–O_c–W from 786 to 822 and 797 cm^{-1} for HPW/*β*--CD and HPW/HP-*β*-CD, respectively. These shifts can be attributed to the formation of hydrogen bonds, as reported by some authors, thus indicating the complexation of HPW with cyclodextrin.[38,39]

The Raman spectra of both supported and unsupported $H_3PW_{12}O_{40}$ (Fig. 2) were also recorded. The spectrum of pure HPW exhibits typical metal–oxygen vibrations of the Keggin structure: symmetric and asymmetric W=O_d stretching at

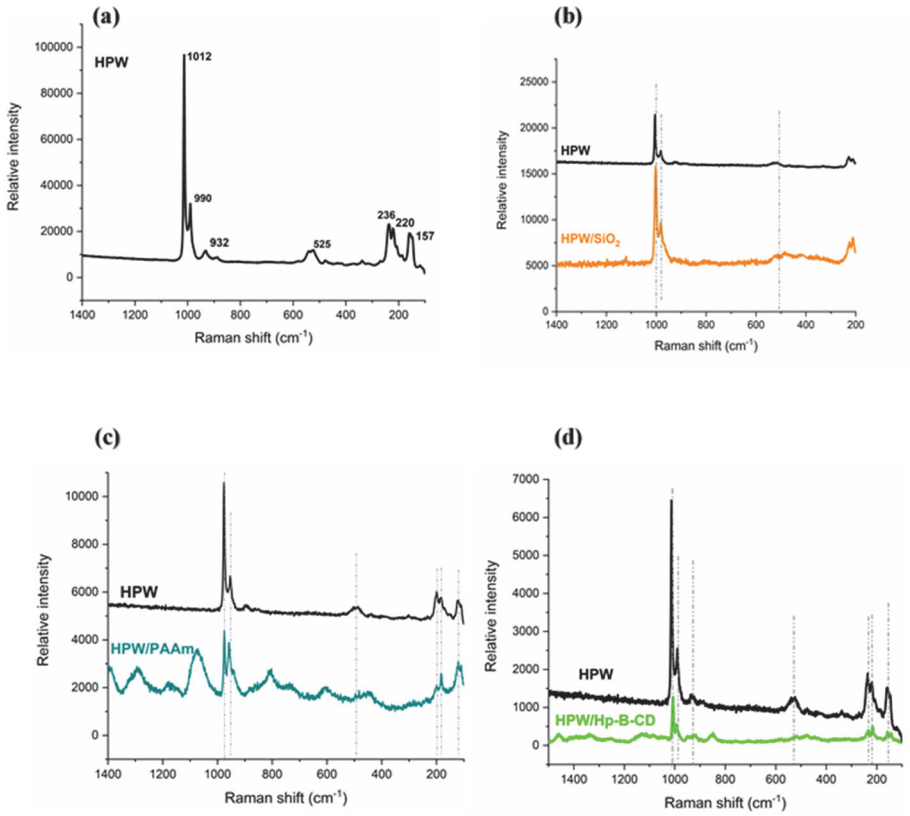

Fig. 2. Raman spectra of different catalysts, HPW (a), HPW and HPW/SiO_2 (b), HPW and HPW/PAAm (c) and Hp-*β*-CD, HPW and HPW/Hp-*β*-CD (d).

1012 and 990 cm^{-1}, asymmetric W–O_b–W at 932 and 525 cm^{-1}, and asymmetric W–O_c–W at 236 and 220 cm^{-1}.[37] In the support presence, the most intense vibration band corresponding to W=O_d shows a decrease in intensity, whatever the nature of the support, which is consistent with the FT-IR results, suggesting a strong interaction between the Keggin anion and the support, due to the high electron density of the tungsten-terminal oxygen bond.

The XRD patterns of HPW, SiO_2 and HPW/SiO_2 are presented in Fig. 3a. HPW shows sharp diffraction peaks in the 2θ range of 5.6–34.6°, characteristic of its triclinic phase (JCPDS Card No. 50-0655).[40,41] SiO_2 displays a broad peak between 15 and 23°, indicating its amorphous nature. The XRD pattern of HPW/ /SiO_2 shows weak peaks at 2θ around 9 and 20°, confirming the presence of HPW's triclinic structure. The low intensity of these peaks suggests a homogeneous dispersion of HPW (pore size: 84.3 Å) on the SiO_2 surface (250–74 μm).[7]

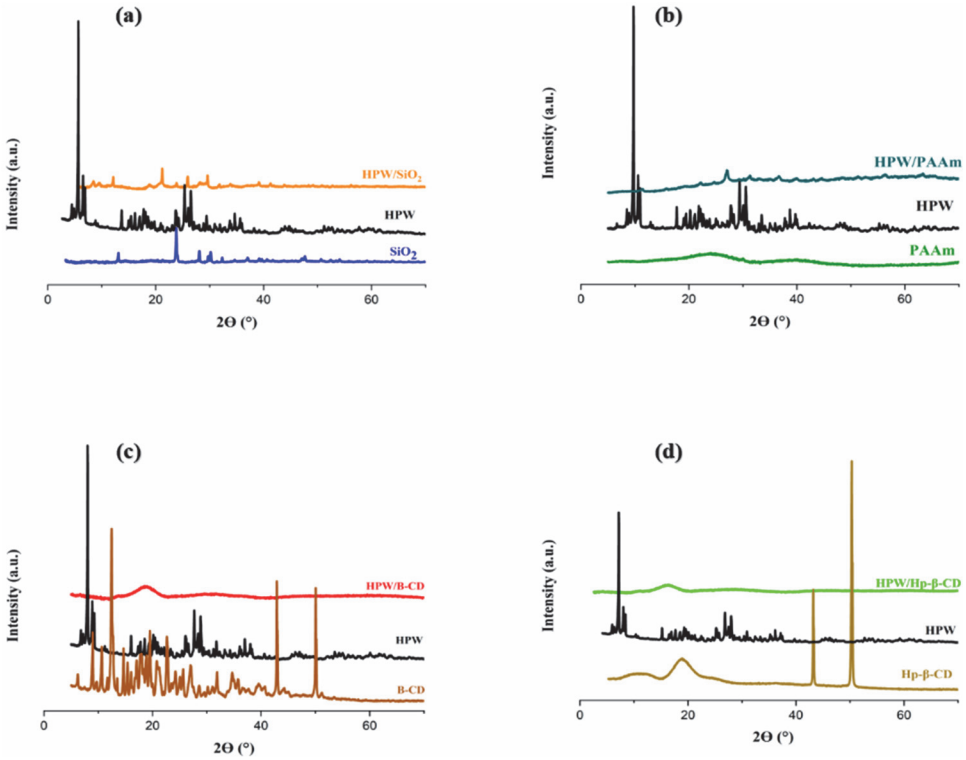

Fig. 3. X-ray diffraction patterns of SiO_2, HPW and HPW/SiO_2 (a), PAAm, HPW and HPW/PAAm (b), β-CD, HPW and HPW/β-CD (c) and Hp-β-CD, HPW and HPW/Hp-β-CD (d).

Fig. 3b shows the XRD patterns of the PAAm and HPW/PAAm. With PAAm alone, a broad peak extending between 2θ 17 and 32° was observed. After introduction of the heteropolyacid, no peaks characteristic of its tricilinic structure

were observed in the 2θ range between 10 and 20°, and only the peak located at 2θ 27° was observed with higher intensity. These results show that HPW is well inserted into the polymer cavities.

The XRD pattern of β-CD (Fig. 3c) displays multiple sharp lines between 2θ 0 and 50°, with dominant peaks at 10, 40 and 48°, confirming its crystalline nature.[42] In contrast, the XRD pattern of the HPW/β-CD complex shows the disappearance of all characteristic peaks of HPW and β-CD, replaced by a broad diffraction peak in the 10–20° 2θ range. This result suggests that β-CD, with its hydrophobic inner cavity and hydrophilic outer surface, can form inclusion complexes *via* host–guest interactions and hydrogen bonds with cyclodextrin cavities which can disrupt the β-CD structure.

Similarly, HP-β-CD exhibits a broad peak between 15 and 25°, along with sharper peaks at 41 and 50°, indicating the presence of small crystalline domains within an otherwise amorphous matrix.[43] After HPW incorporation, the XRD pattern of HPW/HP-β-CD resembles that of HPW/β-CD, with a broad peak between 2θ 10 and 20°, confirming the formation of similar inclusion complexes in both systems.

SEM

The SEM micrograph of HPW/SiO_2 (Fig. 4) reveals irregularly shaped blocks and rod-like structures, characteristic of the SiO_2 support. HPW is observed as white spherical nanoparticles, heterogeneously dispersed across the surface, forming a relatively uniform layer. These morphological features are consistent with the XRD analysis. Elemental mapping by EDX confirms the presence of silicon, tungsten and oxygen, supporting the successful immobilization of HPW on the silica surface.

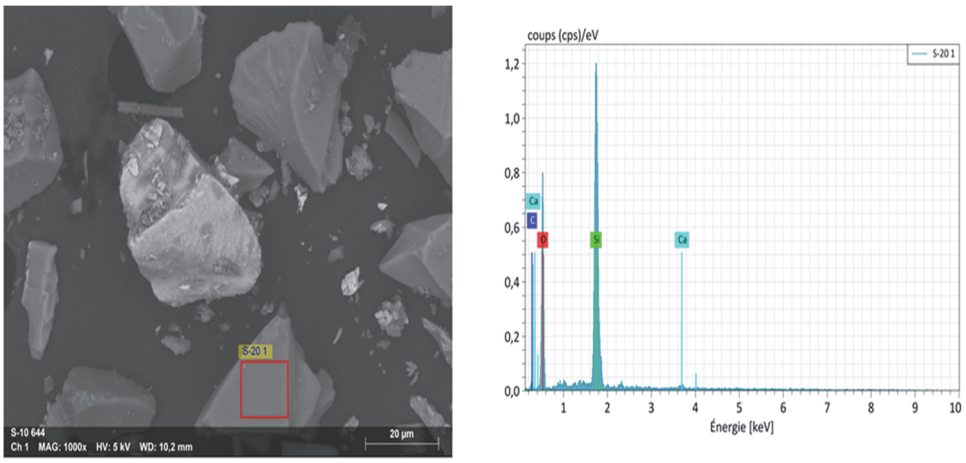

Fig. 4. SEM and elemental analysis (EDX) of HPW/SiO_2.

The SEM image of PAAm displays a smooth, dense surface with craters of varying diameters, Fig. 5. Upon HPW incorporation, the HPW/PAAm system exhibits a rougher surface morphology, with visible fissures and embedded HPW nanoparticles both at the surface and within the hydrogel matrix. These changes likely result from interactions between the HPW species and the functional groups of the polyacrylamide network. The encapsulation of HPW and the formation of cross-linking zones within the hydrogel are thus revealed by the morphological transformation.

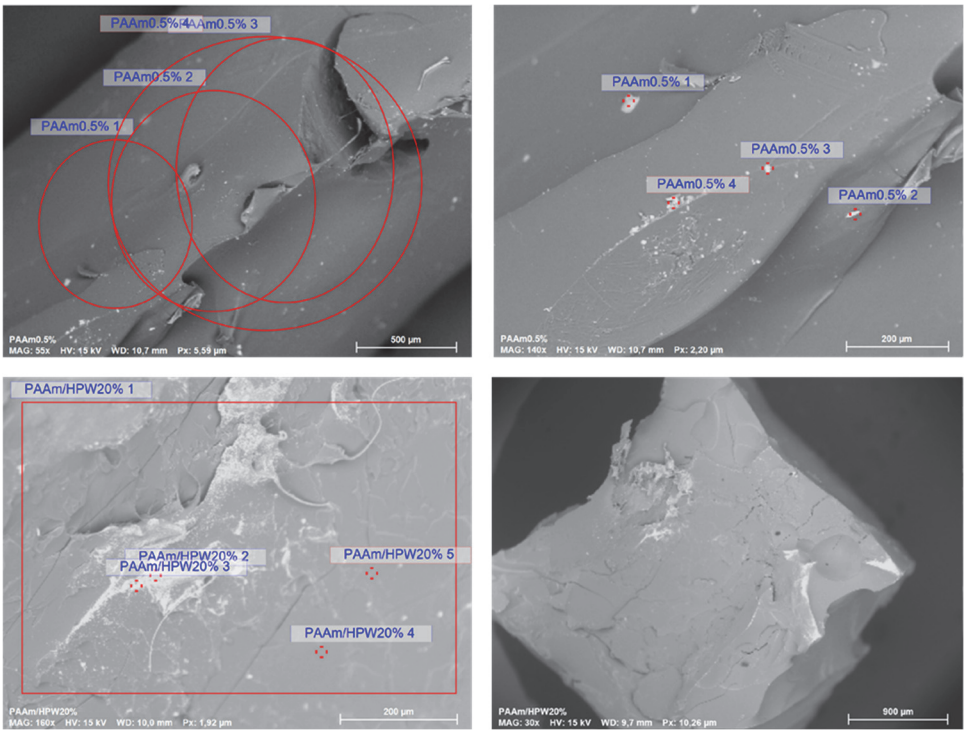

Fig. 5.SEM images of PAAm and HPW/PAAm.

At 20-µm magnification, the SEM images of HPW/*β*-CD and HPW/HP-*β*-CD materials reveal distinct morphologies. HPW/*β*-CD shows dark- and light-toned blocks with relatively flat surfaces, whereas HPW/HP-*β*-CD presents cauliflower--like aggregates and flat blocks surrounded by fine particles. These differences highlight morphological variations between the two systems. However, unlike in hydrogel-based systems, it remains difficult to confirm complexation or the inclusion of HPW within the cyclodextrin matrices based solely on SEM observations. EDX analysis confirmed the presence of tungsten in both systems, indicating the successful incorporation of HPW despite the morphological differences (Fig. 6).

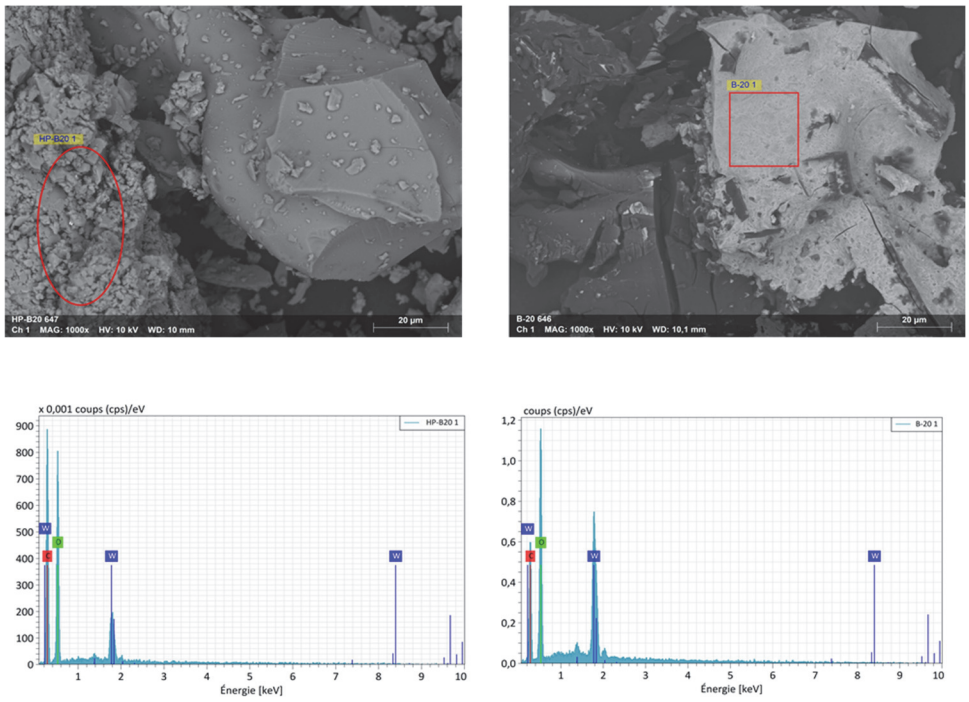

Fig. 6. SEM and elemental analysis (EDX) of HPW/*β*-CD and HPW/Hp-*β*-CD.

Catalytic results

The catalytic performances of bulk HPW and supported HPW systems, namely HPW/SiO_2, HPW/PAAm, HPW/*β*-CD and HPW/HP-*β*-CD, are summarized in Table II. The supports alone exhibited varying levels of catalytic activity, with methyl oleate yields of 40, 32, 9 and 8 % for *β*-CD, SiO_2, PAAm, and HP-*β*--CD, respectively. This intrinsic activity can be attributed to the basicity of the supports, originating from functional groups such as hydroxyl (OH) groups on silica and *β*-CD, and amino groups (NH_2) in polyacrylamide. It is well known that esterification and transesterification reactions are favoured by basic catalysts such as sodium or potassium methoxides, hydroxides and carbonates.[5] Bulk HPW showed the highest activity, achieving a methyl oleate yield of 97 %, attributable to its strong Brønsted acidity and high availability of acid sites in a homogeneous medium. However, upon immobilization, the catalytic performance of HPW decreased, with yields of 94, 69, 41 and 29 % observed for HPW/PAAm, HPW/*β*-CD, HPW/SiO_2 and HPW/HP-*β*-CD, respectively.

Among the supported catalysts, HPW/PAAm exhibited exceptional performance with a methyl oleate yield (94 %) nearly matching that of the bulk HPW (97 %). These results are similar to those obtained with an oleic acid:methanol:catalyst mole ratio of 1:29:0.025,[31] indicating that with less drastic conditions

(1:9:0.008) good results can be obtained. The efficiency of the HPW/PAAm catalyst is likely due to the three-dimensional cross-linked network of polyacrylamide, which allows for homogeneous dispersion of active sites throughout the matrix. The high catalytic activity can therefore be ascribed to the full availability of the protonic acid sites of HPW, effectively catalysing the esterification reaction.

TABLE II. Methyl oleate yields (%) as a function of catalyst type. Reaction temperature and time of 60 °C and 3 h, pressure:1 at, stirring: 300 rpm, oleic acid/methanol/catalyst mole ratio was 1/9/0.008

Catalytic system	Methyl oleate yield, %
HPW (bulk)	97
SiO_2	32
HPW/SiO_2	41
PAAm	9
HPW/PAAm	94
β-CD	40
HPW/*β*-CD	69
HP-*β*-CD	8
HPW/HP-*β*-CD	29

The HPW/*β*-CD system produced 69 % methyl oleate, which is significantly lower than the yield obtained with the HPW/PAAm system (94 %). This may be due to the hydrophobic nature of *β*-CD, which can restrict the accessibility of polar reagents such as methanol. The reduced catalytic activity of HPW/*β*-CD and HPW/SiO_2 is likely due to the strong hydrogen bonding interactions between HPW protons and hydroxyl groups on the supports, which reduce the availability of acidic sites for catalysis. Assuming a stoichiometric ratio of five *β*-CD units per Keggin unit in the HPW/*β*-CD system, it is likely that the hydrophobic cavities of *β*-CD develop a preferential affinity for the reactants, favouring the formation of microreactors composed of *β*-CD, oleic acid and methanol. In this configuration, HPW, being hydrophilic, acts peripherally to catalyse the surface reaction. This hypothesis is supported by scanning electron microscopy observations, which show that heteropolyacid molecules are surrounded by *β*-CD units.

The HPW/HP-*β*-CD catalyst only gave a yield of 29 %, lower than that of the *β*-CD (40 %) and SiO_2 (32 %) supports alone. This suggests not only a lack of basic sites but also a reduction in accessible acidic sites. The difference in performance between HPW/HP-*β*-CD and HPW/*β*-CD – despite their similar structures observed in XRD, can be attributed to steric hindrance caused by hydroxypropyl substituents in HP-*β*-CD, which likely obstruct reagent access to HPW active sites.

The catalytic efficiency obtained with a reaction temperature and time of 60 °C and 3 h and oleic acid:methanol:catalyst mole ratio of 1:9:0.008, across the systems follows the order: HPW (97 %) > HPW/PAAm (94 %) > HPW/*β*-CD (69 %) > HPW/SiO_2 (41 %) > HPW/HP-*β*-CD (29 %).

In the esterification of oleic acid, the HPW/PAAm catalytic system appears to be a more promising candidate than PW/UiO/CNTs–OH[44] and HPW/OMS–SO_3H[45] because it achieves a similar yield (93–95 %) but with better operating conditions (oleic acid/methanol/catalyst mole ratio of 1:9 *versus* 30:1 and 14.27:1, and a reaction temperature of 60 *vs.* 69 and 120 °C, respectively). In addition, the system can be reused several times without loss of catalytic activity. It should be noted that the HPW/*β*-CD system can also be considered attractive with a yield of 69 %.

Catalyst leaching was investigated by performing the oleic acid esterification reaction followed by FT-IR analysis of the reaction media (Fig. 7). After 1 h of methanolysis with HPW/PAAm or HPW/*β*-CD, no characteristic bands of the heteropolyacid were detected in the reaction mixture, confirming that HPW remained immobilized. This demonstrates the successful entrapment of HPW in the PAAm hydrogel network and its effective complexation within the *β*-CD structure.

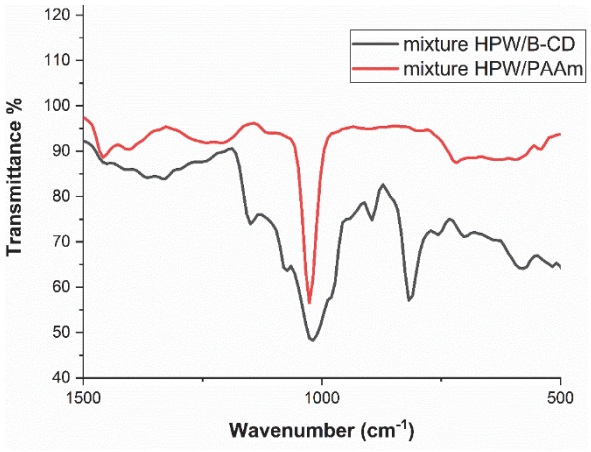

Fig. 7. FT-IR spectra of esterification reaction mixtures in the presence of HPW/PAAm and HPW/*β*-CD.

Stability tests were conducted over multiple cycles (3 h each) under identical reaction conditions (temperature: 60 °C; oleic acid/methanol/catalyst ratio: 1/9/0.008). For HPW/PAAm, the catalyst was separated, washed, dried, and reused. In the case of HPW/*β*-CD, the catalyst was kept at the flask bottom to minimize losses and then washed with ether and reused. Fig. 8 shows the yields of methyl oleate as a function of the number of cycles in the presence of the two catalyst systems, HPW/PAAM and HPW/*β*-CD. After six cycles, HPW/PAAm maintained a consistent methyl oleate yield of 94 %, indicating excellent recyclability and structural robustness. This contrasts with previously reported polymer-based catalysts such as hyper-crosslinked porous polymers, which showed a significant decrease in FAME yield from 99.9 to 42.5 % after just two cycles.[15] These results indicate

that, in this configuration, HPW is physically incorporated into the three-dimensional cross-linked network of the polyacrylamide hydrogel. The polar functional groups of the hydrogel (amide and carboxyl groups) provide interaction sites for the HPW molecules, allowing uniform dispersion in the polymer matrix. The resulting composite maintains the acid activity of HPW while preventing its leaching during catalysis, as observed in similar systems like HPW/SiO_2.[35] Conversely, the HPW/*β*-CD system exhibited structural degradation after only three cycles, in agreement with previous studies,[46,47] suggesting that CD-based materials may lack long-term stability under reaction conditions.

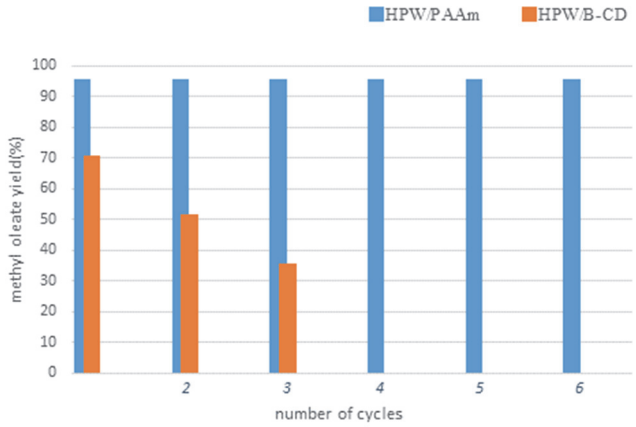

Fig. 8. Reusability of HPW/PAAm and HPW/*β*-CD in esterification reaction.

CONCLUSION

The novelty of this work lies in the use of organic materials as supports to immobilize a soluble polyoxometalate, tungstophosphoric acid ($H_3PW_{12}O_{40}$, HPW). The resulting catalytic systems were tested in the esterification of oleic acid to methyl oleate in the presence of methanol at 60 °C for 3 h. Polyacrylamide hydrogel (PAAm) and cyclodextrins (*β*-CD and HP-*β*-CD) were selected as organic supports, incorporating 20 wt.% HPW. For comparison, HPW supported on silica, a conventional inorganic material, was also evaluated.

Spectroscopic analyses (FT-IR and Raman) confirmed that the Keggin structure of HPW remained intact upon immobilization, regardless of the nature of the support. XRD and SEM results suggest the formation of host–guest inclusion complexes in the HPW/*β*-CD and HPW/HP-*β*-CD systems, and the successful incorporation of HPW into the PAAm hydrogel network.

Regarding their catalytic performance, HPW, HPW/PAAm and HPW/β-CD showed high activity in oleic acid esterification, yielding 97, 94 and 69 % of methyl oleate, respectively, which is significantly higher than the 42 % yield obtained with HPW/SiO_2.

No leaching of the heteropolyacid was detected after 1 h of reaction in the presence of HPW/PAAm or HPW/*β*-CD, as confirmed by FT-IR analysis of the reaction medium after catalyst separation. This highlights the effective retention of HPW within the PAAm network and its stable complexation with *β*-CD.

Catalyst stability tests over multiple cycles (3 h per cycle) revealed excellent reusability for HPW/PAAm, with a constant methyl oleate yield of 94 % even after six cycles. In contrast, degradation of the *β*-CD matrix was observed after only three cycles in the HPW/*β*-CD system.

These results highlight the potential of polyacrylamide hydrogels and cyclodextrins as efficient and environmentally friendly organic supports for the immobilization of a heteropolyacid, paving the way for cleaner and more sustainable catalytic processes.

These new materials have been designed to retain the high Brønsted acidity of HPW while improving its recyclability, dispersion and stability, in particular by minimizing leaching and improving compatibility with the reaction medium.

NOMENCLATURE

PAAm: Polyacrylamide hydrogel
β-CD: β-Cyclodextrin
Hp-*β*-CD: Hydroxypropyl-β-cyclodextrin
CDs: Cyclodextrins
SiO_2: Silica gel
HPW: Tungstophosphoricacid ($H_3PW_{12}O_{40}$)
HPAs: Heteropolyacids
FT-IR: Fourier transform infrared spectroscopy
Raman: Raman spectroscopy
SEM: Scanning electron microscopy
XRD: X-Ray diffraction
EDX: Energy-dispersive X-ray spectroscopy

ИЗВОД

ДОБИЈАЊЕ КАТАЛИЗАТОРА ЗА ЕСТЕРИФИКАЦИЈУ ОЛЕИНСКЕ КИСЕЛИНЕ УКЉУЧИВАЊЕМ $H_3PW_{12}O_{40}$ У ЦИКЛОДЕКСТРИН

FERIEL TOUMI[1], YASMINA IDRISSOU[2,4], TASSADIT MAZARI[1], NICOLAS KANIA[3], ANNE PONCHEL[3], ABDENOUR BOUMACHHOUR[5], NOUARA LAMRANI[1] и CHERIFA RABIA[2]

[1]Laboratory of Applied Chemistry and chemical engineering (LCAGC), Faculty of chemistry, University of Mouloud Mammeri Tizi Ouzou (UMMTO),Tizi Ouzou, Algeria,[2]Laboratory of Natural Gas Chemistry (LCGN), Faculty of Chemistry (USTHB), BP 32, 16111, Algiers, Algeria, [3]Jean Perrin Faculty of Sciences, University of Artois, UCCS - UMR CNRS 8181, Lens, France, [4]Ecole Normale Supérieure Kouba (ENS), Alger, Algeria и [5]Centre de Recherche Scientifique et Technique en Analyses Physico – Chimiques, Bou Ismail, Algeria

У овом раду је циклодекстрин (*β*-CD и HP-*β*-CD) коришћен као матрица за имобилизацију 20 мас. % волфрамфосфорне киселине, $H_3PW_{12}O_{40}$ (HPW) у циљу добијања

катализатора за естерификацију олеинске киселине у метил-олеат коришћењем метанола, који је најчешће коришћени алкохол за ову реакцију. Олеинска киселина је масна киселина која се налази у многим биљним уљима и често се користи као сировина за добијање биодизела. Каталитичке перформансе добијеног хибридног материјала су упоређене са материјалима који су добијени инкорпорирањем HPW у хидрогел полиакриламида (20 мас. % HPW/PAAm) и депоновањем HPW на SiO_2 као конвенционални неорганski носач (20 мас. % HPW/SiO_2). Сви материјали су окарактерисани различитим техникама. У свим случајевима, Кегин структура $H_3PW_{12}O_{40}$ је очувана након имобилизације, што је потврђено FT-IR и Раман спектроскопијом. XRD и SEM анализе су указале на формирање инклузионих комплекса у системима HPW/β-CD и HPW/HP-β-CD, као и успешно инкорпорирање HPW у PAAm матрицу. У реакцији естерификације на 60 °C за 3 h, HPW, HPW/PAAm и HPW/β-CD су показали велику каталитичку ефикасност, достигавши приносе метил-олеата од 97, 94 и 69 %, редом, много веће од приноса који је постигнут са 20 мас. % HPW/SiO_2 (41 %).

(Примљено 27. августа, ревидирано 14. октобра, прихваћено 23. децембра 2025)

REFERENCES

1. S. Liu, Z. Li, K. Han, Y. Wang, S. Niu, J. Liu, J. Zhu, Y. Zheng, *Chem. Eng. Proc. Proc. Intens.* **200** (2024) 109777 (https://doi.org/10.1016/j.cep.2024.109777)
2. G. B. Shimada, A. Cestari, *Renew. Energy* **156** (2020) 389 (https://doi.org/10.1016/j.renene.2020.04.095)
3. B. O. Yusuf, S. A. Oladepo, S. A. Ganiyu, *ACS Omega* **8** (2023) 23720 (https://doi.org/10.1021/acsomega.3c01892)
4. P. Prasertpong, J. Lipp, A. Dong, N. Tippayawong, J. R. Regalbuto, *Catalysts* **13** (2022) 38 (https://doi.org/10.3390/catal13010038)
5. K. A. V. Miyuranga, U. S. P. R. Arachchige, T. M. M. Marso, G. Samarakoon, *Catalysts* **13** (2023) 546 (https://doi.org/10.3390/catal13030546)
6. F. Esmi, S. Masoumi, A. K. Dalai, *Catalysts* **12** (2022) 658 (https://doi.org/10.3390/catal12060658)
7. Z. Wang, L. Liu, *Catal. Today* **376** (2021) 55 (https://doi.org/10.1016/j.cattod.2020.08.007)
8. Y. Patiño, L. Faba, E. Díaz, S. Ordóñez, *J. Environ. Manage.* **365** (2024) 121643 (https://doi.org/10.1016/j.jenvman.2024.121643)
9. M. Alotaibi, Md. A. Bakht, A. I. Alharthi, M. H. Geesi, I. Uddin, H. A. Albalwi, Y. Riadi, *Polycyc. Arom. Compd.* **42** (2022) 3089 (https://doi.org/10.1080/10406638.2020.1852588)
10. J. Alcañiz-Monge, B. E. Bakkali, G. Trautwein, S. Reinoso, *Appl. Catal., B* **224** (2018) 194 (https://doi.org/10.1016/j.apcatb.2017.10.066)
11. C. Leyvison Rafael V. da, C. E. R. Reis, R. de Lima, D. V. Cortez, H. F. de Castro, *RSC Adv.* **9** (2019) 23450 (https://doi.org/10.1039/C9RA04300D)
12. R. P. D. Almeida, R. C. Gomes Aciole, A. Infantes-Molina, E. Rodríguez-Castellón, J. G. Andrade Pacheco, I. D. C. Lopes Barros, *J. Clean. Prod.* **282** (2021) 124477 (https://doi.org/10.1016/j.jclepro.2020.124477)
13. R. Frenzel, D. Morales, G. Romanelli, G. Sathicq, M. Blanco, L. Pizzio, *J. Mol. Catal., A* **420** (2016) 124 (https://doi.org/10.1016/j.molcata.2016.01.026)

14. N. Kumar, R. Gusain, S. Pandey, S. S. Ray, *Adv. Mater. Interf.* **10** (2023) 2201375 (https://doi.org/10.1002/admi.202201375)
15. S. Señorans, E. Rangel-Rangel, E. M. Maya, L. Díaz, *React. Funct. Polym.* **202** (2024) 105964 (https://doi.org/10.1016/j.reactfunctpolym.2024.105964)
16. T. N. Dharmapriya, S.-Y. Wu, K.-L. Chang, P.-J. Huang, *J. Taiwan Inst. Chem. Eng.* **149** (2023) 104997 (https://doi.org/10.1016/j.jtice.2023.104997)
17. S. S. Balula, C. N. Dias, F. Mirante, *Available on SSRN* (2025): https://doi.org/10.2139/ssrn.5387449
18. Z. He, H. Wang, H. Yu, L. Zhang, C. Song, K. Huang, *React. Funct. Polymers* **169** (2021) 105063 (https://doi.org/10.1016/j.reactfunctpolym.2021.105063)
19. E. X. Aguilera Palacios, V. Palermo, A. G. Sathicq, L. R. Pizzio, G. P. Romanelli, *Catalysts* **12** (2022) 1155 (https://doi.org/10.3390/catal12101155)
20. J. Zhu, T. Gotoh, S. Nakai, N. Tsunoji, M. Sadakane, *Mater. Adv.* **2** (2021) 3556 (https://doi.org/10.1039/D1MA00278C)
21. G. Utzeri, P. M. C. Matias, D. Murtinho, A. J. M. Valente, *Front. Chem.* **10** (2022) 859406 (https://doi.org/10.3389/fchem.2022.859406)
22. M. Abbasi, *J. Chinese Chem. Soc*. **64** (2017) 896 (https://doi.org/10.1002/jccs.201600887)
23. D. Boczar, K. Michalska, *Pharmaceutics* **14** (2022) 1389 (https://doi.org/10.3390/pharmaceutics14071389)
24. B. Samannan, J. Selvam, J. Thavasikani, *Asian J. Chem.* **32** (2020) 297 (https://doi.org/10.14233/ajchem.2020.22321)
25. S. Teka, A. Jebnouni, A. A. O. Alrashidi, O. A. Alshammari, N. S. Jaballah, M. S. O. Alhar, M. Majdoub, *J. Mol. Struct.* **1308** (2024) 138044 (https://doi.org/10.1016/j.molstruc.2024.138044)
26. D. S. Dalal, D. R. Patil, Y. A. Tayade, *Chem. Rec.* **18** (2018) 1560 (https://doi.org/10.1002/tcr.201800016)
27. Y. Wu, R. Shi, Y.-L. Wu, J. M. Holcroft, Z. Liu, M. Frasconi, M. R. Wasielewski, H. Li, J. F. Stoddart, *J. Am. Chem. Soc.* **137** (2015) 4111 (https://doi.org/10.1021/ja511713c)
28. S. Aniba, N. Leclerc, C. Falaise, C. Roch-Marchal, S. Akriche, E. Cadot, M. Haouas, *Dalton Trans.* **54** (2025) 12534 (https://doi.org/10.1039/D5DT01317H)
29. M. Segado-Centellas, C. Falaise, N. Leclerc, G. Mpacko Priso, M. Haouas, E. Cadot, C. Bo, *Chem. Sci.* **15** (2024) 15849 (https://doi.org/10.1039/D4SC01949K)
30. F. A. N. Fernandes, *Catal. Res.* **2** (2022) 034 (https://doi.org/10.21926/cr.2204034)
31. Y. Idrissou, T. Mazari, C. Rabia, *J. Iranian Chem. Soc.* **19** (2022) 2553 (https://doi.org/10.1007/s13738-021-02474-8)
32. O. A. Mawlid, H. H. Abdelhady, M. G. Abd El-Moghny, A. Hamada, F. Abdelnaby, M. Kased, S. Al-Bajouri, R. A. Elbohy, M. S. El-Deab, *J. Clean. Prod.* **442** (2024) 140947 (https://doi.org/10.1016/j.jclepro.2024.140947)
33. H. S. Booth (Ed.), *Inorganic Syntheses, Volume I*, McGraw-Hill Book Company, New York, 1939
34. M. T. Pope, *Heteropoly and Isopoly Oxometalates*, Springer-Verlag, Berlin, 1983 (https://link.springer.com/book/9783662120064)
35. Y. Idrissou, T. Mazari, S. Benadji, M. Hamdi, C. Rabia, *React. Kin. Mech. Catal.* **119** (2016) 291 (https://doi.org/10.1007/s11144-016-1042-5)

36. C. Cannilla, G. Bonura, E. Rombi, F. Arena, F. Frusteri, *Appl. Catal., A* **382** (2010) 158 (https://doi.org/10.1016/j.apcata.2010.04.031)
37. C. Rocchiccioli-Deltcheff, M. Fournier, R. Franck, R. Thouvenot, *J. Mol. Struct.* **114** (1984) 49 (https://doi.org/10.1016/S0022-2860(84)87202-6)
38. H. Rachmawati, C. A. Edityaningrum, R. Mauludin, *AAPS PharmSciTech* **14** (2013) 1303 (https://doi.org/10.1208/s12249-013-0023-5)
39. A. Somer, J. R. Roik, M. A. Ribeiro, A. M. Urban, A. Schoeffel, V. M. Urban, P. V. Farago, L. V. D. Castro, F. Sato, C. Jacinto, E. Campesatto, M. S. A. Moreira, A. Novatski, *Mater. Chem. Phys.* **239** (2020) 122117 (https://doi.org/10.1016/j.matchemphys.2019.122117)
40. *Polyoxometalates: From Platonic Solids to Anti-Retroviral Activity*, M. T. Pope, A. Müller, Eds., Kluwer Academic Publishers, Dordrecht, 1994
41. P. Li, Z. Liu, Z. Xia, J. Yang, Optoelect. *Adv. Mater. Rapid Comm.* **17** (2023) 170 (https://oam-rc.inoe.ro/articles/phosphotungstic-acidsilicon-carbide-nanowire-heterostructure-photocatalyst-for-improving-photodegradation-of-rhodamine-b/)
42. D. Han, Z. Han, L. Liu, Y. Wang, S. Xin, H. Zhang, Z. Yu, *Int. J. Mol. Sci.* **21** (2020) 766 (https://doi.org/10.3390/ijms21030766)
43. P. Li, Q. Chen, B. Chen, Z. Liu, *Micro Nano Lett.* **15** (2020) 779 (https://doi.org/10.1049/mnl.2019.0734)
44. X. Xing, Q. Wu, L. Zhang, Q. Shu, *Catalysts* **15** (2025) 412 (https://doi.org/10.3390/catal15050412)
45. Z. Yu, X. Chen, Y. Zhang, H. Tu, P. Pan, S. Li, Y. Han, M. Piao, J. Hu, F. Shi, X. Yang, *Chem. Eng. J.* **430** (2022) 133059 (https://doi.org/10.1016/j.cej.2021.133059)
46. Y. A. Tayade, D. S. Dalal, *Catal. Lett.* **147** (2017) 1411 (https://doi.org/10.1007/s10562-017-2032-6)
47. R. S. Thombal, A. R. Jadhav, V. H. Jadhav, *RSC Adv.* **5** (2015) 12981 (https://doi.org/10.1039/C4RA16699J).

Journal of the Serbian Chemical Society
JSCS-info@shd.org.rs • www.shd.org.rs/JSCS
J. Serb. Chem. Soc. *91* (3) 291–302 (2026)
JSCS–5492
Original scientific paper
Published 26 February, 2026

Optimizing ethylene plant utilities *via* hybrid artificial neural network and first-principles modeling

ALEKSA MILADINOVIĆ[1]*, MIRJANA KIJEVČANIN[2], JOVAN JOVANOVIĆ[2], SABLA ALNOURI[3], VLADIMIR STIJEPOVIĆ[1] and MIRKO STIJEPOVIĆ[2]

[1]*Institute of Chemistry, Technology and Metallurgy, National Institute of the Republic of Serbia, University of Belgrade, Njegoševa 12, 11000 Belgrade, Serbia,* [2]*Faculty of Technology and Metallurgy, University of Belgrade, Karnegijeva 4, 11120 Belgrade, Serbia and* [3]*Gas Processing Center, College of Engineering, Qatar University, Doha, Qatar*

(Received 19 September, revised 22 November, accepted 3 December 2025)

Abstract: In this study, a hybrid modeling approach combining first-principles equations with an artificial neural network was developed to reduce operating costs and carbon emissions in process utility systems of an ethylene plant. The artificial neural network accurately predicted turbine power outputs under various operating conditions, with low maximum absolute percentage errors across all three turbines, demonstrating its ability to effectively capture nonlinear system behavior. The economic analysis showed that natural gas prices have a greater cumulative impact on operating expenses than the carbon tax due to their greater variability. Although the carbon tax has a higher local sensitivity, the steady increase in natural gas prices represents a persistent economic burden. This demonstrates the importance of managing fuel costs and monitoring changes in carbon policy to mitigate sudden increases in operating costs. With increasing output, the operating costs of the propylene and cracked gas turbines rose almost linearly, with the costs per megawatt rising more sharply for the propylene turbine. The ethylene turbine significantly impacted operating expenses despite lower output, showing that small output changes can affect costs. Overall, the proposed methodology provides a reliable framework for optimizing energy performance, predicting fuel consumption and supporting operational decision-making in large-scale processes.

Keywords utility system; modeling; artificial neural network; energy efficiency.

INTRODUCTION

Utility systems are fundamental components in a wide range of industrial applications, from power generation and chemical processing to manufacturing

* Corresponding author. E-mail: aleksa.miladinovic@ihtm.bg.ac.rs
https://doi.org/10.2298/JSC250917090M

and district heating. These systems typically involve complex thermodynamic processes, including heat exchange, phase transformation, and mechanical work, often facilitated through steam turbines, boilers, heat exchangers and multi-stage compressors. They represent a notable example where optimizing operating parameters can yield significant benefits, owing to their inherent susceptibility to energy efficiency losses. Consequently, the optimization of operating parameters in utility systems can lead to substantial energy savings and enhanced overall system performance. To overcome the limitations of purely physical or purely data-driven approaches, hybrid modeling has emerged as a promising framework. Hybrid models integrate deterministic and stochastic elements to leverage the strengths of both domains, achieving the precision and structure of rule-based systems while incorporating the flexibility and uncertainty modeling of probabilistic approaches, ultimately enhancing predictive accuracy, robustness and adaptability in complex environments. In this context, stochastic elements refer to data-driven approaches such as artificial neural networks, which, although deterministic at inference, incorporate stochasticity during training and can effectively capture complex, nonlinear relationships under uncertainty. When applied to utility systems, hybrid modeling can enhance fault detection, predictive maintenance, performance optimization and real-time control.

Equipment like steam turbines and multi-stage compressors, after extended periods of use, lose efficiency and are prone to mechanical wear, performance degradation, and increased maintenance requirements. By leveraging data-driven models, it is possible to monitor the performance of such equipment in real time and implement optimization strategies that extend equipment life and maintain energy efficiency.

Numerous studies have optimized the performance of utility systems using various modeling approaches. Mavromatis and Kokossis[1] developed a turbine hardware model based on Willan's line, while Zhu *et al.*[2] and Li *et al.*[3] used mixed-integer nonlinear programming (MINLP) models to optimize multi-turbine utility systems, achieving cost and coal reductions. Recent work[4–8] has integrated artificial intelligence (AI) techniques, such as artificial neural networks (ANN) and machine learning, to predict performance and improve the operational efficiency of steam turbines and related systems. Various machine learning approaches have been applied to energy systems, including data envelopment analysis with artificial neural networks for petrochemical energy optimization,[4] steam methane reforming control,[5] extreme learning for steam turbine monitoring[6] and regression models for boiler and turbine performance.[7] Despite these advances, few studies[9–11] have combined deterministic models with ANNs to simultaneously increase steam production efficiency and reduce costs. A reduction of 1.4 % in steam production costs was achieved by using a hybrid ANN model to optimize turbine operating para-

meters, as demonstrated by Li *et al.*[9] A hybrid ANN-mechanistic model was developed to accurately characterize the performance of multistage compressors, as shown by Chu *et al.*[10] Another study[11] modeled and optimized a steam turbine power plant with fifteen design variables, resulting in up to a 3.76 % increase in thermal efficiency and a 3.84 % reduction in total cost rate compared to actual plant data. This highlights the potential for hybrid models that utilize both physical principles and data-driven methods for better adaptability and accuracy.

Most existing approaches tend to rely heavily on deterministic models, which may lack flexibility especially when experimental measurement of all required operating parameters is not available. As a result, there is significant potential for further exploration and development of hybrid modeling approaches that combine the strengths of both physical principles and data-driven techniques. Such integrated models may offer higher predictive power and adaptability of neural networks while maintaining the transparency and robustness of first-principles equations.

In this study, a hybrid modeling approach was developed to minimize the operational expenditure of the utility system by integrating deterministic optimization techniques with artificial neural networks, thereby enhancing the system's efficiency, reliability and cost-effectiveness under varying operational conditions.

PROBLEM STATEMENT AND MODEL FORMULATION

The utility system analyzed in this study is illustrated in Fig. 1. Steam is initially generated in a boiler and routed to a high-pressure (HP) steam header, which serves as the central distribution point for steam delivery across the plant. From the HP header, steam is directed to three steam turbines, designated as RT-1, RT-2 and RT-3, each serving distinct process units associated with cracked gas, propylene, and ethylene production, respectively. Additionally, a portion of the HP steam is diverted through a pressure reducing valve (RV-1), which lowers the pressure before routing it into the medium-pressure (MP) steam header and ultimately to the condensate system.

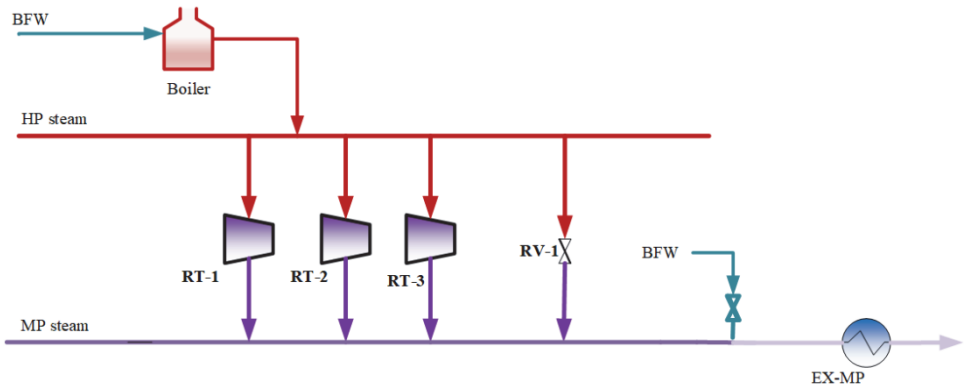

Fig. 1. Utility system.

Within the MP header, the medium-pressure steam is mixed with boiler feed water (BFW) to adjust its thermal state. This mixing reduces the steam temperature to the corresponding saturation temperature at the designated pressure level, thereby ensuring that the steam entering downstream units is saturated rather than superheated. Maintaining saturated steam conditions is essential to protect equipment and ensure optimal performance, particularly for components designed to operate specifically under such conditions.

Although a deterministic model of the boiler is available and can be reliably used to simulate steam generation across a range of operating conditions, modeling the rest of the utility system poses significant challenges.

In particular, the absence of sufficient real-time measurements and detailed operating data for key components – including the steam turbines (RT-1, RT-2 and RT-3), the pressure reducing valve (RV-1), and the downstream steam network – limits the ability to construct a fully deterministic model for the entire system. These components exhibit complex, nonlinear behavior that cannot be accurately captured without comprehensive instrumentation and historical performance data.

To address this limitation, a hybrid modeling approach has been employed. The boiler is modeled using a deterministic, first-principles framework grounded in thermodynamic laws, ensuring accurate representation of steam generation processes. For the remaining components of the utility system, an artificial neural network (ANN) is developed using available historical operational data. The ANN is trained to capture the nonlinear relationships and dynamic behavior of these units, effectively compensating for the lack of detailed physical models and real-time measurements.

This hybrid approach combines the strengths of both modeling paradigms – physical accuracy from the deterministic model and adaptive predictive capability from the ANN. As a result, it enables a more comprehensive and practical representation of the entire utility system, supporting improved performance analysis, operational optimization, and informed decision-making under variable plant conditions. Therefore, the primary goal of this work is to optimize the utility system with respect to steam generation, aiming to reduce operating expenses (OPEX) and simultaneously lower CO_2 emissions. By minimizing the amount of steam generated (and consequently the natural gas consumption required in the boiler) both economic and environmental benefits can be achieved.

The boiler hardware model (BHM) was taken from the study of Shang and Kokossis,[12] which considers the relationship between fuel input, heat loss, and the resulting steam output. The fuel requirement (Q_{fuel}) is calculated based on the heat added to the steam (Q_{steam}) and the heat losses (Q_{loss}):

$$Q_{\text{fuel}} = Q_{\text{steam}} + Q_{\text{loss}} \tag{1}$$

The heat, Q_{steam}, can be estimated from the following relation:

$$Q_{\text{steam}} = M_{\text{HP}}(C_p T_{\text{sat}} + q) \tag{2}$$

where C_p represents the specific heat of saturated steam (kJ kg^{-1} K^{-1}), T_{sat} is the temperature of the saturated steam (K), q denotes the specific heat load of fuel (kJ kg^{-1}) and M_{HP} is the mass flow rate of high-pressure steam (t·h^{-1}); the heat losses are estimated from:

$$Q_{\text{loss}} = (aM_{\text{HPmax}} + bM_{\text{HP}})(C_p T_{\text{sat}} + q) \tag{3}$$

where a and b represent regression parameters adjusted on the basis of the experimental data and M_{HPmax} is the maximum steam mass flow rate through the boiler (t h^{-1}).

By combining Eqs. (2) and (3), the total energy input from fuel combustion, Q_{fuel}, can be calculated using the following equation:

$$Q_{\text{fuel}} = (aM_{\text{HPmax}} + (1+b)M_{\text{HP}})(C_pT_{\text{sat}} + q) \quad (4)$$

The BHM is a deterministic model for predicting the fuel demand of a boiler based on its size, load and operating conditions. It takes into account heat losses and thermodynamic properties, making the model more realistic compared to constant efficiency assumptions.

Due to the lack of measurement data for key operating parameters- in particular for the outlets of the three turbines feeding into the MP header, their efficiencies, and the outlet conditions of RV-1 – the remaining utility system cannot be accurately modeled using conventional deterministic methods. Therefore, an artificial neural network (ANN), presented in Fig. 2, is used to capture the system behavior under these conditions.

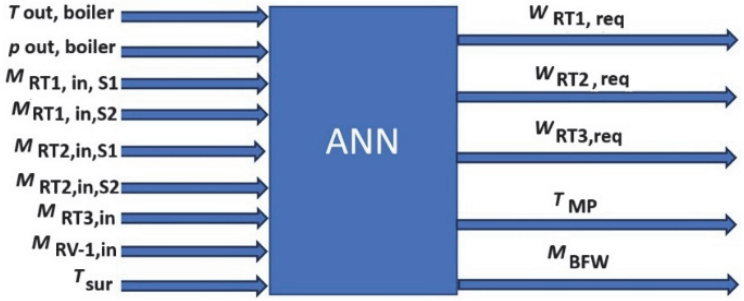

Fig. 2. The implemented artificial neural network.

The input data for the ANN – including the outlet temperature and pressure of the boiler stream, the inlet steam mass flow rates to the two sections of turbine RT-1, to the two sections of turbine RT-2, to turbine RT-3, to the pressure reduction valve RV-1 and the ambient temperature – are obtained directly from the plant measurement system.

By combining the above-mentioned BHM and the artificial neural network (details are given in the Supplementary material to this paper), a new hybrid model was developed using Python, specifically the Keras library.[13] Conventional linear and nonlinear models typically require larger datasets and often struggle to capture complex system interactions. In contrast, our hybrid model is more efficient and achieves comparable or improved performance with substantially less data. Although it demonstrates improved prediction accuracy over the deterministic model, its applicability is subject to certain constraints. The hybrid framework is valid only within the operational range covered by the training data and underlying assumptions, which include steady-state and dynamic conditions corresponding to boiler loads. Additionally, the neural network component of this hybrid model cannot account for unmeasured disturbances. The primary purpose of this model is to reduce operating costs and simultaneously lower CO_2 emissions, as quantified using the following equations:

$$M_{\text{HP}} = M_{\text{RT1,in}} + M_{\text{RT2,in}} + M_{\text{RT3,in}} + M_{\text{RV-1,in}} \quad (5)$$

$$M_{\text{MP}} = M_{\text{RT1,out}} + M_{\text{RT2,out}} + M_{\text{RT3,out}} + M_{\text{RV-1,out}} + M_{\text{BFW,MP,NN}} \quad (6)$$

All the following mass flow rates, M_i, are given in tons per hour (t h^{-1}) and are defined as: M_{HP} – required for the high-pressure steam; $M_{\text{RT1,in}}$ – required inlet for the cracked gas turbine;

$M_{RT2,in}$ – required inlet for the propylene turbine; $M_{RT3,in}$ – required inlet for the ethylene turbine; M_{MP} – of the medium-pressure steam header; $M_{RT1,out}$ – of the cracked gas turbine outlet; $M_{RT2,out}$ – of the propylene turbine outlet; $M_{BFW,MP,NN}$ – boiler feed water stream entering the MP header, which is estimated using the ANN.

Eq. (5) defines the steam mass flow in the high-pressure steam header (HP) as the cumulative sum of the inlet mass flows to the three steam turbines and the RV-1(MRV-1,in). Eq. (6) defines the steam mass flow rate in the medium-pressure (MP) steam header as the cumulative sum of the outlet mass flows from the three steam turbines, the outlet of RV-1(MRV-1,out) and the boiler feed water stream entering the MP header. The boiler feed water stream is estimated using the artificial neural network. The total heat output and natural gas (NG) flow rate, are given by the following relations:

$$Q = M_{BFW}(h_L - h_{BFW}) + M_{HP}(h_{SH} - h_L) \quad (7)$$

$$M_{NG} = \frac{Q}{0.85LHV} \quad (8)$$

where Q is the total heat output (MW), M_{BFW} is the mass flow rate of the boiler feed water (t h^{-1}), h_L is the specific enthalpy of the liquid water at operating pressure (kJ kg^{-1}), h_{BFW} is the specific enthalpy of the boiler feed water (kJ kg^{-1}), h_{SH} is the specific enthalpy of the superheated steam leaving the boiler (kJ kg^{-1}), M_{NG} is the mass flow rate of natural gas (kg s^{-1}) and LHV is the lower calorific value of natural gas (MJ kg^{-1}).

Eqs. (7) and (8) quantify the required fuel input for boiler heating and determine the corresponding amount of natural gas needed to provide this thermal energy. In Eq. (8), 0.85 means that 85 % of the energy from the combustion of natural gas is actually transferred to the boiler as useful heat. Eq. (9) defines the operational expenditure, *OPEX*, as the sum of the cost of the required natural gas and the carbon tax associated with the corresponding CO_2 emissions resulting from its combustion:

$$OPEX = M_{NG} \times Pr(NG) + M_{NG} \times EF(CO_2) \times CTX \quad (9)$$

where Pr(NG) is the price of natural gas (\$·kg^{-1}), $EF(CO_2)$ is the emission factor for CO_2 (kg CO_2·kg^{-1} NG) and CTX is the carbon tax (\$·kg^{-1}).

OPEX is minimized based on the following constraints:

$$|W_{RTi,req} - W_{RTi,NN}| \leq 0.01, \text{ for } i = 1,2,3 \quad (10)$$

$$M_{MP} \geq M_{MP,req} \quad (11)$$

where $W_{RTi,req}$ is the required (or actual) power output of turbine i (MW), $W_{RTi,NN}$ is the predicted power output of turbine i, obtained from the artificial neural network (MW) and $M_{MP,req}$ is the required mass flow rate in the medium-pressure steam header (t h^{-1}).

Eq. (10) states that the discrepancy between the required output of the three turbines and the values predicted by the neural network must be minimized, while Eq. (11) enforces the mass balance condition for the medium-pressure steam line, which states that the incoming steam mass flow must be equal to the medium-pressure steam demand.

The proposed hybrid model integrates a deterministic BHM, which is used to compute the required fuel input based on thermodynamic principles, with an artificial neural network (ANN) module that supplements the system by providing additional data necessary for imposing model constraints.

Parameter estimation

The parameters for this hybrid model of the boiler and the utility system given in Table I, were estimated based on historical operating data from the utility system.

TABLE I. Parameters of the boiler and the utility system

Boiler		Utility system	
M_{HP} / t h^{-1}	169	$T_{out,boiler}$ / °C	465
M_{BFW} / t h^{-1}	178	$p_{out,boiler}$ (bar)	102
h_{BFW} / kJ kg^{-1}	502.4	$M_{RT1.in,\ S1}$ / t h^{-1}	86.0
h_{L} / kJ kg^{-1}	1416.4	$M_{RT1.in,\ S2}$ / t h^{-1}	45.4
h_{SH} / kJ kg^{-1}	3280.1	$M_{RT2.in,\ S1}$ / t h^{-1}	60.0
Q / MW	132.6	$M_{RT2.in,\ S2}$ / t h^{-1}	46.3
LHV / MJ kg^{-1}	52.5	$M_{RT3.in}$ / t h^{-1}	22.9
M_{NG} / kg s^{-1}	3	$M_{RV\text{-}1.in}$ / t h^{-1}	0.06
M_{HPmax} / t h^{-1}	260	T_{sur} / °C	15
a	0.0126		
b	0.2156		

In addition, in estimating the ANN parameters, the optimization framework was used to identify the optimal operating conditions of the utility system for input into the neural network. These parameters were rescaled by normalizing the input parameters to a dimensionless range between –1 and 1. For each variable, the normalized (optimized) values were computed according to:

$$x_{opt} = 2\frac{x_{in} - x_{min}}{x_{max} - x_{min}} - 1 \tag{12}$$

where x_{in} is the actual input value, and x_{min} and x_{max} represent the lower and upper bounds of the corresponding parameter. This transformation ensures that all parameters are optimized consistently within their feasible range.

After constructing the neural network, the weight matrices were initialized for each layer. Specifically, W_1 and W_2, corresponding to the first and second hidden layers, were generated with dimensions [12×9], while the output layer matrix W_3 was generated with dimensions [5×12]. In addition, bias vectors were created for each layer: c_1 and c_2 for the hidden layers (each containing 12 elements) and c_3 for the output layer (containing 5 elements). Thus, both hidden layers consisted of 12 neurons, whereas the output layer comprised 5 neurons.

For clarity and reproducibility, the complete numerical values of the generated weight matrices (W_1, W_2, W_3) and bias vectors (c_1, c_2, c_3) can be provided upon request.

After the weight and bias matrices were generated, the pre-activation values Z and activation values A were estimated (see Supplementary material, Eqs. (S1) and (S2), respectively). The input values, as previously mentioned, were normalized prior to the calculations.

RESULTS AND DISCUSSION

The results obtained from the hybrid modeling framework demonstrate its capability to accurately simulate the dynamic behavior of the utility system under diverse operating conditions. Fig. 3 illustrates the relationship between operating expenditure (*OPEX*) and two important economic factors: natural gas price (on the

left *y*-axis) and carbon tax (on the right *y*-axis). Each variable is shown as a function of its own OPEX range, reflecting its individual impact on system costs.

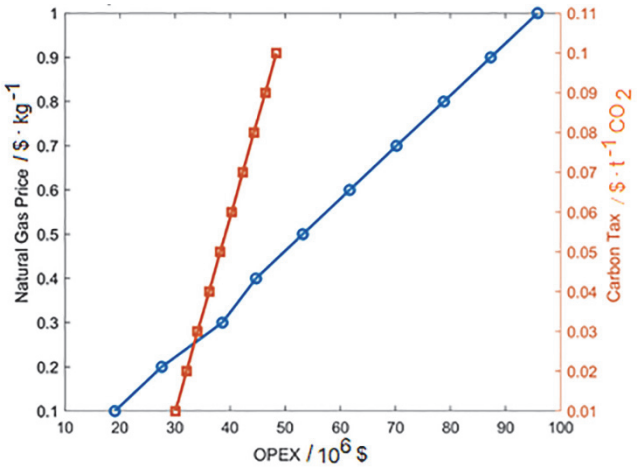

Fig. 3. Correlation between operational expenditure, natural gas price and carbon tax.

Fig. 3 shows that the price of natural gas has a much greater impact on operating expenses than the carbon tax. The trends show a positive linear correlation between *OPEX* and both variables. While the carbon tax curve has a steeper local slope, the natural gas price varies over a much wider range of operating expenditures, implying that natural gas price exerts a greater cumulative influence on *OPEX* over the entire operating window. The natural gas price exhibits a consistent and gradual increase across a wide range of operating expenses, suggesting a stable but cumulative economic burden. In contrast, the carbon tax exhibits higher local sensitivity, suggesting that even small increases in carbon cost policies within certain thresholds can lead to noticeable *OPEX* fluctuations.

In Fig. 4 the effects of cracked gas turbine power output, propylene turbine power output and ethylene turbine power output, on operational expenditure are presented. Fig. 4a shows that increasing the cracked gas turbine output from 7 to 14 MW leads to an almost linear increase in operating costs, from about $ 32.8 million to $ 38.9 million. This indicates that the cracked gas turbine has a significant and direct impact on operating costs, likely because it provides most of the mechanical power in the system. The steady increase indicates a cost-dependent relationship, possibly related to fuel consumption, load conditions, or efficiency degradation at higher loads.

Moreover, Fig. 4b demonstrates a similar trend for the propylene turbine, where operating costs rise from about $ 41.3 million to $ 48.6 million as output increases from 7 to 12 MW. The steeper increase compared to Fig. 4a suggests that the propylene turbine has an even greater marginal cost per MW, possibly due to

the particular operating conditions or energy conversion efficiency. This result underlines the importance of carefully managing the output of this turbine to minimize cost impact. Similarly, Fig. 4c demonstrates the relationship between the output of the ethylene turbine and *OPEX*, where the output range is smaller (1.25 to 2.4 MW). *OPEX* increases slightly from around $ 38.5 million to $ 39.6 million. While the absolute increase is smaller than in the previous cases, the relatively large increase over a narrow range indicates that even small increases in ethylene turbine output can affect system costs.

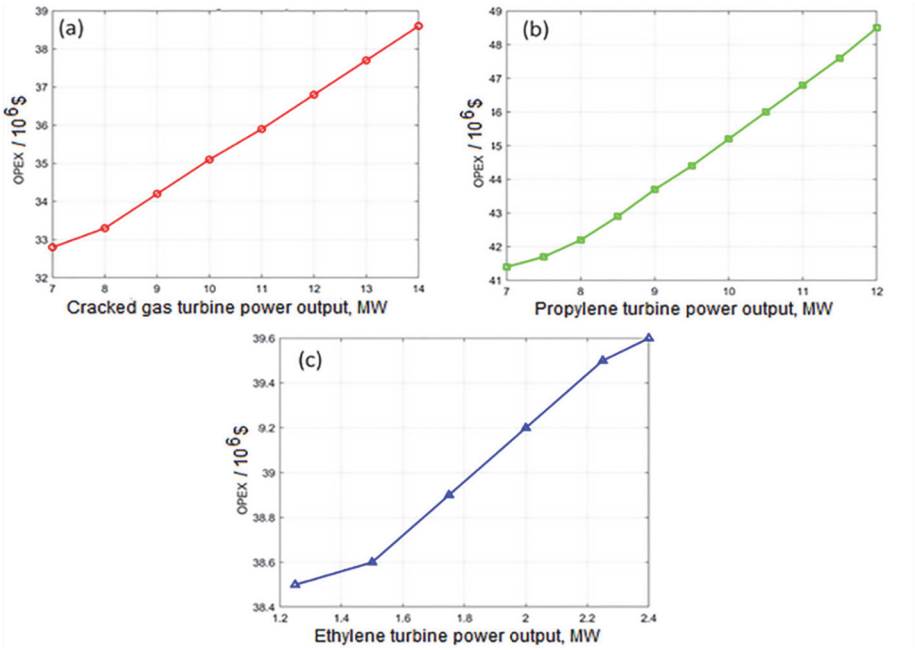

Fig. 4. Effect of: a) cracked gas turbine power output, b) propylene turbine power output and c) ethylene turbine power output, on operational expenditure

CONCLUSION

In this study, a hybrid modeling approach was developed that combines first-principles equations with artificial neural network models to reduce operating costs and lower carbon emissions. The ANN model was trained to predict the required turbine power outputs under different operating conditions. The deviation between the predicted and actual turbine performance served as an important performance measure to evaluate the accuracy of the model. The results show a high agreement between the ANN predictions and the measured data, with low maximum absolute percentage error values for all three turbines. These results confirm the ability of the ANN to effectively capture the nonlinear behavior of steam-driven systems under variable loads. The results also show that the natural gas

price has a much larger cumulative impact on operating costs than the carbon tax, primarily due to its broader range of variation within the operating window. While the carbon tax demonstrates a steeper local slope, indicating high sensitivity to incremental changes, the natural gas price trend is more gradual but sustained, suggesting a consistent and growing economic burden. This difference highlights the importance of fuel cost management and diversification strategies, as well as the need to monitor evolving carbon policy thresholds that could trigger sudden increases in operating costs. The cracked gas and propylene turbines show a sharp, near-linear increase in operating costs as output increases, with the propylene turbine showing a greater increase in cost per MW. The ethylene turbine, while operating in a lower range, also has a noticeable impact on OPEX, indicating that even small changes in output can affect system costs. The proposed methodology provides a reliable and efficient framework for optimizing energy performance, predicting fuel consumption and supporting decision-making in large thermal process systems.

NOMENCLATURE

ANN – Artificial neural network
a – Regression parameter adjusted on the basis of the experimental data
BFW – Boiler feed water
BHM – Boiler hardware model
b – Regression parameter adjusted on the basis of the experimental data
C_p – Specific heat of saturated steam (kJ kg^{-1} K^{-1})
CTX – Carbon tax (\$ kg^{-1})
c_i – i = 1,2,3, bias vector
EF(CO_2) – Emission factor for CO_2 (kg CO_2 kg^{-1} NG)
HP – High pressure
h_{BFW} – Specific enthalpy of the boiler feed water (kJ kg^{-1})
h_L – Specific enthalpy of the liquid water at operating pressure (kJ kg^{-1})
h_{SH} – Specific enthalpy of the superheated steam leaving the boiler (kJ kg^{-1})
LHV – Lower calorific value of natural gas (MJ kg^{-1})
M – Steam mass flow rate (t h^{-1})
MINLP – Mixed integer nonlinear programming
MP – medium pressure
M_{BFW} – Mass flow rate of the boiler feed water (t h^{-1})
$M_{BFW,MP,NN}$ – Boiler feed water steam entering the MP header estimated by ANN (t h^{-1})
M_{HP} – Mass flow rate of HP steam (t h^{-1})
M_{HPmax} – Max. steam mass flow rate through the boiler (t h^{-1})
M_{MP} – Mass flow rate of MP steam (t h^{-1})
$M_{MP,req}$ – Required mass flow rate of MP steam (t h^{-1})
M_{NG} – Natural gas mass flow rate (kg s^{-1})

SUPPLEMENTARY MATERIAL

Additional data and information are available electronically at the pages of journal website: https://www.shd-pub.org.rs/index.php/JSCS/article/view/13552, or from the corresponding author on request.

Acknowledgement. This research has been financially supported by the Ministry of Science, Technological Development and Innovation of Republic of Serbia (Contract No: 451-03--136/2025-03/200026 and 451-03-136/2025-03/200135).

ИЗВОД

ОПТИМИЗАЦИЈА РАДА СИСТЕМА ПАРЕ У ФАБРИЦИ ЕТИЛЕНА ПОМОЋУ ХИБРИДНОГ МОДЕЛА ВЕШТАЧКЕ НЕУРОНСКЕ МРЕЖЕ И МОДЕЛА ЗАСНОВАНОГ НА ФУНДАМЕНТАЛНИМ ПРИНЦИПИМА

АЛЕКСА МИЛАДИНОВИЋ[1], МИРЈАНА КИЈЕВЧАНИН[2], ЈОВАН ЈОВАНОВИЋ[2], SABLA ALNOURI[3], ВЛАДИМИР СТИЈЕПОВИЋ[1] и МИРКО СТИЈЕПОВИЋ[2]

[1]Институт за хемију, технологију и металургију, Институт од националног значаја за Републику Србију, Универзитет у Београду, Његошева 12, 11000 Београд, [2]Технолошко–металуршки факултет, Универзитет у Београду, Карнегијева 4, 11000 Београд и [3] Gas Processing Center, College of Engineering, Qatar University, Doha, Qatar

У овом раду је развијен модел који комбинује фундаменталне једначине и вештачку неуронску мрежу у циљу смањења оперативних трошкова и емисије CO_2 у оперативним системима фабрике етилена. Вештачка неуронска мрежа може да прецизно предвиди снагу три турбине под различитим оперативним условима са ниском максималном апсолутном грешком, што демонстрира способност мреже да прецизно прикаже нелинеарно понашање система. Економска анализа система је показала да цене природног гаса имају већи, кумулативни утицај на оперативне трошкове од пореза на CO_2 због њихове веће варијабилности. Иако порез на CO_2 има већи непосредан утицај, стални раст цена природног гаса представља дугорочно, економско оптерећење. Ово указује на значај управљања трошковима горива и праћење промена у политици заштите од утицаја CO_2 како би се ублажила нагла повећања оперативних трошкова. Са порастом снаге, оперативни трошкови пропиленске и крек-гас турбине расту готово линеарно, при чему је уочен израженији раст трошкова по мегавату код пропиленске турбине. Етиленска турбина је имала значајан утицај на оперативне трошкове упркос нижем производном капацитету, што указује да чак и мале промене у снази имају утицај на трошкове. Предложена методологија пружа поуздан оквир за енергетску оптимизацију, предвиђање потрошње горива и подршку у доношењу одлука у великим, индустријским процесима.

(Примљено 17. септембра, ревидирано 22. новембра, прихваћено 3. децембра 2025)

REFERENCES

1. S. P. Mavromatis, A. C. Kokossis, *Chem. Eng. Sci.* **53** (1998) 1585 (https://doi.org/10.1016/s0009-2509(97)00431-4)
2. Q. Zhu, X. Luo, B. Zhang, Y. Chen, S. Mo, *Energy* **97** (2016) 191 (https://doi.org/10.1016/j.energy.2015.12.112)
3. Z. Li, W. Du, L. Zhao, F. Qian, *Ind. Eng. Chem. Res.* **53** (2014) 11021 (https://doi.org/10.1021/ie402438t)
4. Y.-M. Han, Z.-Q. Geng, Q.-X. Zhu, *Energy Convers. Manage.* **124** (2016) 73 (https://doi.org/10.1016/j.enconman.2016.07.002)
5. Y. Wang, X. Cui, D. Peters, B. Çıtmacı, A. Alnajdi, C. G. Morales-Guio, P. D. Christofides, *Dig. Chem. Eng.* **12** (2024) 100173 (https://doi.org/10.1016/j.dche.2024.100173)

6. G. Zhou, X. Li, J. Liu, D. Yu, F. Wang, J. Wan, in *Proceedings of Prognostics and System Health Management Conference*, Harbin, China, 2017, , pp. 1–7 (https://doi.org/10.1109/phm.2017.8079195)
7. M. G. R. Shuvo, N. Sultana, L. Motin, M. R. Islam, in *Proceedings of the 1st International Conference on Artificial Intelligence and Data Analytics*, Riyadh, Saudi Arabia, 2021, pp. 170–175 (https://doi.org/10.1109/caida51941.2021.9425308)
8. H. Zhao, *arXiv* (2020) preprint, arXiv:2002.02402 (https://doi.org/10.48550/arxiv.2002.02402)
9. Z. Li, L. Zhao, W. Du, F. Qian, *Chin. J. Chem. Eng.* **21** (2013) 520 (https://doi.org/10.1016/s1004-9541(13)60530-3)
10. F. Chu, F. Wang, X. Wang, S. Zhang, *Neural Comput. Appl.* **24** (2013) 1259 (https://doi.org/10.1007/s00521-013-1347-5)
11. F. Hajabdollahi, Z. Hajabdollahi, H. Hajabdollahi, *Appl. Soft Comput.* **12** (2012) 3648 (https://doi.org/10.1016/j.asoc.2012.06.006)
12. Z. Shang, A. Kokossis, *Comput. Chem. Eng.* **28** (2004) 1673 (https://doi.org/10.1016/j.compchemeng.2004.01.010)
13. F. Chollet, *Keras*, 2015 (https://keras.io).

Journal of the Serbian Chemical Society
JSCS-info@shd.org.rs • www.shd.org.rs/JSCS
J. Serb. Chem. Soc. 91 (3) S114–S115 (2026) *Supplementary material*

SUPPLEMENTARY MATERIAL TO

Optimizing ethylene plant utilities *via* hybrid artificial neural network and first-principles modeling

ALEKSA MILADINOVIĆ[1]*, MIRJANA KIJEVČANIN[2], JOVAN JOVANOVIĆ[2], SABLA ALNOURI[3], VLADIMIR STIJEPOVIĆ[1] and MIRKO STIJEPOVIĆ[2]

[1]*Institute of Chemistry, Technology and Metallurgy, National Institute of the Republic of Serbia, University of Belgrade, Njegoševa 12, 11000 Belgrade, Serbia,* [2]*Faculty of Technology and Metallurgy, University of Belgrade, Karnegijeva 4, 11120 Belgrade, Serbia and* [3]*Gas Processing Center, College of Engineering, Qatar University, Doha, Qatar*

J. Serb. Chem. Soc. 91 (3) (2026) 291–302

PROBLEM STATEMENT AND MODEL FORMULATION

Artificial neural network (ANN) is used to capture the system behavior (illustrated in Fig. 1 in the main body of the paper).

This configuration defines the input layer of the ANN with nine nodes, each corresponding to one of the input parameters. Specifically, the input data was normalized to the range [-1,1] using min-max normalization and fed into a feedforward neural network consisting of two hidden layers with twelve nodes each and an output layer with five nodes. The forward pass of the hidden layers of the network is calculated by applying a linear transformation followed by a non-linear activation function. The linear transformation consists of a weighted sum of the inputs plus a bias term:

$$Z = (\sum_{i=0}^{n} W_i \cdot X_i) + c \quad \text{(S1)}$$

where Z is a pre-activation value, W is a weight matrix associated with the i neuron, c is a bias vector, and X is an input vector for the neuron i.

The used non-linear activation function (A) is the hyperbolic tangent function, which is implemented in the following equivalent form:

$$A = \frac{2}{1+e^{-2Z}} - 1 \quad \text{(S2)}$$

The output layer consists of five nodes representing the required power of the three turbines ($W_{RT1,\mathrm{req}}$, $W_{RT2,\mathrm{req}}$ and $W_{RT3,\mathrm{req}}$) the temperature of the MP steam before mixing with the BFW and the mass flow rate of the BFW in the mixing process. This level only uses the linear transformation.

* Corresponding author. E-mail: aleksa.miladinovic@ihtm.bg.ac.rs

The neural network was trained with a data set that was split 80 % for training, 10 % for validation and 10 % for testing. The Levenberg–Marquardt backpropagation algorithm, which is characterized by its efficiency and fast convergence in non-linear regression problems, was used for training. The number of training epochs was set to 10000 to ensure sufficient training iterations. The maximum absolute percentage error (MAPE) was used to evaluate the prediction accuracy, as it is a more representative measure of the model's performance, especially when the data contain variables with different magnitudes.

The performance of the neural network component during the training phase is illustrated in Fig. S-1, demonstrating its effectiveness in learning the underlying patterns and relationships within the operational data.

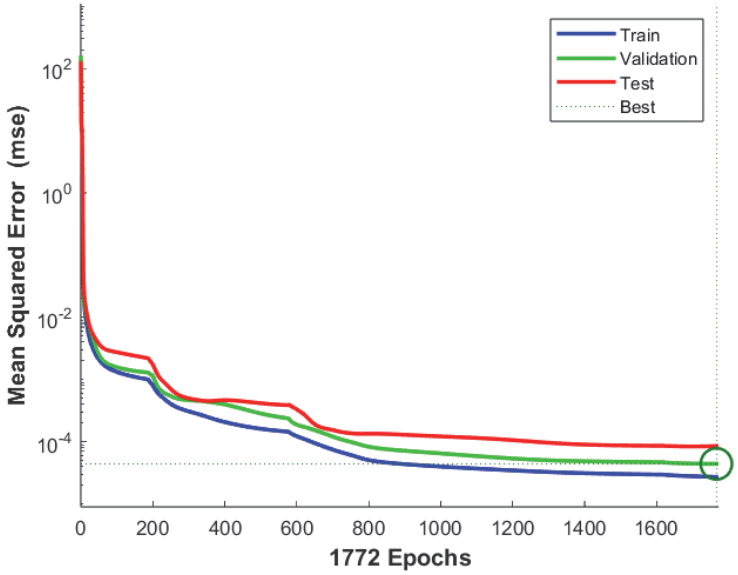

Fig. S-1. Correlation plots of neural network predictions during training, validation, and testing.

The model was trained for 1772 epochs, monitoring the mean squared error (MSE) for the training, validation and test datasets. The training curve shows a rapid initial decrease in error, followed by a slower convergence phase, finally reaching a minimum validation error of 4.4136×10^{-5} at epoch 1766. The close agreement between the training, validation and test curves indicates good generalization and shows that the model was not over-fitted to the training data.

To further evaluate the prediction accuracy, the maximum absolute percentage error (MAPE) was calculated for each of the five output variables. The resulting MAPE values were 0.148 %, 0.221 %, 0.491 %, 0.023 % and 0.199 %, confirming the high precision of the model for all outputs.

Journal of the Serbian Chemical Society
JSCS@tmf.bg.ac.rs • www.shd.org.rs/JSCS
J. Serb. Chem. Soc. 91 (3) 303–316 (2026)
JSCS–5493
Original scientific paper
Published 26 February, 2026

Removal of Pb(II), Cd(II) and Zn(II) from landfill soil and leachate using a graphene oxide membrane

DRAGANA STEVIĆ[1]*, SUNČICA SUKUR[2], RADOVAN KUKOBAT[3], SUZANA GOTOVAC ATLAGIĆ[2], PREDRAG ILIĆ[4], FRANCESCO SIRIO FUMAGALLI[5], ANDREA VALSESIA[5], PASCAL COLPO[5] and SVETLANA POPOVIĆ[1]**

[1]Faculty of Technology Novi Sad, University of Novi Sad, Boulevard cara Lazara 1, Novi Sad, Serbia, [2]Faculty of Natural Sciences and Mathematics, Department of Chemistry, University of Banja Luka, Mladena Stojanovića 2, 78000, Banja Luka, the Republic of Srpska, Bosnia and Herzegovina, [3]Faculty of Technology, Department of Chemical Engineering and Technology, University of Banja Luka, B.V Stepe Stepanovića 73, Banja Luka, the Republic of Srpska, Bosnia and Herzegovina, [4]Institute for Protection and Ecology of the Republic of Srpska, Banja Luka, Bosnia and Herzegovina and [5]European Commission, Joint Research Centre (JRC), Ispra, Italy

(Received 5 May, revised 27 June, accepted 29 October 2025)

Abstract: Since rainwater extracts toxic metals from landfills, creating harmful leachate, developing methods to remove these metals is necessary. This work presents a method of toxic metal ions removal from a loam-type soil consisting of washing the soil with a mild washing agent to extract toxic metals in a leachate, and a purification of the leachate by filtering it through a synthesized graphene oxide (GO) membrane. As washing agents, the pure water and a mild solution of HCl (0.01 M) were tested. The GO membrane was synthesized using natural Madagascar graphite. The solution of HCl showed a significantly higher washing efficiency of Zn(II), Cd(II) and Pb(II) cations than pure water due to its acidic nature. An intrinsic GO membrane with an interlayer distance of 0.68––0.74 nm (before and after filtration) and a thickness of ~0.70 μm yielded rejections of 99.80, 96.15 and 44.00 % for Pb(II), Cd(II) and Zn(II) ions, respectively. Molecular dynamics simulation showed that ions retained in the GO interfaces due to the narrow interlayer distance, leading to membrane fouling. Nevertheless, the high rejections of Pb(II) and Cd(II) support the possibility of purifying landfill soil leachate by the GO membrane.

Keywords: landfill soil; washing; cations; graphene oxide; membrane.

*,** Corresponding authors. E-mail: (*)dragana.stevic05@gmail.com, (**)svetlana.popovic@uns.ac.rs
https://doi.org/10.2298/JSC250505079S

INTRODUCTION

Soil contamination by metals in landfills poses a significant global problem. Since the Industrial Revolution, the presence of metal contaminants in soil has steadily increased due to a range of human activities, including manufacturing, coal combustion, petrochemical spills, atmospheric deposition, mining, waste disposal, wastewater irrigation, the use of agrochemicals (such as pesticides and fertilizers) and soil amendments.[1] Recent studies indicate that metal concentrations in soil are already reaching critical levels, with some approaching or exceeding agricultural threshold values of 14–17 %.[2] Certain metals, such as cadmium and arsenic, can accumulate in food crops at concentrations that are unsafe for human consumption.[2] Hazardous waste landfills are notable sources of toxic metals, including lead, arsenic, chromium, cadmium, zinc, cobalt and nickel, all of which have been detected as common soil contaminants in such areas.[3] Waste decomposes over time in the presence of infiltrated water, forming a dark liquid called leachate.[4] This leachate leaks from the landfill into the surrounding soil, contaminating ecosystems.[5] Over time, it migrates through the soil layers, leading to severe and persistent pollution.[6] Given these risks, the contamination of landfill soils with metals represents a critical environmental challenge that must be addressed to ensure a sustainable future.

Researchers have been actively working on finding new methods for soil remediation and consequent metal removal from contaminated water. Most of the scientific papers deal with soil washing using acids of a bit higher concentration, such as 3 M HCl to remove Cd or a mixture of 0.6 M H_2SO_4 and 0.6 M H_3PO_4 to remove As, Cu, Pb and Zn.[7,8] These methods reach high removal efficiencies, but the soil remains acidic with low production potential. Hence, methods for mild and environmentally friendly landfill soil and leachate treatments are yet to be developed.

Treating washing leachate that contains toxic metals is essential to prevent secondary pollution. Membrane technology for metal ion removal is efficient and has advantages over other methods because of its low energy consumption, environmentally friendly nature, compact design, and scalability.[9] GO membranes are atomically thin and have interlayers that act as natural nanopores for ion separation.[10] Other membrane materials, such as polymers, MOFs, zeolites, MXenes, their composites and mixed-matrix membranes could also be used for ionic separation.[11] These membranes have large pores and cracks that are not suitable for ionic separations, while polymer and mixed-matrix membranes offer high efficiency but low water permeance. On the other hand, GO-based membranes have been widely studied for metal ion filtration in water desalination.[12] To the best of our knowledge, the integrated approach involving landfill soil washing followed by leachate filtration has not yet been documented in the existing literature. While

graphene oxide (GO) membranes have been extensively studied for metal ion removal in various aqueous systems, their application in the treatment of landfill leachate remains underexplored.

This work presents an efficient and environmentally friendly method for soil washing and subsequent leachate membrane filtration. Thus, as mild and environmentally friendly washing agents, pure water and a 0.01 M HCl solution were tested for washing the landfill soil. Further, the novelty of this research lies in using an intrinsic graphene oxide (GO) membrane for leachate filtration and employing molecular dynamics simulation to understand the mechanism of retention. Thus, the objectives of this work are the development of an environmentally friendly landfill soil washing method, the subsequent use of a GO membrane for landfill soil wastewater purification, and elucidation of the metal ion filtration mechanism. The aim is to examine the effectiveness of soil washing with water and diluted acid for future practical implementation, as the simple preparation of an intrinsic GO membrane via vacuum filtration makes the overall method desirable for future application.

EXPERIMENTAL

Landfill soil treatment

Soil from the "Cicanovic Forest", landfill near the Bijeljina region in Bosnia and Herzegovina, was collected from the surface at one location and preserved in a fridge at 5 °C, for the experiments. The jar test method was used to determine the type of soil.[13] A jar was filled with soil up to a third of its volume, and filled with 10 g of detergent and water. The mixture was shaken, and the heights of the sand, silt, and clay layers were measured after 1 min, 2, and 48 h, respectively (Fig. S-1 of the Supplementary material to this paper). The soil composition of 12.5 % clay, 37.5 % silt and 50 % sand according to the soil texture pyramid, was determined to be a loam type of soil.[14]

Pure water and a 0.01 M solution of HCl (prepared from concentrated HCl of analytical purity grade, purchased from Sigma–Aldrich) were used as washing agents. As acidification of soil can affect plant health and productivity,[15] we have used a low concentration of HCl for soil washing to minimize the decrease of the pH and to simulate environmental conditions. The washing process involved mixing of 20 g of soil with 150 mL of H_2O or 0.01M HCl and exposing the mixture to the sonication in an ultrasonic bath (Bandelin, DT 102H, Germany) at a frequency of 50 kHz and a power of 150 W for 15, 30, 45, 60 and 120 min at room temperature so to enhance extraction of metals by breaking the soil aggregates. Samples were then filtered to obtain leachates for further treating by membrane filtration.

Graphene oxide (GO) membrane preparation and leachate filtration

GO was prepared from natural Madagascar graphite using a modified Hummers' method.[16] A dispersion of GO (10 mL) at a concentration of 0.001 wt. % was filtered through a polytetrafluoroethylene membrane (Omnipore, 5 μm PTFE membrane, 47 mm diameter). A thin GO membrane was formed after 2 h of filtration at a pressure of 8×10^4 Pa (Fig. S-2a of the Supplementary material). The leachate containing toxic metals (10 mL) was filtered through the GO membrane at a vacuum of 8×10^4 Pa (0.8 bar, Fig. S-2b of the Supplementary material). The metal ion composition in the permeated water was then analysed.

The membrane's thickness was estimated from the density and mass of the GO membrane on the polytetrafluoroethylene (PTFE) substrate. A GO membrane with a mass of 1 mg on a PTFE substrate (19.625 cm^2 with a membrane diameter of 5 cm) has a thickness of ~0.7 μm, considering the density of GO at room temperature (0.75 g cm^{-3})[17].

Materials characterizations

A Fourier transform infrared (FTIR) spectrophotometer with attenuated total reflectance (ATR-S, IRSpirit Shimadzu, Japan) was used for soil characterization before and after washing. A Raman spectrophotometer (Renishaw, UK), equipped with lasers of λ 532 and 780 nm, was used with a grid resolution of 1200 lines/cm and an integration time per pixel of 5 s. A 100× magnification objective with a numerical aperture of 1.25 was used. Cosmic Ray Removal and baseline correction tools were applied to the spectra before univariate analysis.

A X-ray diffraction (XRD) system (Bruker, Cu K-alpha, λ = 1.5406 Å, X-ray lamp power 1600 W, I = 40 mA and U = 40 kV) was used to characterize the GO membrane before and after water filtration. A Göbel mirror, a 2.5° soller, and a 0.3 mm pinhole were inserted along the primary beam path. A 0.6 mm slit and a 2.5° soller were mounted on the secondary beam path. The 2θ range was from 6 to 90°, with a step size of 0.01° and an integration time per step of 3 s. The surface morphology of the membrane, both before and after water filtration, was characterized using a scanning electron microscope (SEM, JEOL JSM-7800F FESEM, France). The instrument was equipped with an in-lens thermal field emission gun with a Schottky emitter (W-filament). The accelerating voltage was 5 kV, and the probe current was 10 pA. The detector used was an in-chamber Everhart–Thornley SE detector or a lower electron detector (LED).

The ionic conductivity (Hanna, EC 214 Conductivity Meter) and pH (Hanna, pH 211 microprocessor pH meter) were measured in the samples before and after soil washing. A UV–Vis spectrophotometer (UV-1800, Shimadzu, Japan) was used to measure the optical absorbance spectra of the water before and after filtration through the GO membrane. An atomic absorption spectrometer (Perkin Elmer Analyst 400, USA) was used to measure the metal ion concentrations in the water for the future estimation of ion rejection by the membrane.

The rejection percentage of metal ions separated by the GO membrane was calculated using the following expression:

$$\text{Rejection} = 100\left(1 - \frac{c_p}{c_f}\right) \quad (1)$$

where c_f is the concentration of a component in the feed (mg kg^{-1}), and c_p is the concentration of ions in permeate (mg kg^{-1}).

Computational details

Molecular dynamics simulations were performed using the large-scale atomic/molecular massively parallel simulator (LAMMPS)[18] to investigate the ion separation mechanism through the GO membrane. The simulation model consisted of two graphene layers with nanowindows, along with water molecules containing Pb(II), Cd(II) and Zn(II) ions in chloride form to maintain overall charge neutrality. Snapshots were visualized using DS Visualizer.

The GO–GO interlayer distances in the model were varied to be 0.33, 0.40, 0.50, 0.60, 0.70, and 0.90 nm. Circular nanowindows were created on the basal planes of the graphene, applying periodic boundary conditions along the X and Y axes, while the Z axis was defined as a repulsive wall. The simulation box dimensions (in Å) were set as follows: X, –12.31175 to 12.31175, Y:, –34.104 to 34.104 and Z, –150 to 50, with the graphene layers at the center of the coordinate system.

Simulations were carried out in the NVT ensemble, with temperature regulated by the Nosé–Hoover thermostat. The SPC/E[19] water model was employed, and charges for the Pb(II) cations and Cl(I) anions were assigned using the Lennard–Jones (LJ) parameters given in Table S-I of the Supplementary material. A timestep was 1 fs. By varying the interlayer distance, the model evaluated the potential permeance of metal ions through the GO membrane.

RESULTS AND DISCUSSION

Washing of the metal cations of Cd(II), Zn(II) and Pb(II) from landfill soil

Throughout the washing process, both washing agents, *i.e.*, pure water and 0.01 M HCl solution, proved to extract the toxic metals into the landfill wastewater (Fig. 1a and b). The 0.01 M HCl yielded higher percentages of toxic metal cations extraction from the landfill soil than H_2O, likely due to the acidic nature of HCl, which facilitates the dissolution of metals and the formation of metal cations. The landfill soil washing with diluted HCl is the most efficient for Cd (7.58 %), while the removal percentages for Pb and Zn were lower (Table S-II of the Supplementary material). Metal cations diffuse through the soil particles, reaching the outer surface and forming leachate that should be further purified to avoid secondary pollution.

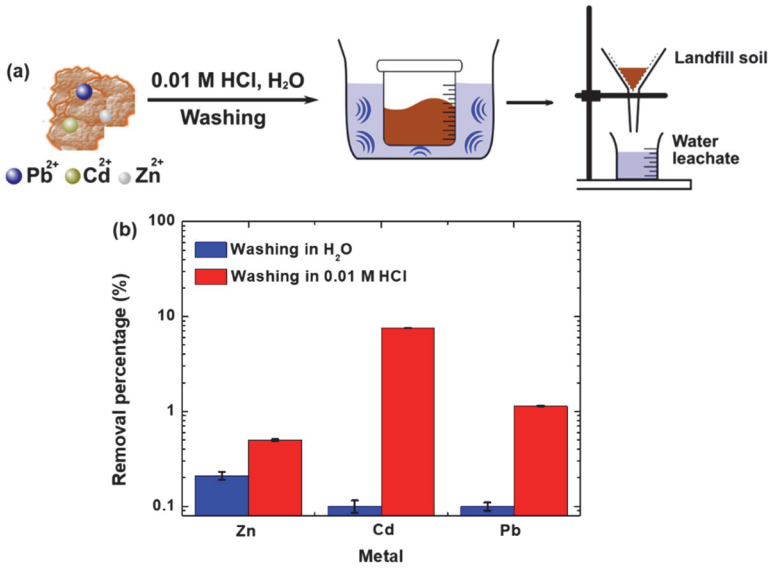

Fig. 1. Landfill soil washing. a) Washing procedure with 0.01 M HCl and H_2O. b) Removal percentage of Zn (II), Cd (II) and Pb (II) cations after ultrasonication.

Surface functional groups on the landfill soil before and after washing

The landfill soil, composed of sand, silt, and clay, also contains Si in the structure. FTIR spectra of the soil washed with H_2O and 0.01 M HCl show a

distinct band at ~1000 cm^{-1} from stretching vibrations of the Si–O group,[20] and a band at ~3500 cm^{-1} from the O–H group in water adsorbed in the soil (Fig. 2 and Figs. S-3 and S-4 of the Supplementary material). The Si–O band is slightly shifted to a lower frequency region after washing with H_2O and 0.01 M HCl, which could be due to possible interactions of H^+ with active sites on the Si–O band (Fig. 2). The Si–O bands of the soil after washing with H_2O and 0.01 M HCl became narrower, and the absolute peak area decreased from 182 to 135 cm^{-1}. The decrease in the Si–O absorption peak area is likely from the removal of vibrational fragments that follow the primary Si–O vibration. The small band at ~1300 cm^{-1} could be assigned to metal–oxygen (Me–O) vibrations in the loam. This Me–O vibrational band disappears after washing with H_2O and 0.01 M HCl, which is attributed to the removal of metal from the soil.

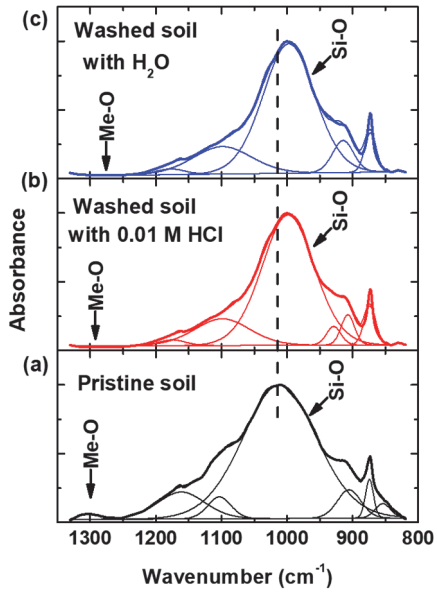

Fig. 2. FTIR spectra of the Si–O band in loam-type soil. a) Pristine soil. b) Soil washed with 0.01 M HCl for 60 min. c) Soil washed with H_2O.

Ionic conductivity of the leachate

Metal ions dissolved from the soil increased the electrical conductivity of the landfill leachate (Fig. S-5 of the Supplementary material). The electrical conductivity of the soil dissolved in 0.01 M HCl and H_2O increased to ~1800 and ~600 μS cm^{-1}, respectively. The electrical conductivity shows an increasing tendency with washing time due to the evolution of ions from the soil, while the pH remains constant and nearly neutral because of the absence of acidic or basic ions in the leachate (Fig. S-5). An increase in the electrical conductivity was anticipated due to the evolved Pb(II), Cd(II) and Zn(II) cations. These metal cations in leachate

were separated using the GO membrane, as will be further discussed from experimental and the GO structure modelling results.

Purification of leachate using an intrinsic GO membrane

Separation of toxic metal cations from a leachate was conducted using an ~0.70 μm thick GO membrane (Fig. 3a–c). The rejection of metal ions by the GO membrane increases with the metal ion hydrated diameter (Fig. 3d). The ionic diameter depends on the number of ligands surrounding the ions, having an increasing tendency in the order of Zn(II) < Cd(II) < Pb(II) cations. Metal ions and molecules can diffuse through nano-windows or defects on graphene-like surfaces, being transferred through the interlayers of GO. The Pb(II) and Cd(II) cations have difficulty permeating between the layers of GO because of the narrow effective width at the GO–GO interfaces, giving rejection as high as ~100 %. Zn(II) cations have a smaller ionic diameter than the GO interlayer distance, permeating between the GO layers at a relatively low rejection of ~40 %. High cation rejection can be assigned to the stacking of GO layers under vacuum. The thin membrane was produced to ensure rapid water filtration through the membrane. The water permeance during metal cation separation shows a decreasing tendency against time from 20.3 L m^{-2} h^{-1} bar^{-1} after 0 h to 7.8 L m^{-2} h^{-1} bar^{-1} after 4 h (Fig. S-6 of the Supplementary material). The decrease in water permeance occurs due to membrane foul-

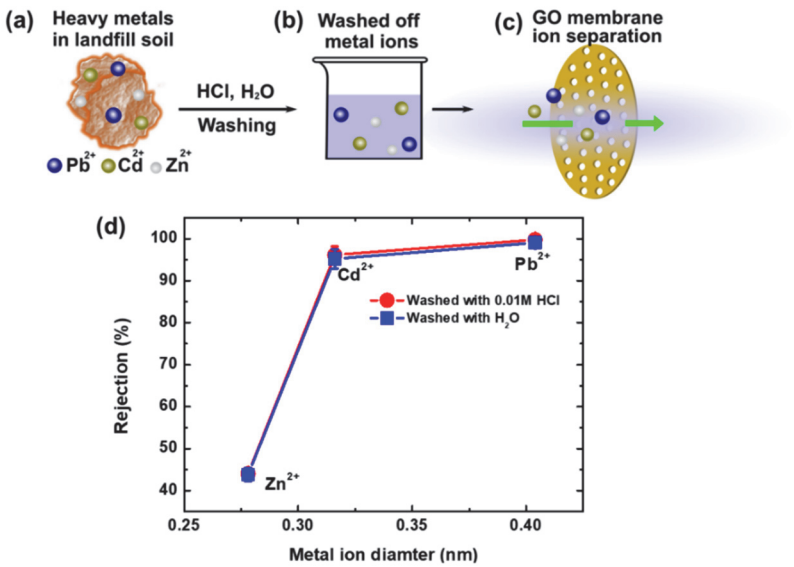

Fig. 3. Toxic metals from landfill soil and their separation. a) Landfill soil contaminated with toxic metals. b) Water containing metal cations of Pb(II), Cd(II) and Zn(II). c) Separation of toxic metals through the GO membrane. d) Rejection of metal cations in 0.01 M HCl and water against their size.

ing. The leachate contains a small quantity of suspended soil particles, which remain on the membrane surface as evidenced by a decrease in the UV–Vis spectra before and after filtration (Fig. S-7 of the Supplementary material).

The structure of the GO membrane before and after leachate filtration

The GO membrane on the PTFE support, produced by vacuum filtration (Fig. S-2), has a layer-like structure. The membrane is composed of GO layers stacked together, forming a compact structure (Fig. 4a_1 and b_1). GO layers have a lateral size of ~0.7 μm,[21] covering the surface of the porous PTFE support. The surface morphology of the GO membrane changed slightly after filtering the landfill water contaminated with metal cations (Fig. 4a_2 and b_2). This can be attributed to the deposition of contaminants onto the GO membrane surface. The GO membrane, both before and after metal cation separation, has a flat surface morphology due to the uniform and flat PTFE substrate on the rigid vacuum filter support. The membrane has a compact structure without cracks, which is important for the future large-scale production of crack-free membranes for landfill cation separation.

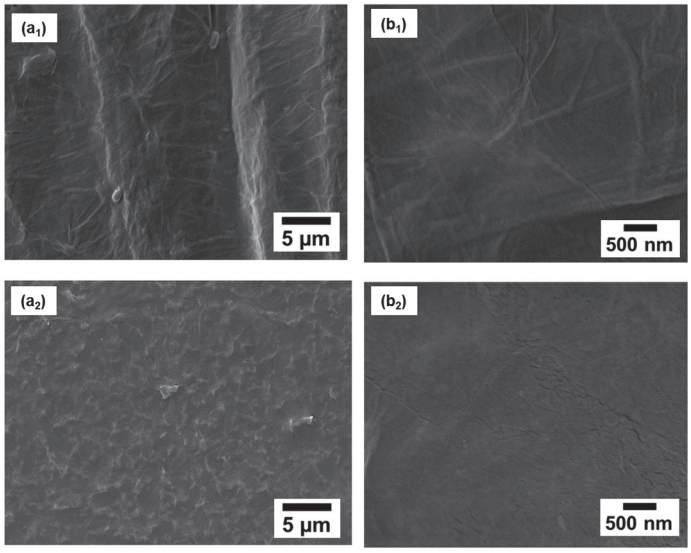

Fig. 4. SEM micrographs of the GO membrane before and after filtration of 10 mL of landfill water contaminated with metal cations; a_1 and b_1: low and high magnification of the membrane before filtration; a_2 and b_2: low and high magnifications of the membrane after filtration. The low and high magnifications were used for better understanding the membrane surface.

The interlayer distance of the GO–GO was examined from XRD patterns in the two-theta region of 8 to 37°. The GO diffraction peak from the (002) crystal plane and the bands from defective GO are prominent both before and after metal

ion filtration (Fig. 5a and b). The absolute intensity of the GO bands decreased after water filtration, which is likely due to the deposition of soil particles onto the surface of the GO membrane. The small soil particles that cause the turbidity of the soil dispersion were separated by filtration through the GO membrane, as confirmed by a decrease in the optical absorbance intensity in the UV–Vis region of 220–500 nm (Fig. S-6 of the Supplementary material). After metal ion separation, the intensity of the XRD peaks decreased, and the position of the (002) band shifted from 12.50 to 11.86° (2θ) due to an increase in the interlayer distance. According to Bragg's law ($2d\sin\theta = \lambda$),[22] the interlayer distance d increased from 0.70 to 0.74 nm. This increase is likely due to the intercalation of water and metal ions into the GO–GO interlayer space.[23] Fortunately, this increase in the interlayer distance is insignificant, which contributes to stable ion separation over time.

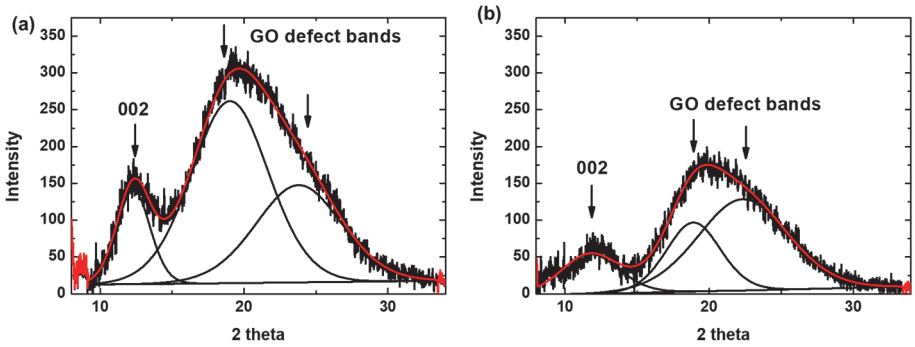

Fig. 5. XRD patterns of GO membranes. a) GO membrane before cation separation; b) GO membrane after ion separation.

The crystallinity of GO membranes before and after ion filtration was examined using Raman spectroscopy with a laser wavelength of 532 nm. Defects were created in the GO during the exfoliation process, and the edges of these defects (referred to as nanowindows) can be identified by oxygen functional groups such as carboxyl, carbonyl, hydroxyl and epoxy.[24] The GO membrane has a prominent G-band from crystalline sp^2 carbon atoms that vibrate in-plane and a D-band from defective sp^3 carbon atoms that are bound with oxygen functional groups (Fig. 6). Metal ions permeate through the GO nanowindows, which are a few nanometers in size.[25] The GO membrane is highly defective, as indicated by a high value of $I_{D/G} = 0.96$. After metal ion permeance, the D-band intensity ratio slightly increased to $I_{D/G} = 0.99$, suggesting an increase in the defects of GO. The slight shift in the G-band suggests the presence of charge transfer interactions between metal cations of Zn(II), Cd(II) or Pb(II) and graphene. Electron charge transfer interactions between unhybridized p_z electrons of sp^2 carbon atoms and d-states of metal cations should occur,[26] leading to the shift in the G-band of GO. The metal ions

could be trapped on the basal plane of GO and in between the layers, leading to the metal ion separation.

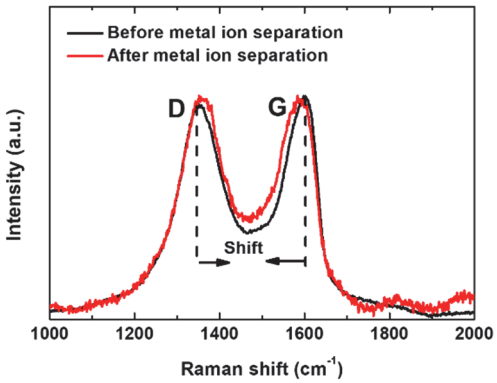

Fig. 6. Raman spectra of the GO membrane recorded at a laser wavelength of 532 nm. The spectra of the GO membranes were recorded before water filtration (black line) and after water filtration (red line).

Metal ion separation mechanism

The mechanism of toxic metal cations retention by GO membrane was modelled using MD simulations. The GO membrane model of two layers served for examination of the ion separation mechanism (Fig. 7). The GO layers have

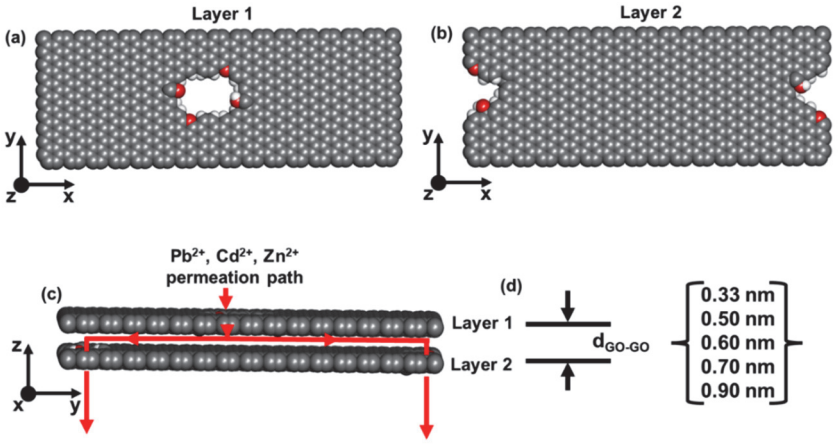

Fig. 7. A unit cell of the GO membrane models with the periodic boundary conditions for molecular dynamics simulation of Pb(II), Cd(II) and Zn(II) cation permeance. a) GO layer 1 with nano-windows of ~1 nm in diameter. b) GO layer 2 with nano-windows of ~1 nm in diameter. c) GO layers with denoted permeance paths for metal ions between the GO layers through the nano-windows. d) Internuclear distances between GO layers used for MD simulations of metal cation permeance.

nano-windows on the basal planes, serving for examination of the ion separation mechanism between the layers (Fig. 7a and b). The metal ions can enter the nano--windows on the basal planes and penetrate between the layers of GO at the interlayer distances of 0.33–0.90 nm (Fig. 7c). The rejection of metal ions by the GO layered membrane depends on the interlayer distance. Ions can freely enter the nano-windows on GO, whose size can reach nearly ~1 nm[27] in diameter. The sizes of the nano-windows on GO cannot be precisely controlled during synthesis. Given that these nano-windows are substantially larger than the metal ions, the interlayer spacing probably constitutes the primary barrier to metal ion rejection.[28] Adjusting the interlayer distance from the completely stacked GO layers at the distance of 0.33 nm to a distance larger than the sizes of the metal ions should lead to ion separation performances that are similar to the experimental results.

The GO membrane with an interlayer distance of 0.33 nm is impermeable to metal ions due to the narrow gap, which leads to their complete exclusion (Fig. S--8 of the Supplementary material). The GO membrane with an interlayer distance of 0.50 nm is permeable to Cd(II) and Zn(II) cations (Fig. S-8), but is impermeable to Pb(II) cations, resulting in their complete rejection (100 %). The experimentally obtained rejection results are compared to the simulated ones for the membrane model with interlayer distance of 0.70 nm (Fig. 8). While the simulation results underestimate the rejection of Zn(II) and Cd(II), they show good alignment with the experimental membrane regarding Pb(II) rejection. The discrepancy in separation performance likely arises from the experimental membrane containing ~500 times more GO layers than the model. Thus, the membrane with an interlayer distance of 0.70 nm would achieve complete rejection of Pb(II) cations.

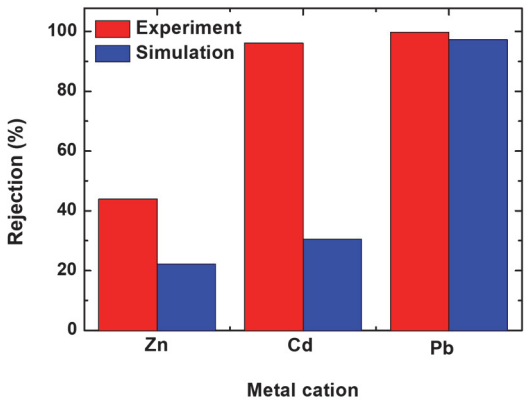

Fig. 8. Rejection against the metal cation for simulated and experimental membrane. We selected the interlayer distance of 0.70 nm for the membrane model because the experimental membrane had the similar interlayer distance, as determined from the XRD pattern using Bragg's law.

CONCLUSION

Landfill soil washing was conducted using H_2O and 0.01 M HCl under ultrasonication, yielding washed-off metal cations of Zn(II), Cd(II) and Pb(II). The soil's structure, determined to be the loam-type, remained similar after washing with both H_2O and 0.01 M HCl, suggesting that further development and enhancement of soil washing with water solvents are promising. The surface area of the loam-type soil increased to 235 $m^2\ g^{-1}$ due to soil activation. The washed-off metal cations were filtered using a GO membrane prepared by vacuum filtration. The GO membrane reached rejections of 99.80, 96.15 and 44.00 % for Pb(II), Cd(II) and Zn(II), respectively. Water permeance showed a decreasing tendency from 20.3 to 7.8 L $m^{-2}\ h^{-1}\ bar^{-1}$ after 4 h of monitoring, which is due to membrane fouling by suspended particles in the leachate. This suggests that the membrane should be used in a series and replaced or washed frequently to achieve stable separations. Molecular dynamics (MD) simulations showed that ion separation occurs at the GO interfaces. Thus, we showed a possibility for a closed cycle of metal cation removal from the soil, which includes both soil washing and GO membrane implementation for metal cation separation.

SUPPLEMENTARY MATERIAL

Additional data and information are available electronically at the pages of journal website: https://www.shd-pub.org.rs/index.php/JSCS/article/view/13361, or from the corresponding author on request.

Acknowledgements. This project has received funding from the European Union's Horizon 2020 research and innovation programme under grant agreement no. 101007417 and from the taxpayers of the Republic of Serbia through the program grant number 451-03-137/2025-03/ /200134.

ИЗВОД

УКЛАЊАЊЕ Pb(II), Cd(II) И Zn(II) СА ЗЕМЉИШТА ДЕПОНИЈЕ И ПРОЦЕДНИХ ВОДА ПОМОЋУ ГРАФЕН-ОКСИДНЕ МЕМБРАНЕ

ДРАГАНА СТЕВИЋ[1], СУНЧИЦА СУКУР[2], РАДОВАН КУКОБАТ[3], СУЗАНА ГОТОВАЦ АТЛАГИЋ[2], ПРЕДРАГ ИЛИЋ[4], FRANCESCO SIRIO FUMAGALLI[5], ANDREA VALSESIA[5], PASCAL COLPO[5] и СВЕТЛАНА ПОПОВИЋ[1]

[1]Технолошки факултет, Универзитет у Новом Саду, Булевар цара Лазара 1, Нови Сад, [2]Природно–математички факултет, Катедра за хемију, Универзитет у Бањој Луци, Младена Стојановића 2, 78000, Бања Лука, Република Српска, Босна и Херцеговина, [3]Технолошки факултет, Катедра за хемијско инжењерство и технологију, Универзитет у Бањој Луци, Булевар војводе Степе Степановића 73, Бања Лука, Република Српска, Босна и Херцеговина, [4]Институт за заштиту и екологију Републике Српске, Бања Лука, Босна и Херцеговина и [5]European Commission, Joint Research Centre (JRC), Ispra, Italy

Будући да кишница екстрахује токсичне метале из земљишта депонија формирајући штетне процедне воде, потребно је развити методе за њихово уклањање. У раду је представљена метода уклањања токсичних металних јона из земље-иловаче, која се обухвата прање земљишта благим реагенсима за испирање, како би се издвојили метали у процед-

ној води, и пречишћавање процедне воде филтрацијом кроз графен-оксид (GO) мембрану. Реагенси за прање H_2O и 0,01 M HCl су тестирани. GO мембрана је синтетисана користећи графит Мадагаскар. Раствор HCl је показао знатно већу ефикасност уклањања Pb(II), Cd(II) и Zn(II) него чиста вода захваљујући киселости. Чиста GO мембрана са растојањем између листова графена 0,68–0,74 nm (пре и после филтрације) и дебљине 0,70 μm је показала проценте одбијања 99,80 % за Pb(II), 96,15 % за Cd(II) и 44,00 % за Zn(II). Молекуларно-динамичка симулација је показала да се задржавање јона одвија на међуповршинама GO слојева, што је довело до прљања мембране. Ипак, високи проценти уклањања Pb(II) и Cd(II) јона указују на могућност пречишћавања процедне воде земљишта депоније помоћу GO мембране.

(Примљено 5. маја, ревидирано 27. јуна, прихваћено 29. октобра 2025)

REFERENCES

1. G. Ondrasek, J. Shepherd, S. Rathod, R. Dharavath, M. I. Rashid, M. Brtnicky, M. S. Shahid, J. Horvatinec, Z. Rengel, *RSC Adv.* **15** (2025) 3904 (https://doi.org/10.1039/D4RA04639K)
2. D. Hou, X. Jia, L. Wang, S. P. McGrath, Y.-G. Zhu, Q. Hu, F.-J. Zhao, M.-S. Bank, D. O'Connor, J. Nriagu, *Science* **388** (2025) 316 (https://doi.org/10.1126/science.adr5214)
3. S. Sahragard, R. Mostafaloo, F. Fanaei, S. Imanian, M. Dehabadi, A. Adibzadeh, N. Nasseh, *Avicenna J. Environ. Health Eng.* **11** (2024) 115 (https://doi.org/10.34172/ajehe.5467)
4. S. M. Hosseini Beinabaj, H. Heydariyan, H. Mohammad Aleii, A. Hosseinzadeh, *Heliyon* **9** (2023) e13017 (https://doi.org/10.1016/j.heliyon.2023.e13017)
5. X. Zhai, Z. Li, B. Huang, N. Luo, M. Huang, Q. Zhang, G. Zeng, *Sci. Total Environ.* **635** (2018) 92 (https://doi.org/10.1016/j.scitotenv.2018.04.119)
6. K. N. B. Armel, B. B. B. Emile, A. K. Daniel, *J. Geosci. Environ. Prot.* **10** (2022) 151 (https://doi.org/10.4236/gep.2022.101011)
7. M.-S. Kim, N. Koo, J.-G. Kim, S.-H. Lee, *Appl. Sci.* **11** (2021) 6398 (https://doi.org/10.3390/app11146398)
8. K. Cho, E. Myung, H. Kim, C. Park, N. Choi, C. Park, *Int. J. Environ. Res. Publ. Health* **17** (2020) 3133 (https://doi.org/10.3390/ijerph17093133)
9. S. P. Bera, M. Godhaniya, C. Kothari, *J. Basic Microbiol.* **62** (2022) 245 (https://doi.org/10.1002/jobm.202100259)
10. G. Liu, W. Jin, N. Xu, *Chem. Soc. Rev.* **44** (2015) 5016 (https://doi.org/10.1039/C4CS00423J)
11. W. Jin, G. Liu, N. Xu, *Organic-Inorganic Composite Membranes for Molecular Separation*, Series on Chemical Engineering, Vol. 05, World Scientific (Europe), London, 2017 (https://doi.org/10.1142/q0084)
12. F. A. Janjhi, D. Janwery, I. Chandio, S. Ullah, F. Rehman, A. A. Memon, J. Hakami, F. Khan, G. Boczkaj, K. H. Thebo, *ChemBioEng Rev.* **9** (2022) 574 (https://doi.org/10.1002/cben.202200015)
13. A. Jeffers, *Soil Texture Analysis "The Jar Test."*, https://hgic.clemson.edu/factsheet/soil-texture-analysis-the-jar-test/
14. E. J. Coopersmith, B. S. Minsker, M. Sivapalan, *Hydrol. Earth Syst. Sci.* **18** (2014) 3095 (https://doi.org/10.5194/hess-18-3095-2014)
15. Z. Rengel, in *Soil Health and Climate Change*, B.P. Singh, A. L. Cowie, K. Y. Chan, K. Y., Eds., *Soil Biology*, Vol. 29, Springer, Heidelberg, 2011, pp. 69–85 (https://doi.org/10.1007/978-3-642-20256-8_4)

16. D. C. Marcano, D. V. Kosynkin, J. M. Berlin, A. Sinitskii, Z. Sun, A. Slesarev, L. B. Alemany, W. Lu, J. M. Tour, *ACS Nano* **4** (2010) 4806 (https://doi.org/10.1021/nn1006368)
17. R. J. Jiménez Riobóo, E. Climent-Pascual, X. Díez-Betriu, F. Jiménez-Villacorta, C. Prieto, A. De Andrés, *J. Mater. Chem., C* **3** (2015) 4868 (https://doi.org/10.1039/C4TC02883J)
18. A. P. Thompson, H. M. Aktulga, R. Berger, D. S. Bolintineanu, W. M. Brown, P. S. Crozier, P. J. In 'T Veld, A. Kohlmeyer, S. G. Moore, T. D. Nguyen, R. Shan, M. J. Stevens, J. Tranchida, C. Trott, S. J. Plimpton, *Comput. Phys. Commun.* **271** (2022) 108171 (https://doi.org/10.1016/j.cpc.2021.108171)
19. P. Mark, L. Nilsson, *J. Phys. Chem., A* **105** (2001) 9954 (https://doi.org/10.1021/jp003020w)
20. A. P. Rawat, V. Kumar, P. Singh, A. C. Shukla, D. P. Singh, *Soil Sediment Contam. Int. J.* **31** (2022) 15 (https://doi.org/10.1080/15320383.2021.1900071)
21. Z. Liu, W. Liu, X. Xie, W. Zhao, Y. Wen, Q. Wang, B. Ou, *IOP Conf. Ser. Earth Environ. Sci.* **252** (2019) 022022 (https://doi.org/10.1088/1755-1315/252/2/022022)
22. W. H. Bragg, W. L. Bragg, *Proc. R. Soc. London, A* **88** (1913) 428 (https://doi.org/10.1098/rspa.1913.0040)
23. B. Lee, K. Li, H. S. Yoon, J. Yoon, Y. Mok, Y. Lee, H. H. Lee, Y. H. Kim, *Sci. Rep.* **6** (2016) 28052 (https://doi.org/10.1038/srep28052)
24. M. Krishnamoorthy, M. Veerapandian, K. Yun, S.-J. Kim, *Carbon* **53** (2013) 38 (https://doi.org/10.1016/j.carbon.2012.10.013)
25. C. Ogata, M. Koinuma, K. Hatakeyama, H. Tateishi, M. Z. Asrori, T. Taniguchi, A. Funatsu, Y. Matsumoto, *Sci. Rep.* **4** (2014) 3647 (https://doi.org/10.1038/srep03647)
26. P. A. Khomyakov, G. Giovannetti, P. C. Rusu, G. Brocks, J. Van Den Brink, P. J. Kelly, *Phys. Rev., B* **79** (2009) 195425 (https://doi.org/10.1103/PhysRevB.79.195425)
27. R. Kukobat, M. Sakai, H. Tanaka, H. Otsuka, F. Vallejos-Burgos, C. Lastoskie, M. Matsukata, Y. Sasaki, K. Yoshida, T. Hayashi, K. Kaneko, *Sci. Adv.* **8** (2022) eabl3521 (https://doi.org/10.1126/sciadv.abl3521)
28. B. Mi, *Science* **343** (2014) 740 (https://doi.org/10.1126/science.1250247).

Journal of the Serbian Chemical Society
JSCS@tmf.bg.ac.rs • www.shd.org.rs/JSCS
J. Serb. Chem. Soc. *91* (3) S116–S121 (2026) *Supplementary material*

SUPPLEMENTARY MATERIAL TO

Removal of Pb(II), Cd(II), and Zn(II) from landfill soil and leachate using a graphene oxide membrane

DRAGANA STEVIĆ[1]*, SUNČICA SUKUR[2], RADOVAN KUKOBAT[3], SUZANA GOTOVAC ATLAGIĆ[2], PREDRAG ILIĆ[4], FRANCESCO SIRIO FUMAGALLI[5], ANDREA VALSESIA[5], PASCAL COLPO[5] and SVETLANA POPOVIĆ[1]**

[1]Faculty of Technology Novi Sad, University of Novi Sad, Boulevard cara Lazara 1, Novi Sad, Serbia, [2]Faculty of Natural Sciences and Mathematics, Department of Chemistry, University of Banja Luka, Mladena Stojanovića 2, 78000, Banja Luka, the Republic of Srpska, Bosnia and Herzegovina, [3]Faculty of Technology, Department of Chemical Engineering and Technology, University of Banja Luka, B.V Stepe Stepanovića 73, Banja Luka, the Republic of Srpska, Bosnia and Herzegovina, [4]Institute for Protection and Ecology of the Republic of Srpska, Banja Luka, Bosnia and Herzegovina and [5]European Commission, Joint Research Centre (JRC), Ispra, Italy

J. Serb. Chem. Soc. *91* (3) (2026) 303–316

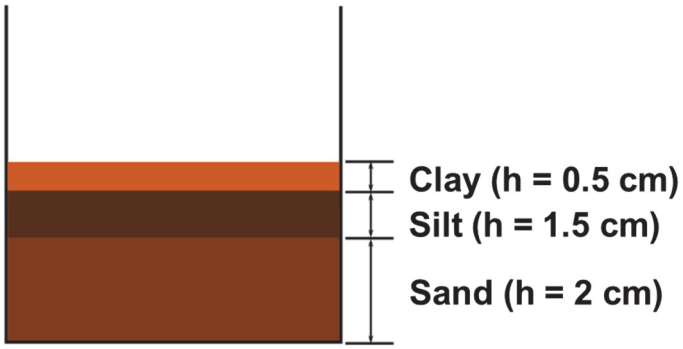

Figure S-1. Soil type was determined from the soil texture pyramid after sedimentation of 48 h. The soil fractions including clay on the top, silt in the middle and sand on the bottom were formed during the sedimentation process. The heights of each soil fraction are given in the figure.

*,** Corresponding authors. E-mail: (*)dragana.stevic05@gmail.com, (**)svetlana.popovic@uns.ac.rs

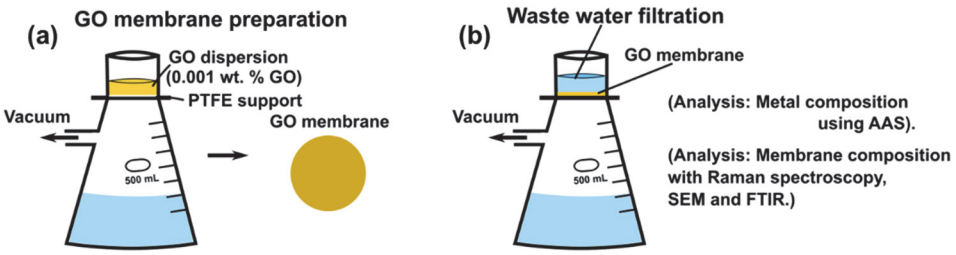

Figure S-2. Vacuum filtration. (a) Filtration of 10 mL of GO dispersion (0.001 wt. %) through polytetrafluoroethylene membrane at the vacuum of 8×10^4 Pa. (b) Filtration of washed off water through the GO membrane.

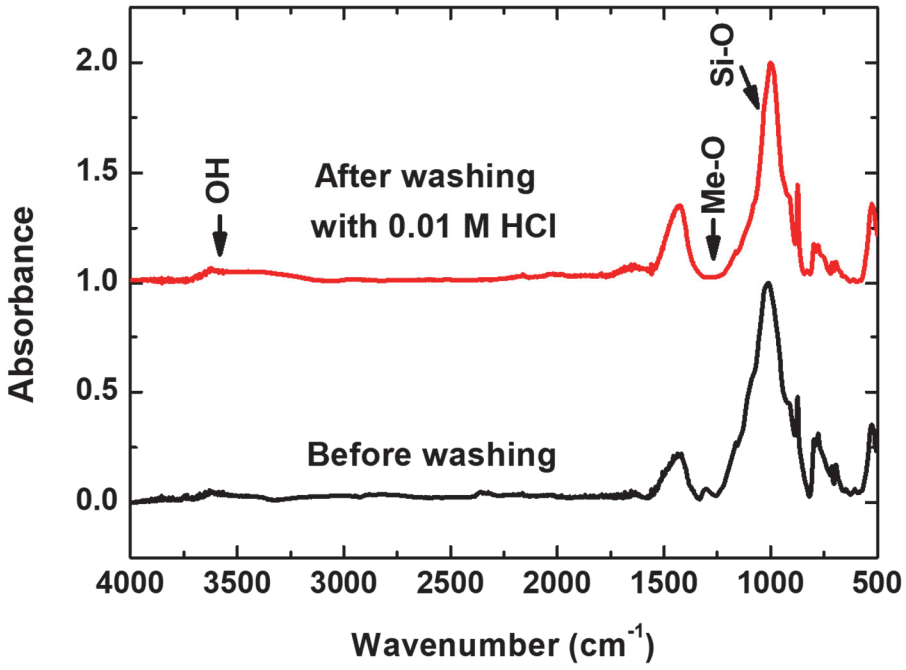

Figure S-3. FTIR spectra of the soil before and after washing with 0.01 M HCl for 60 min.

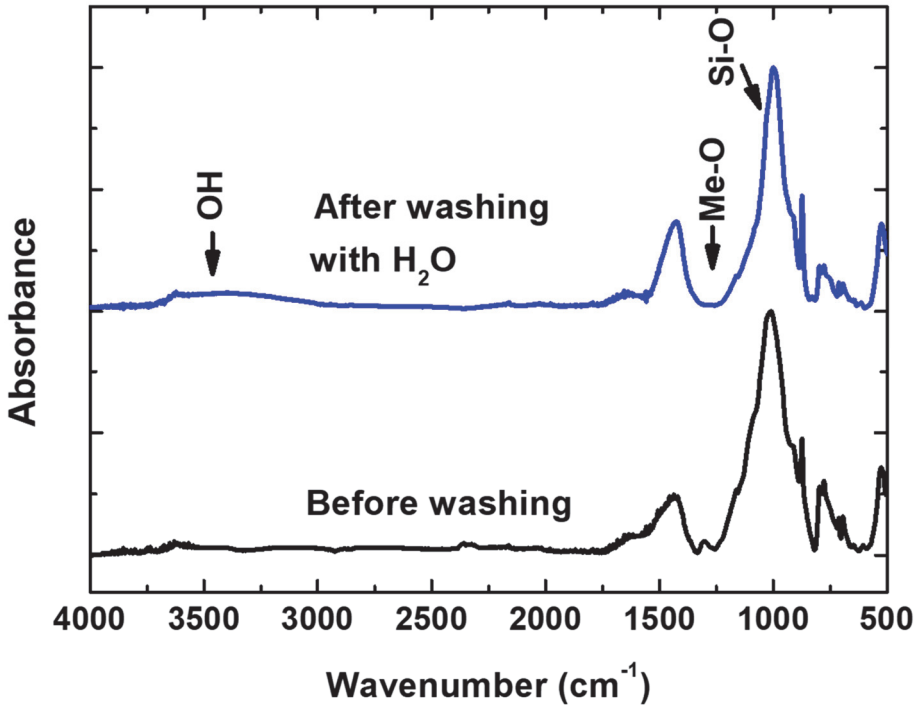

Figure S-4. FTIR spectra of the soil before and after washing with H_2O for 60 min.

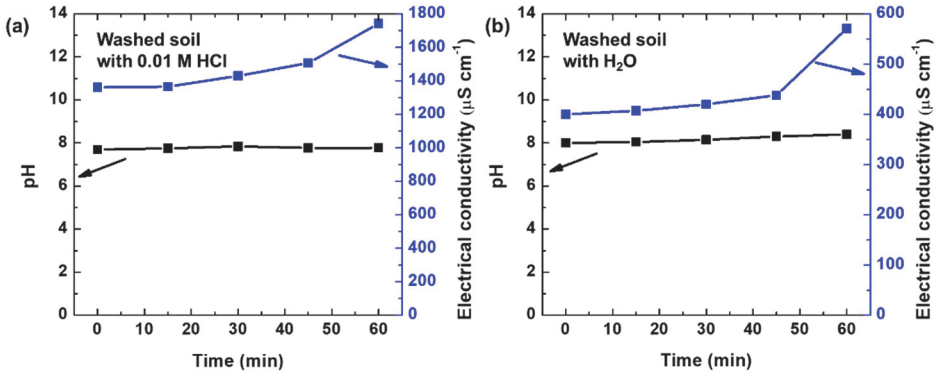

Figure S-5. pH and electrical conductivity of the landfill leachate. (a) The soil washed with 0.01 M HCl. (b) The soil washed with H_2O. The washing time of soil was 60 min.

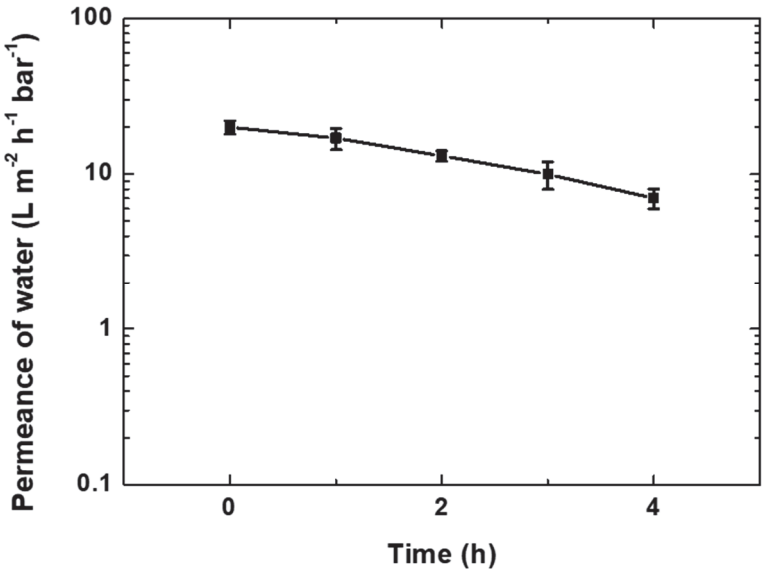

Figure S-6. Permeance of landfill soil wastewater against time.

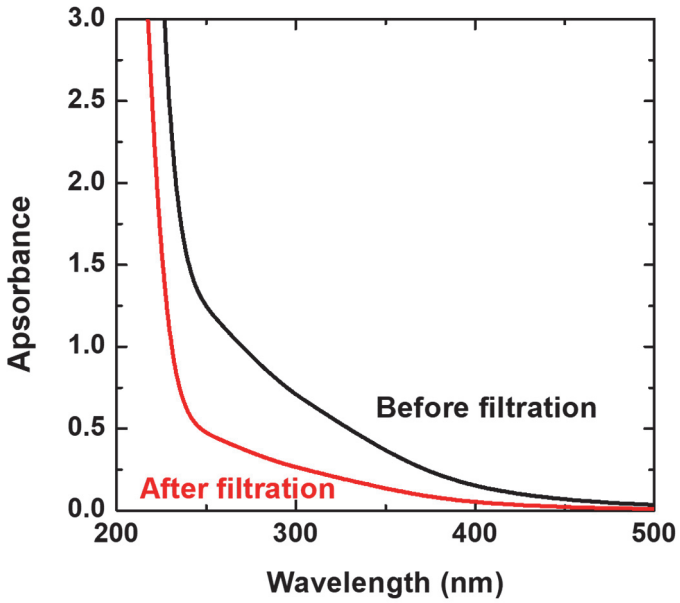

Figure S-7. UV-vis spectra of the soil suspension before and after filtration through GO membrane.

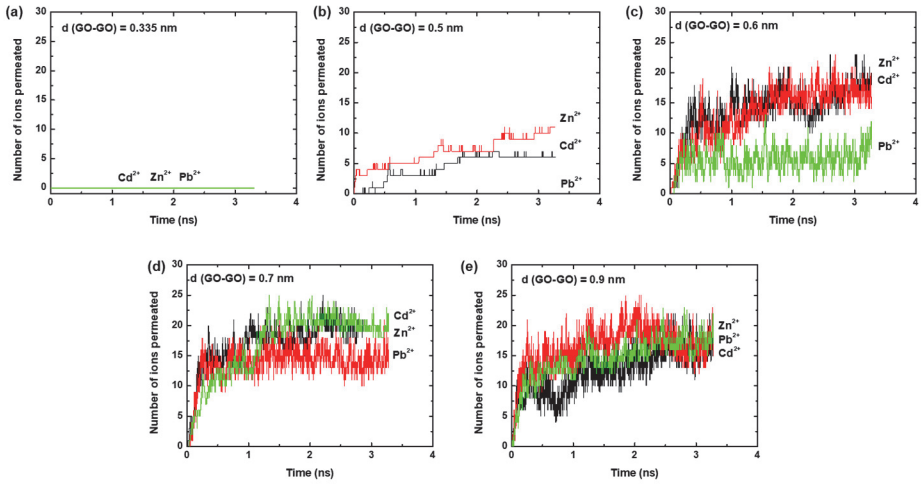

Figure S-8. Number of permeated ions through the GO membrane against simulation time. (a – e) The interlayer distance was increased from the completely stacked GO layers of 0.335 to 0.90 nm. Zn^{2+} ions are in red, Cd^{2+} ions in black, and Pb^{2+} ions in green color.

Table S-I. Force field parameters including atomic weights, charges, and Lennard-Jones(LJ) σ and ϵ parameters for MD simulations of metal ion permeance through the GO membrane.

Molecule	Mass (1.66×10^{-27} kg)	Charge (e)	LJ σ (nm)	LJ ϵ (K)	References
C (-C=)	12.011	0	0.336	28	(1)
C (C-O-H)	12.011	0.15	0.355	35.2	
O (C-O-H)	15.9994	-0.585	0.307	85.5	
H (C-O-H)	1.00794	0.435	0	0	
C (C-O-C)	12.011	0.25	0.38	35.2	
O (C-O-C)	15.9994	-0.5	0.3	59.5	
C (C-H)	12.011	-0.115	0.355	35.2	
H (C-H)	1.00794	0.115	0.242	15.1	
Pb	207.2	2	3.829	0.662	(2, 3)
Zn	65.38	2	2.763	0.124	
Cd	112.411	2	2.537	0.228	
Cl	35.453	-1	4.4	0.1	

Table S-II. The efficiency of toxic metals removal by washing from soil and from leachate by GO membrane separation.

Metal cations content in washing medium			Water filtration by GO membrane	
Metals	Washed with H_2O (%)	Washed with 0.01 M HCl (%)	Rejection after washing with H_2O (%)	Rejection after washing with 0.01 M HCl (%)
Zn	0.21	0.52	43.80	44.00
Cd	0.10	7.58	95.20	96.15
Pb	0.10	1.14	99.05	99.80

REFERENCES

1. H. Khanmohammadi, B. Bayati, J. Rahbar-Shahrouzi, A.-A. Babaluo, A. Ghorbani, *J. Environ. Chem. Eng.* **7** (2019) 103040 (https://doi.org/10.1016/j.jece.2019.103040).
2. F. Vallejos-Burgos, F.-X. Coudert, K. Kaneko, *Nat. Commun.* **9** (2018) 1812 (https://doi.org/10.1038/s41467-018-04224-6).
3. Y. Zheng, A. Zaoui, *Solid State Ion.* **203** (2011) 80 (https://doi.org/10.1016/j.ssi.2011.09.020).

Journal of the Serbian Chemical Society
JSCS-info@shd.org.rs • www.shd.org.rs/JSCS
J. Serb. Chem. Soc. *91* (3) 317–330 (2026)
JSCS–5494
Original scientific paper
Published 26 February, 2026

Ameliorating heavy metal-induced oxidative stress in valerian: The role of melatonin

ELVISA HODŽIĆ[1]*, MILICA BALABAN[2], SEBILA REKANOVIĆ[1] and HALID MAKIĆ[1]

[1]*Biotechnical faculty, University of Bihać, Luke Marjanovića bb, 77000 Bihać, Bosnia and Herzegovina and* [2]*Faculty of Natural Sciences and Mathematics, University of Banja Luka, Mladena Stojanovića 2, 78000 Banja Luka, Bosnia and Herzegovina*

(Received 1 April, revised 17 April, accepted 16 July 2025)

Abstract: Heavy metals ubiquitously found in soil and water, represent a serious environmental problem that disrupts plant mineral nutrition homeostasis, osmotic balance and metabolism. The application of some biostimulants can alleviate these disruptions. Melatonin as a signal molecule, and antioxidant plays an important role in plant growth and stress tolerance due to its ability to directly neutralize reactive oxygen and nitrogen species. The reduction or mitigation of heavy metals adverse effects in valerian plants grown in open field conditions using melatonin was investigated in this study. High-pressure liquid chromatography coupled with a fluorescence detector was used to identify and quantify melatonin concentration in valerian root extracts. Also, the physiological and biochemical status of plants under abiotic stress was examined, especially in 100 μM melatonin pre-treated plants. Higher concentrations of endogenous melatonin were measured in roots of Cd and Zn treated plants. Melatonin application alleviated the negative effect of Cd, particularly evident in Cd-melatonin treatment which restored or enhanced bioactive compound levels. Melatonin effectively mitigates Cd and Zn-induced stress in valerian by enhancing both non-enzymatic and enzymatic antioxidant systems and promoting the synthesis of protective compounds. These findings highlight melatonin's potential as a sustainable biostimulant to support plant resilience and productivity in heavy metal-stressed environments.

Keywords: abiotic stress; heavy metals; phytomelatonin; *Valeriana officinalis* L.

INTRODUCTION

Melatonin has been known as a non-toxic and universal molecule, naturally occurring in plants and humans.[1] Melatonin (*N*-acetyl-5-methoxytryptamine), an indoleamine synthesized from tryptophan and secreted by the pineal gland in

* Corresponding author E-mail: elvisa.hodzic@unbi.ba
https://doi.org/10.2298/JSC250401048H

animals, has also been detected in plant chloroplasts and mitochondria, where it is synthesized through several metabolic pathways. It has been found in almost all forms of organisms (invertebrates, algae, fungi and bacteria). The established melatonin concentration in different plant species vary from 2 to 5000 μg/g of dry matter. The measured concentrations are affected by plant genotype, development stage, plant tissue analyzed and environmental conditions (salinity, temperature, ultraviolet light, heavy metals).[2]

Melatonin actively reacts with free radicals and stimulates various physiological, morphological and biochemical plant features, from seed germination to biological yield.[3] Melatonin is involved in development processes, circadian rhythms regulation, promotion of photosynthesis, fruit ripening, chlorophyll preservation and leaf senescence, among others.[2,4] The role of melatonin in reducing plants' stress is achieved by upregulating stress-related genes that scavenge reactive oxygen species (ROS) and improve antioxidant capacity of plants.[5,6]

Abiotic stress, which influences plant growth and reducibility is associated with osmotic and oxidative stress, ionic imbalance and cell metabolism dyshomeostasis.[7] Most heavy metals, assigned as abiotic stressors, cause continuous production of ROS in the chloroplast, mitochondria, and peroxisomes, which can cause oxidative stress in plants and result in the unexpected consequence of heavy metal toxicity.[8]

Valeriana officinalis is a well-known medicinal plant widely used in phytotherapy for its calming, sedative and anxiolytic effects, primarily attributed to its root extracts. It is commonly used to alleviate sleep disorders, anxiety, and nervous tension. In human phytotherapy, polyphenols are valued for their strong antioxidant, anti-inflammatory and protective properties, contributing to the prevention of chronic diseases such as cardiovascular disorders, neurodegenerative conditions and certain cancers.[9]

The negative effect of different heavy metals can be mitigated through exogenous melatonin, directly improving the stress tolerance of different plant species by scavenging ROS, and indirectly, by increasing antioxidant activities, photosynthetic efficiency and metabolite content.[10]

The identification and quantification of endogenous melatonin in valerian leaves and roots, as well as the modulation of secondary metabolites, reactive species detoxification and antioxidant upregulation by exogenous melatonin and heavy metals, cadmium and zinc, have not been carried out so far. To better understand the role of melatonin in plants subjected to the maximum allowed concentrations of cadmium and zinc, a set of experiments was conducted on valerian (*V. officinalis* L.). The assessment of potential protective role of melatonin in mitigating heavy metal stress effects in valerian, enhancing antioxidant defense mechanisms, regulating nutrient and protein metabolism and modulating enzymatic act-

ivity related to oxidative stress was determined. The study highlights a strong correlation between phenolic content and antioxidant activity, particularly in leaves. Melatonin pre-treatment improved plant tolerance to oxidative stress caused by heavy metals, suggesting its potential role in enhancing valerian resilience and its suitability for phytoremediation in contaminated environments.

EXPERIMENTAL

Valerian seedlings were obtained from a local herb collector. The valerian seedlings were immersed in water and 100 μM melatonin solution for 48 h, in the dark, after which the plants were planted in open field conditions. The soil showed a slightly acidic pH reaction, with pH in KCl being 5.56, suitable for growing most medicinal plants. The experiment included six treatments: *i*) control (valerian seedlings immersed in water for 48 h; *ii*) Cd (15 mg/L cadmium sulfate solution treatment after planting in open field conditions); *iii*) Zn (3 g/L zinc sulfate solution treatment); *iv*) melatonin (valerian seedlings were immersed in a 100 μM melatonin solution, for 48 h, in the dark, prior to planting); *v*) melatonin and Cd (melatonin pre-treatment and cadmium sulfate treatment); *vi*) melatonin and Zn (melatonin pre-treatment and zinc sulfate treatment). Three replicates (9 plants per replicate) were used for each treatment. Plants were sampled at the end of October, lyophilized at –50 °C for 25–30 h (VaCo 2, Zirbus Technology, GmbH, Germany) and stored at 4 °C until extraction. All analyses were performed in triplicate.

Chemicals

All solvents and reagents were of analytical or the highest grade available. Water (HPLC grade), methanol (HPLC grade), ethanol (HPLC grade), melatonin (HPLC grade), quercetin-3--beta-D-glucoside, 2,2-diphenyl-1-picrylhydrazyl (DPPH), Folin–Ciocalteu reagent, 2,4,6-Tris-(2-pyridyl)-*s*-triazine (TPTZ), Tween 20, phenylmethylsulfonyl fluoride (PMSF) were purchased from Sigma–Aldrich. Hydrochloric acid, nitric acid, hydrogen peroxide, acetic acid, sodium hydroxide, zinc(II) hydroxide, cadmium(II) hydroxide, sodium bicarbonate were purchased from Lachner. Gallic acid, Trolox, ferric chloride anhydrous, ferrous sulfate heptahydrate, sodium acetate trihydrate, magnesium carbonate, polyvinylpyrrolidone (PVP), copper(II) chloride, ammonium acetate, sodium dihydrogen phosphate, potassium-sodium tartrate, neocuproine and pyrogallol were purchased from Acros. All solutions were prepared in distilled water.

Melatonin analysis

Melatonin direct extraction with methanol was performed under dark artificial light.[11] Weighted lyophilized valerian roots were mixed with methanol in total volume of 10 mL. After 15 – 17 h of shaking at 4 °C in the dark, 30 min ultrasonic treatment was performed at the same temperature (WiseClean WUC, Witeg GmbH, Germany). Prior to vacuum evaporation (Rotavapor R-215, Buchi Switzerland), the tubes were centrifuged at 6000 rpm for 30 min (Alresa Mod, Digicen). The extracts were dissolved in 1 mL of methanol, filtered (0.45 μm) and analyzed with high-pressure liquid chromatography (HPLC, Agilent 1100 Series) coupled with a fluorescence detector (FLD), reversed phase C18 gravity column (Nucleodur, 3 μm particle diameter, Macherey-Nagel, Germany) and integrated pre-cell as well as programmed mobile phase consisting of 20 % methanol: 80 % water. The flow rate of the analyte was 1.5 mL/min, at 25 °C.

Heavy metal and macro-elements determination

Perkin–Elmer Analyst 400 atomic absorption spectrophotometer (AAS) was used to determine heavy metal concentrations. Lyophilized valerian leaves and roots were digested with 3

mL of concentrated HNO_3, 3 mL of H_2O_2 and 1 mL of concentrated HCl in closed polytetrafluoroethylene (PTFE) vessels in a microwave oven. All determined metals were atomized in an oxidizing light blue flame formed by mixture of compressed air (10 L/min) and acetylene (2.5 L/min). Contents of Cd, Zn, Mg and Ca were established respectively at the wave lengths: 228.8, 213.7, 285.2 and 422.7 nm, using the deuterium background for correction of signal for Cd and Zn.

Total phenol and flavonoid determination

Folin–Ciocalteu (FC) colorimetric method in alkaline medium was used to analyze the total phenols from 30 % ethanol extracts.[12] Samples or gallic acid standards (200 μL) were mixed with 1 mL of FC reagent, followed by 800 μL Na_2CO_3 after 5 min. After 2 h incubation in the dark, absorbance was read at 760 nm. The results were expressed as mg of gallic acid equivalents (GAE) per g of extract. Chang *et al*. colorimetric method was used to determine the flavonoid content.[13] Quercetin was used for the calibration curve. Samples or standards were mixed with ethanol, aluminum chloride, potassium acetate and water, then incubated for 30 min at room temperature. Absorbance was measured at 415 nm, with blanks prepared by replacing aluminum chloride with distilled water.

Antioxidant activity

Benzie and Strain method was used, for the determination of ferric reducing antioxidant power.[14] Reduction potential substances react with potassium ferricyanide in forming the ferrocyanide (absorption maximum at 593 nm). Also, the antioxidant capacity of extracts was measured on the basis of the stable 1,1-diphenyl-2-picrylhyorazyl (DPPH) free radical scavenging activity according to the method described by Soler-Rivas and coworkers.[15] Apak *et al*. method was used to measure the cupric reducing antioxidant capacity of plant root and leaf extracts. Trolox was used as a standard, and the reduction potential was expressed as $TEAC_{CUPRAC}$ in mmol equivalents of trolox g dry matter (mmol/L).[16] All experiments were measured using PhotoLab 6600 UV–Vis spectrophotometer (Xylem Analytics Germany Sales GmbH & Co. KG, WTW).

Protein content determination

Protein concentration was determined by Lowry *et al*., and calculated by comparison with a standard curve using BSA as a standard.[17] For protein and enzyme activity determination, lyophilized valerian leaves and roots were powdered in liquid nitrogen and kept at –20 °C to analysis.

Spectrophotometric analysis of peroxidase activity (E.C. 1.11.1.7)

For the peroxidase activity determination, modified Teisseire and Guy method was used.[18] The increase in absorbance at 430 nm (ε_{430} = 12 mM^{-1} cm^{-1}) was monitored. The reaction was initiated by adding 3.43 mM H_2O_2 to a mixture containing 50 μL of sample, 10.3 mM pyrogallol and Na phosphate buffer (pH 6.4) at 37 °C. The activity is expressed as μmol/(mg protein min).

Statistical analysis

The data were analyzed using SPSS Statistics, v. 23.0. Analysis of variance (ANOVA) was conducted and significance of differences among treatments and time dependence were tested using the least significant difference (*LSD*). Differences were significant at the $*p < 0.05$ probability level.

RESULTS AND DISCUSSION

Having ascertained that melatonin could effectively ameliorate Cd and Zn--induced phytotoxicity in valerian, the actions were taken to estimate whether this toxicity had an effect on melatonin biosynthesis. Fig. 1 shows the results of endogenous melatonin in the roots of valerian after treatment with exogenous melatonin (100 μM) and heavy metals. Valerian, as a plant with exceptional medicinal properties, showed significant concentrations of melatonin in roots, with values of 3.14±0.102 μg/g dry weight and 2.75±0.006 μg/g.

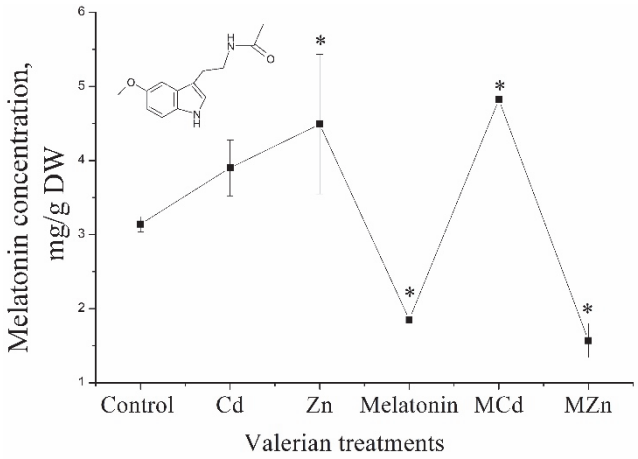

Fig. 1. Melatonin in valerian roots under heavy metal treatment and melatonin pre-treatment. M – melatonin; *Tukey test; $p < 0.05$.

The results indicate that melatonin concentration in the roots increased in response to heavy metal treatments, both in the presence and absence of exogenous melatonin. However, this increase was not observed in the Zn and melatonin treatment, suggesting a possible interaction that limits melatonin accumulation under this specific condition. As shown in Fig. 1, the highest concentration was observed in the roots of plants treated with Zn ions, and with melatonin and Cd ions (4.491 and 4.879 μg/g), which are 30 and 35 % higher concentrations compared to the control roots. There was a decrease in endogenous melatonin content in samples pre-treated with melatonin. This observation aligns with earlier findings, suggesting a complex regulation of melatonin biosynthesis in response to external stress factors like heavy metals.

There are lots of evidences that confirm a great influence of heavy metal ions on the content of compounds with hormonal function. Melatonin synthesis occurs in parallel with melatonin degradation in the chloroplasts and cytoplasm, and the resulting melatonin metabolite, 2-hydroxymelatonin, also acts as a signaling molecule for the induction of defense genes. Melatonin content in paddy rice shoots

was increased under the influence of Cd, suggesting that melatonin could play a crucial role in adjusting the response of different parts of the plant to Cd.[19] In wheat seedlings, exogenous melatonin increased endogenous melatonin and, as a result, enhanced root and shoot growth under cadmium toxicity.[20]

Valerian shows a significant ability to accumulate cadmium in both roots and leaves (Fig. 2A). Higher concentrations of Cd were observed in all three treatments with exogenously added melatonin (melatonin, melatonin+Zn, melatonin+Cd).

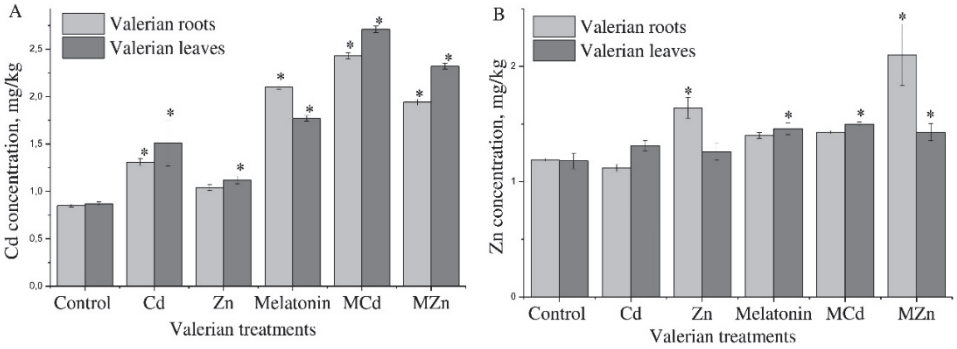

Fig. 2. Cd (A) and Zn (B) concentration in valerian roots and leaves. The data are presented as means of three replicates. M – melatonin; *Tukey test; $p < 0.05$.

The accumulation of Cd in valerian organs treated with Zn was increased compared to the control (0.851 and 0.868 mg/kg in root and leaf) with amounts to 1.038 mg/kg in root and 1.121 mg/kg in valerian leaf. Cd ions showed a greater possibility of translocation, which is a prerequisite for efficient phytoextraction and accumulation of metals in the aerial parts of plants. Melatonin also showed a positive effect in plants pre-treated with this hormone in terms of the accumulation of larger amounts of Cd. Increased accumulation occurs in examined plant species treated with both Zn and Cd. Thus, the concentration of Cd in the roots of plants treated with Zn and melatonin was 2.431 mg/kg of valerian root, which is twofold higher compared to treated plants with zinc without melatonin (1.310 mg/kg). A similar increased accumulation of Cd was observed in the leaves.

It is important to note that of the total amount of ions that are bound by the roots, only a part is absorbed into the cells. Melatonin may enhance the effectiveness of valerian in phytoremediation, particularly in the context of Cd contamination. By promoting the accumulation and translocation of Cd, melatonin could support the use of valerian in soil decontamination efforts, especially in slightly polluted soils.

Zinc belongs to a group of moderate mobility within plant tissues. In the case when its concentration in the soil is low, the intensity of transmission from older to younger parts of the plant was extremely weak. In case the concentration in the

external environment is high, it accumulates in the roots.[21] The study demonstrates that melatonin, both exogenously applied and naturally present in valerian, plays a significant role in ameliorating the phytotoxicity induced by heavy metals. The results suggest that melatonin enhances the concentration of endogenous melatonin in roots, especially under the influence of Cd, which may contribute to the plants defense mechanisms against heavy metal stress.

Potato weed is a hyper accumulator of Cd with high Cd tolerance. Under conditions of low Cd concentration, melatonin not only improved the activity of antioxidant enzymes, but also improved the transfer of Cd to the cell wall and vacuoles, removing Cd away from sensitive parts of the cell, and accelerating its absorption.[22]

The influence of melatonin and heavy metals on the content of macro elements is shown in Fig. 3. The results showed the presence of a high concentration of Mg (Fig. 3A), and even higher Ca contained in valerian leaves (Fig. 3B).

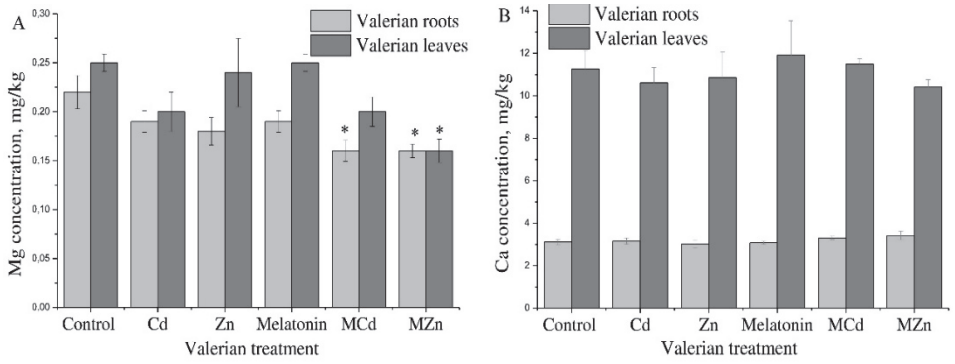

Fig. 3. Mg (A) and Ca (B) concentration in valerian roots and leaves. The data are presented as means of three replicates. M – melatonin; *Tukey test; $p < 0.05$.

Under higher Cd levels, macronutrients are somewhat decreased. Because Cd and mineral nutrients share identical pathways for transport, they have similar effects on balance at an ionic level.[10] Exogenously added melatonin did not prominently affect the changes in Mg and Ca concentrations compared to the control. A statistically significant decrease in magnesium concentration occurred in plants pre-treated with melatonin and treated with Cd and Zn. The reduction referred to both analyzed plant organs, compared to the control. Ca levels remained relatively stable across treatments, with no significant changes. The heavy metal interaction with soil matrix is decisive for the phytoremediation concept. In principle, soil particles sorption reduces the activity of metals in the system. Higher capacity of cation exchange leads to higher sorption and immobilization of metals. In acidic soils, the desorption of metals bound in the soil solution is stimulated due to the participation of H^+.[23]

The uptake of metals into plant roots is a complex process involving the transfer of metals from the soil to the root surface and within the root cells. Understanding the uptake process is difficult due to the complex nature of the rhizosphere, which is in continuous dynamic change in interaction with the plant root, the soil that creates it, and the microorganisms that live within the rhizosphere.[23]

The results of spectrophotometric determination of total phenols and flavonoids concentration in ethanol extracts of valerian roots and leaves are shown in Table I. The concentration of phenolic compounds in valerian root ranged from 26 to 37 mg/g of lyophilized root material, while in its leaves the values ranged from 70 mg/g in melatonin pre-treated plants to 95 mg/g of lyophilized leaf in melatonin and Zn treated plants. Treatment of valerian with Cd ions had an inhibitory effect on the content of total phenolic compounds in the roots of this plant, although the reduction was not statistically significant.

TABLE I. Total phenol and flavonoid content (mg/g) in valerian roots and leaves under different treatments; ^{a,b,c} – different letters indicate statistically significant difference; *Tukey test, $p < 0.05$

Treatment	Total phenol content		Flavonoid content	
	Roots	Leaves	Roots	Leaves
Control	27.54 ± 0.661^{ab}	83.79 ± 0.457^{d}	3.04 ± 0.085^{a}	45.34 ± 0.972^{b}
Cd	26.58 ± 0.613^{a}	73.67 ± 0.581^{a}	3.23 ± 0.167^{a}	35.03 ± 1.972^{a}
Zn	37.31 ± 0.144^{d}	77.44 ± 0.687^{c}	5.14 ± 0.285^{b}	45.08 ± 1.047^{b}
Melatonin	31.67 ± 0.977^{c}	69.43 ± 0.688^{b}	5.37 ± 0.259^{b}	35.37 ± 0.591^{a}
Cd + Melatonin	31.11 ± 0.681^{bc}	77.66 ± 0.622^{c}	4.88 ± 0.294^{b}	52.69 ± 0.740^{c}
Zn + Melatonin	28.36 ± 0.808^{abc}	94.36 ± 0.547^{e}	6.61 ± 0.235^{c}	56.62 ± 0.538^{c}

Heavy metal concentration is considered a crucial parameter that affects the response of plants in secondary metabolism production. Lower levels of heavy metals enhance the production and higher concentrations inhibit the synthesis of secondary metabolites in plants.[24] Treatments induced different responses in valerian leaves. Namely, under the influence of Cd and Zn ions, and with melatonin and Cd ions, there was a statistically significant decrease in the phenol content compared to the control. Plants pre-treated with melatonin, with and without zinc contamination, show a higher content of total phenols.

The content of flavonoids in valerian roots ranged from 3 to 7 mg/g of lyophilized plant material, while in valerian leaves, flavonoid concentrations were from 35 to 57 mg/g. The valerian leaf shows a seven to fifteen times higher concentration of flavonoids than the root. A statistically significant increase in the concentration of flavonoids in valerian root occurs in all included treatments, except for the treatment with Cd ions which inhibited the production of these secondary metabolites. Zinc and melatonin treatment showed the highest flavonoid content in valerian leaves, followed by cadmium and melatonin treatment. Cd reduced

flavonoid levels substantially. Variations in the content of phenolic compounds in plants result from a large number of factors, which, in addition to genetic factors, include the area of cultivation as well as numerous environmental factors. Biotic and abiotic stress (pathogens, viruses, mechanical damage, temperature extremes, UV radiation, imbalance in mineral nutrition, heavy metal and herbicide pollution, drought, salinity) cause an increase in the level of phenolic compounds in vegetative shoots and roots.[25] The addition of melatonin improved the anthocyanin content in tomato plants under Ni stress and in rosemary herb under Cr stress.[26] Melatonin has many physiological functions in plants, and the most researched function is the prevention of oxidative damage caused by various abiotic stressors such as salinity,[27] low temperatures[28] and the toxic effects of cadmium. The content of total phenols, flavonoids and proanthocyanides gradually improved with melatonin treatment in berries.[29]

In the results of the CUPRAC test, significantly higher ability of valerian leaves to reduce Cu ions was observed (two to three times) compared to the root (Fig. 4A).

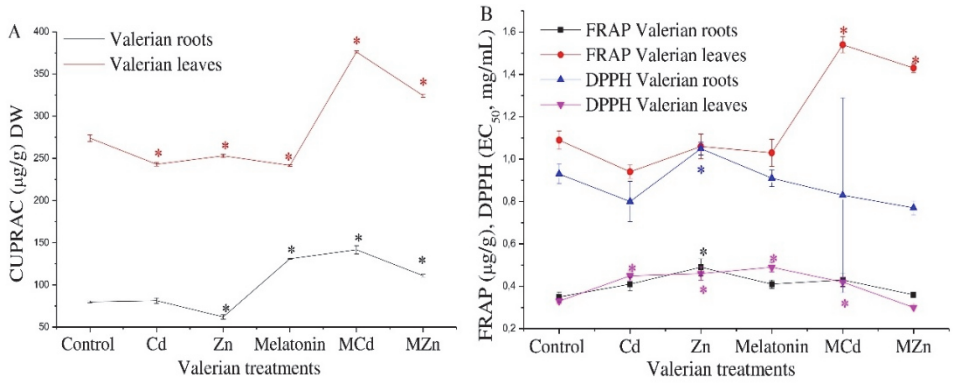

Fig. 4. Antioxidant activity estimated by CUPRAC (A), FRAP and DPPH (B) test. The data are presented as means of three replicates; *Tukey test, $p < 0.05$.

In all five treatments, the ability to reduce Cu^{2+} in valerian roots was significantly increased, while in leaves, the reduction ability was reduced in plants treated with Cd and Zn ions (243.05 and 253.05 μg/g) compared to the control (273.93 μg/g). Exogenous melatonin in combination with heavy metal treatment also shows a significant positive effect on the reduction of Cu ions, in both roots and leaves.

According to the test results, the ability to neutralize DPPH radicals in valerian roots treated with Cd ions is higher (0.8 mg/mL) compared to untreated roots (0.93 mg/mL, Fig. 4B). Exogenous melatonin also increased the ability to neutralize DPPH radicals in valerian root (0.91 mg/mL) compared to the control. Likewise, the roots of plants pre-treated with melatonin show a greater ability to neutralize DPPH radicals with an increased concentration of Cd (0.83 mg/mL) and Zn (0.77

mg/mL) ions, which indicates an increase in antioxidant capacity in situations of oxidative stress caused by cadmium ions. The valerian leaf, with higher content of phenolic compounds found, shows a several times greater ability to neutralize DPPH radicals than the root. Valerian leaves grown on soil contaminated with cadmium (0.45 mg/mL) and zinc (0.46 mg/mL) ions, as well as plants pre-treated with exogenous melatonin (0.49 mg/mL), show a significantly reduced ability to neutralize DPPH radicals.

Valerian plants grown on soil contaminated with cadmium and zinc ions show an increased root reduction capacity (0.41 and 0.49 μg/g, respectively, Fig. 4B). Exogenous melatonin also caused a significant increase in reducing power (0.41 μg/g) compared to the control root (0.35 μg/g). Unchanged reducing capacity is observed only in valerian roots treated with zinc and melatonin. In contrast to the roots, a slightly reduced reducing capacity of valerian leaves occurs in plants treated with Cd and Zn (0.94 and 1.06 μg/g), as well as in those pre-treated with melatonin (1.03 μg/g). The increase in the concentration of cadmium and zinc in plants pre-treated with melatonin influenced the increase in the reducing capacity of valerian leaves.

The research results show increased antioxidant activity of plants, especially in the leaf in all applied biochemical tests. The increased antioxidant activity of the leaves of both plant species can be attributed to the increased content of total phenols, compared to the root. There is a very high correlation between the content of phenol and the ability to reduce Fe^{3+} and Cu^{2+}, as well as to neutralize DPPH radicals. The antioxidant activity of melatonin is enhanced in the roots of the analyzed plants, as the root is probably the most frequently mentioned plant organ in earlier research as a potential site of melatonin biosynthesis. The results suggest that melatonin might boost the plants' reducing capacity, enhancing their ability to counteract oxidative damage and potentially assisting in metal detoxification processes.

An increased content of soluble proteins is observed in valerian roots treated with Cd (21.70 mg/g) and Zn (21.70 mg/g) ions compared to the control (11.76 mg/g) as shown in Fig. 5A.

Pre-treatment with melatonin slightly increased the protein content of valerian root, but the increase was not statistically significant. However, melatonin pre--treatment and cadmium ions significantly increased the protein content of valerian roots. Zn with melatonin did not have the same effect. In the valerian leaf, on the other hand, in all six treatments, a statistically significant increase in soluble proteins concentration was observed, compared to the control. There was no increase in peroxidase activity in the leaves (Fig. 5B). It is possible that the defensive activity of peroxidases is based on the protection of plants in the roots, where a statistically significant increase in enzyme activity is observed. Also, the applied

concentration of cadmium ions might not have been toxic for these very resistant plant species.

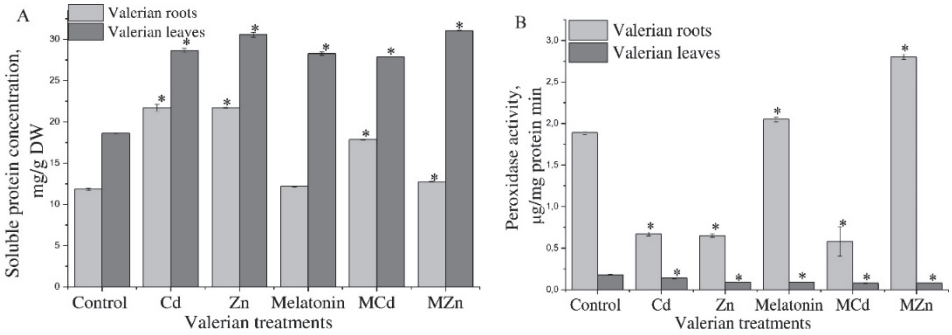

Fig. 5. Total soluble protein concentration (A) and peroxidase activity (B) in valerian roots and leaves under heavy metal treatment and melatonin pre-treatment. The data are presented as means of three replicates; * Tukey test, $p < 0.05$.

Enzyme activity in the leaves was reduced in all applied treatments compared to untreated plants. In general, the most significant increase in peroxidase activity occurs in valerian roots pre-treated with melatonin, plants grown on soil contaminated with zinc ions (2.80 μmol/(mg protein min)).

Melatonin enhances plant metabolism and antioxidant enzymes activity and initiates the ascorbate–glutathione cycle to counteract the effects of heavy metal stress.[30] Heavy metal stress disrupts the balance between reactive oxygen species generation and detoxification by the antioxidative protection system in plants.[31] Plants resist stress-induced ROS production and related adversities by directly neutralizing and removing them or indirectly by controlling the uptake, transport, translocation and sequestration of heavy metals. In the earlier study, authors showed melatonin may act as a free-radical scavenger and broad-spectrum antioxidant, protecting plant tissues from oxidative damage. It could also stimulate antioxidant enzyme production or enhance the activity of other antioxidants to further protect the plant.[32] The increase of endogenous melatonin mitigates cadmium toxicity by balancing H_2O_2 homeostasis and activating antioxidant defense systems in wheat.[33] Melatonin treated plants improve their growth and yield under heavy metal stress conditions. Exogenous melatonin applications can be the trigger for endogenous melatonin production in plants, thereby building up heavy metal tolerance.[2,34] Melatonin application methods vary, including pre-treatment of roots or foliar application just before stress exposure, with some studies exploring repeated applications. Interestingly, seed priming with melatonin has shown lasting effects on stress tolerance, even with a single application, especially for crops like rice, soybean and cucumber, often grown in large-scale agriculture. However,

more research is needed to understand the long-term effects of melatonin treatment and its impact on unpredictable stress conditions.

CONCLUSION

Cadmium and zinc exposure induce significant physiological and biochemical stress in *Valeriana officinalis*, disrupting antioxidative balance, reducing phenolic and flavonoid contents and impairing nutrient homeostasis, particularly in leaves. The application of melatonin alleviates these stress effects and enhances the plant defense mechanisms by elevating antioxidant activity, increasing peroxidase enzyme levels, promoting the accumulation of protective compounds and enhancing soluble protein levels. The heavy metal concentration and exposure duration could be the controlling factors for the synthesis of endogenous melatonin. Melatonin might help to confer the heavy metal stress tolerance in valerian due to the increase of endogenous melatonin under Cd and Zn stress conditions, and modulated metal uptake.

Melatonin acts as a potent bio-stimulant and stress-mitigating agent, improving antioxidant capacity, biochemical composition and nutrient balance in valerian under heavy metal exposure. These findings highlight melatonin's potential as a sustainable and effective strategy to enhance plant resilience and phytochemical quality in contaminated environments. Gaining deeper insight into melatonin-mediated signaling and responses could help maintain crop productivity in soils contaminated with heavy metals. However, additional research is essential to fully uncover the roles of melatonin and enable its effective and sustainable application in agriculture.

ИЗВОД

МЕЛАТОНИН КАО МОДУЛАТОР ТОКСИЧНОСТИ ТЕШКИХ МЕТАЛА И АНТИОКСИДАТИВНА ЗАШТИТА У ВАЛЕРИЈАНИ

ЕЛВИСА ХОЦИЋ[1], МИЛИЦА БАЛАБАН[2], СЕБИЛА РЕКАНОВИЋ[1] и ХАЛИД МАКИЋ[1]

[1]Биотехнички факултет, Универзитет у Бихаћу, Луке Марјановића bb, 77000 Бихаћ, Босна и Херцеговина и [2]Природно–математички факултет, Универзитет у Бања Луци, Младена Стојановића 2, 78000 Бања Лука, Босна и Херцеговина

Тешки метали, свеприсутни у земљишту и води, као озбиљан еколошки проблем, ремете хомеостазу минералне исхране биљака, осмотску равнотежу и метаболизам. Примена неких биостимуланата може ублажити поремећај. Мелатонин као сигнални молекул и антиоксидант игра важну улогу у расту биљака и толеранцији на стрес због своје способности да директно неутралише реактивне врсте кисеоника и азота. У овом раду је испитано смањење или ублажавање штетних ефеката тешких метала код биљака валеријане узгајаних на отвореном пољу употребом мелатонина. Течна хроматографија високог притиска са флуоресцентним детектором коришћена је за идентификацију и квантификацију концентрације мелатонина у екстрактима корена валеријане. Такође, испитан је физиолошки и биохемијски статус биљака под абиотским стресом, посебно код биљака

претходно третираних мелатонином од 100 μM. Веће концентрације ендогеног мелатонина измерене су у корену биљака третираних Cd и Zn, са сличним резултатима у концентрацијама протеина. Примена мелатонина ублажила је негативан ефекат Cd, што је посебно очигледно код третмана Cd-мелатонином који је обновио или повећао нивое биоактивних једињења. Мелатонин ефикасно ублажава стрес изазван Cd и Zn код валеријане побољшавајући и неензимске и ензимске антиоксидативне системе и промовишући синтезу заштитних једињења. Ови налази истичу потенцијал мелатонина као одрживог биостимуланса за подршку отпорности и продуктивности биљака у окружењима оптерећеним тешким металима.

(Примљено 1. априла, ревидирано 17. априла, прихваћено 16. јула 2025)

REFERENCES

1. M.A. Altaf, Y. Hao, H. Shu, M. A. Mumtaz, S. Cheng, M. N. Alyemeni, P. Ahmad, Z. Wang, *J. Hazard. Mater.* **454** (2023) 131468 (https://doi.org/10.1016/j.jhazmat.2023.131468)
2. E. Hodžić, S. Galijašević, M. Balaban, S. Rekanović, H. Makić, B. Kukavica, D. Mihajlović, *Turkish J. Chem.* **45** (2021) 737 (https://doi.org/10.3906/kim-2012-7)
3. E. Hodžić, M. Balaban, B. Kukavica, S. Rekanovic, in *Melatonin: Production, Functions and Benefits*, A. R. Martínez, F. L. Muñoz, J. Egea, Eds., Nova Science Publishers, Hauppauge, New York, 2021 (ISBN: 978-1-53619-031-1)
4. N. Zhang, H. J. Zhang, B. Zhao, Q. Q. Sun, Y. Y. Cao, R. Li, et al., *J. Pin. Res.* **56** (2014) 39 (https://doi.org/10.1111/jpi.12095)
5. M. H. Siddiqui, S. Alamri, Q. D. Alsubaie, H. M. Ali, A. A. Ibrahim, A. Alsadon, *Ecotox. Environ. Saf.* **180** (2019) 656 (https://doi.org/10.1016/j.ecoenv.2019.05.043)
6. R. Colombage, M. B. Singh, P. L. Balla, *Int. J. Mol. Sci.* **24** (2023) 7447 (https://doi.org/10.3390/ijms24087447)
7. F. Godoy, K. Olivos-Hernández, C. Stange, M. Handford, *Plants* **10** (2021) 186 (https://doi.org/10.3390/plants10020186)
8. T. Chen, Y. Su, *Human Ecol. Risk Assess.: An Int. J.* **24** (2018) 1550 (https://doi.org/10.1080/10807039.2017.1416580)
9. C. H. Shekhar, H. Kırmızıbekmez, *Phytochem. Rev*. (2024) (https://doi.org/10.1007/s11101-024-10061-x)
10. Md. N. Hoque, Md. Tahjib-Ul-Arif, A. Hannan, N. Sultana, S. Akhter, Md. Hasanuzzaman, F. Akter, Md. S. Hossain, Md. A. Sayed, Md. T. Hasan, M. Skalicky, X. Li, M. Brestič, *Intern. J. Mol. Sci*. **22** (2021) 11445 (https://doi.org/10.3390/ijms222111445)
11. M. B. Arnao, J. Hernandez-R, *Phytochem. Anal*. **20** (2009) 14 (https://doi.org/10.1002/pca.1083)
12. V. L. Singleton, R. Orthofer, R. M. Lamuela-Raventos, *Meth. Enzym*. **299** (1999) 152 (https://doi.org/10.1016/S0076-6879(99)99017-1)
13. C. C. Chang, M. H. Yang, H. M. Wen, J. C. Chern, *J. Food Drug Anal.* **10** (2002) 178 (https://doi.org/10.38212/2224-6614.2748)
14. I. F. F. Benzie, J. J. Strain, *Meth. Enzym*. **299** (1999) 15 (https://doi.org/10.1016/S0076-6879(99)99005-5)
15. C. Soler-Rivas, J. C. Espin, H. J. Wichers, *Phytochem. Anal*. **11** (2000) 330 (https://doi.org/10.1002/1099-1565(200009/10)11:5<330::AID-PCA534>3.0.CO;2-G)

16. R. Apak, K. Güçlü, B. Demirata, M. Özyürek, S. E. Çelik, B. Bektaşoğlu, K. Işıl Berker, D. Özyurt, *Molecules* **12** (2007) 1496 (https://doi.org/10.3390/12071496)
17. O. H. Lowry, N. J. Rosebrough, A. L. Farr, R. J. Randall, *J. Biol. Chem.* **193** (1951) 265 (https://doi.org/10.1016/s0021-9258(19)52451-6)
18. H. Teisseire, V. Guy, *Plant Sci.* **153** (2000) 65 (https://doi.org/10.1016/S0168-9452(99)00257-5)
19. Y. Jiang, S. Huang, L. Ma, L. Kong, S. Pan, X. Tang, H. Tian, M. Duan, Z. Mo, *Antioxidants* **11** (2022) 776 (https://doi.org/10.3390/antiox11040776)
20. W. Zeng, S. Mostafa, Z. Lu, B. Jin, *Front. Plant Sci*. **13** (2022) 847175 (https://doi.org/10.3389/fpls.2022.847175)
21. A. Baran, *Ecol. Chem. Eng., A* **19** (2012) 669 (https://doi.org/10.2428/ecea.2012.19(07)069)
22. Y. Tang, L. Lin, Y. Xie, J. Liu, G. Sun, H. Li, Z. Liu, Z. Huang, Z. He, L. Tu, *Int. J. Phytorem*. **20** (2018) 295 (https://doi.org/10.1080/15226514.2017.1374341)
23. H. Obata, M. Umebayashi, *J. Plant Nutr*. **20** (1997) 97 (https://doi.org/10.1080/01904169709365236)
24. M. H. Ibrahim, Y. Chee Kong, N. A. Mohd Zain, *Molecules* **22** (2017) 1623 (https://doi.org/10.3390/molecules22101623)
25. L. Chalker-Scott, *Adv. Bot. Res*. **37** (2002) 103 (https://doi.org/10.1016/S0065-2296(02)37046-0)
26. M. S. Jahan, S. GuO, A. R. Baloch, J. Sun, S. Shu, Y. Wang, G. J. Ahammed, K. Kabir, R. Roy, *Ecotox. Environ. Saf*. **197** (2020) 110593 (https://doi.org/10.1016/j.ecoenv.2020.110593)
27. J. Li, J. Liu, T. Zhu, C. Zhao, L. Li, M. Chen, *Int. J. Mol. Sci.* **20** (2019) 1735 (https://doi.org/10.3390/ijms20071735)
28. J. Li, J. Xie, J. Yu, J. Lyv, J. Zhang, D. Ding, N. Li, J. Zhang, E. P. Bakpa, T. Yang, T. Niu, F. Gao, *Front. Plant Sci.* **13** (2022) 998293 (https://doi.org/10.3389/fpls.2022.998293)
29. Y. Xu, Y. Li, K. G. Maffucci, L. Huang, R. Zeng, *Molecules* **22** (2017) 2080 (https://doi.org/10.3390/molecules22122080)
30. M. Moustafa-Farag, A. Mahmoud, M. B. Arnao, M. S. Sheteiwy, M. Dafea, M. Soltan, A. Elkelish, M. Hasanuzzaman, S. Ai, *Antioxidants* **9** (2020) 809 (https://doi.org/10.3390/antiox9090809)
31. S. Singh, P. Parihar, R. Singh, V. P. Singh, S. M. Prasad, *Front. Plant Sci.* **6** (2016) 1143 (https://doi.org/10.3389/fpls.2015.01143)
32. E. Hodžić, M. Balaban, N. Šuškalo, S. Galijašević, D. Hasanagić, B. Kukavica, *J. Serb. Chem. Soc.* **84** (2019) 11 (https://doi.org/10.2298/JSC180504070H)
33. J. Ni, Q. Wang, F. A. Shah, W. Liu, D. Wang, S. Huang, S. Fu, L. Wu, *Molecules* **23** (2018) 799 (https://doi.org/10.3390/molecules23040799)
34. S. Menhas, X. Yang, K. Hayat, T. Aftab, J. Bundschuh, M. B. Arnao, Y. Zhou, P. Yhou, *J. Plant Growth Regul*. **41** (2022) 922 (https://doi.org/10.1007/s00344-021-10349-8).